WAVE AND TIDAL, TES, DNV GL

Quantification of uncertainty in sub-sea acoustic measurement, and validation of wave-current kinematics, at a tidal energy site

---

GEORGE CROSSLEY

This thesis is submitted in partial fulfilment of the requirements for the award of an Engineering Doctorate, jointly awarded by the University of Edinburgh, the University of Exeter, and the University of Strathclyde.

The work presented has been conducted under the industrial supervision of DNV GL Energy as a project within the Industrial Doctoral Centre for Offshore Renewable Energy (IDCORE).

It is impossible to record physical or biological processes everywhere all of the time. Therefore it is useful to develop numerical models, validated at a discrete number of real data points, to estimate process characteristics at selected points in space and time. Prerequisites to the development of numerical models are applicable theories and accurate field data. This study looks at a numerical model designed to simulate the velocity inflow characteristics to a Blade Element Momentum model, which can be used to conduct loads and performance optimization on tidal turbine design. The inflow model combines the kinematics of tidal currents and wind generated waves, applying pre-existing theory, using generic inputs. The model is validated and calibrated using field measurement data from a UK site with a particular focus on the interaction between wave and current velocities. A significant proportion of this study is given to the accurate characterisation of sea data recorded using Doppler Current Profilers (DCPs), the current state-of-the-art in ocean measurement. A ’Virtual’ DCP is developed numerically in order to quantify inaccuracies in the recording of certain parameters and to improve validation of the model. The Virtual Doppler Current Profiler is a tool which is applicable to the tidal energy industry and oceanography as a whole, in quantifying and minimising inaccuracies inherent in the recording of certain parameters with DCPs; turbulence intensity, for example could overestimated by up to 50 %, dependent on current and wave conditions. The tool is of further use in the estimation of directional surface elevation (3D) spectra, another novel aspect of this work, presented here. The thesis goes on to demonstrate that representing the interactions between wave and current velocities linearly, simulates a close and reasonable comparison with measurements taken. This is the first study of its kind, comparing theoretical and measured water particle velocities at tidal turbine scale, and the methodology would allow for similar studies at different sites to be conducted, to further support the use of linear wave-current interactions in the simulation of subsurface water particle kinematics.

Declaration

I declare that this thesis has been composed solely by myself and that it has not been submitted, either in whole or in part, in any previous application for a degree. Except where otherwise acknowledged, the work presented is entirely my own.

George Crossley
September 2017

Executive Summary

As developers seek to convert the energy of the tides into electricity, sub-sea turbines must be designed to perform well in increasingly harsh conditions. Such energetic seas have historically been avoided, hence measurements taken below the surface in strong tidal currents and large waves are relatively few, and the theory behind these interactions is underdeveloped. This thesis compares measurements of subsurface velocity taken in the field, at a UK site proposed for development, to the velocity outputs of a model capable of combining waves and currents in a number of ways. In particular the interaction between waves and currents is investigated. The methodology incorporates a novel virtual velocity measurement instrument to measure the model flow, replicating the physical instruments used at sea, such that direct comparisons can be made between the two data-sets. Model and field velocities show good agreement across a range of current speeds and wave heights, with a range of metrics used to demonstrate the suitability of the model, based on linear wave-current theory, for this site. The wave-current interaction module is calibrated, with linear superposition of wave and current velocities proving a suitable representation of field velocities. Calculation of a dispersion relationship affected by mean current velocity marginally improves calibration with field data. Analysis of other sites using the tools developed will further validate this type of model, which in combination with blade element momentum theory, is able to predict pre-construction site specific loads on tidal turbines.

Doppler Current Profilers (DCPs) are able to measure subsurface water particle kinematics and sea surface elevation simultaneously, however assumptions made by these instruments jeopardise detail when recording in highly energetic seas, particularly where waves and turbulent tidal currents combine. Models developed to optimise the design of tidal turbines require correct site specific inputs to accurately reflect the conditions that a turbine may encounter through its lifetime, moreover, the kinematics of these models must be accurately validated. To overcome the limitations in DCP measurements a 'Virtual' Doppler Current Profiler (VDCP) is developed (Crossley et al. 2017), enabling quantification of error in site characteristics, and 'like for like' comparisons of field and model kinematics that has never previously been documented. The numerical model developed incorporates tidal currents, waves and turbulence combined linearly to output subsurface velocity based on conditions from the field which have been averaged over ten minute intervals. The inputs are simple, time averaged characteristics (current magnitude, direction, and profile; wave height, period and direction, turbulence intensity and turbulence length-scale) and the model outputs velocities over a two dimensional grid that develops with time. The VDCP samples this flow as if it were the very instrument in the field that recorded the data used for validation. Taking into account the heading, pitch and roll of the instrument a data set directly comparable to that measured in the field is generated.

The VDCP is initially used in quantifying error in wave and turbulence statistics, demonstrating a phase dependency of velocity measurements averaged between beams and providing a theoretical error for wave and turbulence characteristics sampled under a range of conditions, in order to improve tidal site characterisation. Spectral moments of the subsurface longitudinal wave orbital velocities recorded by the VDCP can be between 0.1 and 9 times those measured at a point for certain turbulent current conditions, turbulence intensity measurements may vary between 0.2 and 1.5 times the input value in low wave conditions and turbulence length scale calculations can vary by over ten times the input value, dependent on both current and wave conditions. The methodology can be used to determine a theoretical error in any site characterisation parameter for any set of wave, current and turbulence conditions.

Results of the model validation using the VDCP show that the tidal flow model, and in particular the newly developed wave-current interaction module, is effective in simulating field subsurface velocities over a range of depths, for waves of up to $3m$ significant wave height and currents of up to $3.5ms^{-1}$. The model is effective in reproducing the wave climate using both measured and modelled surface elevation spectra, and tests, with marginal improvements, the effect of modifying the dispersion equation to account for currents. Field and model velocities compare well over the frequency range dominated by waves, showing only small underestimations in model standard deviations with respect to those from field data, at depths close to the sea surface. At the low frequency end of the modelled spectra, where large turbulent eddies dominate, there is some deviation in model accuracy, particularly during the ebb tide where recorded turbulence parameters are extremely variable, creating uncertainty due to a relatively small sample size. Between field and model velocity maxima, some scatter is observed, potentially providing uncertainty in the estimation of ultimate loads. Model and field damage equivalent velocities, used in the determination of fatigue loads, agree well. Results suggest that a linear wave-current representation of subsurface velocities at this particular tidal site is applicable. Care should be taken when interpreting this result due to the relatively small sample size, and the possibility of site specific nuances, and as such further studies are proposed.

The Virtual DCP model is a novel development which has proven its usefulness in the work contained in this thesis and in the analysis of commercial field data. It is extremely versatile, adapting to a range of configurations and set up criteria such that it can be used in the quantification of DCP measurement error for a range of flow characteristics. This information is useful in the design of tidal turbines (and other sub-sea structures) as well as for oceanographic and biological processes. The tidal flow model developed extends beyond the capability of similar numerical models with the capability to model the interaction between waves and currents according to a number of different options. Combined with the VDCP, which samples from the model flow field, a system is created that can be effectively calibrated to find the best model solution to replicate flows at a tidal site measured by a 'real' DCP over a broad range of sea conditions and water depths. The purpose is to ensure that models used to predict the sub surface velocities in the field are suitable and a key question was to understand whether the linear super-position of linear wave models and a turbulent current flow provides a realistic model of the particle kinematics with a view to undertaking loads analysis of a tidal stream turbine. Comparisons of this kind have not previously been documented, and this thesis lays out the path to improved site characterisation and model validation, as well as drawing conclusions on useful methods for modelling flows impacted by waves.

Acknowledgements

This work was supported by the Industrial Centre for Offshore Renewable Energy (IDCORE) with funding from the Energy Technologies Institute and the Research Councils Energy Programme [grant number EP/J500847/1] and DNV GL. The author would like to thank DP Energy for supplying the field data and Applied Renewables Research Ltd for their assistance with DCP data analysis. I would like to offer a huge thank you to my supervisors, in particular Doctors Armando Alexandre, Steven Parkinson and Helen Smith, who guided me through this process patiently and with constant encouragement. To my family and my friends, many of whom are now quite sure of the difference between waves and tides, I will always be grateful for unwavering support in all aspects of life over the last four years.

Contents

List of Figures

List of Tables

Nomenclature

α	Relative direction between waves and currents
β	Power law exponent
χ	Displacement from initial position in x direction
η	Surface elevation
μ_{ij}	Covariance of variables i and j
Ω	Absorption coefficient
ω	$2\pi/T$ = Wave angular frequency
ω_a	Absolute wave angular frequency (as seen by a stationary observer)
ω_r	Relative wave angular frequency (in the moving frame of reference)
$\overline{u}$	Mean current velocity
Φ	Velocity potential
ϕ	Phase function
ρ_{ij}	Correlation of variables i and j
σ	Mean directional spreading per frequency
σ	Standard deviation
σ_c	Directional spread with sine function per frequency
τ	Time lag
θ	Mean direction per frequency
θ_b	Beam angle from vertical
$\tilde{n}_i$	Non-dimensional frequency parameter, where $i = u, v, orw$
ζ	Displacement from initial position in z direction
${}^pL_i$	Length scales, where $p = x, y, orz$ and $i = u, v, orw$
a	Wave amplitude
$ATAN2$	Four quadrant inverse tangent
b_i	Along beam i velocity
c	Constant
C_a	Absolute wave celerity (as noted by stationary observer)
C_r	Relative wave celerity (as noted by observer moving with the current)
C_{ij}	Co-spectrum of i and j
d	Water depth

D_p	Peak direction
EI	Echo Intensity
f	Frequency
g	Acceleration due to gravity
G_{ij}	Cross-spectra of i and j
H	Heading
H_s	Significant wave height
k	$2\pi/\lambda$ = Wave number
k_a	Absolute wave number
k_r	Relative wave number
L	Wavelength
M	Velocity beam to earth transformation matrix
m_n	n^{th} Spectral moment
$MDIR$	Mean direction of spectrum
N	Number
n	Normal vector to the surface
P	Pitch
Q_{ij}	Quad-spectrum of i and j
R	Roll
r	Point described by x, y, and z
RM	DCP Rotation Matrix
S	Refers to a spectrum (dependent on context)
S_η	Spectrum of surface elevation
S_{ii}	Auto-spectrum of flow speed variation in i direction
S_{ij}	Cross-spectrum of flow speed variation in i or j directions
$SDIR$	Directional spread
$SDIR_c$	Integrated directional spreading
T	Period
t	Time
T_a	Absolute period
T_e	Energy period
T_i	Time scales, where $i = u, v, orw$
T_m	Mean period
T_p	Peak period
T_r	Relative period
T_z	Zero crossing period
TF	Transfer function (between surface elevation and another wave signal)

TI	Turbulence Intensity
TI_p	Turbulence intensity, where $p = x, y, orz$
u	Velocity in x direction (horizontal)
U_0	Longitudinal velocity measured by DCP prior to rotation
v	Boundary velocity vector
V_0	Lateral velocity measured by DCP prior to rotation
w	Velocity in z direction (vertical)
$w*$	Window function
W_0	Vertical velocity measured by DCP prior to rotation
x	Horizontal displacement
y	Lateral displacement
z	Vertical displacement
z_{ref}	Reference depth
U	Generic velocity (i.e. in any direction)

Chapter 1

Introduction

The movement of the earth and its moon, with respect to the sun cause large bodies of water to move around the surface of the earth, generating tides. With the rise and fall of each tide, great volumes of water flood into and ebb out of our seas, rushing around the coast, accelerating through straits and narrows, and driving many biological processes; putting energy into marine and coastal ecosystems. It may also be a valuable source of energy for use by humans. Where the tidal range and bathymetric features around a coastline are suitable, tidal currents, moving at high speeds, can be used to generate electricity.

1.1 Tidal stream industry

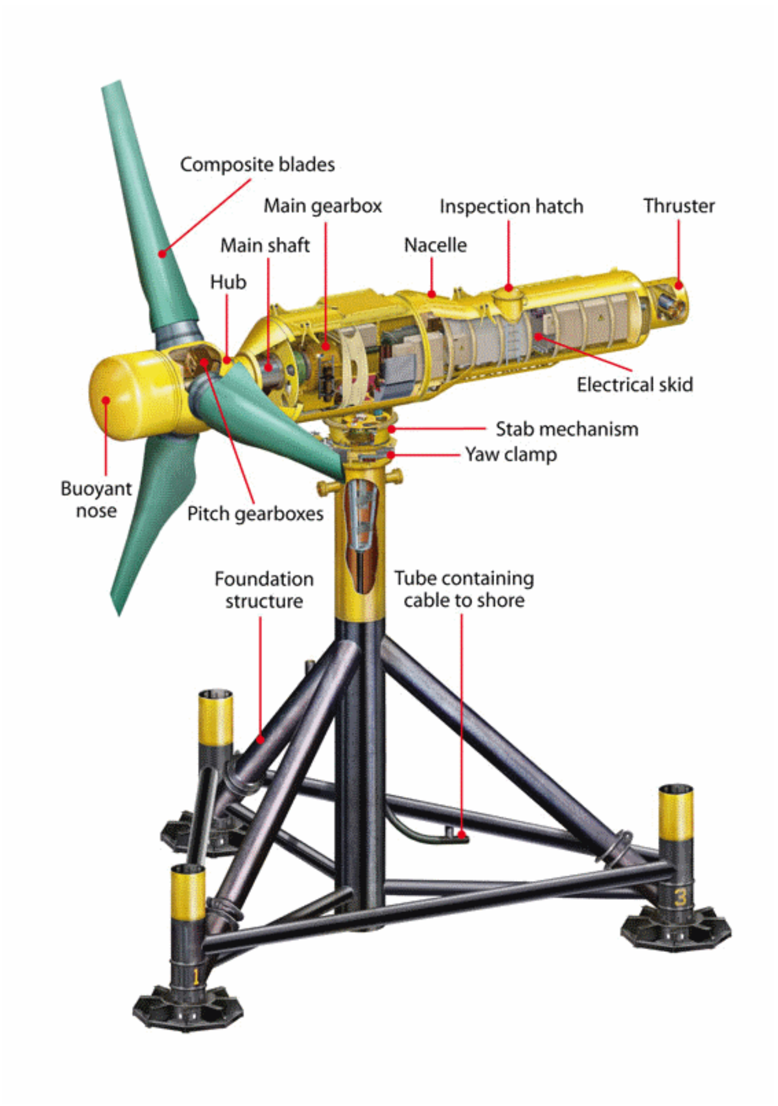

Figure 1.1: Diagram of Alstom 1MW Tidal Turbine

The most common technology for converting tidal energy into electricity uses a rotor with hydrofoil blades designed to spin a generator. These turbines most typically have three blades, rotating about a horizontal axis (Atlantis Resources Limited 2017)(Andritz Hydro Hammerfest 2017), as seen in figure 1.1, however there are designs with less (Tocardo 2017) and more (Sabella 2017) blades, as well as with vertical axes. Turbines can be mounted on the seabed or suspended from near the surface by a gantry or moored float. Design choices are made based on factors that aim to reduce the cost of tidal energy, including yield, efficiency, reliability and maintainability. In 2016 power was supplied to the grid from the Pentland Firth in Scotland, where the first turbines, of the largest proposed multi-turbine tidal stream array (MeyGen 2013), began operation. Several other devices in Europe and Canada are successfully installed and operating, and developers are increasingly looking to exploit tidal energy globally. Many early prospected UK sites such as the sound of Islay, Kyle Rhea (Neill, Vogler, Goward-Brown, Baston, Lewis, Gillibrand, Waldman & Woolf 2016), and Strangford Lough (Neill, Hashemi & Lewis 2016) were sheltered from ocean waves however as we explore further tidal sites such as the Pentland Firth, Fairhead, and St David's suffer from mean wave heights which may reach extremes of up to 10m. The addition of waves increases the challenge involved in characterising tidal sites and understanding the effects of combined wave-current loads on tidal turbines will be increasingly important in optimizing the performance and resilience of tidal devices as well as in understanding resource availability. Studies have shown that impacts by waves could reduce the theoretical tidal resource by 10% (Lewis et al. 2014), as well as having more localised effects on device components, such as turbine blades (Barltrop et al. 2006), or drive-trains.

1.2 Tidal resource & site characterisation

Tidal resource in this context, is the energy from tidal currents available for extraction. That which can be converted to electricity. The latitude and bathymetry of UK waters lend themselves to a very large tidal resource. The size, and suitability for extraction of the tidal resource in any particular location is dependent on a variety of factors; primarily tidal range, but also local and regional bathymetry as well as meteorological effects. Site characterisation is the process through which the suitability of a site for tidal energy is determined and also can go on to provide the information that will inform numerical models for long-term and future predictions. Acoustic Doppler (AD) technology is commonly used in measurement of the subsurface velocities and sea surface elevation required to characterise a site. Upward looking devices emit sound pulses from transducers which are reflected by particles suspended in the water column returning a signal to the instrument (see figure 1.2). The signal is frequency shifted according to the velocity in the pulse direction at which the particle was travelling. By emitting pulses at high frequency and trigonometrically transforming the resultant velocities in combination with two or three other transducer records, a three-dimensional velocity time-series can be calculated. The assumption being that the flow is homogeneous over the volume between the instrument's transducer beams (Lu & Lueck 1999*b*).

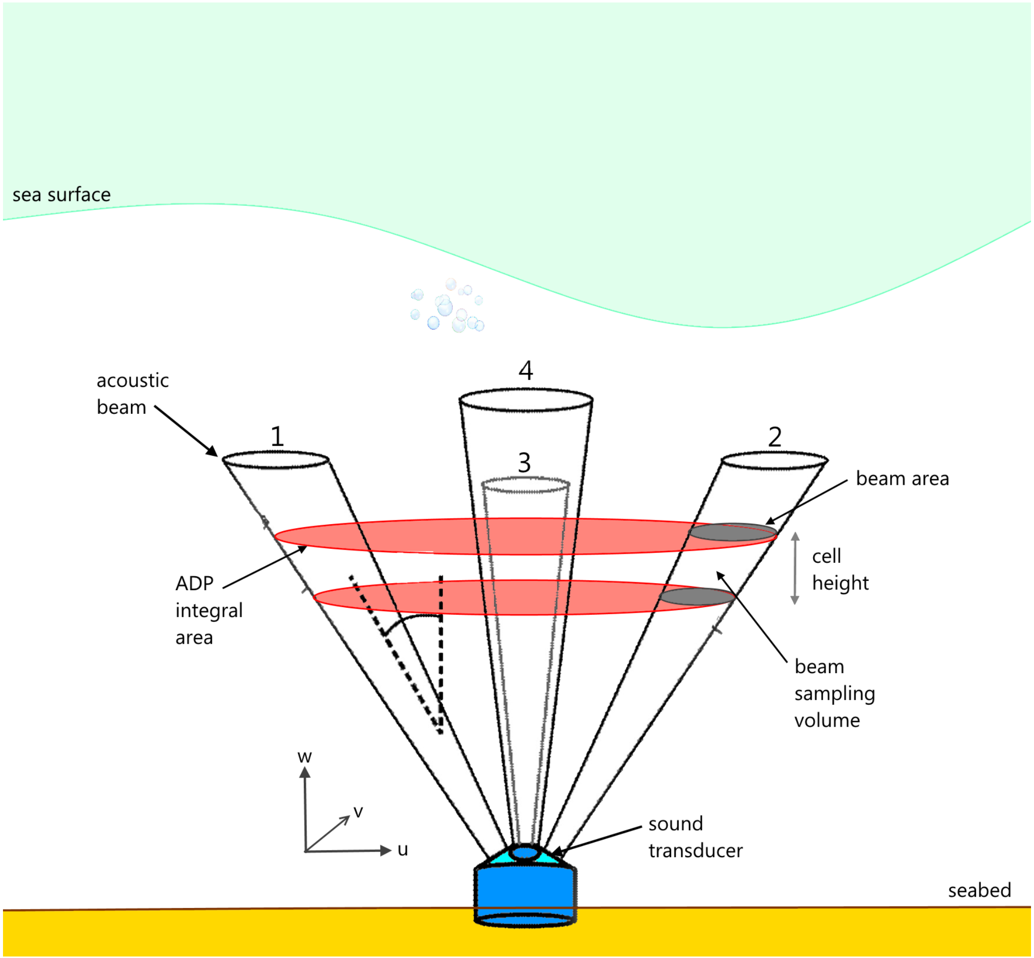

Figure 1.2: Diagram of 4 beam Doppler Instrument

This is effective for measuring mean current conditions; however, the smaller fluctuations resulting from waves and turbulence can be obscured by this method (Nystrom et al. 2007). Measurement of tidal flows is discussed in greater detail in chapter 3 and limitations and theoretical errors in the measurement of waves and turbulence are discussed in chapter 6. The analysis conducted in these studies aims to allow improvements in site characterisation such that a full and accurate description of the conditions a turbine might encounter can be defined.

1.3 Numerical modelling; ocean, sea and water particle

Numerical modelling of the ocean reduces the cost and effort that would be required to physically measure everywhere, all of the time. In the tidal energy context models are designed at scales ranging from kilometres (e.g. entire oceans) to millimetres (e.g. turbine blade tips). These models have the potential to estimate conditions over large areas and time-scales, requiring only a relatively small number of field measurements to validate them. In this study turbine scale models are investigated. In order to optimise the design of tidal stream turbines, many of which will be exposed to sea conditions, robust design procedures are required. This includes the use of validated models to represent current kinematics in the presence of waves and turbulence for pre-construction site-specific load calculations. Numerical models vary in fidelity from highly computationally expensive fluid dynamic models to less intensive models such as Tidal Bladed, developed by DNV GL (Garrad Hassan), which is a Blade Element Momentum model (see section 5). The difference in the models is in the detail, and whilst a computational fluid dynamic model may be able to simulate specific elements of a model to a high degree of accuracy over a number of days, other numerical models such as Tidal Bladed may be able to simulate the results of a large number of conditions (in less detail) in a matter of hours. This is further discussed in chapter 5.

Wave-current interaction, at the time of writing, is the subject of much research and is the focus of this study, which aims to summarise experimental and theoretical research, to investigate improved methods for measuring marine conditions, and to validate models for the prediction of combined wave and current sea states. The kinematics caused throughout the water column by a passing wave are likely to be substantially modulated by the addition of current. Observation of waves over extreme currents will immediately indicate a change in the wave profile. Following currents will reduce wave steepness whilst opposing currents will steepen waves, and in extreme cases result in wave breaking. This is a consequence of current effects on wave celerity and hence wavelength and period, which in turn have impacts on subsurface pressure and kinematics. Current speed and direction will effect waves in different ways and therefore the propagation of waves from one current region to another will cause changes in wave speed, length and hence height, with the possibility of also causing refraction. The challenge is to model the kinematics caused by this effect throughout the water column such that engineers of offshore structures can make siting and design decisions based on the predicted loading effects of waves in tidal areas.

1.4 Motivations & Hypothesis

Numerical modelling of the sea is important for many aspects of science and engineering to estimate and predict behaviours and characteristics of the water, it's contents, and it's surroundings. In order for models to be practical to use, within the limitations of modern computing power, assumptions must be drawn, and these assumptions must be proved to be reasonable within the bounds of their chosen application. In this study a model is developed to simulate a flow field which is in turn used to undertake loads and performance optimization of tidal turbines. Waves are likely to have effects on the resilience, and performance of tidal turbines and it is therefore important to effectively model waves and their interaction with tidal currents. The model is based upon existing theory, which has typically been formulated for relativity low current speeds, and assumes a linear interaction between wave and current velocities. Relatively few studies of waves in high speed currents environments have been undertaken and therefore the hypothesis to be proved is hence:

' The assumption that wave and tidal current velocities interact linearly is reasonable for determination of the inflow to a tidal turbine.'

1.5 Objectives

The study will validate, and calibrate, the kinematics of the wave-current interaction module of a numerical tidal flow model with data taken from the field. To achieve this several steps must be taken:

1. Development of wave-current interaction module
2. Development of a Virtual Doppler Current Profiler

3. Characterisation of field data at tidal site
4. Effective comparison of model and field kinematics

Development of wave-current interaction module. Firstly to adapt an existing tidal flow model to enable incorporation of the new module. Secondly to develop the new module based on existing theory to incorporate the flexibility that will allow for a range of options to be chosen by which to enable calibration to field data.

Development of a Virtual Doppler Current Profiler. The development of a numerical code that replicates the behaviour of a Doppler Current Profiler. This code should be versatile enabling the representation of instruments of a range of configurations, and should cope with changes in orientation, measurement depth, and a range of flow conditions. An option to display the virtual instrument should also be available to enable a better understanding of functionality. This tool will be used to determine theoretical error in the measurement and characterisation of tidal flows.

Characterisation of field data at tidal site. A multi-stage process that will require extraction of data from measurement instruments, processing, quality checking and analysis. The VDCP can be used in the estimation of directional surface elevation spectra (by locating beam intercepts with the surface) and also for theoretical corrections to wave and turbulence statistics.

Effective comparison of model and field kinematics. Model outputs must be compared to field data to enable validation and calibration of the wave-current module. To do this direct comparisons must be made. The VDCP will again be used, this time sampling the simulated flow, as if it were an instrument in the field, such that limitations in the measurement process are restricted.

1.6 Thesis outline

A tidal flow model is developed, and described in chapter 5, that combines theory of waves, currents and turbulence to rapidly simulate subsurface velocities for a broad range of sea conditions. To validate the theory behind the model it is necessary to have field data that is directly comparable to the outputs of a model. The 'Virtual' Doppler Current Profiler described in chapter 6 'samples' from the tidal flow model as if it were a real instrument recording velocities at sea. The VDCP model is used for two purposes. Firstly it is used in order to investigate and quantify the limitations and error arising from estimates of wave and turbulence sub-surface velocity characteristics measured by a DCP at sea. The study uses the VDCP under a range of environmental and set up conditions enabling, in particular, improved estimation of the turbulence intensity and length scale inputs to the tidal flow model. Secondly the VDCP is used to facilitate a 'like for like' comparison between measured field data and sampled model data, as in chapter 7. Flow data containing simultaneous measures of subsurface velocity and surface elevation from a UK tidal site for development was measured with a 5 beam TRDI Sentinel V deployed in the winter of 2014/2015. The configuration of the TRDI DCP set-up and its positioning at the site are input into the VDCP. Specific sea conditions are selected from the data and fed to the flow model which simulates subsurface velocities based on averaged current, wave and turbulent conditions. The VDCP is used to sample the simulated tidal flow enabling 'beam-to-beam' comparison of model and field kinematics, subsequently eliminating the assumptions made about the flow when resolving to three dimensional velocities.

Chapter 2

Background theory

The background will explain theory developed for waves, and turbulence in tidal currents, as well as exploring previous research into the interactions between waves and currents, from both an experimental and a numerical perspective. The tidal flow model (chapter 5), that has been developed for validation in tidal sites experiencing wave-current conditions, is based upon theory outlined below, looking in particular at waves, turbulent currents and their interaction. Measurement (chapter 3) of these conditions is also largely based around the theory presented in this chapter, which will often be referred back to.

2.1 Waves

To avoid the complexity of solving the full hydrodynamic equations for water wave motion it is often sensible to use a linear approximation, avoiding non-linear terms. The following equations (starting at equation 2.5) make the assumption that wave height is small in relation to wavelength, and this is found to be a suitable model for ocean waves in many situations. Steep waves or waves in shallow water are better described by higher order, non-linear theories and are essential to understanding the development of sea-state spectra, however linear theory provides a simplistic method that can be usefully applied in order to describe the sea-state for deep and intermediate water depths. This section assumes wave kinematics by means of the velocity potential. This helps describe all relevant fluid properties including particle displacements, velocities and accelerations as well as surface elevation, slope and dynamic pressure.

2.1.1 Velocity potential and linear theory

Velocity potential is a scalar potential introduced in 1788 (Anderson 1998) that is used in potential flow theory. It is continuous and describes fluid velocity over the entire domain with the capacity to define both regular and irregular waves. Linear theory, in its capacity for modelling ocean waves, assumes the fluid is irrotational, inviscid and incompressible. A fluid velocity vector can be written as the gradient of a scalar velocity potential $\Phi(x, y, z, t)$

$$\nabla \Phi = u \tag{2.1}$$

Assuming incompressibility, density is assumed to be constant through time and space such that $\nabla . u = 0$ throughout the fluid, where u is velocity. The kinematic boundary condition dictates that fluids at the boundary must remain, yielding the Neumann boundary condition for a solid surface, $n.\nabla\Phi = n.v$, where v is the boundary velocity vector and n is a normal vector to the surface. At the free surface if waves that occur are assumed to have small amplitude, compared to their wavelength and the water depth, then at still water level:

$$\frac{\partial \Phi}{\partial z} = \frac{\partial \zeta^t}{\partial t} \tag{2.2}$$

where ζ is the vertical displacement in the free surface with time (t). For an inviscid, irrotational flow (Φ) with constant density, conservation of momentum leads to the unsteady Bernoulli equation which applied to the free surface, and assuming surface tension forces are negligible gives the single free surface condition, for vertical displacement (z) is equal to depth (h), and g is acceleration due to gravity:

$$\frac{\partial^2 \Phi}{\partial t^2} = -g\frac{\partial \Phi}{\partial z} \tag{2.3}$$

Waves are also subject to the radiation condition and the resultant equation for linear wave theory is given in equation 2.4 where ω is the wave angular frequency and wave phase is described by ϕ.

$$\Phi(x, y, z, t) = Re\{\phi(x, y, z)e^{-i\omega t}\} \tag{2.4}$$

In linear wave theory the most important assumption is that wave height is small in comparison to wavelength. Sir George Airy first presented linear wave theory in 1845 and it is commonly referred to by his name (Goda 2010). It can be presented in the form:

$$\Phi(x, y, z, t) = a\frac{g}{\omega}\frac{\cosh(k(z + h))}{\cosh(kh)}\sin(k(x\cos\theta + y\sin\theta) + \omega t + \phi) \tag{2.5}$$

Where a is the wave amplitude and g is acceleration due to gravity. x, y, and z specify location in the longitudinal, lateral and vertical planes respectively, where z is positive upwards and zero at the free surface. h is the water depth such that $z + h = 0$, k is the wave number $(k = 2\pi/\lambda)$, θ is the wave direction. Reference for other symbols can be found in the nomenclature contained in the front matter. This linear approximation (equation 2.5) is accurate for small ratios of the wave height to water depth (for waves in shallow water), and small ratios of wave height to wavelength (for waves in deep water).

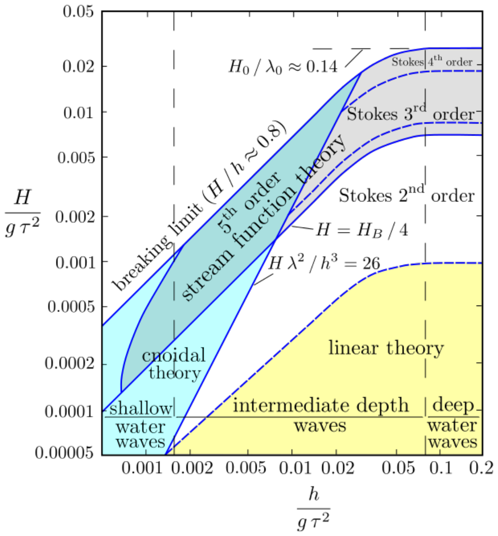

Figure 2.1: Validity of theories for periodic water waves (Méhauté n.d.)

By the superposition of numerous waves described in this way (Eq. 2.5) a representation of a realistic sea surface can be modelled, where individual waves are not interacting. From the velocity potential (Eq. 2.5) can be derived a number of kinematic descriptors including displacement (Eqs. 2.6 and 2.7) and velocity (Eqs. 2.8 and 2.9) in multiple directions.

$$\chi = a\frac{\cosh k(z+h)}{\sinh(kh)}\cos(kx-\omega t+\phi) \tag{2.6}$$

$$\zeta = a\frac{\sinh k(z+h)}{\sinh(kh)}\sin(kx-\omega t+\phi) \tag{2.7}$$

$$u = ak\frac{g}{\omega}\frac{\cosh(k(z+h))}{\cosh(kh)}\cos(kx-\omega t+\phi) \tag{2.8}$$

$$w = ak\frac{g}{\omega}\frac{\sinh(k(z+h))}{\cosh(kh)}\sin(kx-\omega t+\phi) \tag{2.9}$$

Here χ and ζ refer to the displacement, in the horizontal and vertical, of a water particle from its undisturbed position x or z, and u and v are velocities in x and z directions (horizontal and vertical). Where h tends to infinity, i.e. for deep water, the equations are greatly simplified, reducing as in equations 2.10, 2.11, 2.12 and 2.13.

$$\chi = a\exp(kz)\cos(kx-\omega t-\phi) \tag{2.10}$$

$$\zeta = a\exp(kz)\sin(kx-\omega t-\phi) \tag{2.11}$$

$$u = ak\frac{g}{\omega}\exp(kz)\cos(kx-\omega t) \tag{2.12}$$

$$v = ak\frac{g}{\omega}\exp(kz)\sin(kx-\omega t) \tag{2.13}$$

Water particle motions are illustrated in Figure 2.2 for waves over a finite or "intermediate" depth, as in equations 2.6 and 2.7. For waves in deep (infinite depth) water ellipses are circular as described by equations 2.10 and 2.11.

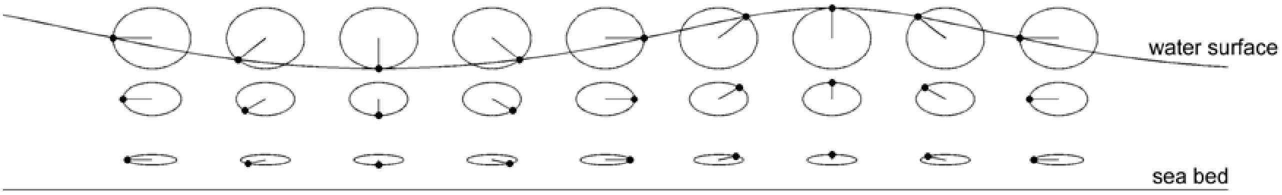

Figure 2.2: Linear Wave Particle Motions in finite depth

2.1.2 Dispersion relation

The dispersion relation describes the effect of dispersion on waves travelling in water, describing the dispersion of frequencies, implying that waves of different wavelengths travel at differing phase speeds. It therefore relates wave frequency to wavelength. Water waves may also exhibit amplitude dispersion, however this is a non linear effect that will not be discussed here. For a given angular frequency ω and depth h, there is a single wave number k. The wave number $k = 2\pi/L$ where L is wavelength. The dispersion relation implies that long period waves propagate faster than short period waves, and as such the wave speed, or celerity, defined as $C = L/T$, where T is wave period. A storm generates many wave frequencies and as these waves propagate away from the source, they begin to group. Waves of similar phase velocities group together allowing conservation of energy. Long wavelength waves of the same wavelength will all travel at the same speed and will move faster than waves of shorter wavelength. As a result, waves of a particular wavelength will tend to group together and waves of different wavelengths will tend to disperse, hence the name (Whitham 1974). The dispersion equation is commonly presented as shown in equation 2.14, or for deep water, as in equation 2.15.

$$\omega^2 = gk \tanh kh \tag{2.14}$$

$$\omega^2 = gk \tag{2.15}$$

$\omega = 2\pi/T$ and $k = 2\pi/\lambda$, hence substituting into equation 2.15 we can solve for wavelength in deep water analytically as seen in equation 2.16. However for finite depth it is necessary to use iterative numerical methods for given water depth and wave height. The method by Guo (2002) is given in section 2.4.3.

$$\lambda_{deep} = \frac{gT^2}{2\pi} \tag{2.16}$$

Wave pass a specified point at phase speed, c_p

$$c_p = \frac{\lambda}{T} = \frac{\omega}{k} \tag{2.17}$$

Substituting equation 2.14 into 2.17 gives equation 2.18 for finite depths and equation 2.19 for deep water where $\tan kh$ tends to 1.

$$c_p = (\frac{g}{k} \tan kh)^{1/2} \tag{2.18}$$

$$c_{p(deep)} = \sqrt{\frac{g}{k}} \tag{2.19}$$

Wave energy propagates at a different speed known as group speed and is written as below, in equation 2.20.

$$c_g = \frac{\partial \omega}{\partial k} \tag{2.20}$$

Substituting the dispersion equation (2.14) would give equation 2.21 which for deep water becomes equation 2.22.

$$c_g = \frac{1}{2} c_p (1 + \frac{2kh}{\sinh 2kh}) \tag{2.21}$$

$$c_{g(deep)} = \frac{c_p}{2} \tag{2.22}$$

Based on the dispersion equation (2.14) group speed generally increases with wavelength, as shown in the equations above. However in shallow water where phase speed is no longer dependent on wavelength it is said that waves are non-dispersive. In general sites prospecting for tidal energy development are in intermediate to deep water (typically 30-60m) and hence shallow water situations are not discussed in detail here. At tidal sites, strong currents need to be accounted for. Current velocity (varying with depth) and direction will change the propagation and dispersion of waves. It is hence appropriate to study the system in a frame of reference moving at a uniform current velocity such that an absolute angular velocity and wave number can be determined. This is discussed in section 2.4.

2.1.3 Irregular waves

The surface of the ocean rarely looks like that depicted in figure 2.2, however for many situations one can superpose numerous of the regular waves described above in order to create the irregular sea surface elevation that you would expect to see at sea. These sinusoidal wave components will be of a range of amplitudes, periods and directions such that (from ζ in equation 2.6):

$$\eta = \sum_{n=1}^{\infty} a_n \sin(k_n(x\cos\theta_n + y\sin\theta_n) - \omega_n t + \phi_n) \tag{2.23}$$

Where a is the wave amplitude, k is the wave number, x and y are locations in the horizontal plane, ω is the wave angular frequency, ϕ is the wave phase, and the subscript n denotes the individual regular wave form. The sum of the variances of the component waves is proportional to the total energy, E, of the wave system such that:

$$E = \sum_{n} \frac{1}{2} a_n^2 \tag{2.24}$$

It is useful to describe wave information in the frequency domain, as a wave spectrum which can used to describe the distribution of different regular wave components with respect to frequency and direction. The spectrum can then be summarised in terms of various parameters including measures of wave height, period and directionality. The directional variance spectrum describes how energy in the wave field is distributed with frequency, f, and direction θ (Eq. 2.25). Alternatively this can be broken down into functions describing either the total energy at each frequency (Eq. 2.27) or the distribution of energy at each frequency with direction (Eq. 2.26). D is the directional spreading function.

$$\sum_{f}^{f+\delta f} \sum_{\theta}^{\theta+\delta\theta} \frac{1}{2} a_n = S(f,\theta)\delta f \delta\theta \tag{2.25}$$

$$S(f,\theta) = S(f)D(f,\theta) \tag{2.26}$$

The frequency spectral density ($S(f)$), often referred to simply as the wave spectrum, describes how energy in the wave field is distributed with frequency (i.e. for each individual wave period).

$$S(f) = \int_0^{2\pi} S(f,\theta)\mathrm{d}\theta \tag{2.27}$$

Assuming that phases are distributed randomly between zero and π the sea surface elevation will follow a Gaussian distribution. The directional spreading function satisfies the properties

$$\int_0^{2\pi} D(f,\theta)d\theta = 1 \tag{2.28}$$

$$D(f,\theta) \leqslant 0 \text{ for } [0\ 2\pi] \tag{2.29}$$

2.1.4 Spectral moments and wave parameters

The omnidirectional spectrum previously described can be reasonably summarised by wave height(Eq. 2.31), period(Eqs. 2.32, 2.33, 2.34) and directional descriptors(Eqs. 2.38, 2.39). In order to calculate these parameters it is necessary to take moments of the spectrum as in equation 2.30. Moments (m) of spectra are frequently used in this study in comparing field and model spectra with a single characteristic. The zeroth moment is the area under spectral curve, equivalent to the total variance, or energy, of the wave system. Moments greater than zero give increasing weight to higher frequencies, and negative moments mean the opposite, giving greater weight to lower frequencies. Primarily zeroth and first moments are used in this study, in order to capture primarily, the energy in the spectra, as well as focusing on the effect of higher frequency elements of the waves.

$$m_n = \int_0^{\infty} f^n S(f) \mathrm{d}f \tag{2.30}$$

Wave height and period measurements can be calculated from the spectral moments. The significant wave height, H_s, is the mean of the highest third of the waves in a time-series of waves representing a certain sea state. This corresponds well with the average height of the highest waves in a wave group. H_s computed on the basis of a spectrum, is referred to as H_{m0}.

$$H_s = 4\sqrt{m_0} \tag{2.31}$$

The mean wave period, T_m, is the mean of all wave periods in a time-series representing a certain sea state, or the inverse of the average frequency in the spectrum.

$$T_m = \frac{m_0}{m_1} \tag{2.32}$$

The peak wave period, T_p, is the wave period with the highest energy, where f_p is the frequency at which $S(f)$ reaches its peak value.

$$T_p = \frac{1}{f_p} \tag{2.33}$$

Wave energy period (T_e or T_{-10}) is the variance-weighted mean period of the one-dimensional period, or the total wave power in deep water.

$$T_e = \frac{m_{-1}}{m_0} \tag{2.34}$$

2.1.5 Spectral directionality

The mean direction, θ_m at each frequency is given in equation 2.35.

$$\theta_m(f) = ATAN2\left[\int_0^{2\pi} D(f,\theta)\sin(\theta)d\theta,\ \int_0^{2\pi} D(f,\theta)\cos(\theta)d\theta\right] \tag{2.35}$$

The four-quadrant inverse tangent function ($ATAN2(y,x)$) uses logic on the signs of x and y to resolve the 180 degree ambiguity in direction. For the directional spread (σ_i) of energy about the mean direction there are two methods commonly used either according to line moments (l) or circular moments (c).

$$\sigma_l(f) = \left[\int_0^{2\pi} D(f,\theta)(\theta - \theta_m)^2 d\theta\right]^{1/2} \tag{2.36}$$

$$\sigma_c(f) = \left[\int_0^{2\pi} D(f,\theta) \Big[2\sin\Big(\frac{\theta - \theta_m}{2}\Big)\Big]^2 d\theta \right]^{1/2} \tag{2.37}$$

The circular moment definition (Eq. 2.37) approximates the line moment definition for narrow directional bandwidths and can be calculated directly from measured data without the need to estimate the directional spreading function. The average direction ($MDIR$) and spread ($SDIR$) are defined respectively as

$$MDIR = ATAN2\left[\int_0^{\infty} S(f)\sin(\theta_m(f))df, \ \int_0^{\infty} S(f)\cos(\theta_m(f))df \right] \tag{2.38}$$

$$SDIR = \frac{1}{m_0}\int_0^{\infty} S(f)\sigma_m(f)df \tag{2.39}$$

2.1.6 Model spectra

For the modelling of waves representative of those at sea it is useful to create a standard form for the frequency spectrum and directional distribution of a sea-state. The standard shape for a sea spectrum would be determined by wind input, bottom friction, dissipation (by white-capping) and non-linear interactions between wave components. Swell waves are those that have propagated away from the area where the a wind had generated them, and their steepness decreases over the distance travelled, reducing non-linear interactions. Local wind generated waves however, are likely to be steeper, with greater influence from non-linear interaction. This may result in multiple peaks in a spectrum where multiple swells and local wind waves combine.

Uni-modal spectra in deep water generally belong to a family given by equation 2.40 for α, β, r, $s < 0$ and $\gamma \geq 1$.

$$S(f) = \alpha f^{-r}\exp(-\beta f^{-s})\gamma^{\delta(f)} \tag{2.40}$$

Where

$$\delta(f) = \exp(-\frac{1}{2}(\frac{f - f_p}{\sigma f_p})^2) \tag{2.41}$$

and it is usually assumed (as in Mackay (2012)) that

$$\sigma = 0.07 \text{ for } f < f_p \text{ and } \sigma = 0.09 \text{ for} f \leqslant f_p \tag{2.42}$$

α is the scale parameter, β is the location parameter (by frequency), γ is the peak enhancement factor, and r and s define the shape of the spectrum. The peak frequency of the spectrum is

$$f_p = (\frac{s\beta}{r})^{1/s} \tag{2.43}$$

The spectra most commonly referred to for ocean conditions are the Pierson-Moskowitz, Bretschneider, and the JOint North Sea WAve Project (JONSWAP)spectra (Hasselmann et al. 1973). The Pierson-Moskowitz spectrum for fully developed seas fixes α, r, s, γ at $5.0 \times 10^{-4}, 5, 4, 1$ respectively leaving only beta free to determine the energy in the spectrum. The JONSWAP spectrum allows α, β and γ free whilst r and s are fixed at 5 and 4 respectively. This allows for the greater peaks in spectral shapes cognisant of fetch limited wind-seas. This type of spectra are illustrated in Figure 2.3. Using equation 2.40, JONSWAP spectra take a γ value of

3.3, whilst the Bretschneider spectrum uses a γ value of 1. Gamma and Ochi spectra vary r and s values in equation 2.40 as below.

- **Gamma** spectra, r is left free, $s = r - 1$ and $\gamma = 1$.
- **Ochi** spectra, r is left free, $s = 4$ and $\gamma = 1$.

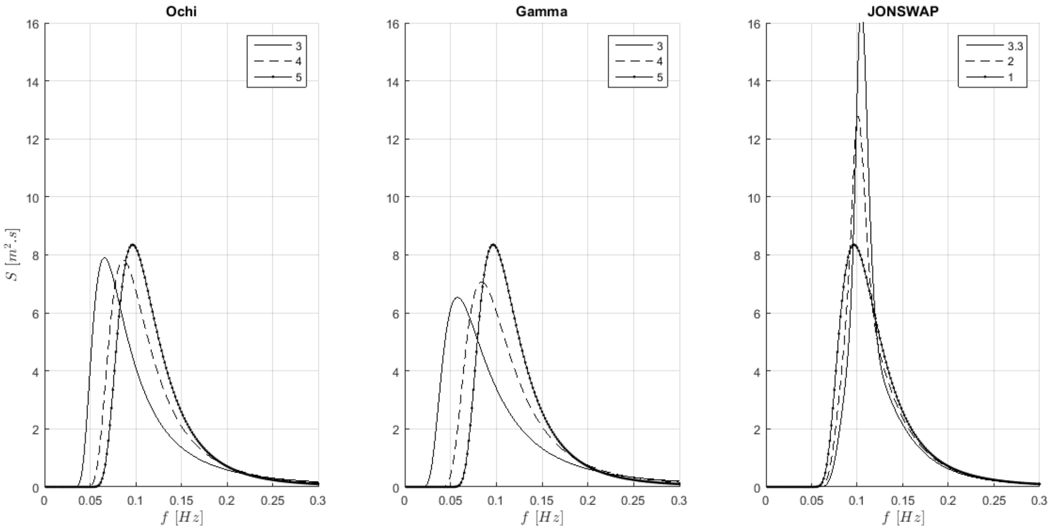

Figure 2.3: Model wave spectra for $\gamma = 1 - 5$

Moments of the spectra (m) can be found explicitly when $\gamma = 1$ as in equation 2.44.

$$m_n = \frac{\alpha}{s}\beta^{(n-r+1)/s}\Gamma\Big(\frac{r-n-1}{s}\Big) \text{ for } n < r - 1 \tag{2.44}$$

$$\Gamma(z) = \int_0^\infty t^{z-1}e^{-t}dt \tag{2.45}$$

If $\gamma \neq 1$ a numerical integration must be used.

2.1.7 Model directional distributions

The wrapped normal distribution in equation 2.46 is an example of a commonly used form of the directional distribution.

$$D(\theta, f) = \frac{1}{\sigma_l(f)\sqrt{2\pi}}\sum_{k=-\infty}^{\infty} exp\Bigg[-\frac{1}{2}\Big(\frac{\theta - \theta_m(f) - 2\pi k}{\sigma_l(f)}\Big)^2\Bigg] \tag{2.46}$$

σ_l is the line moment spread parameter as in equation 2.36. The summation over k ensures all energy outside of 0 and 2π is included, however in most practical cases the summation may be taken between $k = -2$ and $k = 2$. For JONSWAP type spectra (i.e. fetch limited) the directional distribution is bimodal at frequencies above twice the peak frequency. Ewans (2001) directional distribution uses a double Gaussian distribution to model this bi-modality.

$$D(f, \theta) = \frac{1}{\sigma_m(f)\sqrt{8\pi}}\sum_{k=-\infty}^{\infty}\Bigg[exp\Bigg[-\frac{1}{2}\Big(\frac{\theta - \theta_1(f) - 2\pi k}{\sigma_m(f)}\Big)^2\Bigg] + exp\Bigg[-\frac{1}{2}\Big(\frac{\theta - \theta_2(f) - 2\pi k}{\sigma_m(f)}\Big)^2\Bigg]\Bigg] \tag{2.47}$$

$$\theta_1(f) = \frac{\theta_m + \Delta\theta(f)}{2} \tag{2.48}$$

$$\theta_2(f) = \frac{\theta_m - \Delta\theta(f)}{2} \tag{2.49}$$

$\Delta\theta$ is the separation between the peaks of the two modes and σ here is a function of frequency rather than the directional spread it described previously.

$$\Delta\theta = 14.93 \text{ for } f < f_p \tag{2.50}$$

$$\Delta\theta = \exp\left[5.453 - 2.750\Big(\frac{f}{f_p}\Big)^{-1}\right] \text{ for } f \geqslant f_p \tag{2.51}$$

$$\sigma_m = 11.38 + 5.357\Big(\frac{f}{f_p}\Big)^{-7.929} \text{ for } f < f_p \tag{2.52}$$

$$\sigma_m = 32.13 - 15.39\Big(\frac{f}{f_p}\Big)^{-2} \text{ for } f \geqslant f_p \tag{2.53}$$

The distribution above is very similar to previous formulations in the way that spread varies with frequency. However previous models had assumed a uni-modal distribution where this model becomes bimodal at frequecies greater than $2f_p$. For swell seas however, there is less evidence of bimodal distribution and as such the wrapped normal distribution is preferred, using, for σ_l

$$\sigma_l(f) = 6 + 4\Big(\frac{f}{f_p}\Big)^{-5} \text{ for } f < f_p \tag{2.54}$$

$$\sigma_l(f) = -36 + 46\Big(\frac{f}{f_p}\Big)^{-0.3} \text{ for } f \geqslant f_p \tag{2.55}$$

2.2 Current

The longitudinal current flow profile in a tidal strait typically takes the form of a power law curve due to sea bottom roughness.

$$u(z) = u(z_0)\Big(\frac{h+z}{h}\Big)^{\beta} \tag{2.56}$$

$$\text{for } 0 \geqslant z \geqslant -d \tag{2.57}$$

Here $z = 0$ at the sea surface, h is the water depth, z_0 is a reference height for the mean velocity, and $\overline{u}$ is the mean velocity. The standard power law exponent, β, is typically 1/7 (Lewis et al. 2016).

2.3 Turbulence

Turbulence refers to fluctuations in current speed over a relatively short time-scales, usually less than ten minutes. It is therefore possible to distinguish turbulent events from the predictable longer term changes of the tide. It is less simple to distinguish between turbulent and wave effects, particularly in high energy, high frequency conditions. However models exist for turbulence that can facilitate the separation of significant kinematic components. Turbulence is typically caused by friction of the sea bottom, and changes in water temperature. Flow over bathymetrical variations causes changes in friction and forces water across temperature gradients resulting in eddies of varying scale and motion. Below is a list of factors with the potential to cause or effect turbulence (Tennekes & Lumley 1972):

1. Bed roughness
2. Height above bed
3. Depth of channel
4. Width of channel
5. Length of channel
6. Shape of channel
7. Bathymetrical features upstream
8. Bathymetrical features downstream
9. Thermal behaviour of site
10. Ocean currents
11. Weather
12. River/drainage outflow
13. Coriolis effect
14. Stable, unstable and neutral thermal effects
15. Wind

Turbulent intensity, TI is the most commonly used parameter for defining turbulence with respect to tidal energy development, using mean current velocity ($\overline{u}$), standard deviation (σ) and variance (u') of velocity.

$$TI = \frac{\sqrt{\langle u'^2 \rangle}}{\overline{u}} = \frac{\sigma_u}{\overline{u}} \tag{2.58}$$

Typical average turbulent intensity values at tidal energy sites are in the range 0 to 15%. An asymptotic relationship with mean current speed is typically displayed with high turbulent intensity towards slack tide periods due to the relationship between standard deviation and velocity as velocity becomes small. Turbulence intensity is typically greater near the sea bed where roughness induces turbulent structures, however during instances of waves it is common to see turbulent intensity increase in the top of the water column.

The way in which a site's turbulent characteristics are represented typically depends on what it is you want to know about the flow. Turbulent intensity is the most widely used and accepted illustration of turbulence for understanding behaviour at sites for tidal energy development. This is a useful metric for understanding the stochasticity of the flow, however it does not reveal information about size and scale of turbulent structures. Typical descriptors used by the wind industry include longitudinal, lateral and vertical turbulent intensities as well as length scales, coherence, and shear stresses. Further to this, representations of intermittency and correlation can be useful descriptors. Spatial and temporal structure functions are typically used in the context of turbulent dissipation rate, a measure more commonly used in the field of physical oceanography. Turbulent Kinetic Energy (TKE) presents peaks in the fluctuation of components in three dimensions. Coherent Turbulent Kinetic Energy (CTKE) uses the Reynolds Shear Stresses in the planes of two velocity components presenting peaks in fluctuations of two velocity components. Understanding of turbulence at tidal sites is limited by the amount of good quality data available.

2.3.1 Turbulence Models

Though turbulence could potentially be derived from laws of conservation of mass, momentum and energy, using water temperature, salinity, pressure, density and water motion in three dimensions, the turbulent process is chaotic and hence small variations in inputs and boundary conditions can result in major differences in outputs. Hence a statistical approach is typically used to determine turbulence at a particular site (Burton et al. 2001). A number of relationships describing turbulence have been developed mostly involving a combination of theoretical consideration and empirical fits (Mann 2006, Kaimal et al. 1972, von Karman 1948). Many of these relationships draw upon the wind energy industry, and few have been validated for tidal sites. The Von Karman model (von Karman 1948) has been shown to be well suited (Parkinson & Collier 2016) to turbulence in tidal environments and is presented here in both its basic and improved form.

Basic Von Karman For the longitudinal component of turbulence, S_{uu} represents the auto-spectrum of longitudinal flow speed variation:

$$\frac{fS_{uu}(f)}{\sigma_u^2} = \frac{4\tilde{n}_u}{(1 + 70.8\tilde{n}_u^2)^{5/6}} \tag{2.59}$$

σ_u is the standard deviation of longitudinal flow speed variation and $\tilde{n}_u$ is a non-dimensional frequency parameter incorporating the length scale of longitudinal turbulence, ${}^xL_u$ and the mean flow speed, $\overline{u}$:

$$\tilde{n}_u = \frac{f\ {}^xL_u}{U} \tag{2.60}$$

The corresponding auto-spectra for the lateral and vertical components of turbulence are:

$$\frac{fS_{ii}(f)}{\sigma_i^2} = \frac{4\tilde{n}_i(1 + 755.2\tilde{n}_i^2)}{(1 + 282.3\tilde{n}_i^2)^{11/6}} \tag{2.61}$$

Where:

$$\tilde{n}_i = \frac{f\ {}^xL_i}{\overline{u}} \tag{2.62}$$

Improved Von Karman The improved Von Karman model includes greater detail, incorporating surface roughness and Coriollis effect. It also draws out a model for the atmospheric boundary layer (as used for the wind energy industry) which would not be theoretically valid under water.

$$\frac{fS_{uu}(f)}{\sigma_u^2} = \beta_1 \frac{2.987\tilde{n}_u/a}{(1 + (2\pi\tilde{n}_u/a)^2)^{5/6}} + \beta_2 \frac{1.294\tilde{n}_u/a}{(1 + (\pi\tilde{n}_u/a)^2)^{5/6}} F_1 \tag{2.63}$$

The corresponding auto-spectra for the lateral and vertical components of turbulence are:

$$\frac{fS_{ii}(f)}{\sigma_i^2} = \beta_1 \frac{2.987(1+(8/3)(4\pi\tilde{n}_i/a)^2)(\tilde{n}_i/a)}{(1+(4\pi\tilde{n}_i/a)^2)^{11/6}} + \beta_2 \frac{1.294\tilde{n}_i/a}{(1+(2\pi\tilde{n}_i/a)^2)^{5/6}} F_2 \tag{2.64}$$

The parameters are defined as follows:

$$F_1 = 1 + 0.455\exp[-0.76(\tilde{n}_u/a)^{-}0.8] \tag{2.65}$$

$$F_2 = 1 + 2.88\exp[-0.218(\tilde{n}_i/a)^{-}0.9] \tag{2.66}$$

$$\beta_1 = 2.357a - 0.761 \tag{2.67}$$

$$\beta_2 = 1 - \beta 1 \tag{2.68}$$

$$a = 0.535 + 2.76(0.138 - A)^0.68 \tag{2.69}$$

$$A = 0.115[1 + 0.315(1 - z/h)^6]^{2/3} \tag{2.70}$$

$$h = u^*/6f \tag{2.71}$$

$$C = 2SPR\sin(|\lambda|) \tag{2.72}$$

$$u^* = (0.4U - 34.5fz)/\ln(z/z_0) \tag{2.73}$$

z_0 is the surface roughness length and C is the Coriolis parameter where SPR is the speed of rotation of the earth and λ is the latitude.

Supposing the velocity components $(i, j = u, v, w)$ of a three-dimensional turbulent current are measured at two separate points r and r' at positions x, y, z and x', y', z' respectively then the Euclidean distance between the two points is defined by $d\tau$.

$$d\tau = \sqrt{(x - x')^2 + (y - y')^2 + (z - z')^2} \tag{2.74}$$

The standard deviations of the velocity signal i and j are denoted by σ_i and σ_j respectively. A generalised cross-correlation function, between the velocity component i and j at two points separated in space can be written:

$$\rho_{ij}(d\tau) = \frac{C_{ij}(d\tau)}{(\sigma_i\sigma_j)} \tag{2.75}$$

Where:

$$C_{ij}(\tau) = \lim\inf \frac{1}{\tau\int_0^{\tau} i(x, y, z)j(x', y', z')} \tag{2.76}$$

The nine turbulent length scales are defined as follows:

$$^{x}L_i = \int_0^{\infty} \rho_i i(x' - x)d(x - x') \tag{2.77}$$

$$^{y}L_i = \int_0^{\infty} \rho_i i(y' - y)d(y - y') \tag{2.78}$$

$$^{z}L_i = \int_0^{\infty} \rho_i i(z' - z)d(z - z') \tag{2.79}$$

The method assumes Taylor's frozen turbulence hypothesis (Taylor 1937), such that a velocity spectra can be used to describe the auto-spectral density of the current, and flow coherence is defined empirically. The turbulent flow field generated consists of dimensionless wind speed deviations (δ) where $\overline{u}$ is the mean current velocity and TI is the turbulence intensity, hence the instantaneous turbulent current velocity, u, can be calculated.

$$u = \overline{u}(TI\delta + 1) \tag{2.80}$$

The turbulent time series are generated and stored before running the TFM model as 3 components of normalised, zero mean, unit standard deviation flow speed deviations. In order to combine turbulence into the model, Taylors frozen wake hypothesis must be assumed, since the grid of velocity time-series is generated in the 2D ($y - z$) plane. As such the x dimension becomes time. The point number, N, in the time-series, which equates to the x location can be estimated based on the depth dependent mean current velocity, u, as follows:

$$N = \frac{f_t x}{\overline{u}} \tag{2.81}$$

Where f_t is the frequency at which the turbulence time-series has been generated.

2.4 Wave-current interaction

Understanding how waves and current combine is not only important in understanding the incident loads on offshore, submerged structures but in the measurement of waves, which are often measured indirectly by means of pressure or velocity fluctuations (as discussed in section 3.2.1). Unless the current is properly identified it may be inaccurate to estimate wave properties. Further to this the wave energy spectra could be substantially modified by the presence of currents, with the possibility of greater extremes in wave events.

The first evidence of investigation into wave-current interactions was by Unna (1942) and later by Barber (1948). These theories were developed by Stewart & Longuet-Higgins (1960) showing that a current does work on waves at a certain rate, and introducing the concept of radiation stress. Bretherton & Garrett (1969) then included the concept of action conservation. Wave-current theory became well established through various literature of the late 20th century (Peregrine & Thomas 1978, Phillips et al. 1968, Srokosz 1985, Swan 1972, Whitham 1974). The analytical Stream function proposed by Dean (1965) gives a numerical expression for fully non-linear waves using a Laplace equation and two non-linear free surface boundary conditions. Nichols & Hirt (1973) studied the inclusion of fluid viscosity before Dalrymple (1974, 1977) helped to developed the theory with Dean, including a shear current within a rotational fluid, which by initiating a moving coordinate system (at wave celerity) enables accurate comparison with analytical models for shear flow and 1/7th law current profiles. Furthermore wave kinematics can be calculated right up to the sea surface where Wheeler (or other) stretching methods had previously been used. Eastwood & Watson (1989) unfortunately never published the complete solution, though an analytical Stokes finite amplitude wave on a bilinear sheared current was solved with a fifth order solution that was significantly less computationally demanding than the stream function method developed by Dalrymple.

Whilst understanding of unsteady hydrodynamic loads such as turbulence can be somewhat transferable from the wind turbine industry wave loading brings a different challenge. Of primary concern to tidal device designers will be root-out of plane bending of turbine blades, as well as torque and thrust fluctuations, caused by apparent attenuation in velocity and attack angle of the flow. Barltrop et al. (2006) showed that linear theory in steep waves did not accurately represent bending moments in turbine blades, and out of plane bending moments were found to fluctuate by fifty percent around the mean, whilst thrust and torque fluctuations showed good agreement with linear models. Jesus Henriques et al. (2014) showed good agreement with linear theory through tank testing. Mccann (2007), though not including current, used TidalBladed (Garrad Hassan 2012) in comparison with EMEC site data to show that wave height and period were the significant drivers of loading whilst Milne et al. (2010) developed experiments for oscillatory motion showing through theory and simulation that wave period, height, and direction as well as hub height and overall depth have a significant effect on blade loading.

Substantial theoretical numerical modelling and scale testing has been achieved in the last century to understand the way in which waves and currents interact, and a huge number of lessons have been learned, however conflicting results have led to uncertainty in this area. As more tidal and wave energy devices are deployed and sites prospected, more data is available from real sea situations, largely in the form of Acoustic Doppler Current Profiler (ADCP) data. This opens up the possibility of comparing and improving existing models and theories with real conditions, with the potential to optimise the design of offshore structures in areas of extreme waves and tides.

2.4.1 Effect of current on wave kinematics

To the stationary observer a wave appears to move with celerity C_a, and a current velocity $U \sin\alpha$ is present, where α is the relative direction between waves and currents. But to an observer moving at the speed of the current there appears to be no current velocity and instead the waves have velocity C_r.

$$C_r = C_a - \overline{u} \sin\alpha \tag{2.82}$$

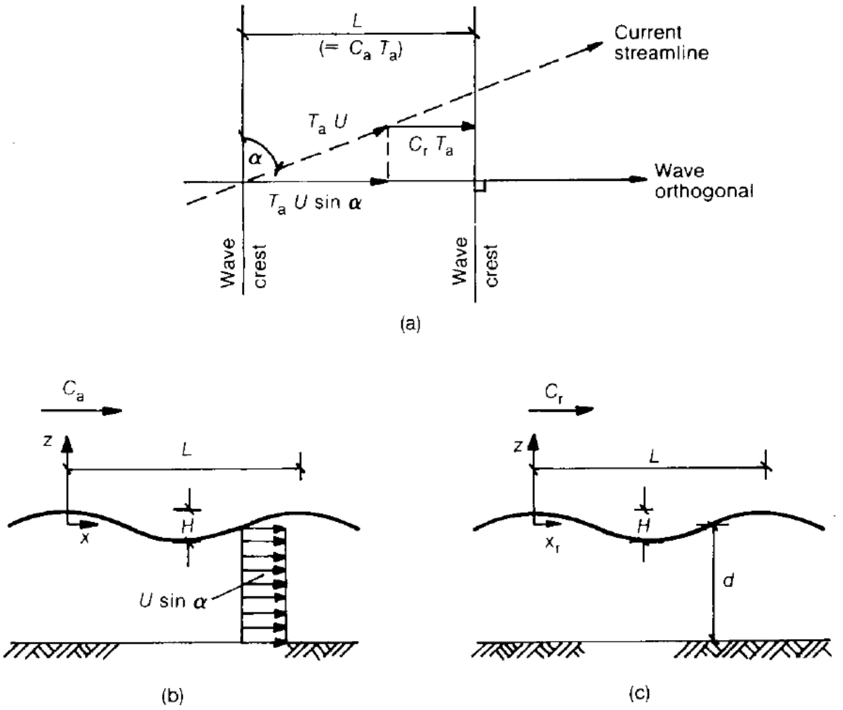

Figure 2.4: Defining sketches for wave on current: (a) wave and current directions; (b) waves in a stationary frame of reference containing wave orthogonal; (c) waves in moving frame of reference containing wave orthogonal Hedges (1987)

Waves pass the stationary observer over a period T_a and the moving observer over a period T_r and hence

$$C_a = \frac{L}{T_a} \tag{2.83}$$

$$C_r = \frac{L}{T_r} \tag{2.84}$$

Combining equations 2.82 and 2.83 gives

$$\frac{1}{T_r} = \frac{1}{T_a}\left(1 - \frac{T_a \overline{u} \sin\alpha}{L}\right) \tag{2.85}$$

Multiplying throughout by $(2\pi d/g)^{1/2}$ (where d is water depth) non-dimensionalizes the equation. This compares with theory defined by Jonsson et al. (1970).

$$\left(\frac{d}{L_r}\right)^{1/2} = \left(\frac{d}{L_a}\right)^{1/2}\left[1 - \frac{T_a \overline{u} \sin\alpha}{d}\left(\frac{d}{L}\right)\right] \tag{2.86}$$

Where L is the wavelength observed as if moving relative to the current (r) or as if stationary, i.e. absolute (a).

$$L_r = \frac{gT_r^2}{2\pi} \tag{2.87}$$

$$L_a = \frac{gT_a^2}{2\pi} \tag{2.88}$$

2.4.2 Wave periodicity

Wave periodicity can be determined by multiplying equation 2.82 by wave number $k(= 2\pi/L)$. ω_r is the relative wave angular frequency (in the moving frame of reference), and ω_a is the absolute wave angular frequency (as seen by a stationary observer).

$$\omega_r = \omega_a - k\overline{u}\sin\alpha \tag{2.89}$$

$$x_r = x_a - t\overline{u}\sin\alpha \tag{2.90}$$

Equation 2.90 describes a coordinate system moving at current speed $\overline{u}$. Hence in the moving frame of reference waves appear to be propagating on still water and as such can be described by linear theory.

$$\eta = \frac{H}{2}\cos(kx_r - \omega_r t) \tag{2.91}$$

Then by substituting equations 2.89 and 2.90 gives equation 2.92.

$$\eta = \frac{H}{2}\cos(kx - \omega_a t) \tag{2.92}$$

As in equations 2.8 and 2.9, relative to the moving frame of reference, horizontal and vertical velocities are described

$$u_r = \frac{H}{2}\omega_r\frac{\cosh(k(z+h))}{\sinh(kh)}\cos(kx_r - \omega_r t) \tag{2.93}$$

$$w_r = \frac{H}{2}\omega_r\frac{\sinh(k(z+h))}{\sinh(kh)}\sin(kx_r - \omega_r t) \tag{2.94}$$

To the stationary observer the horizontal component of velocity is described as in equation 2.95 having substituted for ω_r and x_r in equations 2.89 and 2.90.

$$u_a = \overline{u}\sin\alpha + u_r \quad = \overline{u}\sin\alpha + \frac{H}{2}(\omega_a - k\overline{u}\sin\alpha)\Big(\frac{\cosh k(z+h)}{\sinh kh}\Big)\cos(kx - \omega_a t) \tag{2.95}$$

The absolute vertical velocity can be described as in equation 2.96.

$$w_a = w_r \quad = \frac{H}{2}(\omega_a - k\overline{u}\sin\alpha)\Big(\frac{\sinh k(z+h)}{\sinh kh}\Big)\sin(kx - \omega_a t) \tag{2.96}$$

Taking the full derivative the velocity with respect to time allows estimation of water particle accelerations as discussed in further detail by Hedges (1987).

$$\frac{du_a}{d_t} = \frac{H}{2}(\omega_a - k\overline{u}\sin\alpha)^2\Big(\frac{\cosh k(z+h)}{\sinh kh}\Big)\sin(kx - \omega_a t) \tag{2.97}$$

$$\frac{dw_a}{d_t} = -\frac{H}{2}(\omega_a - k\overline{u}\sin\alpha)^2\Big(\frac{\sinh k(z+h)}{\sinh kh}\Big)\cos(kx - \omega_a t) \tag{2.98}$$

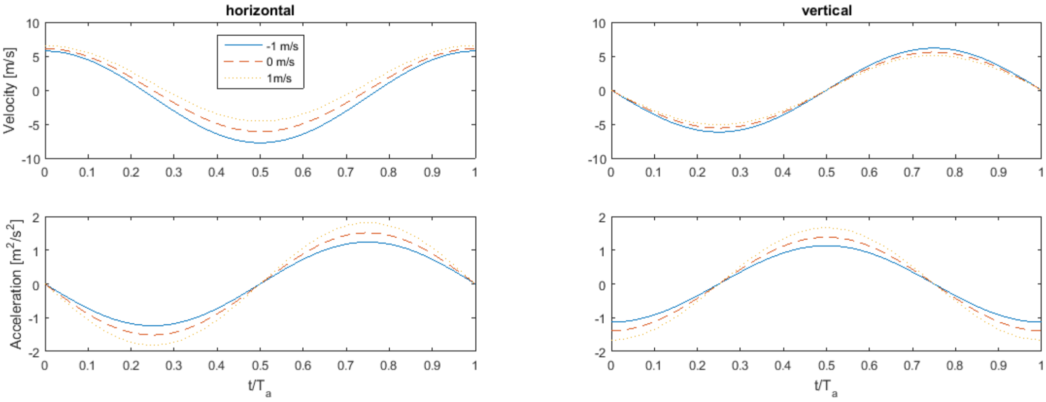

Figure 2.5: Effect of current on wave velocities and accelerations in the horizontal and vertical directions: $H = 5m$, $T_a = 10s$, $d = 20m$, $z = -5m$

In figure 2.5 one can see the effect of current on waves. u_a has its mean modified by the presence of current as well as its variation about the mean. v_a is also modified though its mean remains about zero. Equally the accelerations remain about a mean of zero though variation in the peaks and troughs at differing current speeds is notable.

2.4.3 Relative wave properties

In order to carry out many of the calculations outlined above in the presence of currents it is necessary to know certain relative wave properties (as seen by an observer moving at current speed). These can be calculated from absolute wave properties (as seen by the stationary observer). For a current that is uniform with depth the relative angular velocity is related to the absolute angular velocity by:

$$\omega_r = \omega_a - k\overline{u} \tag{2.99}$$

For a depth varying current, according to Hedges & Lee (1992) an equivalent uniform current (U_e) can be used.

$$U_e = \frac{1}{\epsilon}\int_{-\epsilon}^{0} \overline{u}(z)dz \tag{2.100}$$

$$\epsilon = \frac{\tanh(kh)}{k} \tag{2.101}$$

The wave number is related to the relative frequency by the dispersion equation, 2.14, so an iterative procedure is required to calculate the absolute frequency from the observed frequency and current velocity. The method here was developed by Guo (2002), using logarithmic matching, with maximum relative error of 0.75%. It can be considered the first approximation for an iteration method if more accuracy is required, however it is useful under practical conditions or for inclusion in wave computer models.

1. Make first guess for the wave number, k_0 by solving

$$\omega_a^2 = gk_0 \tanh k_0 h \tag{2.102}$$

2. Calculate first guess for equivalent uniform current

$$\overline{u}_{e0} = \frac{1}{\epsilon_0} \int_{-\epsilon_0}^{0} \overline{u}(z) dz \tag{2.103}$$

$$\epsilon_0 = \frac{\tanh(k_0 h)}{k_0} \tag{2.104}$$

3. Make a next guess at the wave number by solving

$$\sqrt{g k_1 \tanh k_1 h} = \omega_a - k_0 \overline{u}_{e0} \tag{2.105}$$

4. Improve solution iteratively

$$U_{en} = \frac{1}{\epsilon_n} \int_{-\epsilon_n}^{0} \overline{u}(z) dz \tag{2.106}$$

$$\epsilon_n = \frac{\tanh(k_n h)}{k_n} \tag{2.107}$$

5. Then solve

$$\sqrt{g k_{n+1} \tanh k_{n+1} h} = \omega_a - k_n \overline{u}_{en} \tag{2.108}$$

6. Terminate having converged to specified tolerance

2.4.4 Effect of currents on wave spectra

For realistic sea-states it is useful to look at a spectrum of irregular waves. For long crested waves on deep, quiescent water, progressing onto a current without undergoing refraction a ratio for the spectral density of the surface elevation at each instance can be determined, where $S_{\eta\eta}(\omega_a)$ is the spectrum on still water and $S_{\eta\eta}(\omega_a, \overline{u})$ is that with an underlying current.

$$\frac{S_{\eta\eta}(\omega_a, \overline{u})}{S_{\eta\eta}(\omega_a)} = \frac{\omega_r^2}{\omega_a^2} \frac{1}{\left(1 + \frac{2\overline{u}\omega_r}{g}\right)} \tag{2.109}$$

As described previously, waves on a following current reduce in surface elevation and lengthen, whereas for opposing currents they gather in steepness and shorten, also increasing their spectral density. In extreme cases of opposing currents the energy of the waves cannot propagate onto the current incurring wave breaking at the boundary or in lesser extremes the growth of waves on the current will eventually incur breaking. An upper limit to the surface elevation spectral density is given by Phillips equilibrium range constant (Phillips 1958). Phillips proposed a limit to surface elevation due to white-capping, resulting from waves reaching a finite height and becoming 'detached' from the remainder of the water. This is typically a result of long fetch and sustained wind. However effects may also result from currents and as such there is a limit to the maximum spectral density of the spectrum as a function of frequency, as described by equation 2.110.

$$S_{\eta\eta ER}(\omega_a, \overline{u}) = \left(\frac{A * g^2}{\omega_r^5}\right) \frac{1}{\left(1 + \frac{2\overline{u}\omega_r}{g}\right)} \tag{2.110}$$

Here ER refers to equilibrium range and $A*$ is a numerical constant, the value of which has been the subject of much research (Thomson et al. 2013) and typically is in the range 0.006 to 0.024. The value of this parameter is chosen in the following section (5) and has greatest effect during opposing currents when the relative wave period is decreased.

When the spectrum for waves encountering current has been established the spectra for velocity (S_{uu}) and acceleration ($S_{\dot{u}\dot{u}}$) can be determined, for example by using equation 2.95 and equation 2.97

$$S_{uu}(\omega_a, \overline{u}) = \omega_r^2 \Big(\frac{\cosh^2 k(h+z)}{\sinh^2 kd} \Big) S_{\eta\eta}(\omega_a, \overline{u}) \tag{2.111}$$

$$S_{\dot{u}\dot{u}}(\omega_a, \overline{u}) = (\omega_r^2) S_{uu}(\omega_a, \overline{u}) \tag{2.112}$$

The methodology described here is used in the developed model and is further discussed in section 5.

2.4.5 Wave effect on tidal resource

Lewis et al. (2014) showed, using a 7 year SWAN model of the north west European shelf seas, that at 18 UK tidal sites the significant proportion of the wave climate propagated at an oblique angle to the major axis of tidal flow with the average inline wave climate being 2.25m less in height and 2s less in period in comparison. Further analysis using a dynamically wave coupled COAWST modelling system found that waves significantly reduced the current velocity profile with a theoretical resource reduction of 10% for every meter increase in wave height (dependent on direction and period). Further work showed the potential for resource reduction, due to enhanced bottom friction in combination with wave radiation stresses, to be up to 20% Hashemi et al. (2015). The research enforces the necessity to carefully evaluate wave climate whilst selecting sites for tidal energy development.

2.4.6 Related studies

Interactions between waves and currents have been studied both numerically and with physical experiments. Studies have been conducted using computational fluid dynamics (CFD), and using linearised numerical models similar to that developed here. Many experiments have also been conducted in tanks and at sea, on water particle behaviour as well as on model turbines. CFD models have been compared to linear models, to tank measurements and to limited real sea data. Linear models have been compared to tank measurements in terms of kinematics and in terms of loads and performance of turbines and continuing technological improvements enable tanks to more closely replicate real sea conditions. This study, however, fills a gap in previous research, comparing real sea data, circumventing the limitations of measurement instruments, to a linearised numerical model. Furthermore these comparisons are conducted over a broader range of sea conditions and subsurface depths than in previous work. The results of this study should therefore be examined alongside the research that is summarized in the section below when exploring possibility of installing tidal turbines at sites that may experince wave conditions.

2.4.7 Computational Fluid Dynamic modelling/Numerical Investigations

Markus et al. (2013) develop a Reynolds averaged Navier-Stokes method (including volume of fluid method and Fenton's wave theory(Fenton 1990)) allowing wave-current interaction for a depth-varying current and non-linear waves. This is compared to a linear superposition method of pure wave and pure current loads.

Peak loads were significantly higher in the CFD model than those predicted by a linear method. Details on the validation conducted at a test site are not publicly accessible, highlighting the need for the comparisons conducted in this study. Fleming & Willden (2013), using a similar computational fluid dynamic (CFD) model, showed waves to have a detrimental effect on the mean power of tidal turbines in the order of 15-20%, with thrust fluctuating 10-20% about the mean. Olabarrieta et al. (2010) presented a Eulerian wave-current model able to include free surface elevation and wave-current interaction at any angle, successfully validating against a number of tank tests including those of Kemp & Simons (1983), Klopman (1994), and Umeyama (2005). Faudot & Dahlhaug (2012) investigated two different methods of inserting added mass in to Blade Element Momentum (BEM) theory, comparing experimental and theoretical results, and showing little effect on blade loads except for non-stiff blades or extreme waves. A number of other models have been developed and an increasing number of tank tests on scale turbines carried out to validate the models ((Galloway 2013)(Luznik et al. 2013)). The method of analysing real sea data undertaken in this study (chapter 6) would provide a useful reference for comparison with the flow characteristics generated using the computational fluid dynamic methods used here.

Markus et al. (2013) create a wave channel with the Finite Volume Method (FVM) using Computational Fluid Dynamics (CFD) to numerically solve unsteady Reynolds Averaged Navier-Stokes (RANS) equations. The averaging process results in Reynolds stresses which are modelled in the channel using the Shear Stress Transport (SST) turbulence model. Wave interaction can be modelled using the Volume of Fluid (VOF) method. Fenton's non-linear wave model based on Dean's stream function approach was incorporated, due to its validated performance in Stokes and Cnoidal domains, allowing for generation of a wide range of offshore conditions. Results of numerical investigations prove inputs to be closely comparable with theoretical predictions, calculated by the Fenton method for a uniform current profile, except close to the sea bed where there are underestimations of horizontal velocity up to 6% and vertical velocity up to 18%.

Olabarrieta et al. (2010) considers several experimental studies, including those in section2.4.8, in the validation of an Eulerian wave current model, capable of inclusion of variation of the free surface and the effect of a non-hydrostatic pressure field. The model presented is not restricted to shallow waters and is also capable of modelling currents and waves in all directions. The model is shown to accurately solve the vertical structure of combined flows for all angles according to comparisons with tank tests. From this basis a large range of conditions could be modelled. Between the wave crest and trough an increase in flow is achieved in following current cases with the converse for opposing cases. This is due to Stokes drift, or the wave induced mass flux acting on the direction of wave propagation. For perpendicular cases reduction in flow is noted overall but with intensification in the lower water column agreeing with Musumeci et al. (2006). Just below the trough level a reduction in velocity occurs for following cases and the opposite for opposing cases with incident angle of current and wave effecting this intensification proportionally. These changes are also enhanced by the increase of wave height and decreasing period. At intermediate depth reduction of flow is observed for following cases. Corroborating with previous work it is also shown that following wave-current conditions induce a decrease in apparent bed roughness. This enforces the need to consider propagation angle due to the completely different results that can ensue. It is suggested that two-step hydrodynamic models should therefore include the effect of vertical Reynolds stresses induced by wave motion.

2.4.8 Tank testing

In the last decade numerous tank tests of scaled turbine rotors have been undertaken. Some of these tests are summarised and discussed below. Whilst there are some discrepancies, overall good agreement has been observed in tests, particularly with regards to loads (torque and thrust) and in-plane and out-of-plane bending moments. These tests demonstrate the applicability of loads modelling methods, in particular Blade Element Momentum methods, when compared with experimental tank data. The flow model developed in this work validates the wave-current inflow to a similar model (TidalBladed Garrad Hassan (2012)), hence the applicability of this work to the ensuing study. Caution should be taken when interpreting these results when considering the effects of scaling and the relationship between the flow created in a tank with that at sea.

Barltrop et al. (2006) compared tank test results to blade element-momentum (BEM) model predictions for in-plane and out-of-plane bending moments using a 0.4m diameter three bladed rotor. The BEM model incorporates linear wave theory kinematics. In-plane and out-of-plane bending moments were found to fluctuate significantly particularly in the presence of steep waves. For longer waves experimental results were well predicted by linear theory with BEM, however in steeper wave cases fluctuations were often double those predicted. Some hypothetical conclusions were then drawn with regard to a full-scale rotor. Out-of plane and to a smaller extent in-plane bending moments were considered to be significant. Further to this work, Barltrop, Varyani, Grant, Clelland & Pham (2007) compared tank test results to blade element-momentum (BEM) model predictions for torque and thrust using a 400mm three bladed rotor. The BEM model incorporates linear wave theory kinematics. A good comparison is found, implying that BEM in conjunction with linear wave theory can effectively analyse wave-current interaction in the tank. The work in this thesis will build upon this with comparisons of field kinematics and model kinematics based upon linear wave theory. In parametric studies wave frequency has insignificant effect at the frequencies used, whereas fixing tip speed ratio results in a reduction of torque in the presence of waves as well as instances of stall during higher frequency waves. Wave height is shown to apply a steady increase in mean torque particularly for longer waves, with a large increase in the range of variation of torque. Whilst little change in mean thrust is exhibited with increased wave height, an increase in peak thrust of 40% is observed.

Milne et al. (2011) showed, through tank testing of a three bladed 0.78m rotor, that unsteady bending moments are sensitive to frequency and amplitude and though linear theory an quasi-steady BEM are satisfactory in most cases, flow separation and stall phenomenon induce loads far greater than those predicted at lower tip speed ratios. Further work by Milne et al. up until 2013 (Milne et al. 2012)(Milne, Day, Sharma & Flay 2013)(Milne, Sharma, Flay & Bickerton 2013) observed loads of 25% greater than predicted by theory, implying that operational boundaries for tidal turbine designers should be imposed close to stall.

Faudot & Dahlhaug (2012) create a BEM model (with added mass force) with linear wave theory for calculating particle kinematics. This is compared to tank tests conducted using a 1.475m 2 bladed rotor. Mean thrust and torque forces were shown to clearly drop in high waves between relative current numbers leading to stall, due to stall or near stall effects caused by the change in angle attack caused by passing crests and troughs. The three models (Steady BEM, steady BEM with the modified Maniaci method to implement added mass force, and steady BEM with Tidal Bladed's added mass method) were within 1% and showed good agreement with experimental results except for extreme loads in steep, high waves at low relative current number. For these extremes additional dynamic stall and dynamic wake models would be necessary to estimate loads. The incorporation of added mass (for non-uniform flow) was not deemed relevant in this case though it is likely to be significant for non-stiff blades when combined with a blade hydro-elastic model.

Galloway (2013) conducted tank tests using a 0.8m three bladed turbine making comparisons and modifying a BEM model, also making comparisons to existing, wind turbine code FAST from NREL. Root out-of-plane bending was found to be, on average, 4.1 times greater than in-plane bending for wave and yawed conditions, and in terms of increased loading, wave period and wave height were found to be equally significant drivers. Dynamic inflow and stall corrections were considered useful in predicting experimental loads in most cases and best agreement was found inside of the optimum operating conditions of the turbine (i.e. Tip speed ratio 5-6).

Luznik et al. (2013) tested a 0.46m three bladed turbine finding that whilst average power coefficient is very similar during wave scenarios there are significant impacts on blade loading and power production quality, showing a strong correlation between torque and vertical velocity which was of greatest concern at periods of decreasing vertical velocity. Risk of cavitation and boundary layer shearing close to the free surface and also deeper into the water column are also considered a risk in the presence of certain waves.

Jesus Henriques et al. (2014) conducted tank tests with a 0.5m diameter three bladed rotor showing good comparison of measured wave kinematics with linear wave theory. Similar to the previous literature, whilst mean thrust and power coefficients for unsteady flow were close to those for steady flow, substantial cyclic range variations occurred at wave frequency. Where different tip speed ratios were considered the standard deviation of power coefficient remains reasonably constant for steady flow. For wave-current flow standard deviation of power coefficient increases as tip speed ratio decreases which is inconsistent with the work of Gaurier et al. (2013) which found that standard deviation of power coefficient reduces with decreasing tip speed ratio. It is discussed that this discrepancy arises from the Gaurier experiment applying constant torque and fluctuating speed whilst constant speed and fluctuating torque were applied in the Henriques experiment.

2.4.9 Laboratory experiments for wave effect on current profile

The majority of work towards determining the effect of waves on the current profile has been done in a general oceanographic context. However, whilst this is not always directly applicable to tidal energy device design, understanding the flow regime and drawing from the broad experience of physical oceanographers can be useful in many contexts.

Kemp & Simons (1983) ran tests in a laboratory flume with rough and smooth beds measuring velocity with a directionally sensitive laser anemometer. Wave attenuation was found to be greatly increased by an opposing current and reduced by a following current with wave profiles and orbital velocities agreeing well with second order wave theory, which was modified to take current into account. Near bed velocities are decreased by the presence of waves though interactions are not influenced by relative flow directions. In the upper layer mean velocity is dependent on the direction of the wave propagation for increasing wave height. Turbulence intensities and Reynolds stresses were increased near the rough bed due to the presence of waves.

Klopman (1994) performed tests with mono-chromatic, bi-chromatic and random waves without current and with following and opposing current. Velocity shear is found to be reduced in the case of waves on a following current and increased with opposing waves. This change is considered to be mainly dependent on wave energy rather than the shape of the spectrum , whereas the level at which undertow layer and the streaming layer change sign, due to reduction in near bed velocity, is strongly dependant on spectral shape.

The bed boundary layer of relatively shallow, coastal seas is of importance for support infrastructure, in particular cables, and for the support structure and anchoring of the device itself. Substantial research has been done in this field with regard to sediment transport in an oceanographic and coastal context. Van der Kaaij & Nieuwjaar (1987) ran insightful experiments showing wave-current interaction of non-linear non-breaking waves with results from Visser (1986) indicating that whilst increases in bottom friction were seen due to the presence of waves, the theory predicted by Bijker (1967) and Fredsoe (1984) overestimates bottom friction. Musumeci et al. (2006) examined perpendicular interactions finding changes to current velocity close to the bottom and to apparent bottom roughness.

Chapter 3

Measurement and processing

Many instruments and methods are used for measuring conditions at sea. This chapter focuses on measurement and processing of data for sea-surface elevation and sub-sea water particle velocities using bottom mounted acoustic instruments. State-of-the-art devices are described, and their functionality discussed with reference to previous studies. Algorithms typically used for processing of velocity data are given in the text before detail on the method developed for determining surface elevation is presented. Novel methods are presented alongside well established methods for the treatment of data, quality checking, and determination of useful wave and turbulence parameters.

Acoustic Doppler (AD) technology is commonly used in measurement of subsurface velocities and sea surface elevation. Acoustic instruments now enable measurement of both wave characteristics and current velocities, requiring deployment of only one instrument with the capacity to characterise a broad range of conditions. Where previous technologies were able to take accurate single point measurements, state-of-the-art acoustic instruments can take multiple readings over a range of water depths. This allows for a large amount of data to be gathered. Instruments emit sound pulses from transducers which are reflected by obstacles in the water column, whereby a signal is returned to the instrument. In other applications (e.g. SONAR) these obstacles might be fish, or other objects, the location of which is of interest to the user. In determining the distance to the sea surface or to the sea bottom, the 'obstacle' is the air-water interface or the seabed, respectively. Both will return a very strong signal. In applications aimed at determining subsurface velocities obstacles may be debris, bubbles or plankton; anything with sufficient size and of a different density to water. The returned signal is frequency shifted according to the velocity in the pulse direction at which the obstacle was travelling. By emitting pulses at high frequency and trigonometrically transforming the resultant velocities in combination with two or three other transducer records, a three-dimensional velocity time-series can be calculated.

Nortek and Teledyne RD Instruments (TRDI), by whom much of the knowledge in this area has been developed, are the principle manufacturers of marine acoustic Doppler instruments and both offer a broad range of devices, fulfilling the needs of various maritime industries. Instruments mounted on the hulls of vessels are often useful in preliminary investigations for the tidal energy industry, however the studies carried out in this project principally refer to those instruments mounted on the seabed looking upwards at the sea surface. Both manufacturers sell instruments with 1, 3, 4 and 5 acoustic transducers each with their own advantages. An example of a 5 transducer Nortek instrument is shown in Figure 3.1.The functionality of these instruments is described below. Throughout this document the sound emitted from an acoustic transducer will often be referred to as a *'beam'*.

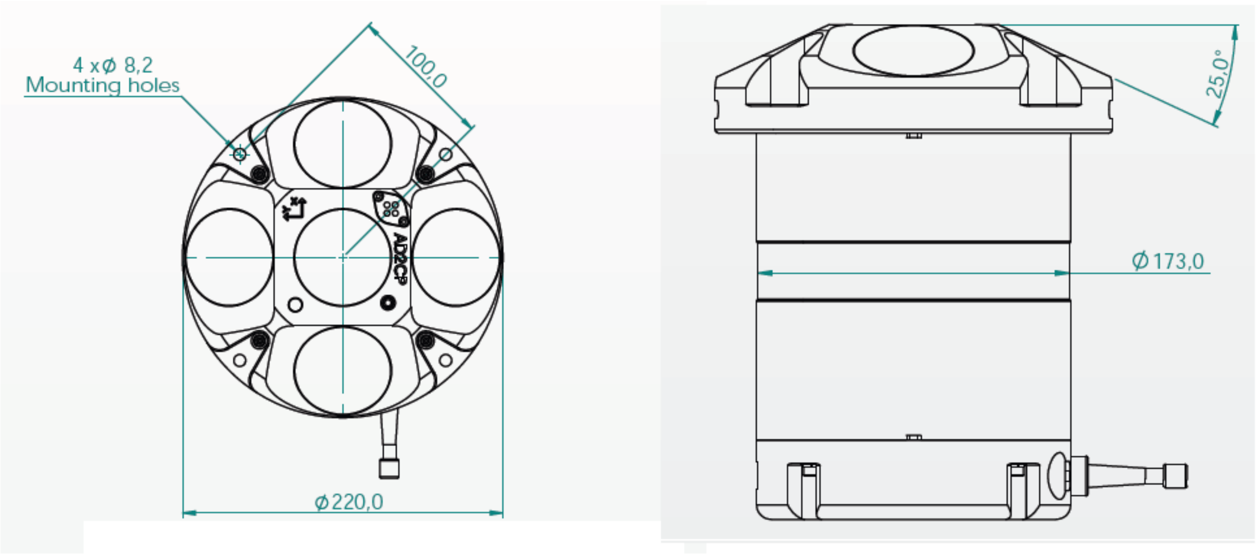

Figure 3.1: Example of a 5 beam DCP (Nortek 2016)

A single beam instrument allows for high frequency measurement of velocity in the direction of the beam and for determining sea surface elevation from signals reflected from the surface at the water-air interface; otherwise known as echo location. This can be useful by itself or in combination with other instruments. A minimum of 3 beams, angled in more than one plane, is required to determine velocity in 3 dimensions; therefore instruments with 3 beams can provide estimates of East North Up (ENU) velocities and also have the potential to track the surface using echo location, with the ability to also provide directional information about the waves (see section 3.2.2). This has obvious advantages over a single beam instrument and has more efficient battery and data storage potential than an instrument with a greater number of beams. A fourth slanted beam, provides a redundancy in the case of one beam failing, or an additional error velocity (if all beams function) to give an understanding of the accuracy of the measurements. Such instruments have the potential to record ENU velocities, sea surface elevation and wave direction. Some three or four beam systems also include a fourth or fifth vertical beam. This allows for a more accurate measurement of the sea surface, as there can be some distortion in surface elevation measurements taken by slanted beams. Furthermore a measure of vertical velocity at a range of depths can be taken on this beam. It is therefore possible to use the vertical beam in combination with the slanted beams to determine ENU velocities to a greater degree of accuracy.

Instruments nominally operate with an acoustic signal frequency of several hundred Hertz, suitable for reflection of small particles in the water column. Returned data is ensembled at several Hertz, storing information on the intensity, amplitude and correlation of recorded samples. Instrument memory also retains system configuration data, including compass and orientation information. A data ensemble consists of the data collected and averaged during the specified ensemble interval. Output data from acoustic instruments is typically stored in either hexadecimal-ASCII or binary format. The Hex-ASCII mode is useful when using a terminal to communicate with, and view data from the instrument whilst the binary mode is useful for high-speed communication with a computer program. Since it is often difficult to link a terminal with the instrument during sea surveys, binary format is more often used for this type of data, such that an external device can be used. Furthermore the binary format uses less storage space and has a faster transmission time than the Hex ASCII format. After completing a data collection cycle, the instrument immediately sends a data ensemble. The data, preceded by a specific code, contains header data, fixed and variable leader data, followed by information such as velocity, correlation magnitude, echo intensity, and percent good data, all with their own specific code that the binary reader will need to identify. Data appears in bytes or bytes per depth cell. Further information on specific instrument data formats can be attained from manufacturers. After the data is extracted from its binary form, it is processed and quality checked as described in section 3.5.

3.1 Subsurface velocities

Upward looking devices, referred to as Doppler Current Profilers (DCPs), emit sound pulses from transducers which are reflected by particles suspended in the water column returning a signal to the instrument. The signal is frequency shifted (Doppler shift) according to the velocity in the pulse direction at which the particle was travelling (Figure 3.2). By emitting pulses at high frequency and trigonometrically transforming the resultant velocities in combination with two or three other transducer records, a three-dimensional velocity time-series can be calculated.

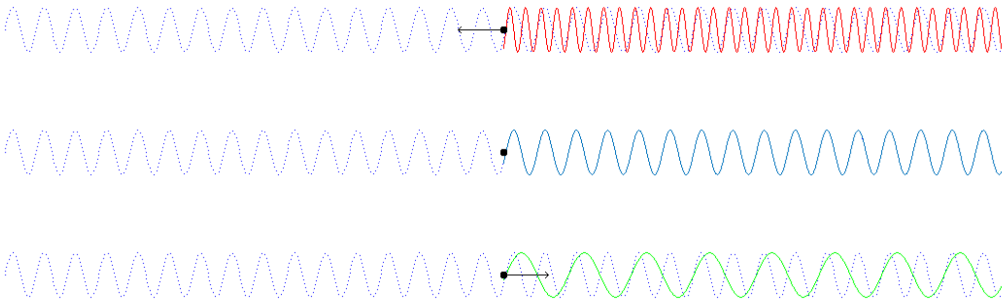

Figure 3.2: Example of the effect of a moving or stationary obstacle on the reflected wave form. Dotted blue line indicates the original (sound) wave. The red line shows the resultant wave reflected off an obstacle moving opposed to the signal direction, and the green line shows that resulting from an obstacle moving away from the signal direction.

In many applications often only one beam is required. To measure velocities in three dimensions more than three beams are desirable, assuming that the flow at any given instant is homogeneous across the area swept by the beams. Three beamed instruments are often used, however offer no redundancy, if one beam should fail. The most common set-up is known as a 'Janus' configuration which is typically used to collect current data from tidal races, and will be the focus of this study. The system comprises 4 beams slanted at 25 degrees to the vertical, separated (in plan view) by 90 degrees. Each transducer emits 'pings' of sound that have a constant frequency. These pings are reflected off particles moving in the water column and return to the instrument. If the particle encountered was moving away from transducer when the sound wave reflected off it the frequency of the sound will be shifted to a lower frequency, and vice versa if the particle was moving towards the transducer (see Figure 3.2). This 'Doppler' shift is used to determine the velocity of the water particle. Each transducer typically emits an acoustic signal of several hundred or thousand Hertz, in pings of between 1 and 20 Hertz, and signals are returned to the instrument from across the entire depth of the water column. Those pings returning from higher up the water column will take longer to return and as such returned signals can be put into depth bins, and averaged. The greater the ping frequency, the greater the accuracy of velocity measurements at the record frequency, accounting for variations in acoustic return of the water, and micro-turbulence. All four along beam velocities (b_1, b_2, b_3, b_4), from each depth bin, can be resolved into ENU velocities (U_0, V_0, W_0).

$$\begin{bmatrix} U_0 \\ V_0 \\ W_0 \\ er \end{bmatrix} = M \begin{bmatrix} b_1 \\ b_2 \\ b_3 \\ b_4 \end{bmatrix} \tag{3.1}$$

Where the matrix,

$$M = \begin{bmatrix} a & -a & 0 & 0 \\ 0 & 0 & a & -a \\ b & b & b & b \\ c & c & -c & -c \end{bmatrix} \tag{3.2}$$

for which,

$$a = \frac{1}{(\sin\theta_b} \tag{3.3}$$

$$b = \frac{1}{4\cos(\theta_b)} \tag{3.4}$$

$$c = \frac{a}{\sqrt{2}} \tag{3.5}$$

To cope with changes in heading, pitch and roll of the instrument the rotation matrix (RM) is applied to the three components of velocity (U_0,V_0,W_0) determined from along beam velocities.

$$\begin{bmatrix} U & V & W \end{bmatrix} = RM \begin{bmatrix} U_0 & V_0 & W_0 \end{bmatrix} \tag{3.6}$$

The rotation matrix considers heading (H), pitch (P) and roll (R); where heading is the rotation about the z axis, pitch is the rotation about the y axis and roll is the rotation around the x axis.

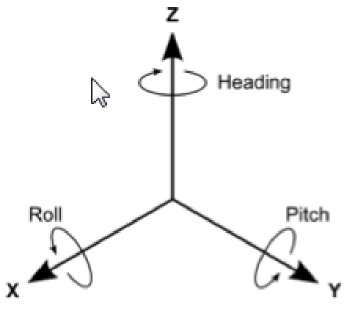

Figure 3.3: Rotation: Heading, Pitch, and Roll

$$RM = \begin{bmatrix} \cos H & \sin H & 0 \\ -\sin H & \cos H & 0 \\ 0 & 0 & 1 \end{bmatrix} \begin{bmatrix} 1 & 0 & 0 \\ 0 & \cos P & -\sin P \\ 0 & \sin P & \cos P \end{bmatrix} \begin{bmatrix} \cos R & 0 & \sin R \\ 0 & 1 & 0 \\ -\sin R & 0 & \cos R \end{bmatrix} \tag{3.7}$$

To determine current velocity magnitude and direction the longitudinal and lateral components of velocity are used, taking the hypotenuse of the two for the magnitude, and the four quadrant inverse tangent of the two for the direction. The four-quadrant inverse tangent ($atan2$) returns values in the closed interval $[-\pi, \pi]$ based on the values of U and V. In contrast, $atan(V/U)$ returns results that are limited to the interval $[-\pi/2, \pi/2]$.

$$MAG = \sqrt{U^2 + V^2} \tag{3.8}$$

$$DIR = ATAN2(U, V) \tag{3.9}$$

In the simulation chapter (5) all directions are set relative to current direction (at zero) and as such MAG is often represented as $\overline{u}$.

Velocities are typically then averaged over 10-15 minute samples. Further processing algorithms are often used to account for error due to side-lobe interference as well as transducer ringing. Side-lobes are sound radiation in unwanted directions which through further reflection can cause interference in the main-lobe of the returned radiation signal. Transducers can generate signal oscillations known as ringing which if not effectively damped will require post-processing to remove them from useful data. These processes are not discussed further here, however they are discussed as the subject of, and alongside a number of other studies (Nystrom et al. 2007)(Nystrom et al. 2002)(Muste et al. 2004). The largest volume of data recorded at tidal sites comes from divergent beam Doppler profilers. Primarily these are used for measuring mean ENU current velocities, as described in the equations above, based on the assumption of homogeneity in the flow between the diverging beams. To some degree turbulence and wave parameters can be extracted from ENU velocity data, however this assumption can convolute the validity of these estimates, since wave and trbulence velocities can fluctuate over short time-scales. Studies have made developments on equipment and processing for measurements made using DCPs. For example Gargett (1994) modified an acoustic instrument such that a beam aimed vertically could be used as an unambiguous measure of vertical velocity as well as a reference with which to quantify bias on slanted beams, whilst determining turbulent kinetic energy and Reynolds stresses. Ott (2002) made improvements to the algorithms used in determining depth specific velocities in situations of non-zero pitch and roll, which was previously subject to error, particularly in strongly sheared currents.

3.2 Surface elevation

Acoustic surface tracking (AST) can provide a direct measurement of the sea surface which complements the other acoustic measurement systems. Relative to many of the other measurement methods discussed AST is quite simple, though it carries its own inherent limitations. In simple terms AST is an inverted echo sounding system that detects, through reflection of sound pulses, the distance to the sea surface. At suitably high frequency with a very narrow beam (1.7 deg), this allows for direct measurement of waves rather than inference of waves from wave velocities. It does not suffer from attenuation effects associated with increasing depth, to the same extent as angled beams, and since the interface between the water and the air has very high acoustic impedance it is possible to achieve a very high signal return. Time series wave statistics such as top 10% (H_{10}) and maximum wave heights (H_{max}) can be estimated, as well as non-directional parameters including frequency. The slanted beams of the instrument used to determine subsurface velocities can also be used to echo locate the sea surface, however are often subject to interference at the typical operating frequency and bin depth. A vertically aimed beam from an upward looking instrument operating at high frequency over bin depths concentrated near the surface can produce far more accurate representations of surface elevation. This study was based upon the Teledyne RDI Sentinel V Instrument, however the method is more widely applicable. The Sentinel V operates in two modes; 'wave' mode and 'current' mode. In wave mode the instrument concentrates on smaller depth bins (or cells) in the upper part of the water column and in current mode the focus is across the entire depth, typically measuring with taller depth cells. This is a method commonly adopted in order to maximise data storage and battery life. It is however possible to distinguish waves in current mode and vice versa, though the larger depth cells of the current mode are likely to inhibit accuracy in determining the surface location.

3.2.1 Background

Pedersen & Nylund (2004) introduced the use of a fifth vertically pointing beam for measurement of the sea surface in the new Nortek AWAC in 2004, showing improvements in surface tracking over the previously used methods of inferring the surface from pressure and subsurface velocity measurements. This was expanded on by Nortek in 2005 (Pedersen, Lohrmann & Krogstad 2005) using a maximum likelihood method (MLM) for wave directional processing using a combined SUV (surface and velocity) method to determine directional surface elevation spectra. Measurements from this Acoustic Wave And Current (AWAC) are later compared to measurements made by a wave buoy (Pedersen, Malzone & Siegel 2005) with good results. In fact the system is designed to make accurate measurements whilst placed on a subsurface buoy and agrees well with data with the exception of number of gaps in certain frequency bands related to the motion of the buoy (Pedersen & Siegel 2006).

Hoitink & Schroevers (2004) compared a 1200 kHz and 600 KHz DCP with corresponding wave buoy estimates in a number of configurations, and found surface tracking to be a more accurate measure of non-directional wave measurements than DCP current velocity, though in some configurations ensemble frequency was found to be an inherent limitation. The DCP were found to predict well the energy density in surface elevation spectra hence predicting wave height well. Overestimation of energy density in high frequency surface elevations resulted in underestimation of wave period though this was concluded to be due to processing tools rather than data acquisition. Direction was also well predicted by the DCPs in comparison to the wave buoy though some limitations were found in the results for directional spread, particularly for the lower frequency DCP. Larger waves were found to suffer from under prediction as well as wave period for which discrepancies increased with wave height due to increased signal to noise ratio (SNR).

Herbers & Lentz (2010) examined data from two upward looking 4 beam (Janus configuration) DCPs at 20 and 45 metre depths. Orbital velocities at six vertical levels were measured to attain cross spectra that were fitted with cosine power uni-modal or bimodal directional distributions of wave energy in order to compare to estimates from a nearby directional Waverider buoy. In low wave and also in relatively energetic conditions mean wave directions agreed well between the buoy and both the shallow and deep DCP. However DCP measurements of directional spread were biased high, particularly from the deep DCP in low energy conditions. This inadequacy is due to the poor signal-to-noise ratio expected in less energetic seas and deeper water. Noise however does not seem to affect estimates of mean direction but significantly degrades directional spreading estimates. It is concluded that this sensitivity is consistent with the effect of random uncorrelated noise reducing the horizontal coherence of velocity measurements in a similar way as affected by increased directional spreading. It is also noted that a comparison with DCP velocity and pressure spectra with a linear theory transfer function and estimates of the relative noise level in raw beam spectra can be useful in quality checking the data and identifying the frequency range over which orbital motion is resolved.

Srisuwan & Work (2013) found, in a comparison between a Triaxys surface following wave buoy and DCP, that most parameters which the DCP derived from wave spectra were highly comparable to the wave buoy data. Discrepancies were largely found at the extremities of frequency where SNR ratios were lower. Further to this it was found that the DCP indicates energy to be more tightly concentrated around the peak direction.

The literature and personal assistance of those at Nortek and Teledyne RDI was invaluable in this research progress. There are several documents listed in the references here (RDI 2001)(Nortek 2008), however a more complete collection can be found on both instrument manufacturers' websites: www.nortek-as.com and www.rdinstruments.com.

Manufacturer Processing Methods

Refined details of manufacturers' (Nortek and RDI) surface elevation determination methods are not publically available, hence the development of the method described in section 3.2, however an outline of two seperate methods is given here; the first without AST, instead using pressure combined with velocity measurements and the second with AST.

PUV Pressure is typically measured with a high resolution piezo-resistive element. The pressure signal (P) is used to estimate the frequency spectrum. The energy in the spectrum is then used to estimate wave height and period. Measurement of the waves' orbital velocities (U and V) gives an estimate for the wave direction. Since these estimates are based on the wave energy distribution and are not a direct measure of the free surface they are considered inferred estimates. Dynamic pressure and orbital velocities, as well as turbulence, are driven by surface waves. The signals associated with these properties are complicated by the fact that wave kinematics attenuate exponentially with depth. The exact behaviour of the attenuation has to do largely with the depth of the water and the wavelength. Further down the water column the signal is increasingly attenuated, and as wavelength decreases (shorter period or higher frequency) the signal again experiences increasing attenuation. Hence waves become more difficult to estimate from great depths or for waves of short period. The PUV approach can not detect waves much higher than 1 second in period due to the attenuation effects associated with the deployment depth and wave frequency therefore if one is only interested in measuring waves then it is not necessary to sample any higher than 2 Hz. The processing is relatively simple and is composed of the following steps (further description is provided in the subsequent text):

1. First perform the transformation on the time series (e.g. Pressure, Velocity) from the time domain to the frequency domain using a standard FFT.
2. Calculate the auto -spectra and cross -spectra for the pressure and two velocities.

3. Apply the transfer functions to the spectra to arrive at the spectra for the free surface.
4. Apply quality control to the spectra (Determine a cut-off frequency and extrapolate).
5. Estimate the wave statistics for height and period using the moments calculations.
6. Calculate the Fourier arguments which will ultimately be used for the directional estimates.

The transfer functions relating velocity to the surface elevation are given in equations 3.33, as Q_i and R_i, and similarly for the pressure as Pr_i:

$$Pr_i(z) = \omega_i \frac{\cosh(k(h+z))}{\sinh(kh)} \tag{3.10}$$

The PUV approach is based on linear wave theory and occasionally situations arise where linear theory is no longer valid and second order effects become increasingly significant, for instance when placing an instrument in increasingly shallower water or in a strong current. The non-linear profile is not accounted for by the PUV transformation and as such, though waves are properly sensed,the wave height will be slightly underestimated. Perhaps the most difficult aspect of classifying sea state from pressure sensing via spectral based estimation is the realization of wave energy at high frequencies. Amongst the problems are the errors in the calculation of moments and cutting off peaks at higher frequency. JONSWAP and Pierson Moskowitz spectra are often used as the basis for extrapolating into the higher frequencies.

SUV Increasingly the typical PUV (pressure, u and v velocity) methods are being replaced by SUV (surface, u and v velocity) methods. The SUV method for measuring waves works in a similar way to the PUV method. Both methods use a triplet of wave-related measurements to estimate wave energy and the first four Fourier coefficients. The Fourier coefficients are used to estimate the standard parameters of direction. The SUV method consists of the acoustic surface tracking (AST) and two horizontal and orthogonal velocities, u and v. The u and v come from the conversion of the Beam to Earth referenced coordinate system as before. Mathematically, the phase relationship of the AST, u, and v is preserved which permits the directional wave processing.
The approach used to detect the surface is relatively simple:

1. Transmit a pulse of a given length
2. Specify a receive window covering the range of all possible wave heights
3. Discretise the receive window into multiple cells (approx. 2.5 cm)
4. Apply a match filter over a series of cells to locate surface
5. Use quadratic interpolation to precisely estimate surface location

The resulting time series of AST range measurements is naturally subjected to false detects. These false detects arise from competing peaks in the echo return from the surface. This may occur if there are targets other than the surface in the acoustic beam's path. False detects require special determination and are identified by analyzing the time series of the free surface. This process begins by identifying range estimates that exceed a specified outlier boundary relative to the mean of the ensemble. This boundary is defined as some multiple of the standard deviation of the ensemble. The clean up step is iteratively performed with increasingly tighter bounds to ensure all false detects are removed. Handling of the false detects involves a simple interpolation of the neighbour values. Finally, if the cumulative number of false detects exceeds 10% of the total number of samples in the ensemble, the ensemble is considered corrupt and discarded. The occurrence of this has proven to be relative low (1- 2%), and wave estimation process can be replaced with one of the backup estimation methods using either the velocity or pressure measurements. Once the time series for the surface has been established, we carry on with the traditional zero-up-crossing method. This is done for determining extreme wave estimates (H_{10}, H_{max}), whereas spectral methods are used for all other wave estimates. The frequency limitation for the measurable waves does not just lie with the Nyquist, sampling limit, but also with the 'footprint' created by vertical beam ensonifying the surface. Naturally, as the range increases, the footprint increases. As a general rule, we follow a Nyquist like reasoning; the frequency limit associated with the footprint is when half the wavelength is on the order of the diameter of the footprint. This clearly is the absolute shortest measurable wave. We can expect that the frequency response begins to roll off just prior to this point.

To summarize, pressure sensing is limited in that it occurs at the bottom of the water column where much of the wave's effects have been attenuated. Surface tracking is only limited by its operational frequency and opacity of the water. The surface tracking method does not suffer from the attenuation effects associated with increasing depth and furthermore estimates waves directly using the time series, as opposed to spectra inferred estimates. Therefore profiles of non-linear and transient waves can be measured as well as being able to estimate time series wave statistics such as top 10% (H_{10}) and maximum wave heights (H_{max}). Pressure and velocity measurements serve as useful compliments to surface tracking, when measuring waves and as such one can have three independent estimators. The method used in this study follows a development on the SUV and PUV processes, using 5 surface tracking beams validated by inference of the surface from velocity and pressure measurements.

3.2.2 Methodology

Acoustic pings are emitted by the instrument transducers exactly as they are for measuring velocities. The DCP measures the echo intensity (EI) returned from each depth bin. **Echo Intensity** is a measure of the strength of the signal that returns to the DCP, and, unsurprisingly, tends to decrease as the distance to a measurement cell increases. Echo intensity typically depends on sound absorption, beam spreading, transmitted power and backscatter coefficient, and can be approximately estimated by equation

$$EI = SL + SV + constant - 20 \log R - 2\Omega R \tag{3.11}$$

In the above equation (3.11) EI is the echo intensity (dB), SL is the source level (dB), SV is the water-mass volume backscattering strength (dB), Ω is the absorption coefficient, and R is the distance from the transducer to the depth cell. The *constant* is relative to a particular DCP at a particular site, and the $20 \log R$ term accounts for beam spreading. The point at which signal strength becomes comparable to the noise level is the maximum range of the DCP. For the Sentinel V, if EI exceeds 120 counts (approximately 0.45 counts per decibel) it is likely that the sound wave emitted from the transducer has reflected off something solid or a significant change in density such as the water-air boundary. Looking at the profile of EI with depth one should see a signal similar to that illustrated in Figure 3.4. There is a clear peak indicating the height of the centre of the depth cell within which the surface is located.

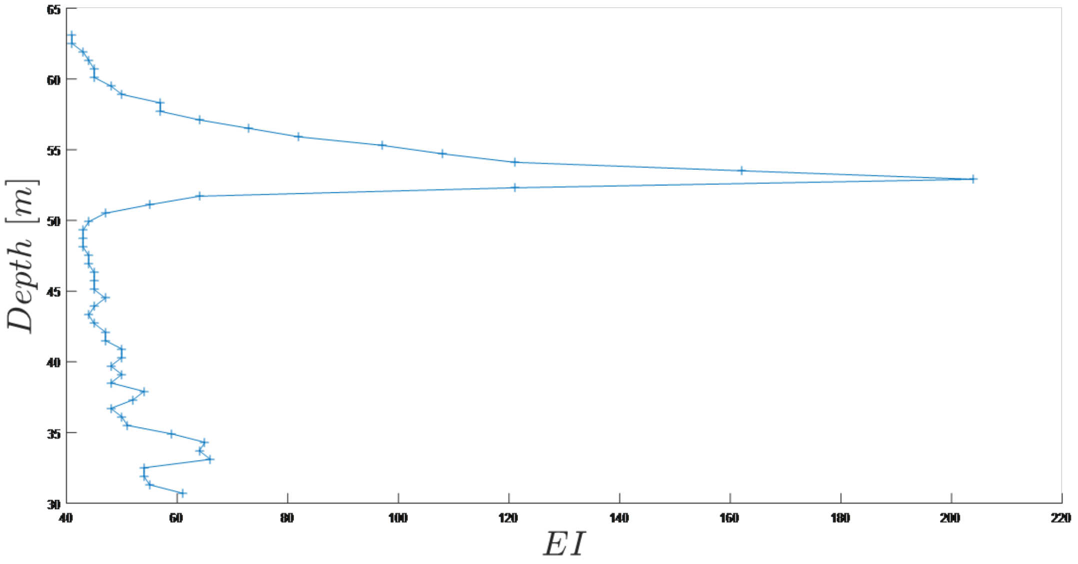

Figure 3.4: Echo intensity over depth profile

In the method developed here, to get around the discretization of the echo intensity to within particular depth cells, points are interpolated cubically using MATLAB's 1D data interpolation function 'interp1', implementing the 'spline' method: Spline interpolation using 'not-a-knot' end conditions. The interpolated value at a query point is based on a cubic interpolation of the values at neighbouring grid points in each respective dimension.

Steps

1. The depth cell at peak EI is identified

2. Interpolation is carried out over a specified number of points (typically <5) either side of the peak for a specified number of points (typically >100)

3. The depth at the peak of the interpolated EI values is found (providing it is close to the original peak).

Figure 3.5 illustrates interpolation of EI around the peak. The depth at which the peak of the interpolated EI values occurs is taken to be the sea surface elevation.

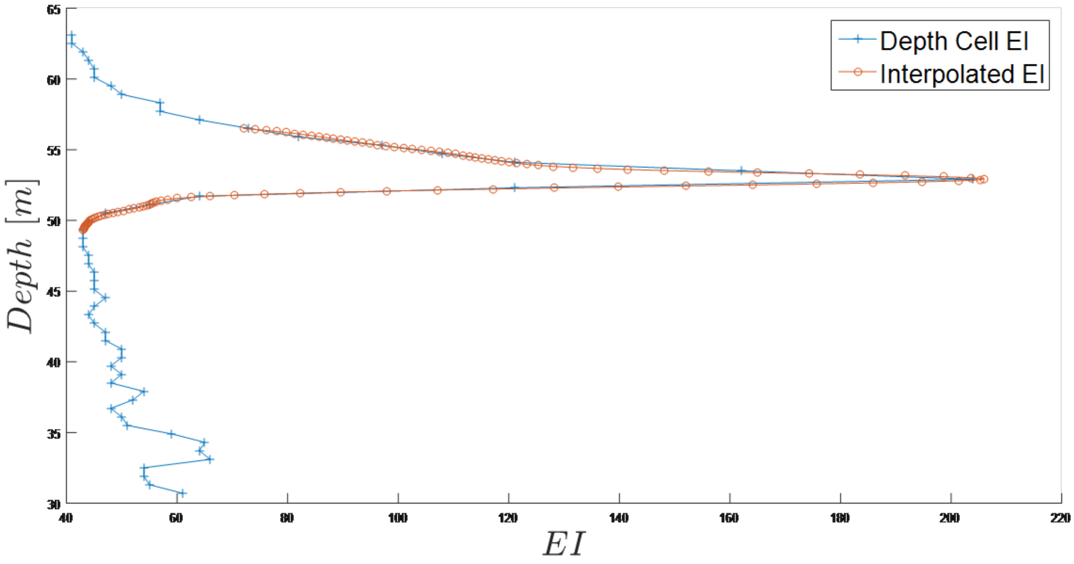

Figure 3.5: Echo intensity over depth profile, showing cubic interpolation around peak for 100 points. Zoomed inset shows peak for interpolation using 1000 points.

In many cases it may be appropriate to account for the reductions in echo intensity caused by distance from the instrument transducer. This must be done before step 1.

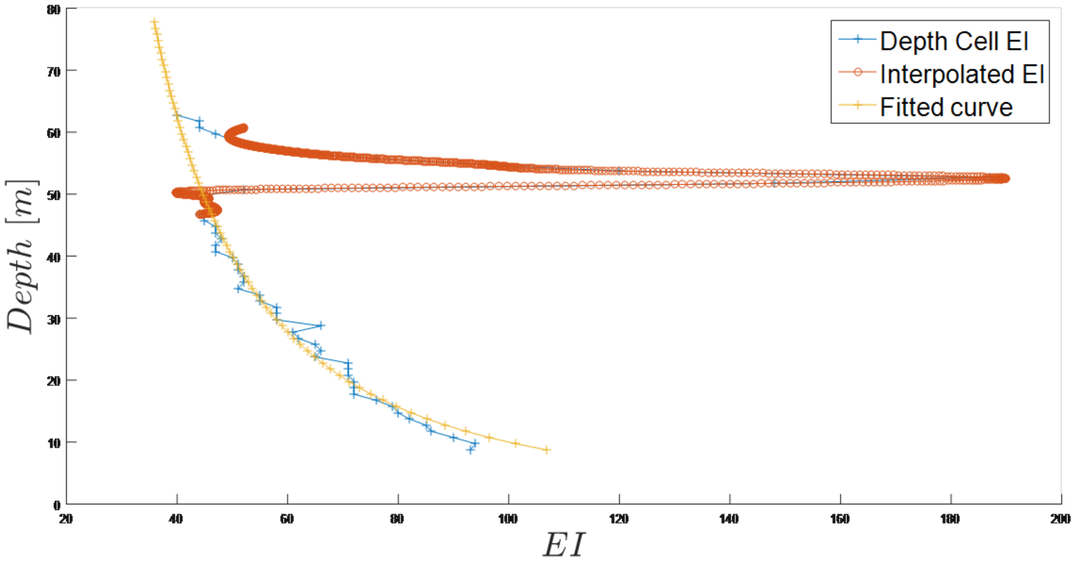

Figure 3.6: Echo intensity reduction with depth. Yellow curve illustrates reduction in intensity with depth.

As illustrated by the yellow, fitted curve in Figure 3.6 echo intensity tends to decrease with distance from the instrument according to an inverse power law of approximately negative 0.5. This is particular to this instrument at this particular site. In many cases the peak is so prominent that modifying for this reduction in EI has a negligible effect on the resultant surface elevation estimate, however there are occasional cases that benefit, particularly when cell size is large (Figure 3.7). The echo intensity accounting for reduction with distance from the transducer, EI_{new}, is calculated from the measured echo intensity EI_{old}:

$$EI_{new}(z) = \frac{EI_{old}}{z/z_0^{-\beta}} \tag{3.12}$$

Where z is the depth of the cell at which the original EI was measured, z_0 is the depth of the first cell and β is the power law (0.5 in this case). This profile will change dependent on site conditions (such as suspended sediment concentration and background noise). Figure 3.7 illustrates the importance of modifying the echo intensity with range, noting that the peak in EI is shifted by in excess of 0.1m. The shift is small, and the occurrence is relatively rare, however minor inaccuracies in sea surface elevation can have broader influences on results.

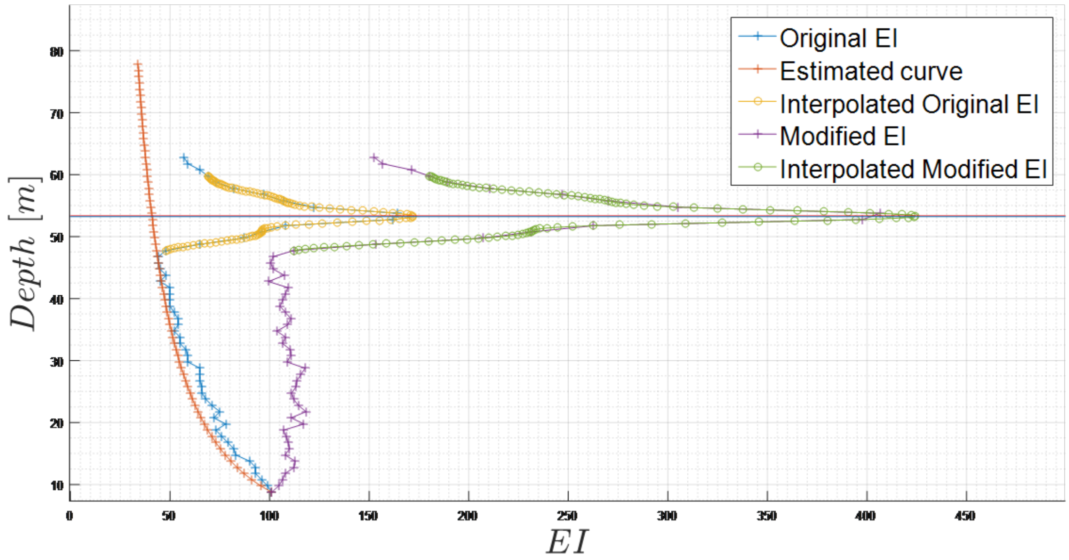

Figure 3.7: Echo intensity modification with depth. Illustrating the importance of echo intensity modification with distance from transducer.

Having isolated the peak in EI this is associated with its specific depth, no longer subject to the discretion of the pre-defined depth cells. Every record is treated in this way until a series of depths, indicating the location of the sea surface is determined. This method produces high resolution surface elevation data which can be used to determine ten minute wave elevation spectra which in turn are used to estimate wave characteristics such as significant wave height and mean period.

Multi-directional wave spectra

A single data point can provide information on the distribution of energy with each frequency component of the waves, whilst having multiple data points allows for an understanding of the directional distribution of this energy. A multi directional wave spectrum provides information on the spectral density, or energy, over a range of frequency components and directions, and it is useful to have a good estimate of this spectrum to understand site wave behaviour. Attaining multi directional wave spectra involves the use of greater than three measurement points separated in space. Using acoustic instruments this is typically 3, 4 or 5 beams. The greater the number of measurement points the greater the accuracy of the measured directional wave spectra.

The method outlined above for a single vertical beam is applied to multiple slanted beams. This requires only minor modification to the code to account for the increased distance of the hypotenuse to the surface. Due to reflection and diffraction at the sea surface the return signal tends to be poorer due to the increased angle of incidence, and smoothing of these signals is also often required.

For each ten-minute instance, a directional spectrum is estimated using an approach derived from several resources (Benoit et al. 1997)(Goda 2010)(Cruz 2008) using a stochastic approach. It is assumed that the wave field can be described by the surface elevation (η) according to the directional spectrum (S), the wave number (k), the wave direction (θ), and the wave frequency (f).

$$\eta(x,y,t) = \int\int \sqrt{2S(f,\theta)dfd\theta} cos[k(x\cos\theta + y\sin\theta) - 2\pi ft + \phi] \tag{3.13}$$

For stochastic methods, it is assumed that the phase function (ϕ) is randomly distributed between 0 and 2π with uniform probability density, inferring that all wave components are independent.

A ten-minute time series of surface elevation is simultaneously taken at 3,4, or 5 locations. First, the cross-spectra (G_{ij}) of every pair of signals are estimated using Fast Fourier Transforms (see appendix A.1), (i and j indicate directional components x, y, z), and second, the directional spreading function (D) is calculated using the relationship between the cross-spectra and the directional spectra:

$$G_{ij}(f) = S(f)\int_0^\infty TF_i(f,\theta)TF_j^*(f,\theta)e^{-ik(x_j - x_j)}D(f,\theta)d\theta \tag{3.14}$$

Here $S(f)$ is the frequency spectrum derived from the surface elevation signal. In the case where multiple surface elevation measurements are not available TF is the transfer function between surface elevation and another wave signal (e.g. pressure, velocity etc.), typically derived using linear wave theory. Since $E(f) \int_0^{2\pi} S(f,\theta)d\theta$ the integral of the directional spreading function (D) over the full range of directions (0 to 2π) should sum to 1 with directional spreading at 0 and 2π should be equal as in the equations below.

$$\int_0^{2\pi} D(f,\theta)d\theta = 1 \tag{3.15}$$

$$D(f,0) = D(f,2\pi) \tag{3.16}$$

Many different methods are available for calculating the spreading function including the Truncated Fourier Series Decomposition Method, Direct Fourier Transform Method, Extended Maximum Likelihood Method (EMLM), Iterated Maximum Likelihood Method (IMLM), Extended Maximum Entropy Principle (EMEP) and Bayesian Directional Method Goda (2010). The code developed for this work has options for IMLM and EMEP, chosen following discussion with RDI instruments, based on calculation speed and accuracy whilst using data from 4 or 5 measurement points.

The Maximum Likelihood Method (MLM) takes a linear combination of the cross-spectra, where D' denotes the modified spreading function.

$$D'(f,\theta) = \frac{1}{S(f)}\sum_{i,j}^{max} \alpha_{ij}(f,\theta)G_{ij}(f) \tag{3.17}$$

The EMLM estimate convolutes the true spreading function with the window function $w * (\theta, \theta')$. Window functions enable a realistic view of the data from a discretized data set and are discussed in greater detail in section 3.5.

$$D'(f,\theta) = \int_0^{2\pi} D(f,\theta) w(\theta,\theta') d\theta' \tag{3.18}$$

The window function is given below such that as the window function approaches the Dirac function the real and estimated directional spreading function become more similar.

$$w(\theta,\theta') = \sum_{i,j}^{max} \alpha_{ij}(f,\theta) H_i(f,\theta') H_j^*(f,\theta') \tag{3.19}$$

A solution is found in Isobe & Kondo (1984) such that:

$$D'(f,\theta) = \frac{\kappa}{\sum_{i,j} H_i(f,\theta) G_{ij}^{-1}) H_j^*(f,\theta)'} \tag{3.20}$$

Where κ satisfies the unit integral condition between 0 and 2π.

IMLM is used in the work by Pedersen, Lohrmann & Krogstad (2005) mentioned previously, using similar instruments to the data in this study and is hence used here. It was derived by Pawka (1982), improving the non-iterative procedure by attempting to match the cross-spectra of the initial MLM with one from the original signals. The quantity ϵ^i is added to the derived spreading function of the previous iteration.

$$\epsilon^i(f,\theta) = \frac{|\lambda|^{\beta+1}}{\lambda\gamma} \tag{3.21}$$

Where

$$\lambda = D(f,\theta) - \Delta_{MLM}^{i-1}(f,\theta) \tag{3.22}$$

The MLM estimate from the cross-spectra (Δ_{MLM}^{i-1}) is based on D', with β and γ being control parameters that support the control of the iterative algorithm, which will halt after a specified number of iterations. It is likely from numerical and laboratory experiments that the iterative method produces more accurate peaks than the extended method (Benoit et al. 1997), though in real seas this is difficult to quantify.

The result for each ten-minute time-series is a directional spectrum similar to that displayed in Figure 3.8 with potential parameters for extraction, as described in chapter 5 including:

- H_s - significant wave height
- T_e - energy period
- T_m - mean period
- T_z - zero crossing period
- T_p - peak period
- $MDIR$ - mean direction of spectrum
- $SDIR$ - directional spread

- θ - mean direction per frequency
- σ - mean directional spreading per frequency
- D_p - peak direction

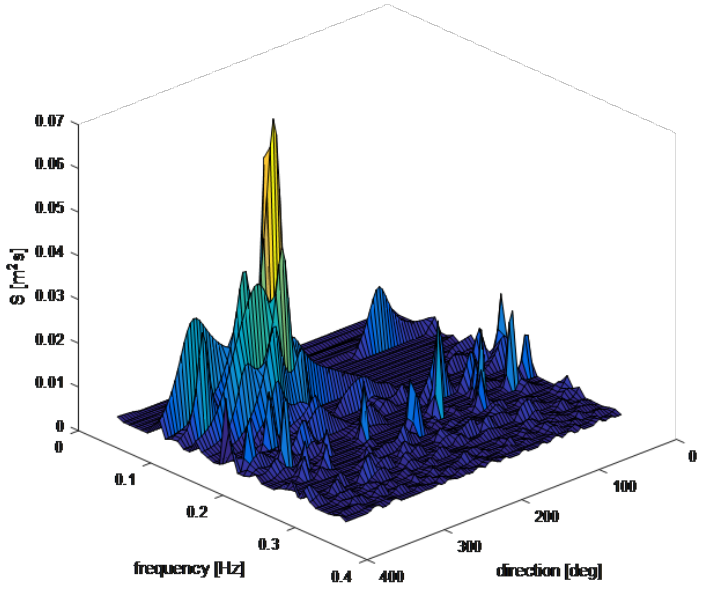

Figure 3.8: Multi directional surface spectrum example. Estimated from 5, ten-minute surface elevation records

Parameters, such as wave height and period, from the directional elevation spectra are compared with those taken from measurements made using the single vertical beam in chapter 4.

Directional estimations

Directional estimates can be made using the cross, co and quad spectra for measured velocities. From the cross spectrum, that is the spectrum of a pair of signals, $G_{ij}(f)$, as in equation 3.14, can be taken the co-spectrum, C_{ij}, and the quad spectrum, Q_{ij}, the real (Re) and imaginary (Im) parts of the cross spectrum. It is normally recommended to average the co- and quad- spectra over at least 10 harmonics before calculating directional properties. Harmonics are integer multiples of the peak frequency, which may appear in the spectrum up to half the sampling frequency. Averaging over multiple of these frequencies results in a smoothed spectrum as seen in section 3.5.

$$C_{ij}(f) = Re(G_{ij}(f)) \tag{3.23}$$

$$Q_{ij}(f) = Im(G_{ij}(f)) \tag{3.24}$$

The mean direction of wave propagation (θ_m), and the root mean square spreading, at frequency f are given by equation 3.25 and equation 3.26, where specific directional components x, y and z are used.

$$\theta_m(f) = ATAN2(Q_{zy}(f), Q_{zx}(f)) \tag{3.25}$$

$$\sigma_c(f) = \sqrt{2(1 - m_1)} \tag{3.26}$$

$$\text{Where: } m_1 = \sqrt{\frac{Q_{zx}^2 + Q_{zy}^2}{C_{zz}(C_{xx} + C_{yy})}} \tag{3.27}$$

The spectrally weighted mean direction and spread can then be calculated according to equations 3.28 and 3.29, where ATAN2 is the four quadrant inverse tangent and S_η is the spectrum of surface elevation.

$$MDIR = ATAN2\left(\int_0^\infty S_\eta(f)\sin(\theta_m(f))df, \int_0^\infty S_\eta(f)\cos(\theta_m(f))df\right) \tag{3.28}$$

$$SDIR = \frac{\int_0^\infty S_\eta(f)\sigma_c(f)df}{\int_0^\infty S_\eta(f)df} \tag{3.29}$$

In using surface elevation, pressure and velocity records, DCP directional measurement has the main advantage over other instruments that by using the depth bins as a virtual array of sensors many degrees of freedom are possible which would not be provided for by other instruments. The separation of these bins means that a far greater aperture is achieved than that which could be achieve by a single point measuring device and hence a more realistic resolution is possible.

RD Instruments (Strong et al. 2000) and Nortek (Pedersen, Malzone & Siegel 2005) both use the Maximum Likelihood Method (MLM) which provides a good trade-off between narrow directional accuracy and false side lobes. Using velocity records this calculation works best for 3 depth cells. Four or more depth cells will improve accuracy but significantly increase computational time. These depth cells should be relatively high in the water column (such that the span between beams is wider) though conservatively below surface level. Band averaging of adjacent frequency bands before inversion can help to smooth the data and increase degrees of freedom.

Whilst DCPs provide reliable information for most useful parameters, implied estimates for the directional distribution can be unreliable, as with other measurement methods including wave buoys. The MLM method allows measurement of multiple directions arriving at the same frequency, however it smears the directional distribution during inversion. 'Spatial Aliasing' occurs when two or more waves of the same frequency occur between two measurement bins. The cross spectrum is therefore no longer unique and the MLM estimate will contain multiple peaks, such that the result is aliased or smeared. For example, over a measurement distance of 40m aliasing will occur for wave frequencies higher than 0.9 rad/s. This effect is often so strong that it is not reasonable to accept an estimate of directionality from phase information alone Waais et al. (2002). The IMLM method is often recommended in which up to 3 iterations will restore most of this energy to the peak. MEM methods have also been proven to produce robust estimates (Kobune & Hashimoto 1986), though some formulations can result in double peaks from uni-modal directional spectra (Lygre & Krogstad 1986). For this reason the IMLM method is most frquenctly used in this body of work.

Linear transfer functions

Linear wave theory discussed in section 2 enables transformation of vertical velocity to surface elevation, based on assumptions discussed in section 2.1. The surface elevation spectrum and velocity spectra (in the horizontal and vertical) are given by equations 3.30, 3.31 and 3.32. In order to incorporate currents when inferring surface elevation from velocity measurements, it is necessary to modify equations by including the dispersion relationship for a vertically weighted background current profile. One can assume a linear interaction between waves and currents, where wave and current velocities are superposed, however this may not be always be accurate, and as such it is important to have a check on the inferred surface elevation.

$$S_\eta(f_i)\delta f = \frac{1}{2}a_i^2 \tag{3.30}$$

$$S_u(f_i, z) + S_{u_y}(f_i, z)\delta f = \frac{1}{2}(a_i Q_i(z))^2 \tag{3.31}$$

$$S_v(f_i, z)\delta f = \frac{1}{2}(a_i R_i(z))^2 \tag{3.32}$$

$$\text{Where:}\quad Q_i(z) = \omega_i \frac{\cosh(k(h+z))}{\sinh(kh)} \tag{3.33}$$

$$R_i(z) = \omega_i \frac{\sinh(k(h+z))}{\sinh(kh)} \tag{3.34}$$

The surface elevation spectrum can be estimated from the vertical velocity spectrum through either equation 3.35 or equation 3.36 .

$$S_\eta(f_i) = \frac{S_u(f_i, z) + S_v(f_i, z)}{Q_i^2(z)} \tag{3.35}$$

$$S_\eta(f_i) = \frac{S_w(f_i, z)}{R_i^2} \tag{3.36}$$

A check ratio is defined in equation 3.37, where deviations from 1 indicate that measurements do not conform to linear theory(Benoit et al. 1997).

$$CR(f_i, z) = \tanh(k(h+z))\sqrt{\frac{S_w(f_i, z)}{S_u(f_i, z) + S_v(f_i, z)}} \tag{3.37}$$

If linear theory holds estimations of surface elevation should be equal regardless of the depth at which the velocity spectrum is taken. Deviation from unity would indicates the necessity for consideration of other theory, including higher order theories such as that defined by Stokes (Goda 2010).

Velocity transfer example A sample data set containing vertical velocity measurements from a DCP is used to estimate the surface elevation. Using the method outlined a surface elevation spectrum for the sea state during the measured time frame can be estimated.

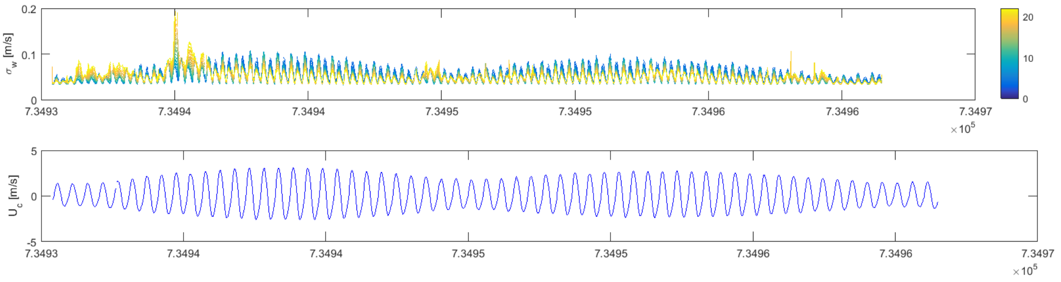

Figure 3.9: Example vertical standard deviation time series compared with average horizontal current time series. Colour bar indicates depth where zero is at the sea surface

From the data presented in figure 3.9 it is clear that fluctuations in vertical velocity are typically greater during higher horizontal current speeds and generally occur closer to the sea bottom, as a consequence of turbulence due to seabed roughness. In various instances however, this is not the case. These instances, where vertical fluctuation is greater near the sea surface, are caused by periods of wave activity.

Taking 30 minute segments of vertical velocity data and converting to the frequency domain by means of a fast Fourier transform method, it is possible to gain a better understanding of conditions. Figure 3.10 shows a period indicating energy between the frequencies expected for ocean waves.

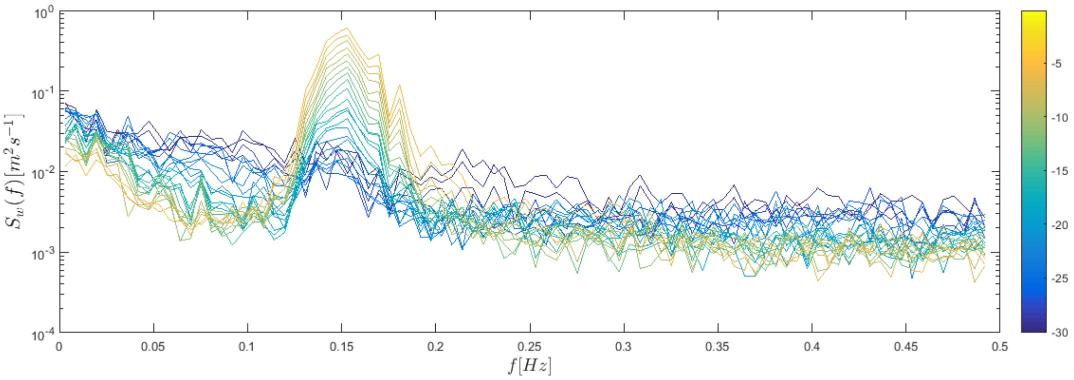

Figure 3.10: Example vertical velocity spectrum during a period of high wave activity. Colour bar indicates depth where zero is the sea surface

At frequencies relative to typical wave periods, greater intensity is seen closer to the sea surface, as explained by theory in section 2. Vertical velocities fluctuating at lower frequency are predominantly caused by turbulence of relatively large length-scales whilst that at higher frequency are a largely result of Doppler noise. The surface elevation spectrum is obtained according to the methods discussed above (section 3.2.2) using the transform illustrated in figure 3.11, a function of depth and frequency.

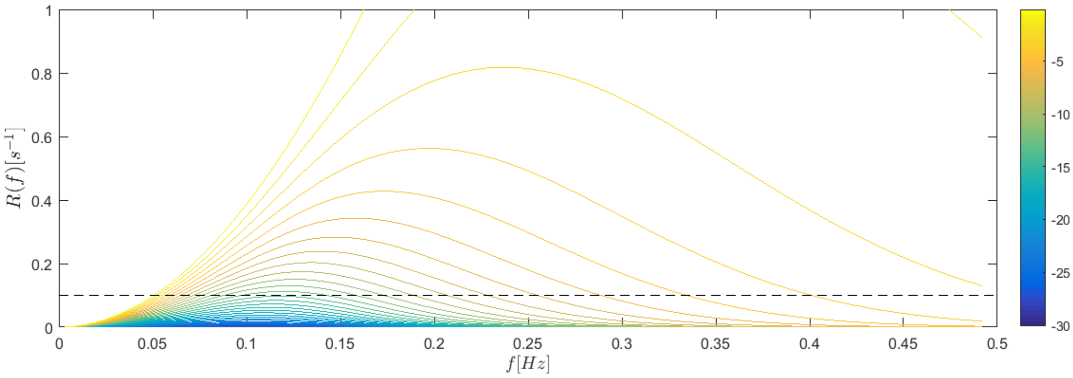

Figure 3.11: Transform (for vertical velocity to surface elevation). Colour bar indicates depth where zero is the sea surface

Figure 3.12 shows the surface elevation spectrum, estimated from the vertical velocity spectra, recorded at a range of depths, by means of the transform above. If linear theory is applicable the surface elevation estimated from the vertical velocities at each depth should be equal. The data used in this example shows a strong correlation around the peak frequency across the range of depths. However as one diverges from peak frequency the correlation weakens, particularly with estimates made from a greater depth. This is because linear wave theory does not apply outside of the frequency range dominated by waves.

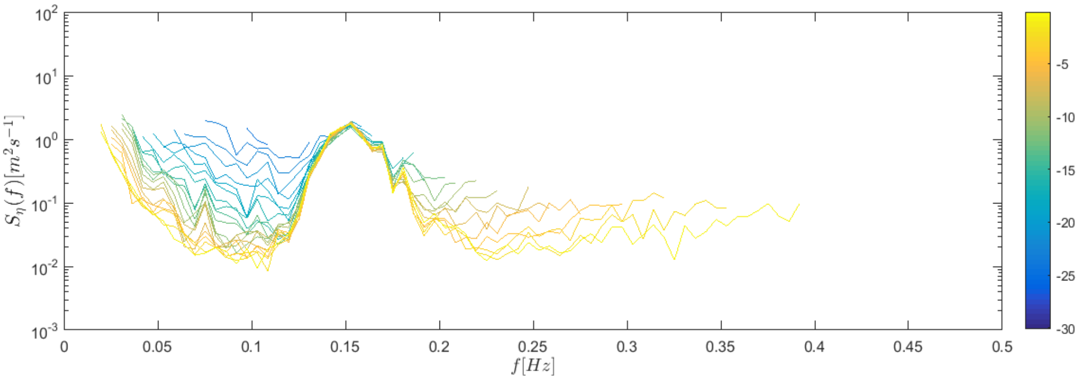

Figure 3.12: Example surface elevation spectrum during a period of high wave activity. Colour bar indicates depth where zero is the sea surface

There are several methods by which it is possible to remove the effects of turbulence and noise from the spectrum. A simple method used here, for the sake of this example, subtracts the 25th percentile of the measured vertical velocity spectrum at respective current velocities before transforming to surface elevation. The result is illustrated in figure 3.13.

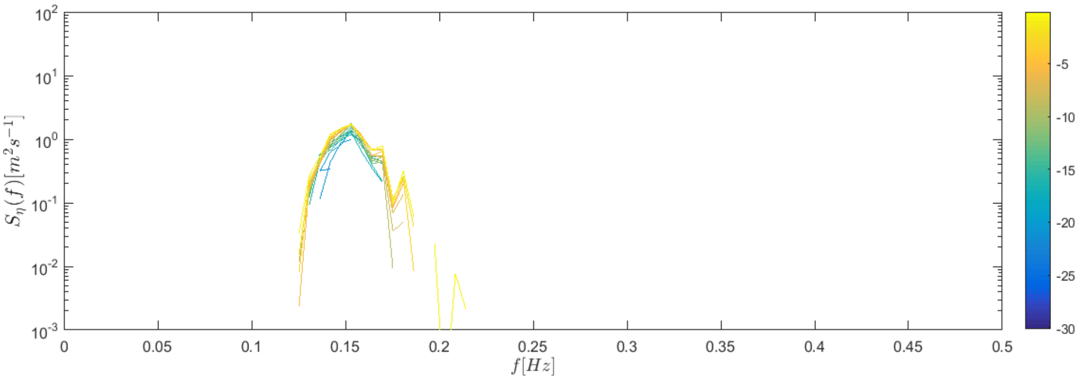

Figure 3.13: Example surface elevation spectrum during a period of high wave activity, corrected for turbulence and noise. Colour bar indicates depth where zero is the sea surface

From the corrected surface elevation spectrum useful parameters can be calculated for describing the sea state, such as significant wave height and period. This is achieved using spectral moments as described in section 2.1.4. Using the method outlined in this section (3.2.2) and section 3.2.2, it is possible to estimate a frequency-direction spectrum for a measured sea state using velocity measurements made by a DCP. The method assumes a depth varying equivalent uniform current, Hedges & Lee (1992). This method is therefore a useful means to extract wave information from DCP velocity measurements, however it should be combined or replaced with AST methods, where AST data is available, since its accuracy is limited due to wave velocities varying across an array in which the DCP assumes homogeneity.

3.3 Turbulence

The measurement of turbulence requires high frequency instruments in order to get a picture of the passage of eddies, and circulations of varying size, as they pass through the point of interest. The energy and variability in the flow can be represented as Reynolds stresses or turbulent kinetic energy, as discussed in section 2. Turbulence intensity and length scale are also useful descriptors of the flow.

During the ReDAPT project (Parkinson & Collier 2016) single beam Doppler instruments mounted on a demonstration turbine were successfully used in determining turbulence parameters at the Falls of Warness tidal site in Scotland. These instruments aimed longitudinally, laterally and vertically, were able to more closely measure velocities in the flow due to the relative acuteness of beam angle to velocity direction compared with the relative angle of a typical upward looking DCP. Turbulence characteristics determined during this time provide reference for much of the turbulence aspect of this study. A number of other studies have also been conducted using Doppler instruments to measure turbulence. A three and a four beam DCP were used in comparison with an Acoustic Doppler Velocimeter (ADV) to determine effectiveness in recording turbulence parameters (Nystrom et al. 2007). Both recorded mean current velocity profiles well for low turbulence intensities however performed less well in higher turbulence intensities. Reynolds stress was well estimated by the 4 beam DCP however neither were capable of measuring turbulent kinetic energy without further assumptions, and could not estimate integral time-scales to within 60 percent.

Using the variance method good results for Reynolds stresses can be calculated from a DCP as compared with an Acoustic Doppler Velocimeter (ADV) however this quickly breaks down with the presence of waves (Souza 2010). A quadratic drag law can be used to compare against Reynolds stress estimates from DCPs in the absence of co-located ADV data. A High Resolution Current Profiler (HRCP) which used a 4 beam pulse to pulse coherent sonar at 307kHz was used to effectively estimate Reynolds stresses (Lohrmann, Hackett 1990) with a fifth vertical beam proving the most effective way to improve accuracy during wave conditions and for instrument tilt. The fifth, vertical beam of a Nortek and TRDI device was again used in (Guerra Paris & Thomson 2017) estimating Reynolds stresses and turbulence kinetic energy production, dissipation rate, and budget due to the possibility of a direct measurement of vertical velocity allowing for estimation of 5 of the six Reynolds stresses total turbulent kinetic energy and anisotropy. This is a considerable improvement of the four beam variance method (Lu & Lueck 1999*b*)(Stacey et al. 1999)(Rippeth et al. 2003).

3.3.1 Turbulence intensity

Standard practice governs that turbulence parameters are taken at specified depths from instances of low wave conditions (i.e. $H_s < 1\text{m}$). Further to this, and in the methodology developed here, wave components within the velocity spectra are removed using the spectrum of surface elevation and linear wave theory. Noise components within the spectra are also removed. Turbulence intensity can subsequently be determined from mean longitudinal flow speed, $\overline{u}$ and the velocity component standard deviation, σ_i, calculated from the (turbulence only) spectrum S_i at frequencies f.

$$TI_i = \frac{\sigma_i}{\overline{u}} \tag{3.38}$$

$$\sigma_i = \sqrt{\int_0^\infty S_i(f)df} \tag{3.39}$$

More simply, turbulence intensity can be determined by calculating standard deviations from velocity time series during low wave instances, however in many data sets, including that used for this study, waves are present throughout to some degree. Removal of noise is also beneficial.

3.3.2 Turbulence length scale

Turbulence length scales refer to the average gust length of eddies circulating in the flow. It is often very difficult to establish this average length accurately due to the extremely stochastic nature of turbulence. Eddies are caused primarily by bathymetric features, and in high energy tidal flows, the passage of water over these features can vary greatly. If eddies are consistent for a sufficient period (i.e. ten minutes) then spectral analysis of velocity measurements can shed light on the length, breadth and depth of these turbulent gusts. In this study three different methods were investigated for estimating turbulence length scales, during low wave conditions.

1. Spectral peak fitting of a simplified model ENU velocity turbulence spectra to a field velocity turbulence spectra
2. VDCP spectral fitting of the field and model along beam velocity spectra using VDCP.
3. Autocorrelation of measured ENU velocity time series.

The first method can give a good indication of length scales, however intrinsic error in the measurement of ENU velocities, as discussed in chapter 6 often skews results. The second method, presented below can be automated to optimise the fit of spectra in comparison with field data all four beams, however is dependent on numerous independent variables, leaving potential for error. The third method is again subject to the limitations of DCP records of ENU velocity. However if this is followed by a theoretical correction for DCP error according to the method described in chapter 6 very good agreement is found when comparing field and model along beam velocity spectra across a range of environmental and DCP set-up conditions, as demonstrated in chapter 7.

Autocorrelation and correction

This method compares a velocity time series taken at a certain point with itself (auto) over time. Cross correlation of velocity time series separated in space can also yield information on length scales. Autocorrelation is ideally measured using a ADV at a fixed point in the flow or a single beam Doppler (SBD) instrument aimed in the direction of the desired length scale measurement. In the ReDAPT project (Parkinson & Collier 2016) SBDs were effectively used in this capacity and the results of this project are referred to frequently in this study. The data used most extensively in this study, however, comes from divergent beam Doppler instruments, in particular the TRDI Sentinel V which has 4 'Janus' beams and a fifth vertically aimed beam for measuring waves. In principle the fifth vertical beam can be used to improve measures of ENU velocities and turbulence parameters such as Reynolds stress and turbulent kinetic energy, as in several studies (Gargett 1994, Vermeulen et al. 2011)(Wiles et al. 2006)(Stacey 2003)(Stacey et al. 1999)(Souza 2010)(Lohrmann, Hackett 1990)(Guerra Paris & Thomson 2017) to overcome the limitations surrounding the assumption of homogeneity in the flow over the volume separating beam measurement locations. However this study adopts a method enabled by the use of the VDCP discussed in chapter 6.

Using the auto-covariance (μ_{ii}) of the velocity spectra (S_{ii}) such that:

$$\mu_{ii}(\tau) = \int_0^{\infty} S_{ii}(f) \cos \pi f \tau df \tag{3.40}$$

The auto-correlation function (ρ_{ii}) can subsequently be written:

$$\rho_{ii}(r, r', \tau) = \frac{\mu_{ii}(r, r', \tau))}{\sigma_i \sigma_i} \tag{3.41}$$

Time-scales are calculated by integrating the auto-correlation function up to the shortest time lag for which it falls to zero:

$$T_i = \int_0^{\rho_{ii}=0} \rho_{ii}(\tau) d\tau \tag{3.42}$$

According to Taylors hypothesis (Taylor 1937) length-scales are estimated according to mean current velocity $\overline{u}$. For example, for the longitudinal component (subscript u) in the longitudinal direction (superscript x):

$$^{x}L_u = T_u \overline{u} \tag{3.43}$$

Figure 3.14 illustrates the model and field velocity spectra for a low wave, high current instance similar to that used in the previous examples, where the length scales input to the model are those estimated from the field data. The field and model beam velocity spectra demonstrate a very reasonable fit for the length scales estimates using the autocorrelation method.

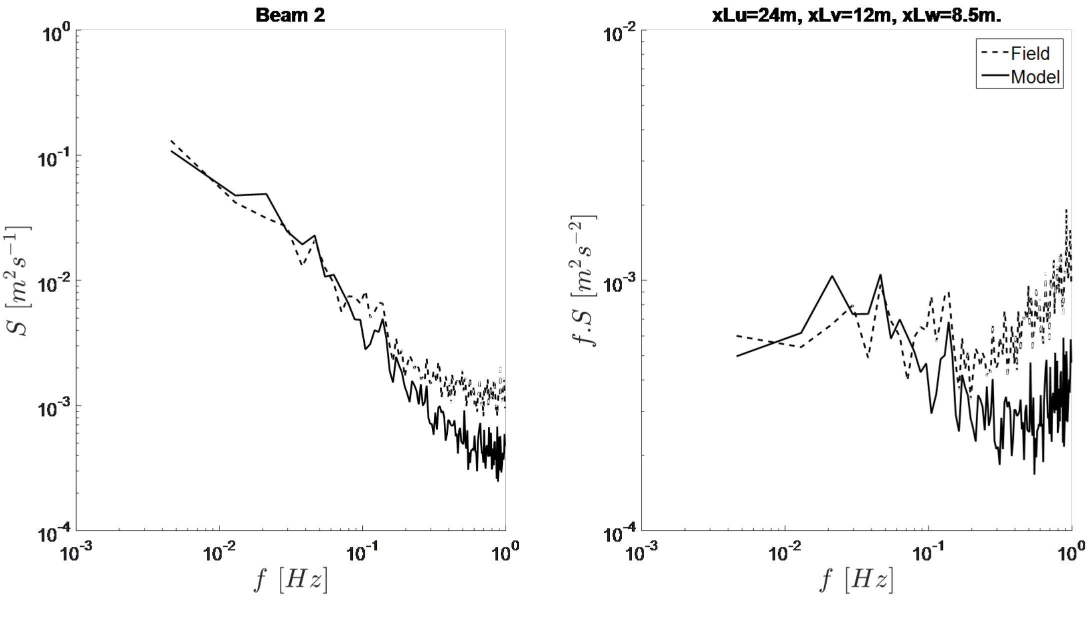

Figure 3.14: Field-model beam velocity comparison with calculated estimates of turbulence length scale. Black dotted line indicates average of similar field instances. Black solid line indicates best match between model and field data at specified range of frequencies.

Having calculated length scale using the autocorrelation method a correction based on theoretical errors determined in chapter 6 can be applied according to environmental and DCP set-up conditions. This is found to give close agreement between model and field spectra across a broad range of environmental and set-up conditions.

Spectral peak fitting A basic Von Karman method is used in this analysis. For the longitudinal component of turbulence where S_{ii} is the auto-spectrum of flow speed variation in u direction:

$$\frac{S_{ii}(f)f}{\sigma_i^2} = \frac{4\tilde{n}_u}{(1+70.8n_u^2)^{(5/6)}} \tag{3.44}$$

σ_u is the standard deviation of longitudinal flow speed variation and $\tilde{n}_u$ is a non-dimensional frequency parameter incorporating the length scale of longitudinal turbulence,${}^{x}L_u$ and the mean flow speed, $\overline{u}$.

$$\tilde{n}_u = \frac{f^{x}L_u}{\overline{u}} \tag{3.45}$$

The corresponding auto-spectra for the lateral and vertical components of turbulence where S_{ii} is the auto-spectrum of flow speed variation in the i direction where $=v$, or w:

$$\frac{fS_{ii}(f))}{\sigma_i^2} = \frac{4\tilde{n}_i(1+755.2\tilde{n}_i m^2)}{(1+282.3\tilde{n}_i^2)^{(11/6)}} \tag{3.46}$$

The Von Karman turbulence spectrum, is therefore sensitive to the inputs specified in table 3.1

Name	Symbol	Sensitivity (power)
Flow speed magnitude	$\overline{\mathbf{u}}$	1
Standard deviation	$\sigma_{\mathbf{i}}$	2
Length scale	${}^{\mathbf{p}}\mathbf{L_i}$	1

Table 3.1: Sensitive parameters for Basic Von Karman Turbulence Model

Flow speed magnitude can be accurately estimated from DCP measurements, transformed to ENU velocities using 2 or more along beam records. Standard deviation can also be estimated from ENU velocities though there are some limitations to the accuracy of this method. The effect of length scale on velocity spectra are investigated.

Initially the effect of varying length scale on the output model spectra is demonstrated. Firstly looking at ENU velocities, as in Figure 3.15, and secondly, looking at the resultant along beam velocities that a DCP would measure in a flow, both for a beam parallel(3.16) to flow direction and for a beam perpendicular (3.17) to flow direction. The model flow is given longitudinal, lateral, and vertical velocity $2ms^{-1}$, $1ms^{-1}$, and $0.1ms^{-1}$ respectively.

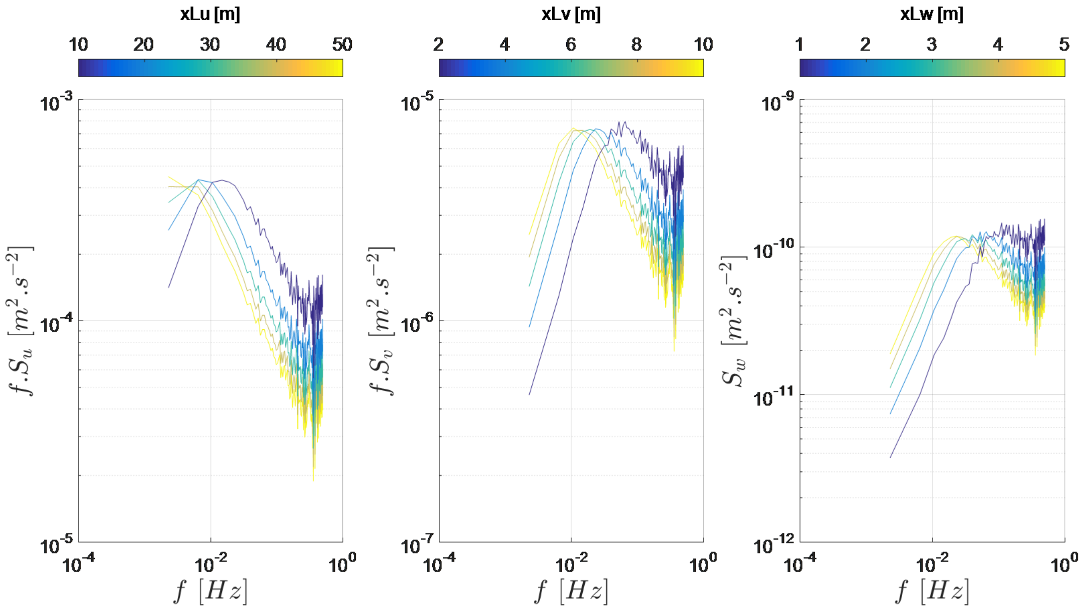

Figure 3.15: Sensitivity of Von Karman turbulent velocity to length scale, for three component directions, for velocity spectra where TIx=10%, TIy=5%, TIz=1%.

Turbulence length scale has a demonstrable effect on the magnitude of the Von Karman velocity spectrum. These curves can be used against field measured ENU velocities to estimate longitudinal, lateral and vertical length scales by matching their individual peaks, irrespective of turbulence intensity and other set-up and environmental conditions.

VDCP spectral fitting The most involved method for establishing length scales uses the VDCP discussed in chapter 6 in order to directly compare model and field along beam turbulent velocities. ENU velocities estimated from DCP measurements are subject to spatial averaging and the assumption of homogeneity between DCP beams. This could be an issue for the measurement of turbulence which can cause significant fluctuations in velocity over a distance equivalent to the separation of DCP beams. To understand how variations in the three length scales applied above would be noticed when measured by a DCP, along beam model velocity spectra are compared. Velocities from along one of the beams parallel to the mean current direction are plotted in Figure 3.16, whilst velocities from one of the beams perpendicular to the mean current direction are plotted in Figure 3.17. Clearly the effect of longitudinal length scale has a greater effect on beams parallel to the mean current direction, and vice versa for the lateral length scale. The influence of vertical length scale is marginally greater on perpendicular beams due to the proportionately lower horizontal velocity in this direction.

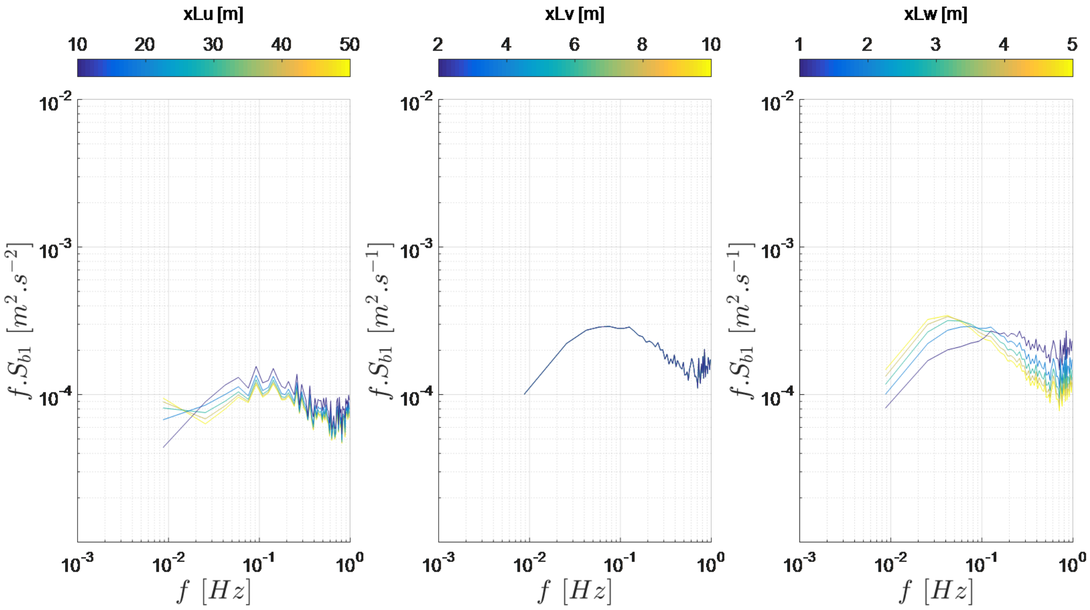

Figure 3.16: Sensitivity of Von Karman turbulent velocity to turbulence length scale for velocity along beam parallel to flow direction

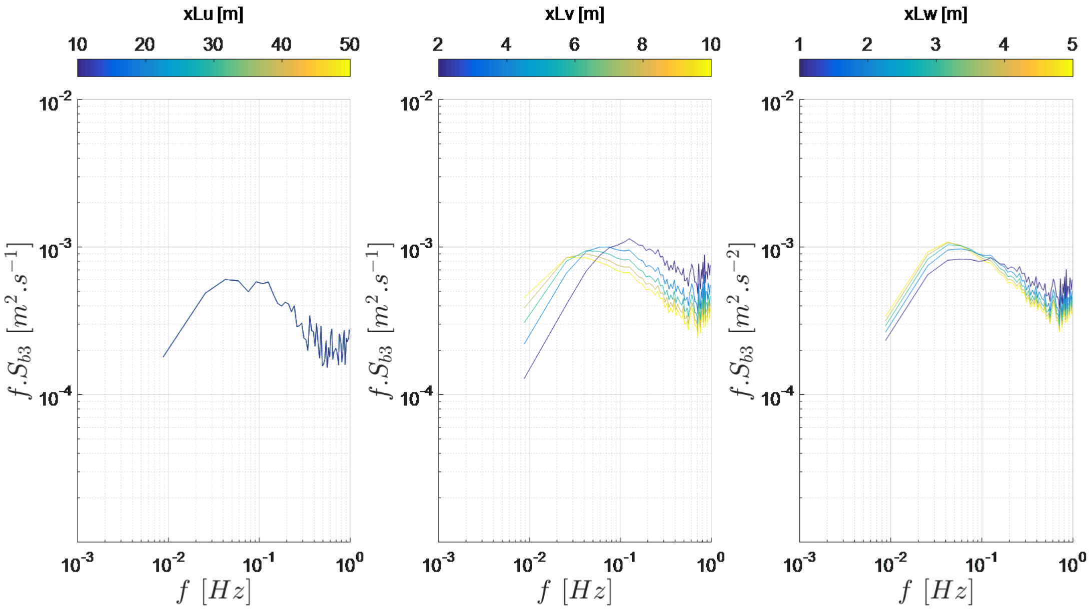

Figure 3.17: Sensitivity of Von Karman turbulent velocity to turbulence length scale for velocity along beam perpendicular to flow direction

Low wave scenarios are taken from the field data in order to analyse the turbulence without the influence of waves. Figure 3.18 shows comparisons of field and model velocity spectra for ENU and along beam velocities, where estimates of model length scales are based on calculations performed in the section 3.3.2 and turbulence intensity is determined according to the method in section 3.3.1 for low wave, high current instances.

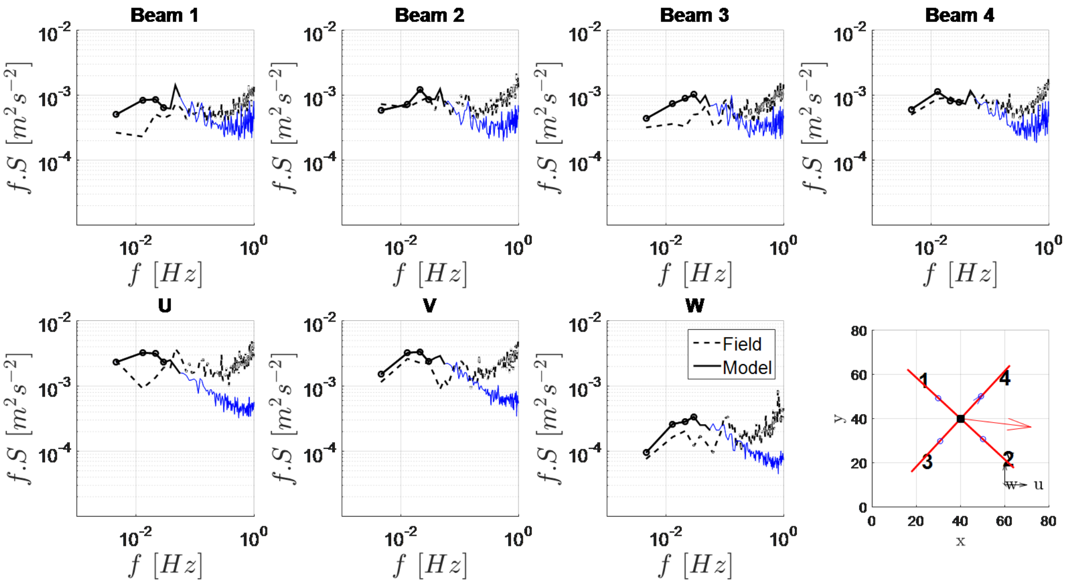

Figure 3.18: Field-model comparison of ENU and along beam velocities, during flood tide, using calculated estimates of length scale; Black dotted line indicates average of similar environmental instances. Coloured line indicates best model estimate whilst black solid line indicates frequencies over which spectra are fitted. Bottom right plot indicates DCP orientation and mean current direction (red arrow).

Beams 2 and 4 show a good correlation between model and field velocity spectra, whilst beams 1 and 3 compare less well. Given that length scales have been calculated from ENU velocity spectra one would expect field ENU velocity spectra match well. However, whilst lateral and vertical spectra have good agreement, the longitudinal velocity is poorly represented. Looking at DCP orientation with respect to mean current direction one can see that beams 2 and 4, which capture length scale more effectively, are closer to the mean positive direction of flow. Looking at ebb flow the same is true; those beams in the direction of mean positive flow (1 and 3) provide a better fit to the model, as seen in Figure 3.19.

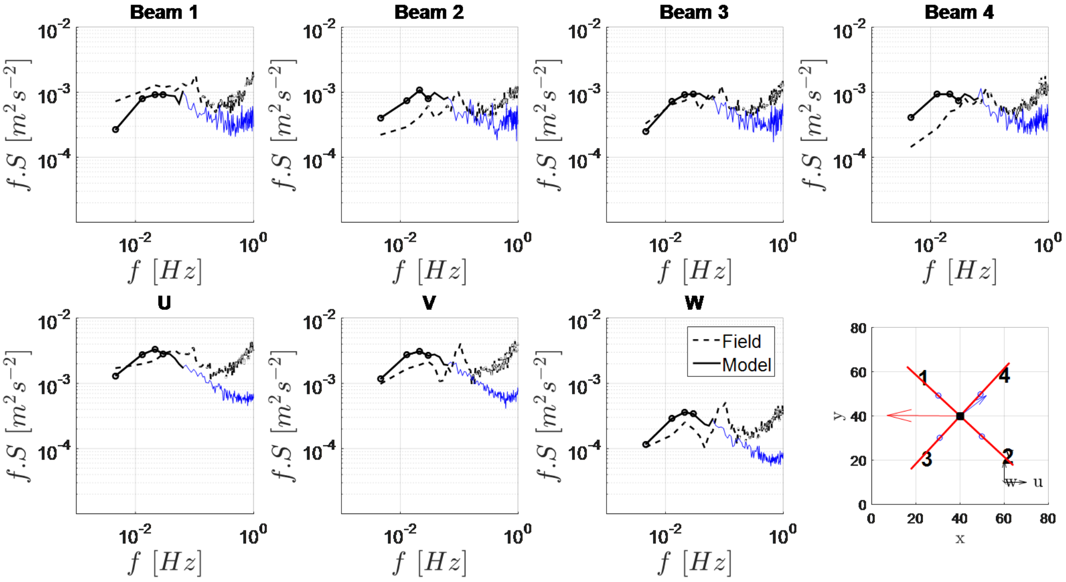

Figure 3.19: Field-model comparison of ENU and along beam velocities, during ebb tide, using calculated estimates of length scale; Black dotted line indicates average of similar environmental instances. Coloured line indicates best model estimate whilst black solid line indicates frequencies over which spectra are fitted. Bottom right plot indicates DCP orientation and mean current direction (red arrow).

To investigate further, a range of length scales around those calculated are used and the velocity spectra are compared numerically by calculating the difference between the field and model spectra and applying a weighting that gives greater significance to the frequencies within the lower range. Figure 3.20 illustrates the model-field comparison using length scales 1, 5, 10, 15 and 20m for all components. The model spectrum that best matches the field spectrum is shown as a solid black line and the length scales of this best fit are given in the title of each sub-plot.

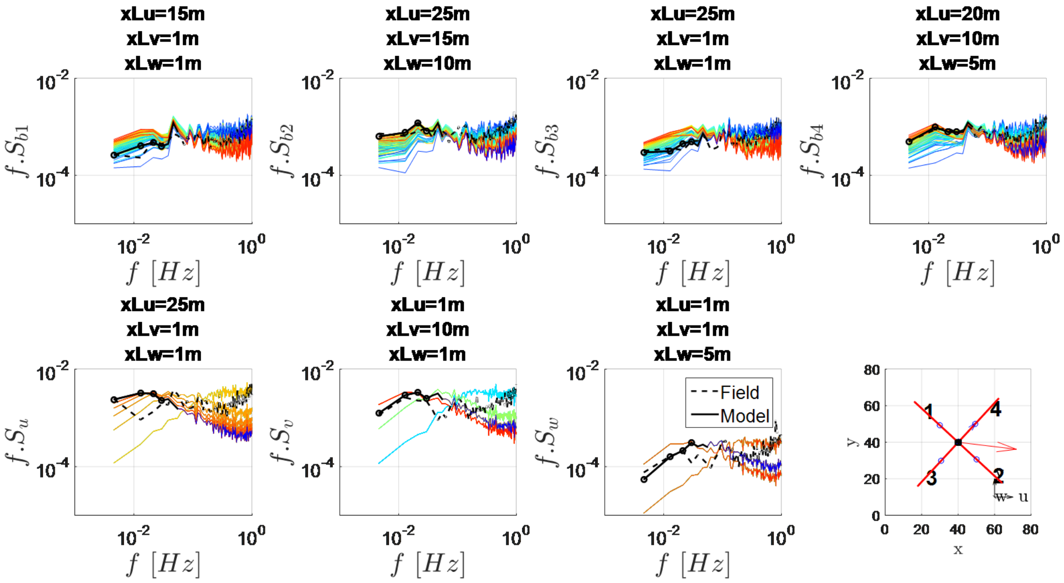

Figure 3.20: Field-model comparison using preliminary estimates of length scale for all four beam velocities, during flood tide. Black dotted line indicates average of similar environmental instances. Coloured lines indicate 27 model guesses, based on 3 estimates for 3 components of length scale. Black solid line indicates best match between model and field data.

Applying the same method to the ebb flow example (low wave, high current) length scales 1, 5, 10, 15 and 20m are used for all components; as in Figure 3.21.

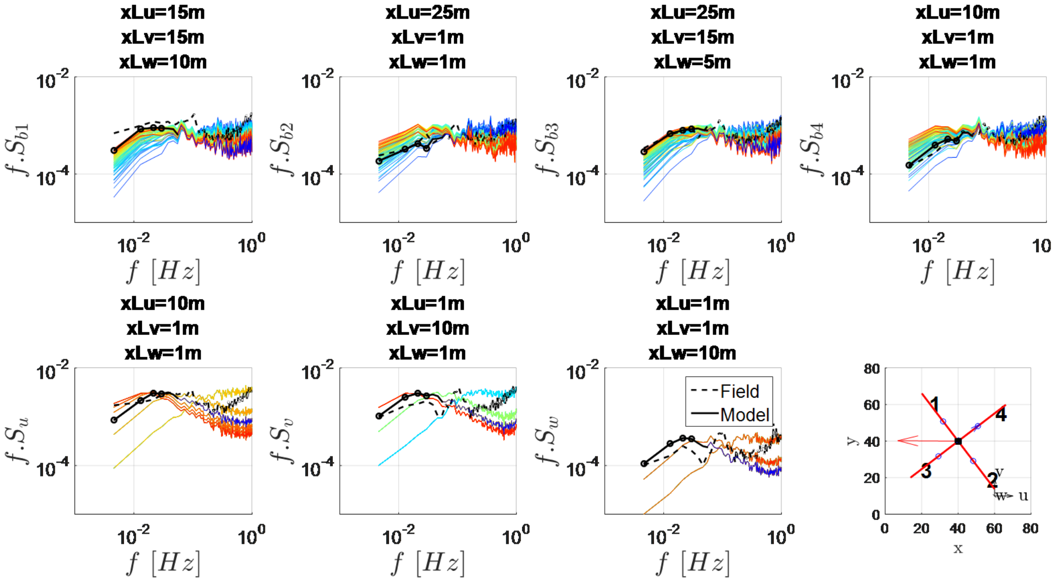

Figure 3.21: Field-model comparison using preliminary estimates of length scale for all four beam velocities, during ebb tide. Black dotted line indicates average of similar environmental instances. Coloured lines indicate 27 model guesses, based on 3 estimates for 3 components of length scale. Black solid line indicates best match between model and field data.

It was found that length scales can be calculated to within a reasonable degree of accuracy using the auto-correlation of the estimated ENU velocities. From these initial estimates a model Von Karman turbulence spectrum can be calculated and fitted to the field spectra of all DCP beams and also the ENU velocity spectra using a range of model length scales based around the initial length scale calculations. The most suitable length scales can then be determined based on shape and fit.

3.4 Noise

DCP measurements are subject to Doppler noise contamination. When exploring mean current velocity information averaging negates any effects of this noise, however in understanding turbulence it is necessary to quantify the noise floor. The noise floor varies with instrument ping frequency, measurement distance from the instrument and must be quantified in order to effectively compare field and model beam velocities. There are several methods used to determine the noise floor in the data. The simplest means to calculate the noise floor is to plot the standard deviation of each signal. In Figure 3.22 below standard deviation is plotted against depth with a third dimension, mean current velocity magnitude plotted according to colour.

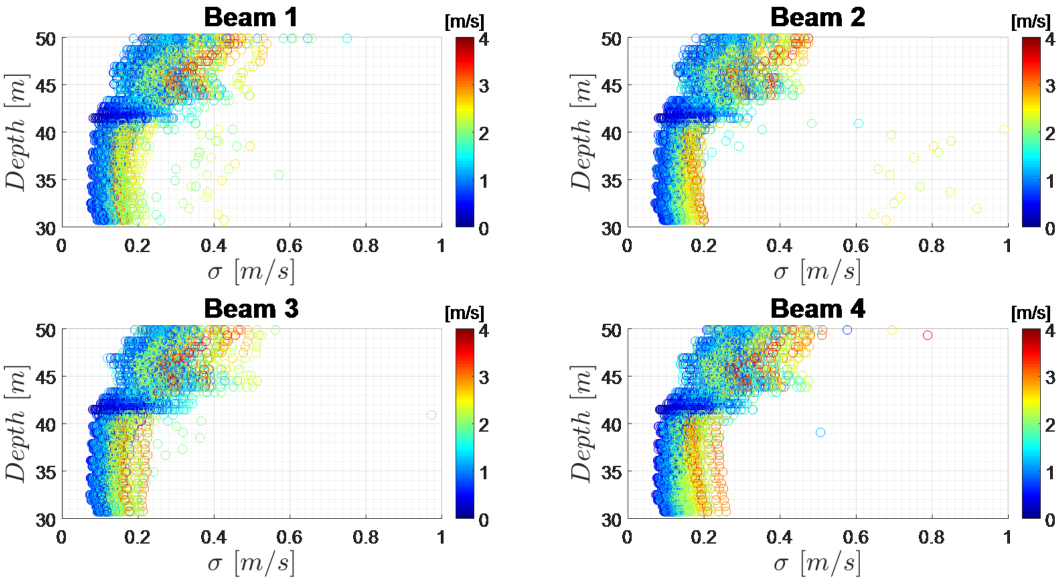

Figure 3.22: Plot of standard deviation with depth and current speed to determine noise floor

It can be seen in Figure 3.22 that there is a consistent standard deviation floor at approximately $0.08ms^{-1}$. This varies with depth and also with mean current velocity. Plotting in a similar way for individual depths and velocity ranges would illustrate an approximate noise floor dependent on these variables.

Fit curve An alternative method, as proposed by (Richard et al. n.d.) fits a curve to the velocity spectra according to the two parameter equation:

$$Y = Kf^{-5/3} + N \tag{3.47}$$

Where K is $C\epsilon^{2/3}$ and N is the power spectral density of the Doppler noise. Here ϵ is the turbulent dissipation rate, and c is a constant. Figure 3.23 shows the curve fitted to the measured along beam velocity spectrum at each beam. The asymptote of this curve indicates N, the variance of the noise floor.

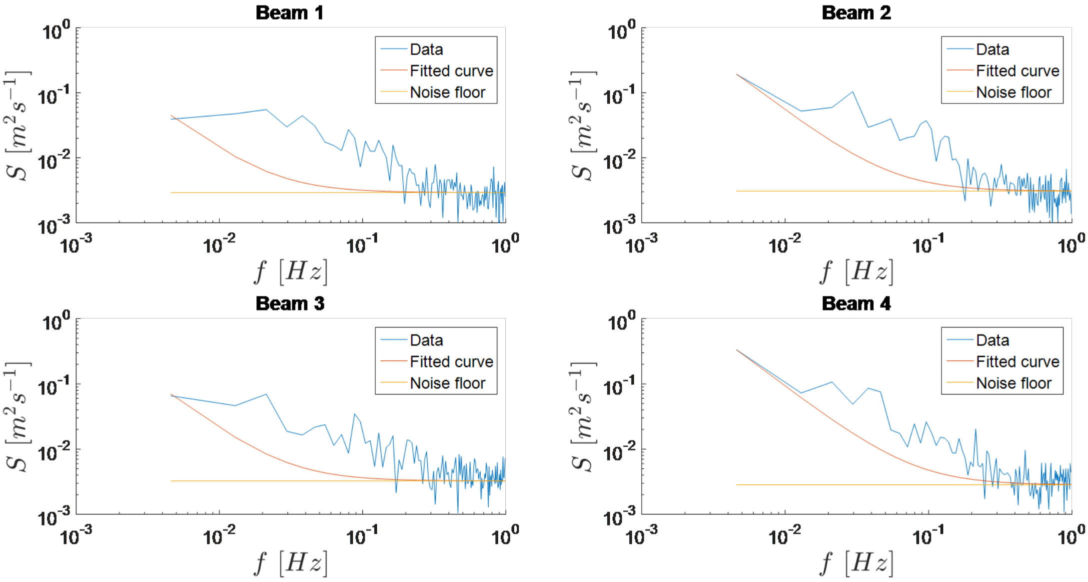

Figure 3.23: Curve fitting to find noise floor in along beam velocity spectrum

The noise floor is averaged over all the beams and applied to the measured time signal to remove the noise.

Removing noise from signal First find the zero mean unit standard deviation, b_i^*, of the signal, where b_i is the velocity along beam i and $\sigma_b i$ is the standard deviation of said signal.

$$b_i^* = \frac{b_i - \overline{b_i}}{\sigma_{b_i}} \tag{3.48}$$

The measured standard deviation is the sum of the true field standard deviation and the standard deviation of the noise. Rearranging the equation below the true field standard deviation is found:

$$\sigma_{measured} = \sigma_{field} + \sigma_{noise} \tag{3.49}$$

The new beam signal is then calculated:

$$b_i = b_i \sigma_{field} + b_i \tag{3.50}$$

3.5 Tools

Alongside the tools developed for processing subsurface velocity (section 3.1) and surface elevation records (section 3.2) a number of other methodologies have been developed to increase data utility. This section describes those tools.

3.5.1 Binary conversion

Instrument manufacturers may provide software for treatment of data, however this is typically supplied to the DCP user themselves and may masks detail useful to the outcomes of this project. A code was developed for extraction of the raw data from the RDI Sentinel V which was modified from existing code developed by Richard Pawlowicz, which can be found at www.eoas.ubc.ca. Further information and code can be found at trac.nccoos.org. Instrument data formats are attainable from manufacturers and enable modification of code to the data of the specific instrument.

3.5.2 Quality checking

All field data will suffer from erroneous points caused by environmental conditions or instrument errors. All data is therefore assured through quality checking, according to the following method which can be applied to along beam velocities, surface elevation, pressure, and depth records, as well as instrument heading, pitch and roll. Before quality checking a velocity time series from a DCP measurement survey may look something like that presented in Figure 3.24, tending to have useless data at the beginning and end as well as sections and individual points of erroneous data resulting from various interference.

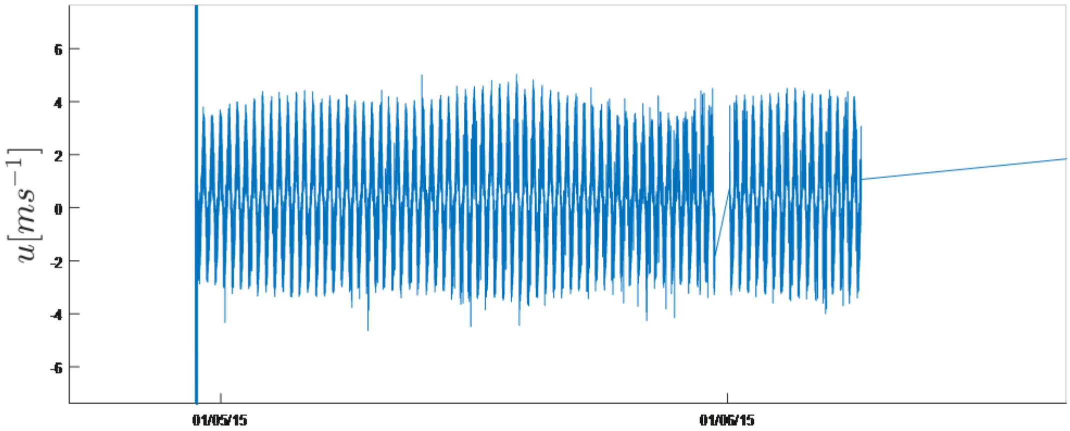

Figure 3.24: Unchecked velocity time-series of data measured by a DCP at an intermediate depth cell. Fluctuations from moving mean can be errors or environmental

The first step is to remove any bad data at the beginning and end of the survey. The period between the device being turned on and secured to its designated location and the period between its removal and being turned off typically contains unwanted data. This data is clearly marked by a rapid change in magnitude of the signal. One can simply locate the date and time of the first and last good quality record by visual assessment and remove unwanted data. The second step is to remove erroneous, sporadic points from within the data set. DCP data quality may be affected by obstructions near any of the transducers, such as bubbles or high sediment content and is particularly likely in such high energy environments as those for tidal energy development.

To improve the overall quality of the data erroneous points can be filtered according to the method suggested below. For this filtering process longitudinal (u), lateral(v), and vertical(w) velocities are treated separately. The method below discusses longitudinal velocity, however the method proposed applies to components in all three dimensions.

1. Calculate the acceleration between consecutive readings, du/dt
2. Calculate the rate of change of acceleration between consecutive readings, $(d^2u)/dt^2$
3. Determine percentile of d^2u/dt^2 within which data appears erroneous.
4. Take the gradient of the absolute velocity, $d|u|/dt$
5. Apply condition, where this gradient is positive, to avoid removing useful data preceding or following an erroneous point.

From the example illustrated in Figure 3.25 a consistent grouping can be observed with occasional outliers. Those points shown in red are in the 99.99th percentile and are considered to be beyond the sensible range for rate of change of acceleration.

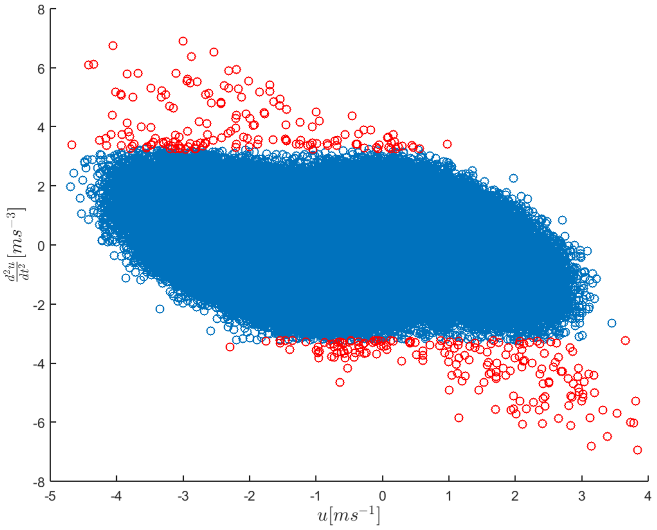

Figure 3.25: Plot of rate of change of acceleration in the stream-wise direction against stream-wise velocity: Blue markers show original data, and red markers show initial indexing of erroneous data.

However this method also occasionally highlights those data points which precede or follow an erroneous measurement, as shown in Figure 3.26.

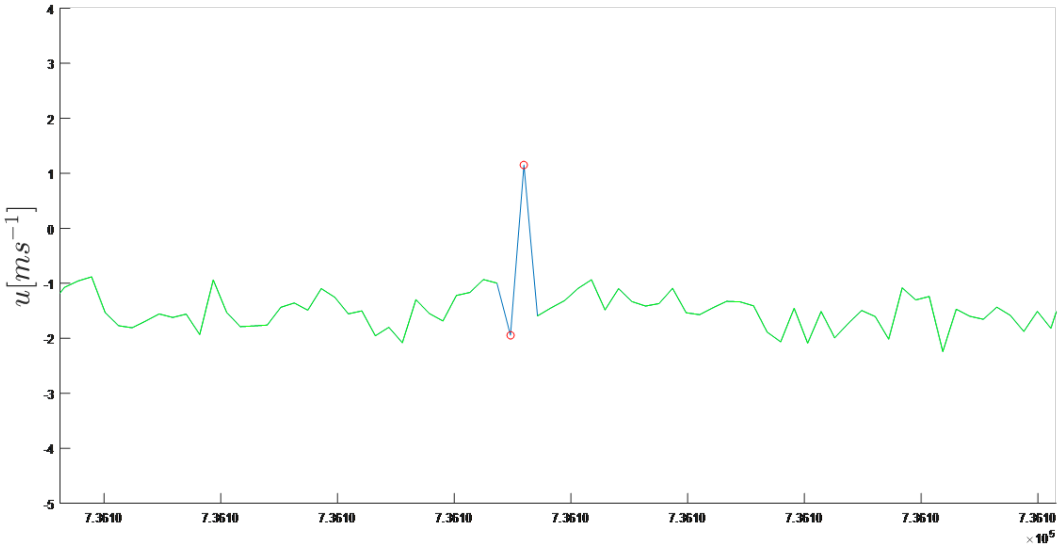

Figure 3.26: Zoomed longitudinal velocity time-series highlighting unnecessary removal of points: Blue line shows original data, green shows quality adjusted data, red circles show initial indexing of erroneous data points.

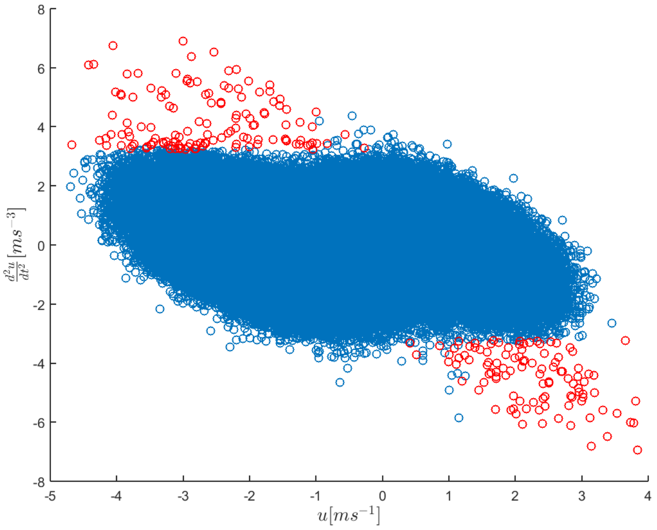

Figure 3.27: Plot of rate of change of acceleration in the longitudinal direction against longitudinal velocity: Blue markers show original data, and red markers show final indexing of erroneous data.

On applying this filtering to the entire data series all erroneous points should be removed as illustrated in Figure 3.28. It is worth doing a visual check on as many points as possible to determine the effectiveness of the chosen filters.

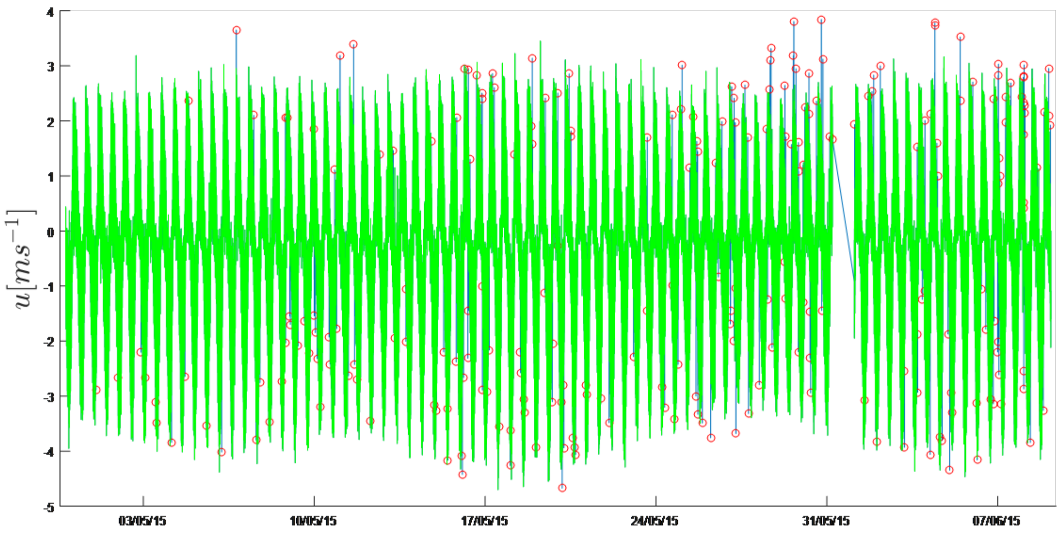

Figure 3.28: Quality checked longitudinal velocity time-series: Blue line shows original data, green shows quality adjusted data, red circles show final indexing of erroneous data points.

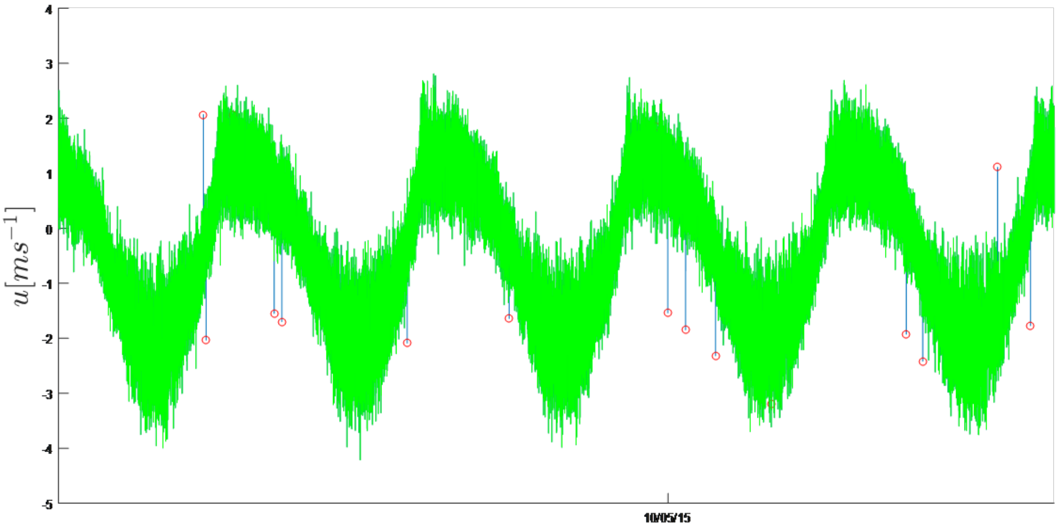

Figure 3.29: Quality checked longitudinal velocity time-series (zoomed): Blue line shows original data, green shows quality adjusted data, red circles show final indexing of erroneous data points.

The same principles are applied for the lateral velocity (v) and vertical velocity (w), as well as for measures of surface elevation. Ten minute periods containing greater than 30% error measurements are discarded from the useful data set.

3.5.3 Weighting

When determining the best model fit to the field data it is necessary to computationally determine the accuracy of the model spectra in relation to the field data. This involves subtracting the model spectrum from the field spectrum. However in the field data is contained some of the noise that could not be removed and also the influence of waves and as such fitting the turbulence model to field data that includes these components would not be useful. Fortunately the region of turbulence that is of particular interest is that in the frequencies below 0.2 Hz, whilst the majority of the wave and noise frequencies occur above 0.2 Hz. Therefore only those points in the spectrum below this frequency are used, as shown by the solid black line in Figure 3.30. To give greater significance to those points at lower frequency the difference between the two spectra is weighted. The first few (user specified) points (as indicated by circular markers) are given the value 1 whilst those remaining subsequent points increase exponentially by $e^{0.2}$.

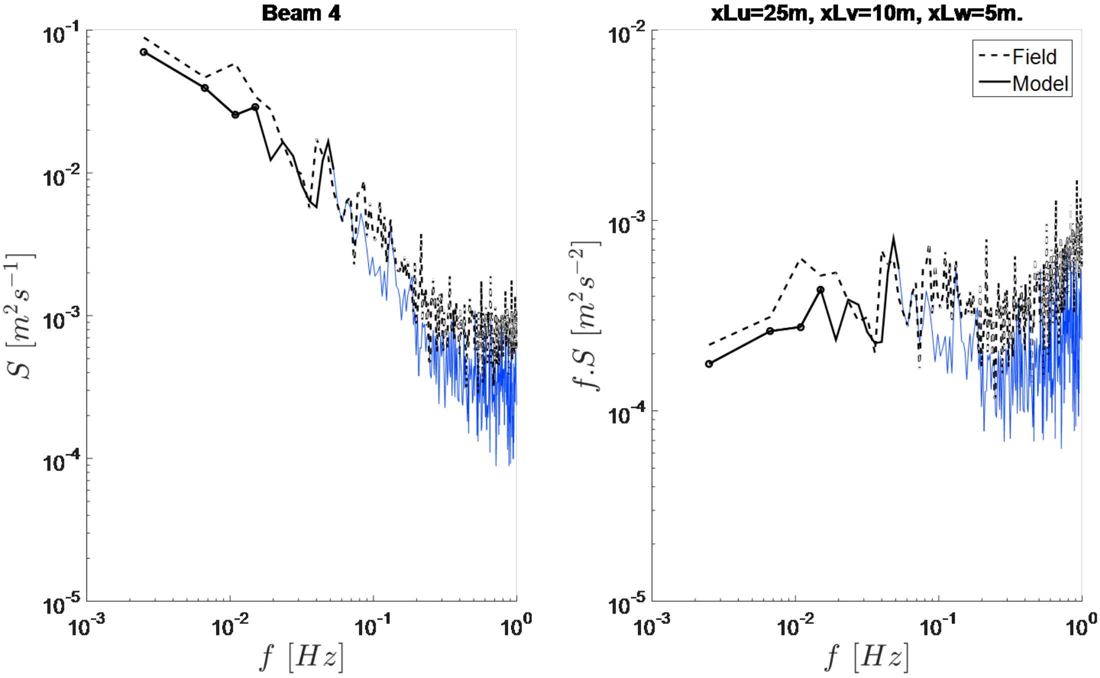

Figure 3.30: Plot illustrating weighting whilst determining accuracy of fit between field and model data; Dotted line indicates field data, solid blue line indicates model spectra, solid black line indicates spectra within frequencies specified for fitting, and circular markers indicate unit weighting.

3.5.4 Averaging and windowing

Figure 3.31 illustrates the effect of averaging over the signal, smoothing the spectrum of the signal to allow for better comparison with other signals. Having calculated the spectral density the averaging method simply takes the mean over a specified number of points in the spectrum, smoothing the output.

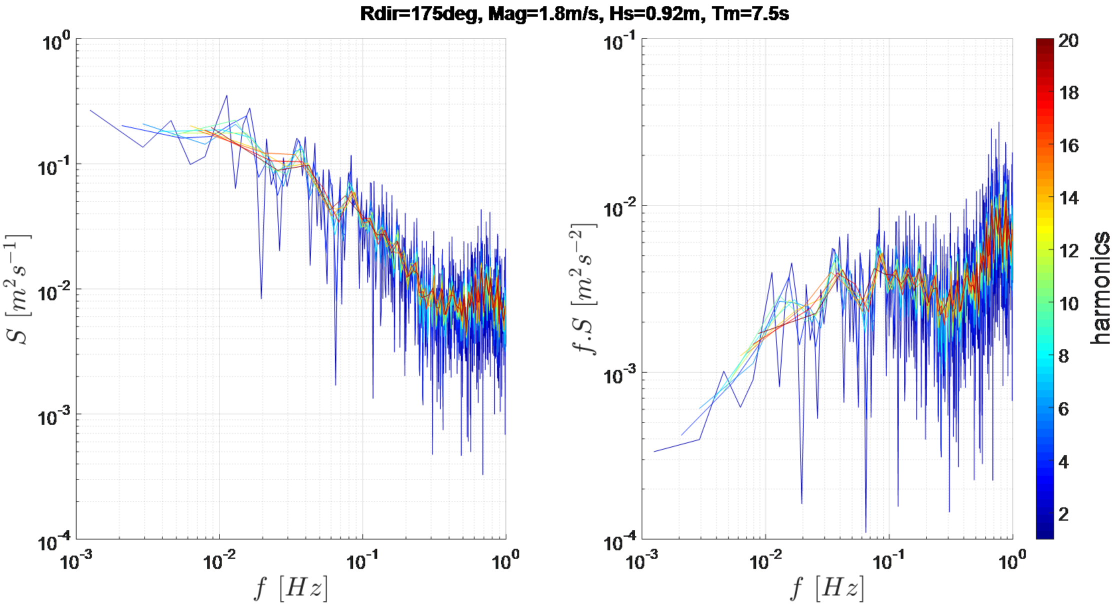

Figure 3.31: Spectral averaging. Colours indicated by colour bar show the number frequency harmonics over which spectra are averaged.

To produce a smooth curve in the spectral density of velocities it is often useful to use a windowing function, which makes it possible to take a small subset of a larger dataset for analysis. When using the simple rectangular method the data set is truncated at either end of the window with no modification. This may not accurately represent a longer time history, therefore in order to more effectively represent the signal in the frequency domain the beginning and end of the window can be modified according to a whole range of different methods, some of which are shown here in Figure 3.32.

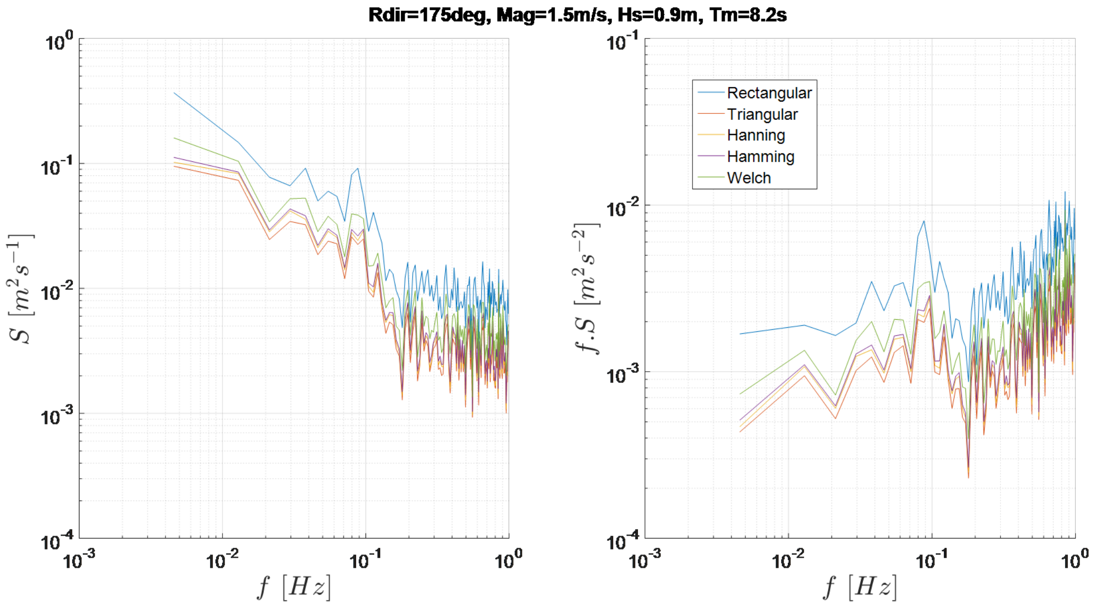

Figure 3.32: Windowing methods

The frequency characteristic of the smoothing window is a continuous spectrum with a main lobe and several side lobes. The centre of the main lobe of a smoothing window occurs at each frequency component of the time-domain signal. The width of the main lobe of the smoothing window spectrum limits the frequency resolution of the windowed signal. Therefore, the ability to distinguish two closely spaced frequency components increases as the main lobe of the smoothing window narrows. As the main lobe narrows and spectral resolution improves, the window energy spreads into its side lobes, increasing spectral leakage and decreasing amplitude accuracy. The side lobe characteristics of the smoothing window directly affect the extent to which adjacent frequency components leak into adjacent frequency bins. Choice of windowing function is often a trade-off between amplitude accuracy and spectral resolution.

For the following windowing methods w is an L point window with coefficients computed according to the following equations and multiplied to the original signal to allow for better processing and analysis of a relatively short signal.

Applying a **Rectangular** window is equivalent to not using any window because the rectangular function just truncates the signal to within a finite time interval. The rectangular window has the highest amount of spectral leakage.

$$w(n) = 1 \tag{3.51}$$

The **Triangular** window goes some may to moderating the losses seen when using a rectangular window. For

L odd:

$$w(n) = \frac{2n}{L+1} \ where \ 1 \leq n \leq \frac{L+1}{2} \tag{3.52}$$

$$2 - \frac{2n}{L+1} \ where \ \frac{L+1}{2+1} \leq n \leq L \tag{3.53}$$

The **Hanning** window has a shape similar to that of half a cycle of a cosine wave. It is useful for analysing transients longer than the time duration of the window and for general-purpose applications.

$$w(n) = 0.5(1 - \cos(\frac{\pi n}{N})) \ where \ 0 \leq n \leq N \tag{3.54}$$

The **Hamming** window is a modified version of the Hanning window. The shape of the Hamming window is similar to that of a cosine wave. The Hanning and Hamming windows are similar, as shown in the previous two front panels. However, in the time domain, the Hamming window does not get as close to zero near the edges as does the Hanning window.

$$w(n) = 0.54 - 0.46\cos(2\pi n/N) \ where \ 0 \leq n \leq N \tag{3.55}$$

Chapter 4

Field data

The methods discussed in the previous chapter 3 were used in the processing of DCP data from a survey conducted in UK waters in December 2014. The dataset is subject to certain confidentiality restrictions, and location cannot be presented. The tidal channel is coastal and currents are accelerated around a headland inside an island. In flood this is from West to East. The Teledyne RDI Sentinel V instrument was set up to record in two modes: 'waves' mode and 'currents' mode. Each operate at different bin depths: the former concentrating on the top 20m of the water column, with 0.6m bin heights, and the latter over the entire water depth, with 1m bin depths. Due to the typical velocity-depth profile of tidal currents, the fastest, and therefore most energetic, currents are in the uppermost part of the water column. Here a floating tidal turbine could access current speeds with the greatest potential for producing electricity. For this reason and because this study is primarily interested in the interaction between wave and current velocities, at depths relevant to a tidal turbine's hub height, 'waves' mode is used. The data gathered and processed from the survey will be used to inform the tidal flow model developed in chapter 5 using statistics averaged over ten-minute instances, some of which require correction according to the methods defined in chapter 6. Furthermore, along beam velocity data will be used to validate the model, and to test model sensitivity to imposed wave-current interaction model options.

A site characterisation study is undertaken providing an overall understanding of the wave, current and turbulence conditions at the site. The time series data is collected into ten-minute ensembles, quality checked and then processed, according to section 3.5.2. For the duration of the survey, which contains two weeks of good quality data, water depth averages 52m with peak flow at $3.7ms^{-1}$ and significant wave height ranging between 0.7 and $5.0m$. Figure 4.1 shows current magnitude and direction, and wave height and direction. The tide floods eastward and ebbs westward, with the flood tide, to the east, containing higher water velocities than the ebb tide, as expected. The site is exposed to waves from the west clockwise around to the south, however the majority of the waves are non-fetch-limited and arrive from the North West approximately following the current direction of the flood tide and opposing it during the ebb tide. There are various instances of waves oblique to current direction, however the majority of wave directions are within 30 degrees to a following or opposing current direction which provides the basis for comparisons of field and model data in section 7.

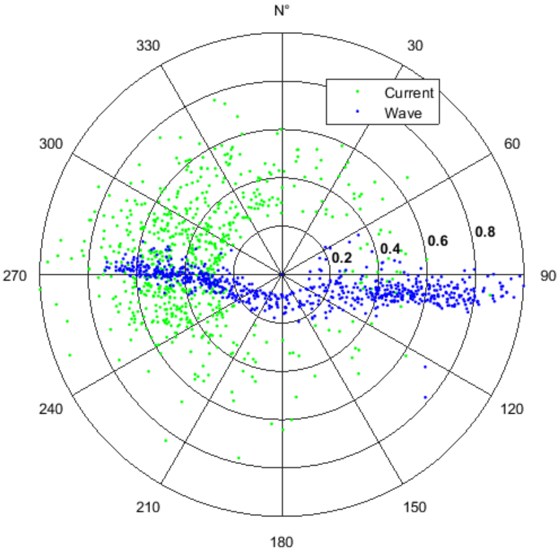

Figure 4.1: Current direction with current magnitude [m/s], wave direction with significant wave height [m].

Along beam velocity data is extracted from the instrument as outlined in section 3.5.1, and can be seen here plotted in Figure 4.2. The data presented in the figure is averaged over ten-minute intervals. Ten-minute instances of along beam velocity will be used for comparison with model outputs. From this plot it can be seen that beams 1 and 2 record positive velocities whilst and beams 3 and 4 record negative velocities and vice versa for the opposite tide direction. This indicates that the direction of the tidal currents lies between the direction of these beam pairs.

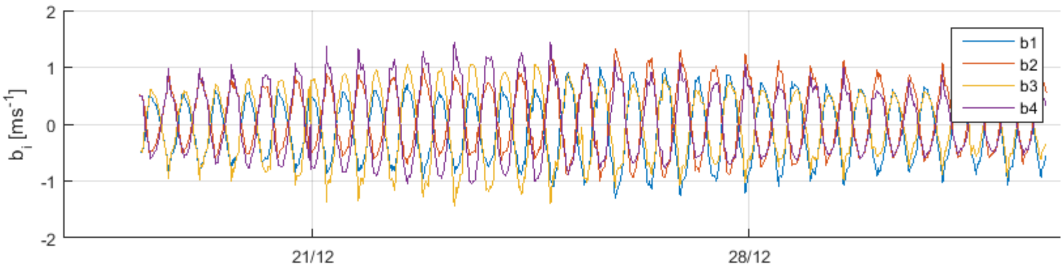

Figure 4.2: Along beam velocity records averaged at ten minute intervals

4.1 Tidal data processing

Three dimensional, ENU, velocities can be resolved using the four diverging beams of the Sentinel V, according to the method explained in section 3.1, using the instrument heading, pitch and roll. These are plotted in Figure 4.3, where U, V, and W indicate East, North and Up velocities respectively. The mean current speed and its direction are calculated from ENU velocities as described in section 3.1, and plotted in figure 4.4.

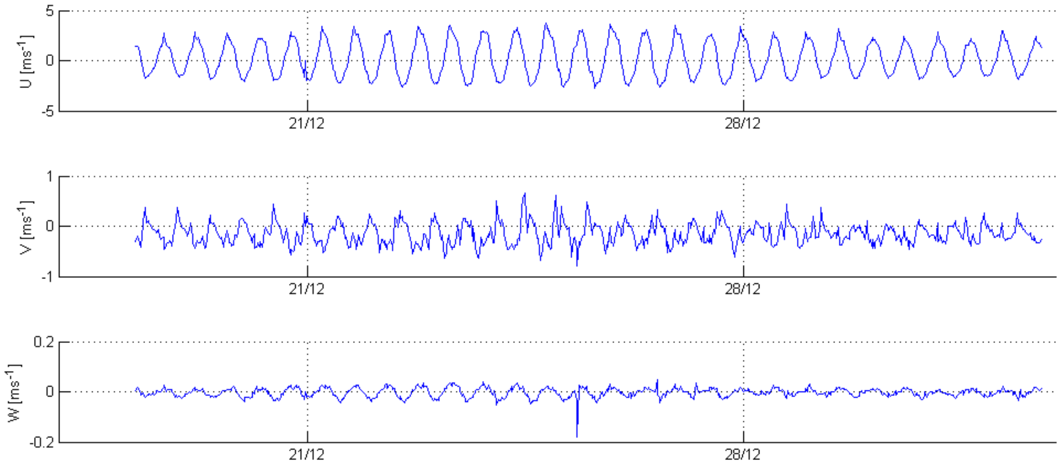

Figure 4.3: East North and Up velocity time-series averaged at ten minute intervals

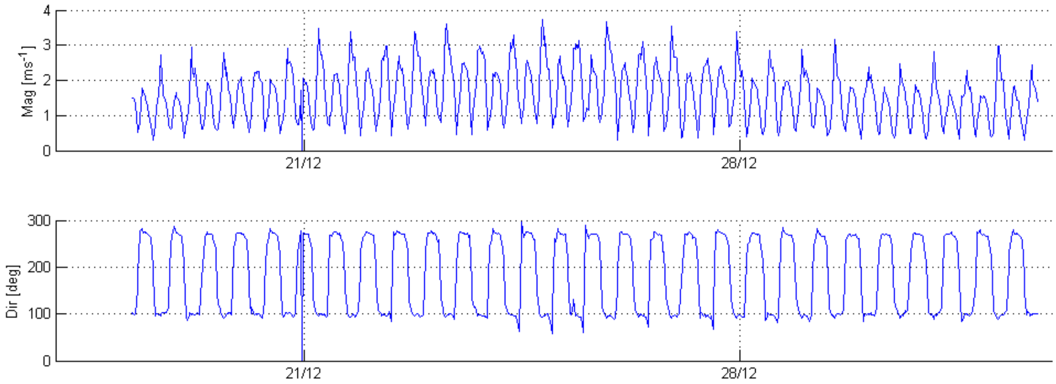

Figure 4.4: Current magnitude and direction time-series averaged at ten minute intervals.

4.1.1 Spectral analysis

Frequency spectra for each ten-minute ensembled time series of 2Hz subsurface along beam velocity are calculated. Analysis is conducted on each ensemble to determine average wave, current and turbulence statistics. Each of these ensembles are binned according to wave-current relative direction, significant wave height and current speed. An example of the frequency spectra for instances of waves in the range 1 to 1.5 m following currents in the range 1 to 1.5 ms^{-1} is given in Figure 4.5, where the black line indicates the avergae of all instances within the specified bin.

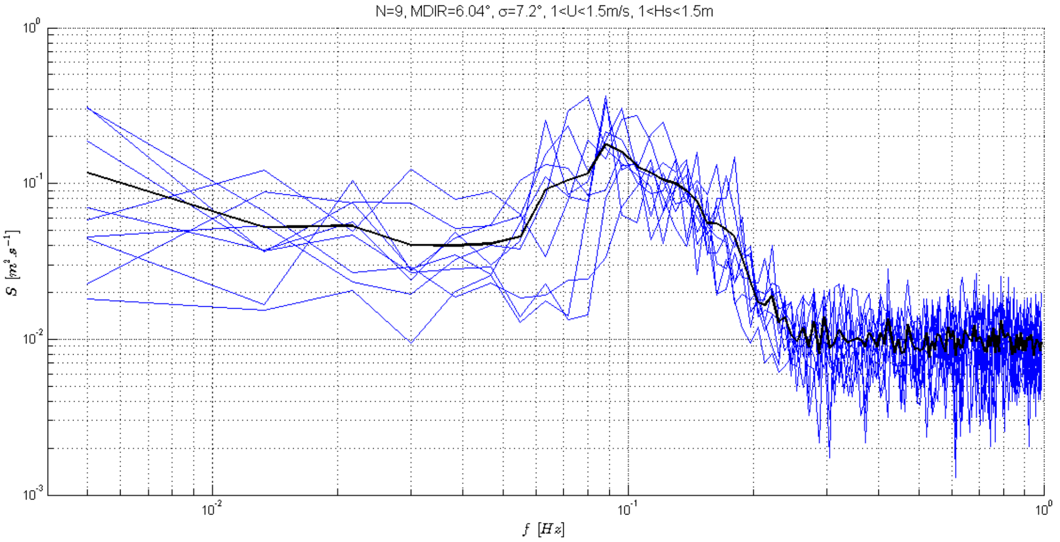

Figure 4.5: Along beam (1) field velocity spectra for waves following current direction for current speeds in the range 1 to $1.5ms^{-1}$ and significant wave heights in the range 1 to $1.5m$. Blue lines indicate individual instances and black line indicates the average of all instances. Title gives average statistics relating to the black line, where $MDIR$ is the mean direction of all instances and σ is the directional spread of all instances.

The same wave height and current velocity range are plotted in Figure 4.6 for all beams and for ENU velocities. Also plotted is the DCP configuration relative to current and wave direction.

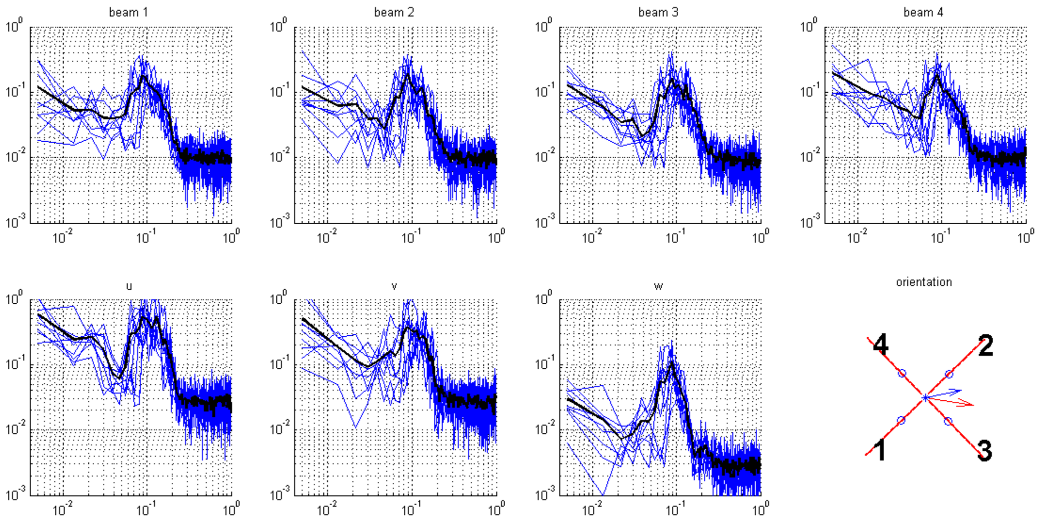

Figure 4.6: Along beam and ENU field velocity spectra for waves following current direction for current speeds in the range 1 to $1.5ms^{-1}$ and significant wave heights in the range 1 to $1.5m$. Bottom right plot indicates DCP configuration, current and wave directions. Blue lines indicate individual instances and black line indicates the average of all instances.

Averaged instances for a range of wave heights and current speeds for waves following and opposing currents are shown in Figure 4.7. Relative current and wave directions (i.e. the difference between wave and current directions) of 0 +/-30 degrees are considered to be following and 180 +/-30 degrees are considered as opposing. Significant wave height (H_s) and current speed ($\overline{u}$) bins are normalised by peak significant wave height (H_{s_p}) and peak current speed ($\overline{u_p}$) respectively, and spectra are normalised around the peak field spectral density. Spectral axes are identical to that given in the example figure 4.5.

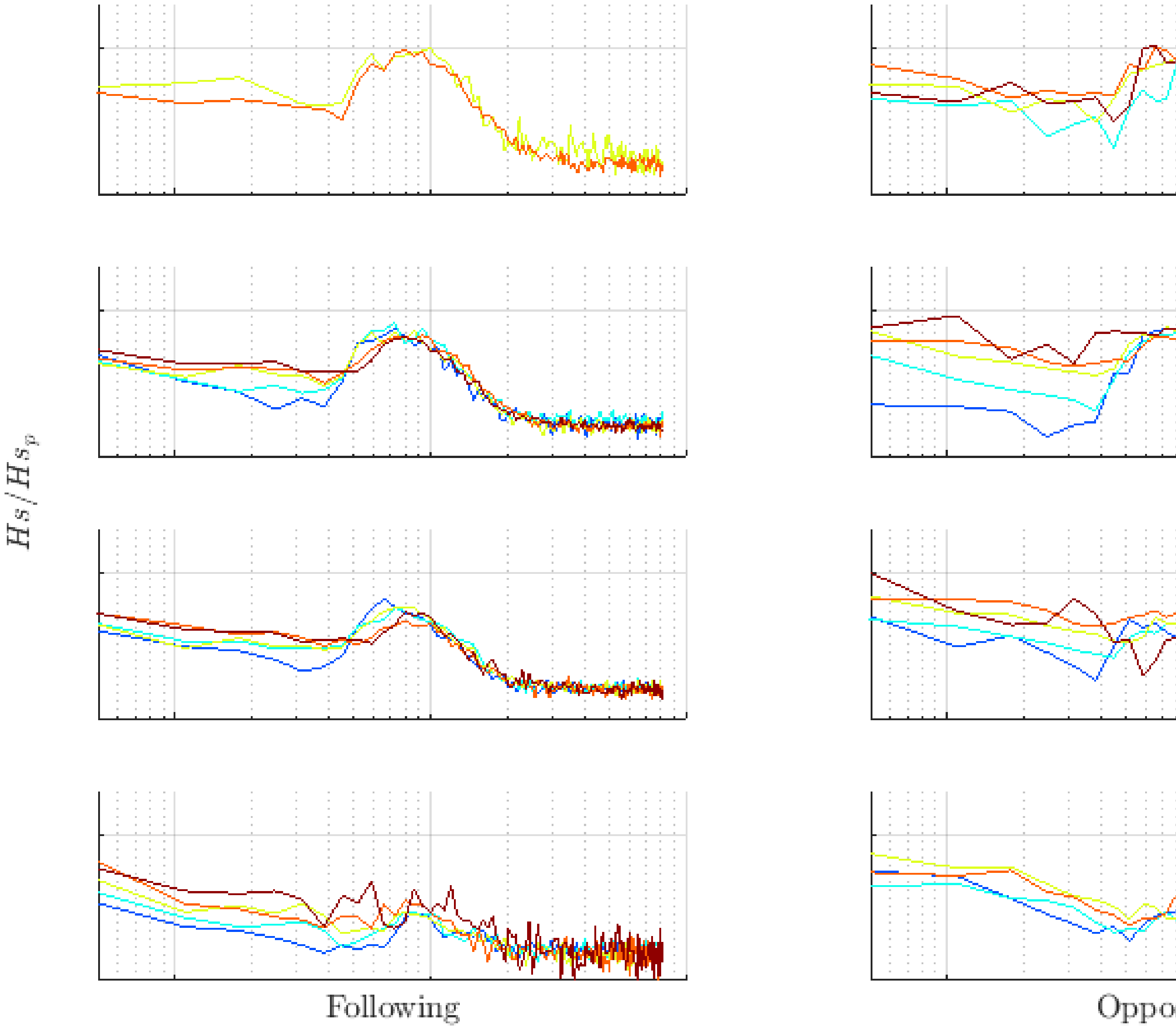

Figure 4.7: Along beam (1) field velocity spectra for waves following and opposing current direction for a range of current speeds and significant wave heights. Wave height and current speed both range between 0 and 1.

4.2 Wave data processing

Omni-directional or multi-directional surface elevation spectra are estimated as in section 3.2, from which mean wave spectral parameters and mean wave directional statistics can be determined. To recap, as in section 3.2.2, omni-directional spectra are determined using a single vertical beam measurement of the surface location, and multi-directional spectra are determined using surface elevations recorded by all five beams. Data from the four slanted beams require some smoothing, and the VDCP (chapter6) is used to determine the exact (x,y) locations where beams pierce the surface, and cross spectral matrices are used to estimate the three-dimensional spectra. Figure 4.8 compares significant wave height and mean period estimated from multi-directional spectra (all 5 beams) and omni-directional surface elevation spectra (single vertical beam).

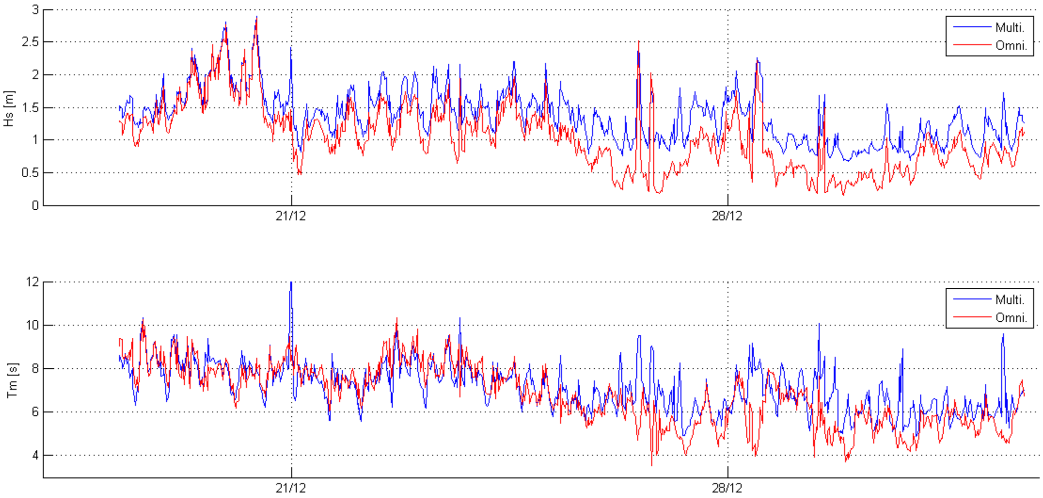

Figure 4.8: Significant wave height and mean period estimated from omni-directional (single vertical beam) and multi-directional (all 5 beams) spectra recorded by echo location of the sea surface.

Some discrepancy between the results is noted and work continues to improve the multi-directional wave spectra processing method. Whilst unable to provide any three-dimensional/direction information, the single vertical beam measurements of the surface provide more accurate measurement of the surface elevation, due largely to apparent angle with the surface and subsequent preferred incidence, reflection and refraction conditions. Figure 4.9 illustrates an example comparing omni-directional spectra; the first averaged from the multi-directional spectrum estimated from the 5 beam method and the second from the vertical beam record. It is observed that the majority of the wave frequency range within the spectra compare well. Below the wave frequency range there is a large discrepancy, however this is of little consequence, since for the subsurface velocities to be modelled, turbulence will dominate this region. Above approximately 0.2Hz (5 second wave periods) the multi-directional spectrum increasingly over predicts the wave energy. This may of consequence to the modelling procedure. These discrepancies are likely to be a consequence of the extra distortion in the signals returned by the 4 slanted beams. Whilst substantial effort has been made to refine this data, intrinsic problems due to reflection and refraction of angled sound pulses on the moving sea surface will always affect the quality of the data.

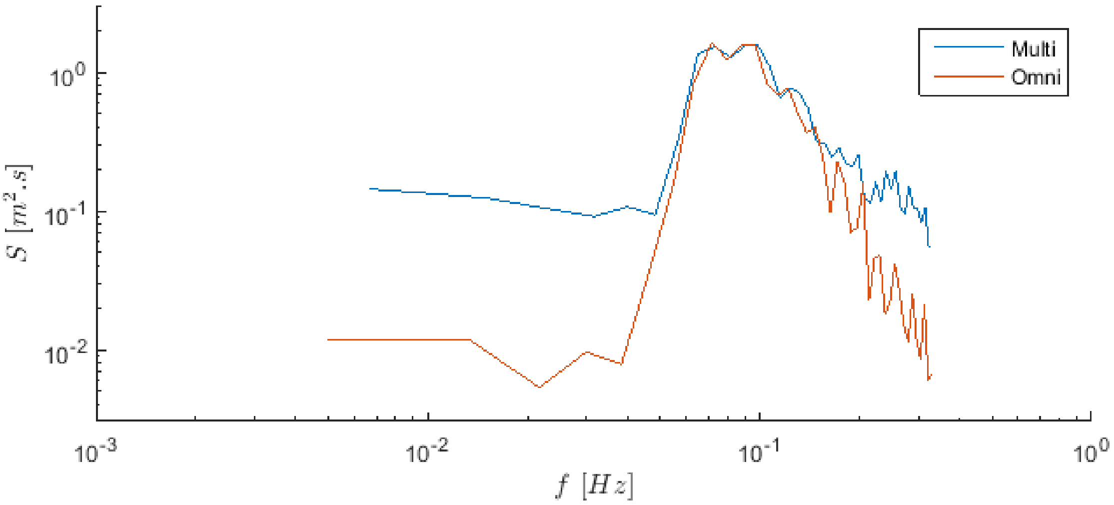

Figure 4.9: Example comparison of omni-directional (from vertical beam record)and multi-directional (from all beam records) spectra estimated from surface elevation data

Field-to-model comparisons conducted in chapter 7 will compare velocities generated using both the multi and omni directional measured spectra as well as model spectra based upon wave statistics such as significant wave height and mean period. No correction for DCP error in wave estimates from subsurface velocities is necessary for this data set, due to the availability of direct surface elevation measurements from the survey. However a further study, outside of the scope of this work aims to understand the limitations in the multi-directional measurement of surface elevation, which is largely a result of the relative angle between the diverging beams and the mean sea surface.

4.3 Turbulence data processing

Turbulence parameters are taken at specified depths from instances of low wave conditions (i.e. $H_s < 1m$). Turbulence intensity can be determined from mean longitudinal flow speed ($\overline{u}$) and the velocity component standard deviation, σ_i, as described in section 3.3. Length scale can be calculated from the field data using the auto-correlation of the ENU velocity spectra, and a correction for DCP error as described in section 3.3. During less than 1m wave conditions, turbulence intensities for all instances are plotted in Figure 4.10 for flood and ebb directions.

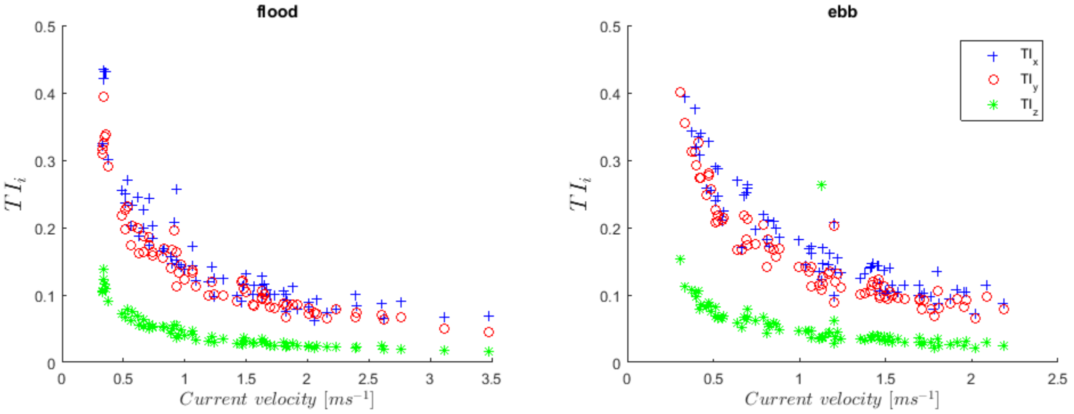

Figure 4.10: Turbulence intensities in three dimensions recorded during periods of low wave activity $< 1m$ during flood and ebb tide

Turbulence intensities follow consistent inverse power law trends with current velocity, as described in table 4.1

Turbulence intensity direction	Symbol	**Flood**	**Ebb**
Longitudinal	$\mathbf{TI_x}$	$0.16\overline{u}^{-0.74}$	$0.17\overline{u}^{-0.82}$
Lateral	$\mathbf{TI_y}$	$0.13\overline{u}^{-0.80}$	$0.14\overline{u}^{-0.80}$
Vertical	$\mathbf{TI_z}$	$0.043\overline{u}^{-0.80}$	$0.05\overline{u}^{-0.83}$

Table 4.1: Turbulence intensity trends

During less than 1m wave conditions, turbulence length-scales for all instances are plotted in Figure 4.11 for flood and ebb directions. Unlike for turbulence intensity, a large amount of scatter is seen in length-scale measurement, particularly as current velocity increases. This will have some implications on comparisons to the model conducted in chapter 7.

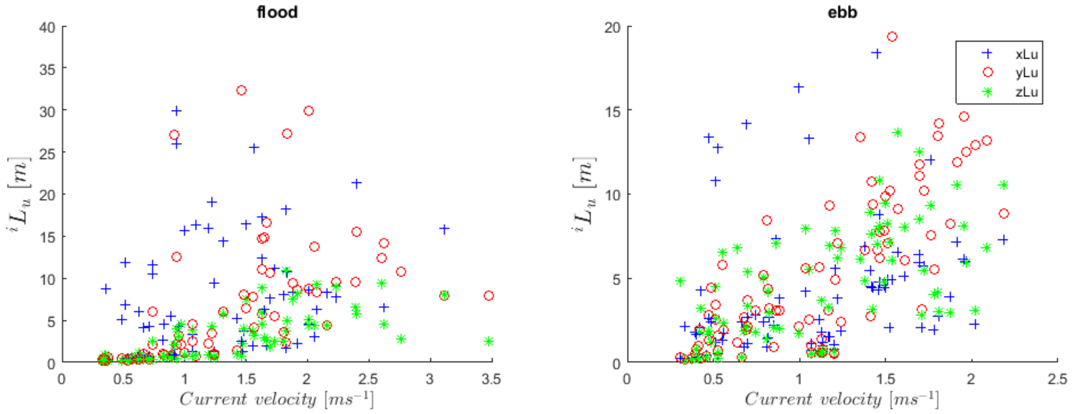

Figure 4.11: Longitudinal components of turbulence length scale recorded during periods of low wave activity $< 1m$ during flood and ebb tide

Despite the large amount of scatter, approximately linear trends in length scales, with current velocity, are followed, as described in table 4.2.

Turbulence length scale direction	Symbol	**Flood**	**Ebb**
Longitudinal	$^{\mathbf{x}}\mathbf{L_u}$	$6.18\overline{u}$	$3.03\overline{u}$
Lateral	$^{\mathbf{y}}\mathbf{L_u}$	$2.54\overline{u}$	$3.21\overline{u}$
Vertical	$^{\mathbf{z}}\mathbf{L_u}$	$1.25\overline{u}$	$2.31\overline{u}$

Table 4.2: Turbulence length scale trends

4.3.1 DCP error correction

Turbulence parameters estimated from DCP velocity spectra are corrected according to a theoretical error determined using the method described in chapter 6 whereby for any set of sea conditions and DCP configuration the error in estimation of parameters has been calculated in order to inform the model inputs. For the purpose of the model described in chapter 5, a correction is applied according to mean current speed during instances of waves less than 1 meter in significant wave height.

Turbulence intensity direction	Symbol	**Flood and Ebb**
Longitudinal	$\mathbf{TI_x}$	$0.6769\overline{u}^{-0.282}$
Lateral	$\mathbf{TI_y}$	$0.6093\overline{u}^{-0.295}$
Vertical	$\mathbf{TI_z}$	$0.3444\overline{u}^{-0.324}$

Table 4.3: Turbulence intensity error corrections

Turbulence length scale direction	Symbol	**Flood and Ebb**
Longitudinal	$^{\mathbf{x}}\mathbf{L_u}$	$0.67\overline{u}$
Lateral	$^{\mathbf{y}}\mathbf{L_u}$	$0.67\overline{u}$
Vertical	$^{\mathbf{z}}\mathbf{L_u}$	$2.32\overline{u}$

Table 4.4: Turbulence length scale error corrections

4.3.2 Model inputs

The turbulence measurement results, as corrected for DCP error, for input to the model are displayed in tables 4.5 and 4.6. Combining linear trends for measurement and correction of length scale results in a single value for each length scale parameter, which is the same (to within a significant figure) for both flood and ebb tides.

Turbulence intensity direction	Symbol	**Flood**	**Ebb**
Longitudinal	$\mathbf{TI_x}$	$0.2303\overline{u}^{-0.455}$	$0.2494\overline{u}^{-0.536}$
Lateral	$\mathbf{TI_y}$	$0.2203\overline{u}^{-0.503}$	$0.2358\overline{u}^{-0.508}$
Vertical	$\mathbf{TI_z}$	$0.1254\overline{u}^{-0.475}$	$0.1368\overline{u}^{-0.508}$

Table 4.5: Turbulence intensity model input, for Von Karman velocity spectra

Turbulence length scale direction	Symbol	**Flood and Ebb**
Longitudinal	$^{\mathbf{x}}\mathbf{L_u}$	9
Lateral	$^{\mathbf{y}}\mathbf{L_u}$	4
Vertical	$^{\mathbf{z}}\mathbf{L_u}$	1

Table 4.6: Turbulence length scale model input, for Von Karman velocity spectra

Values of turbulence intensity in the longitudinal, lateral and vertical directions are within the typical range for tidal sites (Clark et al. 2015). Interestingly turbulence length scale values are found to be fixed over all current speeds following the correction for DCP recording error. The ReDAPT study (Parkinson & Collier 2016) also found that length scales remained fairly consistent over a range of velocities, however at the Falls of Warness site in Orkney, where this data was measured, longitudinal length scales averaged 31.5m as opposed to the 9m longitudinal length scales measured at this particular site. Lateral and vertical length scales were found to be of a similar size. The variation in length of turbulent eddies is likely to be very site specific, particularly influenced by bathymetry.

Chapter 5

Simulation

Simulation of tidal flows enables developers of tidal turbines to expose their concept designs to a range of realistic conditions before investing in scaled and, ultimately commercial, devices that must survive extremely energetic environments. It is important that the potential loads on a tidal turbine are accurately simulated for a range of environmental conditions in combination. With reference to the DNV GL Standard for Tidal Turbines (DNV GL 2015) loads can be categorized as permanent loads, variable functional loads, environmental loads, abnormal tidal turbine loads, deformation loads and accidental loads. Environmental loads are loads which may vary in magnitude, position and direction during the period under consideration, and which are related to operations and normal use of the tidal turbine, such as hydrodynamic loads induced by waves and current, including lift, drag and inertia forces, tidal effects, wind loads, loads due to the control and safety system functions, marine growth, earthquake loads, and snow and ice loads. Further practical information regarding these and other environmental conditions and loads can be found in DNV-RP-C205 (Det Norske Veritas 2007).

Standard approaches for the simulation of environmental conditions in the tidal environment include Computational Fluid Dynamics and linear models. Linear models couple with Blade Element Momentum (BEM) theory (Way & Collier 2012, Togneri et al. 2011) to calculate loads and performance on turbines, at low computational cost. CFD methods typically take the form of Reynolds Averaged Navier Stokes (RANS) equations or Large Eddy Simulations (LES). For a single turbine, mean and unsteady loading due to steady shear flows has been studied by various methods including RANS CFD (Fleming & Willden 2013, McNaughton et al. 2012), and LES CFD, however, the high computational cost of such methods limits their application to single turbine loading over a relatively small number of turbine rotations. Actuator line and disk methods have lower computational cost than blade modelled CFD so are attractive options for analysis of multiple turbines, or BEM methods can be coupled to CFD, i.e. RANS-BEM (Edmunds et al. 2014). This type of simulation however is still relatively computationally expensive, and whilst they may be used for validation or for instances where other methods are less accurate, it would not be feasible, using modern computing power, to attempt to model the loads and performance of a tidal turbine over its lifetime. In this study and in much of the work (and software) of the sponsoring company solving (i.e. Tidal Bladed) the full Navier-Stokes hydrodynamic equations for water wave motion are avoided, instead using linear approximations, in order to avoid non-linear terms, accelerating simulation and analysis.

This chapter builds upon the background theory covered in chapter 2 before detailing the equations used in the model that has been developed. This results in a 2-dimensional model of chosen depth and grid resolution (typically less than 50m square, grid res. 1m) that is tied to linear wave theory and Von Karman turbulence, with the user retaining control over a number of options governing the interaction between waves and currents in order to find the closest fit with field data. Firstly the shape of the wave spectrum is designated. For this there are a wide variety of model spectra input options, or the option to input a measured spectrum. Secondly the wave spectrum can be modified according to one of two methods (not applied to a measured spectrum). Current speed can be input as a uniform or non-uniform profile or alternatively is taken from measured data at the required depth. Finally the equations used to calculate subsurface velocities from surface elevation spectra can be modified for currents such that absolute or relative wave conditions are represented.

The tidal flow model, developed specifically for this work, builds upon existing DNV GL code, and has been designed such that a number of different methods for simulating wave-current interaction can be selected, in order to find the best agreement with data measured at sea. The model combines waves and currents according to Hedges (Hedges 1987) and Phillips (Phillips 1958), using Von Karman (von Karman 1948) turbulence, combining the theory of Veers (Veers 1988) and Taylor (Taylor 1937) to formulate a grid of coherent velocities. The simulated tidal flow defines a velocity time series of specified length at any desired point within a grid of specified size, considering the velocities resulting from waves (U_{wave}), currents ($U_{mean\ flow\ shear}$), and turbulence ($U_{turbulence}$):

$$U_{total} = U_{mean\ flow\ shear} + U_{wave} + U_{turbulence} \tag{5.1}$$

The wave conditions, turbulence conditions and flow shear are simulated separately and combined linearly to form a time series of velocities generated at specified frequency. The turbulence field is generated prior to running the combined model on a grid of specified width, height and cell size. Turbulence is then applied to the model by taking the velocity time series from the nearest point. Decreasing cell size increases turbulence resolution, however increases computational time. Interpolation methods to estimate turbulence velocities at the designated point were found to be largely ineffectual, improving accuracy little due to the spatial coherence of the turbulence simulated. Subsequently the optimum cell size compromising between accuracy and computer time was found to be 2m.

5.1 Waves

Three methods can be used to simulate the wave induced velocities in the flow, all of which are inferred from a description of the sea surface elevation. The preferred method uses measured multi-directional sea surface elevation data. The second method uses measured omni-directional sea surface elevation data. And the third uses a model spectrum based on estimated sea surface elevation spectral parameters, which can then be modified for current according to one of two methods.

5.1.1 Measured wave spectra

The RDI Sentinel V used to gather data for this study (see chapter 4) incorporates a fifth vertical beam which is used to gather information about the waves. This high frequency record can be used to estimate an omni-directional spectrum for very ten-minute sample, or in combination with the other four beams can be used to estimate, every ten-minutes, a multi-directional wave spectrum using the method outlined in 3.2.2.

5.1.2 Model wave spectra

The irregular wave velocity field is defined using linear wave theory from a simulated omnidirectional Bretschneider (2.1.6) sea surface elevation spectrum defined using significant wave height (H_s), mean period (T_m) and a peak enhancement factor of 1. Some further study has gone into distributions of wave height and period in wave current scenarios looking at research conducted in the North Sea around the UK ((Robinson & Tawn 1997) and Norway (Mathisen 1990), around Australia (Lucas & Soares 2015) and in West Africa (Nerzic et al. 2007).

A number of methods are used in modelling the directionality of wave spectra. The simplest option is a normal distribution, alternatively Ewan has developed two theories for directional distributions which are referred to here as 'Ewan's Wind' (Ewans 1998) and 'Ewan's Swell' (Ewans 2001). These are the results of studies made in New Zealand waters where directional distributions have been estimated in both swell and fetch limited seas. In this model the spectrum is given directionality using a cosine2s directional distribution (Krogstad & Barstow 1999) defined with power, s, equal to 1. The simulated spectrum is modified according to the strength and direction of the mean current($\overline{u}$) with respect to the wave direction. The method takes into account current effects on the relative angular frequency and wave number, according to Hedges (1987). Therefore, if currents are included, the spectral density of the surface elevation, S_{η_M}, is modified to give the resultant spectrum, S_η. Where a measured spectrum is used, no modification is made to account for currents as the resultant spectrum is what has been measured by echo location and therefore has been naturally modified by currents already.

$$S_\eta = S_{\eta_M} \frac{\omega_a^2}{\omega_r^2} \frac{1}{1 + 2\overline{u}\omega_a/g} \tag{5.2}$$

A cut off (equilibrium range parameter) is also applied to the spectra, which accounts for white-capping of waves when they become too steep, according to Phillips (1958). A is an empirical constant largely dependent on wind speed, that takes into account wave frequency (ω) and mean current speed ($\overline{u}$).

$$S_{ER} = \frac{Ag^2}{\omega_a^5} \frac{1}{2\overline{u}\frac{\omega_a}{g}} \tag{5.3}$$

Where S_η exceeds S_{ER}, S_η is reduced to S_{ER}. As illustrated for 1 ms^{-1} opposing and following currents in Figure 5.1, where opposing currents are negative and following currents positive. The figure displays the spectrum with relative frequency (observer moving at current speed), such that the wave effect of current on relative period can be observed.

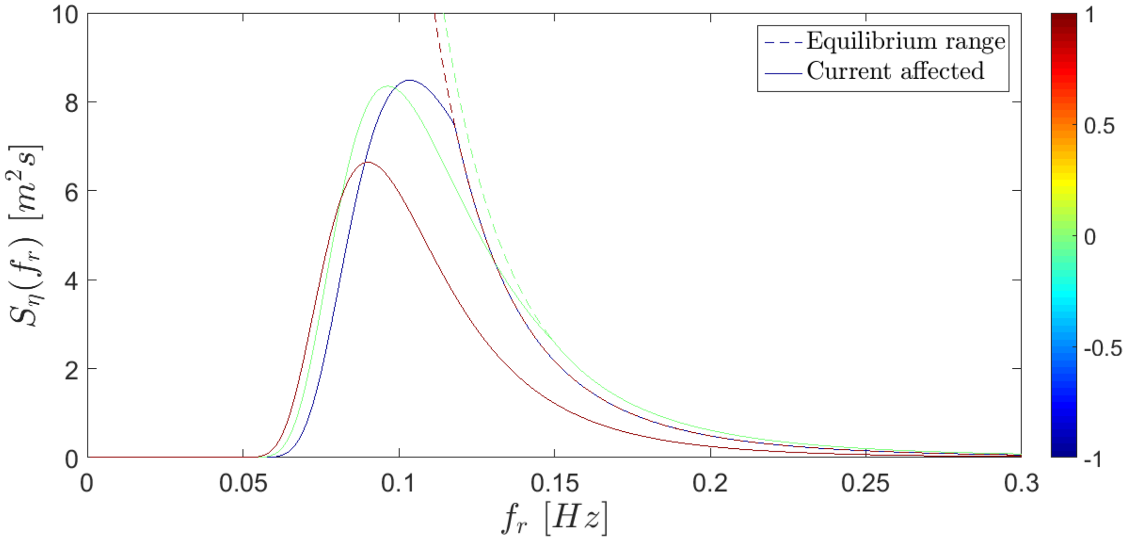

Figure 5.1: Effect of opposing and following currents on typical Bretschneider (H_s: 3m T_m: 8s) spectrum. Plotted with relative frequency.

The immediate effect of current is to increase or decrease the frequency of the waves for opposing and following currents respectively as shown in Figure 5.1. The equilibrium range cut-off is applied at the higher frequencies therefore having a greater effect on the opposing current case.

The spectrum of the stream-wise velocity and the vertical velocity are derived from the surface elevation spectrum(S_η) using linear wave theory (Mackay 2012), depending on the height (h) of the water column , the required depth (z), and the wave direction relative to the current (α). A velocity time series is calculated using an inverse Fourier transform of the velocity amplitudes derived from the velocity spectrum with phase calculated according to wave number, and location.

$$S_u = \omega_r^2 cos\alpha \frac{cosh^2(k_r(h+z)))}{sinh^2(k_r h)} S_\eta \tag{5.4}$$

$$S_v = \omega_r^2 sin\alpha \frac{cosh^2(k_r(h+z)))}{sinh^2(k_r h)} S_\eta \tag{5.5}$$

$$S_w = \omega_r^2 \frac{sinh^2(k_r(h+z)))}{sinh^2(k_r h)} S_\eta \tag{5.6}$$

Relative wave number, k_r and angular frequency, ω_r are calculated iteratively using the dispersion relationship according to Guo (Guo 2002), as described above in section 2.4.3.

Velocity spectra are transformed from the frequency to the time domain firstly by converting to a signal amplitude (a) with phase (ϕ).

$$a = \sqrt{2S_i df} \tag{5.7}$$

$$\phi = 2\pi R \tag{5.8}$$

Where S_i is the velocity spectral density for each component of velocity (i) and R is a uniform distribution of randomly generated numbers. This is then converted to a signal at each specified location. Firstly shifting the phase to the location x and y:

$$\phi_{u,v} = \phi + k_r(x\cos\alpha + y\sin\alpha) + \pi \tag{5.9}$$

$$\phi_w = \phi + k_r(x\cos\alpha + y\sin\alpha) + \frac{\pi}{2}) \tag{5.10}$$

Then the amplitude and phase are reconstructed to form a signal using an inverse Fourier transform. No stretching (i.e. (Wheeler 1969)) has been included to take account for changes in water particle velocities due to deformation of the sea surface. Tidal turbines will tend to avoid at least the top 5 metres of the water column due to severe impact from waves. Furthermore, side-lobe interference in 'real' DCPs will render much of the data in this part of the water column unusable. It is therefore not deemed within the scope of this work to account for changes due to proximity to the sea surface.

Huang Method

Alternatively, in the place of the Hedges method, can be used a method developed by Huang (Kokkinowrachos 1980) for modification of the wave spectrum effected by a current.

$$S_\eta = \frac{4S_{\eta_M}}{\chi(\chi+1)^2} \tag{5.11}$$

Where:

$$\chi = 1 + 4\frac{\overline{u}}{\frac{\omega_a}{g}} \tag{5.12}$$

5.2 Currents

A mean flow shear profile, u, at chosen depth, z, is added; calculated using the mean velocity $\overline{u}$ at reference depth, z_{ref}, according to the power law profile attained from the data survey:

$$u(z) = \overline{u}_{ref}\frac{z}{z_{ref}}^{\beta} \tag{5.13}$$

The exponent β is typically chosen to be 1/7, however a value of 0 can also be used to define a uniform current for some of the investigations described in this paper.

5.3 Turbulence

Turbulence can be included in the current field model and is synthesised, prior to running the combined flow model, numerically using the "Sandia method" for simulating 3 dimensional flows, described in Veers (Veers 1988). The Sandia method has been used extensively to describe turbulent boundary layer flow at land sites in order to compute unsteady loads of wind turbines. Given that tidal races are primarily boundary layer flows the same method has been applied in the characterisation of turbulence flow and prediction of unsteady loading for tidal stream turbines. The method has been applied and validated in a number of studies such as in the ReDAPT project(Parkinson & Collier 2016) and by Milne et al. (Milne, Sharma, Flay & Bickerton 2013) who suggest that Von Karman (von Karman 1948) velocity spectra can provide an accurate representation of tidal site turbulence.

The auto spectral density for the three directional components of turbulence are given in section 2 according to the Von Karman model, in equations 2.59 and 2.61.

An analytical expression for the cross-correlation of flow speed fluctuations in space and time, derived from Taylor's frozen turbulence hypothesis is also associated with Von Karman equations. For the longitudinal component, the coherence, C_u, of points separated by distance δr is given in equation 5.14. Whilst correlation determines the extent to which two variables vary, coherence instead assesses the similarity of variables in the frequency domain.

$$C_u(\delta r, f) = 0.994(A_{5/6}\eta_u - \frac{1}{2}\eta_u^{5/3}A_{1/6}\eta_u \tag{5.14}$$

Where:

$$A_j(x) = x^j K_j(x) \tag{5.15}$$

K_j is a fractional order Bessel function and:

$$\eta_u = 0.747\frac{\Delta r}{L_u(\Delta r, f)}\sqrt{1 + 70.8\Big(\frac{fL_u(\Delta r, f)}{\overline{u}}\Big)^2} \tag{5.16}$$

The local length-scale, L_u, is defined:

$$L_u(\Delta r, f) = 2MIN(1, 0.04f^{\frac{-2}{3}}))\sqrt{\frac{({}^yL_u\Delta y)^2 + ({}^zL_u\Delta z)^2}{\Delta y^2 + \Delta z^2}} \tag{5.17}$$

Here Δy and Δz are the lateral and vertical components of separation, Δr, and ${}^yL_u$ and ${}^zL_u$ are the lateral and vertical length-scales for the stream-wise component of turbulence. Similarly for the lateral and vertical components the corresponding equations are:

$$C_i(\Delta r, f) = \frac{0.597}{(2.869\gamma_i^2 - 1)}(4.781\gamma_i^2 A_(5/6)(\eta_i) - A_(11/6)\eta_i) \tag{5.18}$$

Where,

$$\eta_u = 0.747\frac{\Delta r}{L_i(\Delta r, f)}\sqrt{1 + 70.8\Big(\frac{fL_i(\Delta r, f)}{\overline{u}}\Big)^2} \tag{5.19}$$

And:

$$\gamma_i = \frac{f_i L_i(\Delta r, f)}{\Delta r} \tag{5.20}$$

Again where i is equal to v or w. And the local length-scales are given by:

$$L_u(\Delta r, f) = 2MIN(1, 0.05f^{-2/3})\sqrt{\frac{({}^yL_v\Delta y/2)^2 + ({}^zL_v\Delta z)^2}{\Delta y^2 + \Delta z^2}} \tag{5.21}$$

$$L_u(\Delta r, f) = 2MIN(1, 0.02f^{-1/2})\sqrt{\frac{({}^yL_w\Delta y/2)^2 + ({}^zL_w\Delta z)^2}{\Delta y^2 + \Delta z^2}} \tag{5.22}$$

All three components are assumed to be independent of each other. This is considered to be a reasonable assumption though there may be some correlation of stream-wise and vertical components, due to Reynolds stresses near to the sea-bed.

A turbulent time history is generated for the current field on a grid of equally spaced points in a 2D plane which spans the y and z-axes. The time history of velocities in three dimensions is generated for each of these points such that each point has correct spectral characteristics and each pair of points has the correct coherence and cross-spectral characteristics. For example, for the stream-wise component of velocity (u), the coherence (C_u) of points separated by distance (Δr) is a function of η_u which is defined using the local length-scale (L_u) and the wave number (k) calculated for a range of frequencies (f) at mean current speed ($\overline{u}$). More detail can be found in appropriate turbulence texts (Tennekes & Lumley 1972).

$$\eta_u = \sqrt{(\frac{0.747\Delta r}{2L_u})^2 + (70.8\Delta r k)^2} \tag{5.23}$$

The longitudinal local length scale (L_u) is calculated using lateral and vertical components of longitudinal length scale (${}^yL_u$ and ${}^zL_u$), as well as the lateral and vertical separation of the points (dy and dz).

$$L_u = \sqrt{\frac{({}^yL_u dy)^2 + ({}^zL_u dz)^2}{dy^2 + dz^2}} \tag{5.24}$$

$$k = \frac{2\pi f}{\overline{u}} \tag{5.25}$$

For this model the auto-spectral density is taken from a Von Karman turbulence model with inputs of mean velocity, and nine length-scale parameters as defined in section 2. Turbulence intensities and length scales are calculated from low wave instances in the field data and fitted with trends dependent on mean current velocity. Each trend is then corrected for DCP error according to the method discussed in chapter 6, dependent on wave height and mean current velocity. Length scale components of the lateral and vertical velocities are estimated based on studies conducted during the ReDAPT project (Parkinson & Collier 2016). —

Chapter 6

Virtual Doppler Current Profiler

In this study a 'Virtual' DCP (VDCP) is used to mimic field measurements taken by a generic DCP. The VDCP is developed and used to sample a simulated tidal flow to understand the limitations of this type of measurement instrument whilst recording the small time-scale kinematics of waves and turbulence in tidal currents. Specifically, the study aims to quantify theoretical errors in measurements affecting the design of tidal turbines. Therefore, whilst a range of depths are considered in initial studies, under focus are those wave and turbulence induced velocities at a prospective turbine hub height. Velocity time series combining the effect of currents, turbulence and waves are simulated as described in chapter 5. The VDCP samples ten-minute velocity time series using the commonly used Janus configuration; four transducers separated by 90 degrees in the horizontal plane, each at 25 degrees from the vertical, using the method covered in more detail in section 6.2.

Sampling of combined wave, current and turbulence simulations are presented in the results in section 6.3 highlighting the difficulty in separating and characterising the different components within a flow, and summarizing some of the more critical effects at turbine hub height on measures of wave and turbulence characteristics in realistic combined wave-current flows. Results demonstrate the phase dependency of velocity measurements averaged between two acoustic beams and provide a theoretical error for wave and turbulence characteristics sampled under a range of conditions. Spectral moments of the subsurface longitudinal wave orbital velocities recorded by the VDCP can be between 0.1 and 9 times those measured at a point for certain turbulent current conditions, turbulence intensity measurements may vary between 0.2 and 1.5 times the input value in low wave conditions and turbulence length scale calculation can also vary hugely dependent on both current and wave conditions. The continuation of this work, presented in chapter 7 enables effective comparison of a linear model for tidal flow kinematics against field measurements from UK tidal site data (7),subsequently validating numerical models for the testing of tidal turbines.

6.1 Introduction

Acoustic Doppler technology is versatile in the measurement of sea conditions; however, this technology can be limited in its effectiveness at measuring the small-scale kinematic fluctuations caused by waves and turbulence. This chapter will focus on the characterisation of combined wave and turbulent current conditions at tidal races using Acoustic Doppler (AD) technology. AD technology is commonly used in measurement of subsurface velocities and sea surface elevation. Upward looking devices emit sound pulses from transducers which are reflected by particles suspended in the water column returning a signal to the instrument. The signal is frequency shifted (Doppler shift) according to the velocity in the pulse direction at which the particle was travelling. By emitting pulses at high frequency and trigonometrically transforming the resultant velocities in combination with two or three other transducer records, a three-dimensional velocity time-series can be calculated. The typical assumption is that the flow is homogeneous over the volume between the instrument's transducer beams (Lu & Lueck 1999*a*). This is effective for measuring a range of current conditions; however, the smaller fluctuations resulting from waves and turbulence can be obscured by this method (Nystrom et al. 2007). Improved methods have been published for resolving mean current (Gilcoto et al. 2009)(Ott 2002), turbulence (Gargett 1994)(Vermeulen et al. 2011)(Wiles et al. 2006)(Stacey et al. 1999)(Stacey 2003)(Souza 2010)(Lohrmann, Hackett 1990)(Guerra Paris & Thomson 2017), and wave velocities (Filipot et al. 2013), however this chapter focuses on using a conventional Doppler Current Profiler (DCP) configuration with the aim of improving site characterisation of wave and turbulence sub-surface velocities by working with its limitations. Figure 6.1 gives an illustration of the phase difference between two beams as a wave passes over the sea surface. This is a highly simplified example, however it goes some way to illustrating the difficulty in measuring velocities induced by waves (and turbulence) by averaging across beams separated in horizontal space.

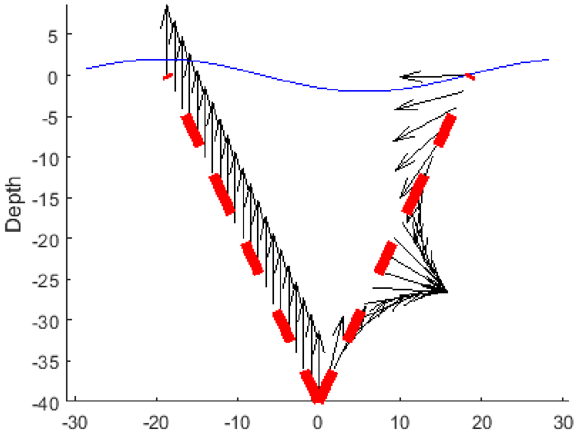

Figure 6.1: Illustration of phase difference between two beams of a DCP during wave passage. Each beam is at 25 degrees, and it is assumed that the phase at each depth on the first beam is zero and that the regular wave crests are parallel to the beam heading.

6.2 Methodology

The methodology proposed here, incorporates a Virtual Doppler Current Profiler (VDCP) which is designed to be a numerical tool that mimics the measurement technique of a real DCP, instead sampling a simulated flow field, and quantifying the theoretical limitations of DCP subsurface velocity measurements.

The VDCP is set up in a typical 'Janus' configuration typically used to collect current data from tidal races. The system comprises 4 beams slanted at 25 degrees to the vertical. The tidal flow model simulates velocities at the beam locations for the specified depth in the 'Earth-fixed' coordinate system which describes the easting, northing and up-down (ENU) velocities in the standard Eulerian frame of reference, according to the model defined in chapter 5 The VDCP samples from this model first converting the simulated velocities at the beam sampling location (u_{b_i}, v_{b_i}, w_{b_i}) into an along beam velocity (b_i), and then (like a physical DCP) resolving all four along beam velocities into ENU velocities (U, V and W). Ten-minute samples of velocity time series, resolved by the VDCP, are then analysed in the frequency domain to determine wave and turbulence characteristics.

A physical instrument would typically emit an acoustic signal at several hundred Hertz, storing information from the returned signal, such as intensity, amplitude and correlation, at several Hertz, and averaging to the specified bin depth, as discussed in section 3.1. These processes are not discussed further here, since the VDCP itself does not use acoustic technology, however they are mentioned in section 3.1 and are discussed as the subject of, and alongside a number of other studies (Nystrom et al. 2007)(Nystrom et al. 2002)(Muste et al. 2004).

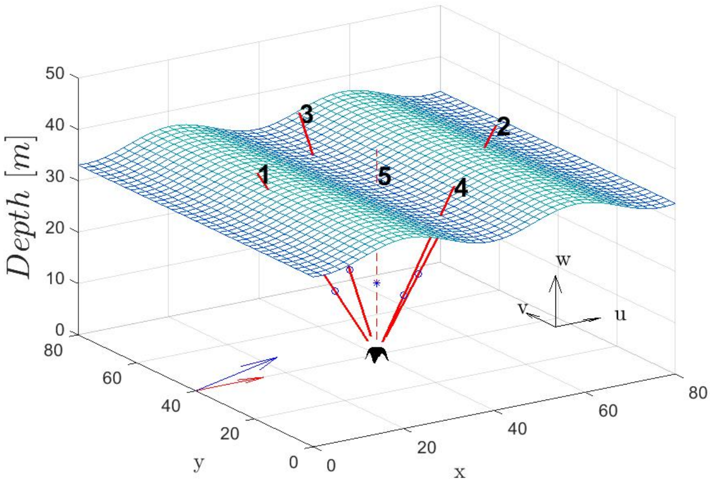

Figure 6.2: Illustration of 'Virtual' DCP. Arrows indicate current (red) and wave (blue) directions.

To cope with changes in heading, pitch and roll of the instrument the rotation matrix (RM) is applied to the three components of velocity (u,v,w) defined in the simulated flow field. The rotation matrix considers heading (H), pitch (P) and roll (R); where heading is the rotation about the z axis, pitch is the rotation about the y axis and roll is the rotation around the x axis.

$$\begin{bmatrix} u \\ v \\ v \end{bmatrix} = RM^{-1} \begin{bmatrix} u_0 \\ v_0 \\ v_0 \end{bmatrix} \tag{6.1}$$

Where,

$$RM = \begin{bmatrix} \cos H & \sin H & 0 \\ -\sin H & \cos H & 0 \\ 0 & 0 & 1 \end{bmatrix} \begin{bmatrix} 1 & 0 & 0 \\ 0 & \cos P & -\sin P \\ 0 & \sin P & \cos P \end{bmatrix} \begin{bmatrix} \cos R & 0 & \sin R \\ 0 & 1 & 0 \\ -\sin R & 0 & \cos R \end{bmatrix} \tag{6.2}$$

Along beam velocities, b_1, b_2, b_3 and b_4 at each specified depth are calculated, from the three components of velocity (u,v,w) at their respective grid points, according to the equations below (Teledyne RDI 2010); where θ_b refers to the angle of the transducer beams from the vertical. The error velocity (er) is assumed to be zero.

$$\begin{bmatrix} b_1 \\ b_2 \\ b_3 \\ b_4 \end{bmatrix} = M^{-1} \begin{bmatrix} u \\ v \\ w \\ er \end{bmatrix} \tag{6.3}$$

Where,

$$M = \begin{bmatrix} a & -a & 0 & 0 \\ 0 & 0 & a & -a \\ b & b & b & b \\ c & c & -c & -c \end{bmatrix} \tag{6.4}$$

And,

$$a = \frac{1}{(\sin \theta_b} \tag{6.5}$$

$$b = \frac{1}{4\cos(\theta_b)} \tag{6.6}$$

$$c = \frac{a}{\sqrt{2}} \tag{6.7}$$

To resolve these along beam velocities back into three components of velocity (U,V,W), as if by a DCP, the reverse method is used, as in section 3.1

$$\begin{bmatrix} U_0 \\ V_0 \\ W_0 \\ er \end{bmatrix} = M \begin{bmatrix} b_1 \\ b_2 \\ b_3 \\ b_4 \end{bmatrix} \tag{6.8}$$

$$\begin{bmatrix} U & V & W \end{bmatrix} = RM \begin{bmatrix} U_0 & V_0 & W_0 \end{bmatrix} \tag{6.9}$$

The difference now is that there is only one set of U,V and W velocities averaged between the four beams, where before u,v and w were known at a point on each beam. Furthermore, included in this calculation is a record of error, which gives an indication of the level of homogeneity between the beam records.

6.3 Results

Investigations were undertaken using numerically simulated current fields accounting for combinations of waves and currents aligned in deep water. By sampling a simulated flow with the VDCP analysis is conducted on the effect of certain variables on recording accuracy of sub-surface velocities. Results are analysed in the frequency domain taking Fourier transforms of ten-minute velocity samples. Any set of environmental conditions and set-up configurations can be simulated to determine the theoretical accuracy of a DCP. In this chapter, a few relevant examples are presented, as in Table 6.1, where a type of sea condition is simulated, and the effect on sampling accuracy is observed when modifying certain environmental or DCP variables. These examples are presented in order to demonstrate the most interesting and relevant results, before combining them to simulate more realistic, and hence applicable, conditions, and quantifying sampling accuracy at the end of the chapter.

Sea condition	Variables
Regular waves	Measurement depth Wave period VDCP Heading Current velocity
Irregular waves	Measurement depth Current velocity
Turbulence	Measurement depth
Irregular Waves and Turbulence	Wave height Turbulence intensity

Table 6.1: Sea conditions and investigation variables.

The sub-surface velocity components of the simulated current field are sampled by depth bin in several ways:

1. Point sampling of the velocities (u, v, w) in Earth coordinates from a point centred directly above the VDCP, see dashed line numbered '5' in Figure 6.2.
2. VDCP averaging of the along beam velocities resolved into (U, V, W) Earth coordinates.

The sampled velocity time-series are parametrised appropriately:

1. When investigating waves, spectral moments are used. Spectral moments define the energy in, and the shape of a spectrum (within a specified frequency range), and can be used to determine parameters such as significant wave height (H_s), mean period (T_m), peak period (T_p), etc. The zeroth and first spectral moments are compared, for consistency, for both regular and irregular waves. The first moment takes into account the distribution of wave frequencies in the spectra and as such it is assumed that the difference between zeroth and first moment will be more noticeable in irregular waves than in regular waves.
2. When investigating turbulence, intensity and length-scale are used.

6.3.1 Waves

Waves of 2 metre height and 5 second period are used for regular and irregular wave cases. Short period waves are chosen since one wavelength or more fits between the separation of the beams, making it easier to demonstrate the relationship between beam separation and wavelength, for a DCP of the chosen configuration. The height of the waves chosen is of little significance for this analysis. Velocities are recorded and the spectral density of each record calculated. The ratio (R_n) of the spectral moments (m_n, where n is the $n^{th} order$) of point sampled and VDCP averaged velocity spectra (S) are calculated to quantify the accuracy of VDCP sampling.

$$R_n = \frac{m_{n_VDCP}}{m_{n_point}} \tag{6.10}$$

$$m_n = \int_0^\infty f^n S(f) df \tag{6.11}$$

In the following analysis zeroth and first order spectral moments are presented. The zeroth moment is useful to characterise the energy in the spectrum whilst the first moment better indicates the frequencies over which this energy is distributed.

Regular waves

Sampling of simulated regular waves presents simple test cases that allow for a better understanding of the more realistic irregular wave cases to follow. In Figure 6.3 the effect of varying measurement depth is investigated. Longitudinal and vertical velocity measurement accuracy fluctuates as a function of measurement depth. The model is idealised, not considering the effect of surface deformation on velocities near the surface, as discussed in section 5.1. Lack of a 'stretching' method (Wheeler 1969) subsequently decreases the validity of those velocities taken at depths indicated by the shaded box.

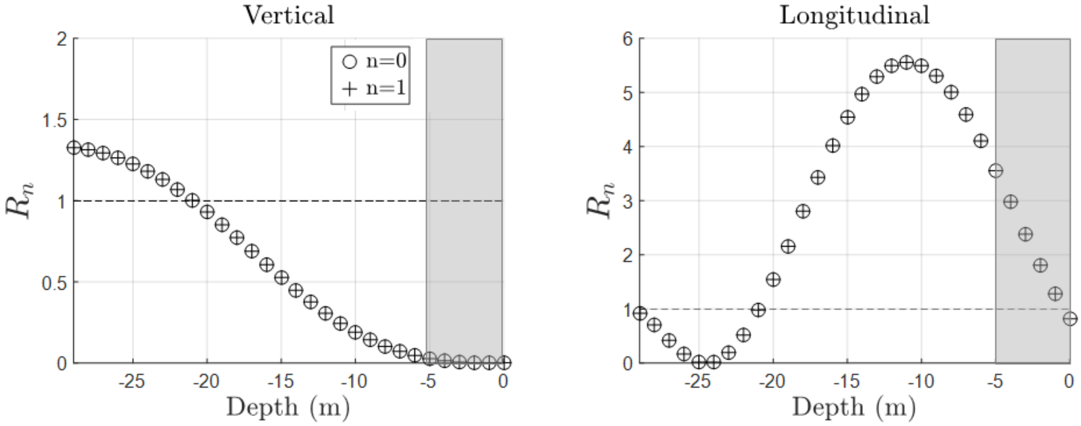

Figure 6.3: Sampling accuracy of VDCP, with sampling depth variation, for a regular wave of 2m height and 5s period. Shaded area indicates inaccuracy due to idealisation of surface deformation.

As a result of averaging across the distance between transducer beams a change in energy levels at particular frequencies is often noted. Figure 6.4 shows that at a specified depth (-20m), and thus beam separation, along beam velocity measurements at locations on two opposing beams are out of phase, and subsequently result in a VDCP measurement that is significantly magnified in amplitude. See equation 6.8.

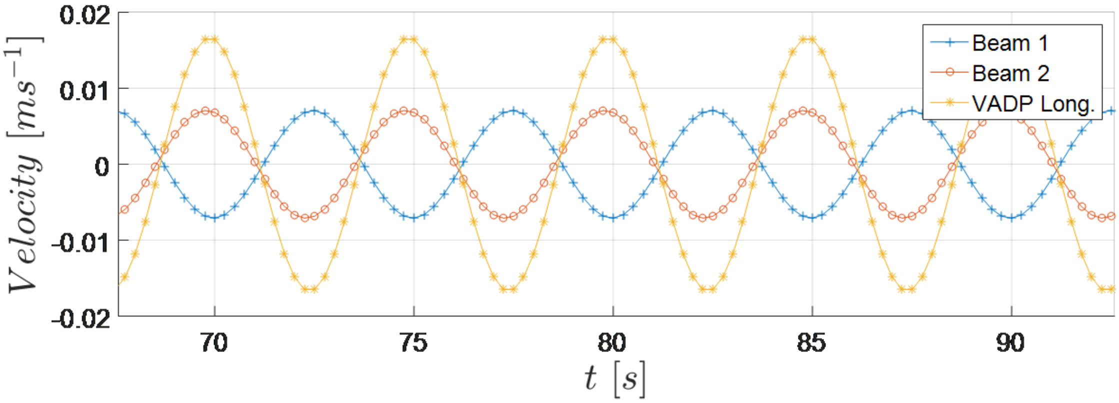

Figure 6.4: Along beam velocity sampled at two points on opposing beams and longitudinal velocity measured by VDCP at -20m depth. Regular wave of height 2m, and period 5s.

The phase difference, $d\phi$, defines the relationship between wavelength and the longitudinal beam separation, dx, between the upstream and downstream beam (1 and 2). It is calculated using the wave number, k, such that $d\phi = kdx$. Beam separation is a function of height, such that $dx = 2h\tan\theta_b$, where h is the vertical distance above the DCP and θ_b is the beam angle from the vertical. Figure 6.5 demonstrates the effect of phase difference on longitudinal velocity measurement accuracy, for the regular wave. VDCP measurement accuracy is good at each full phase cycle (0, 2π, etc).

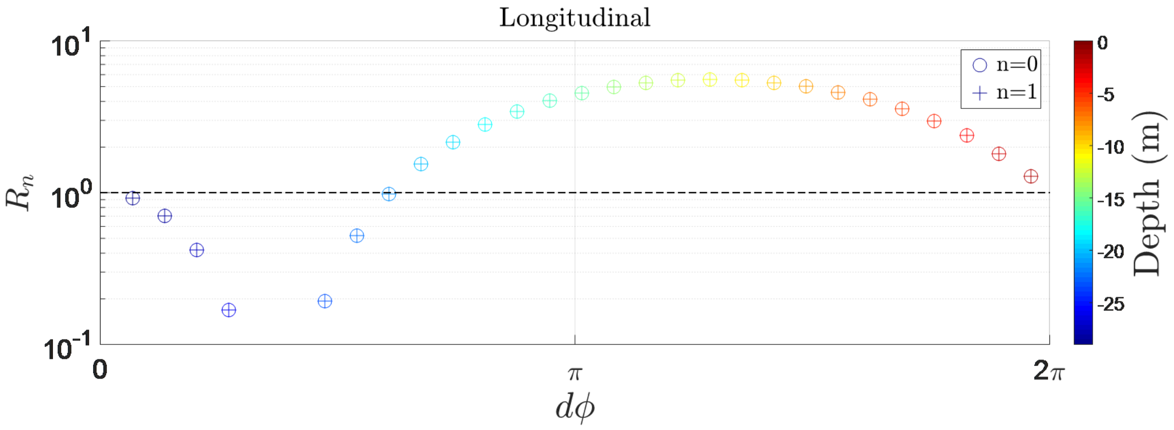

Figure 6.5: Longitudinal velocity sampling accuracy of VDCP, with phase difference due to depth variation across upstream and downstream beams, for a regular wave of 2m height and 5s period.

The effect of varying wave period has a very similar phase relationship to that of changing the sampling depth. Figure 6.6 demonstrates the effectiveness of VDCP vertical and longitudinal velocity sampling with period varying from 5 to 10s, a likely range of periods for waves of 2m significant wave height, given standard steepness limitations (Det Norske Veritas 2007). An optimum depth of -21m (below the sea surface) is chosen from the 5 second period regular wave used in the previous example.

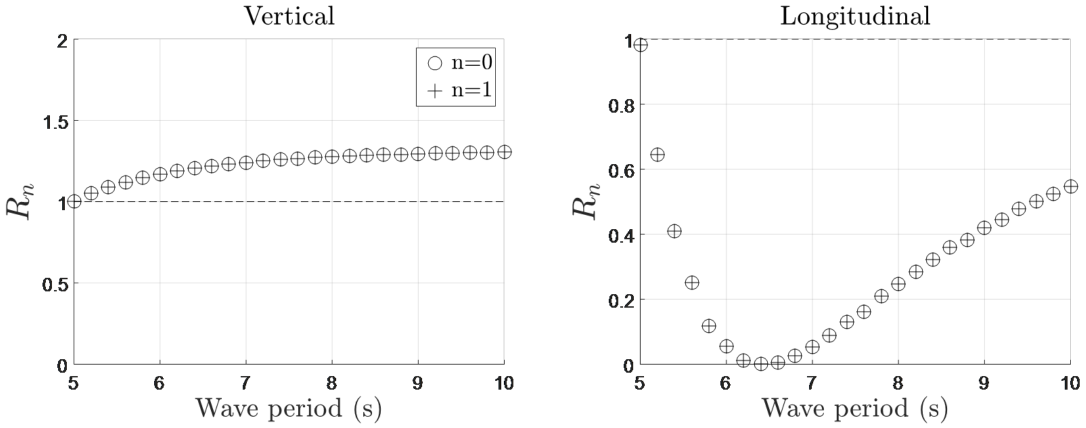

Figure 6.6: VDCP sampling accuracy with wave period variation, for a regular wave of 2m height, sampled at -21m depth.

The VDCP is rotated through 90 degrees around its z axis (heading). With this change in heading comes a variance in the accuracy of VDCP sampling, as seen in Figure 6.7. Vertical and longitudinal velocity sampling accuracy fluctuates as a function of longitudinal beam separation, returning to unity with each full phase cycle (2π), at 0 and 90 degrees.

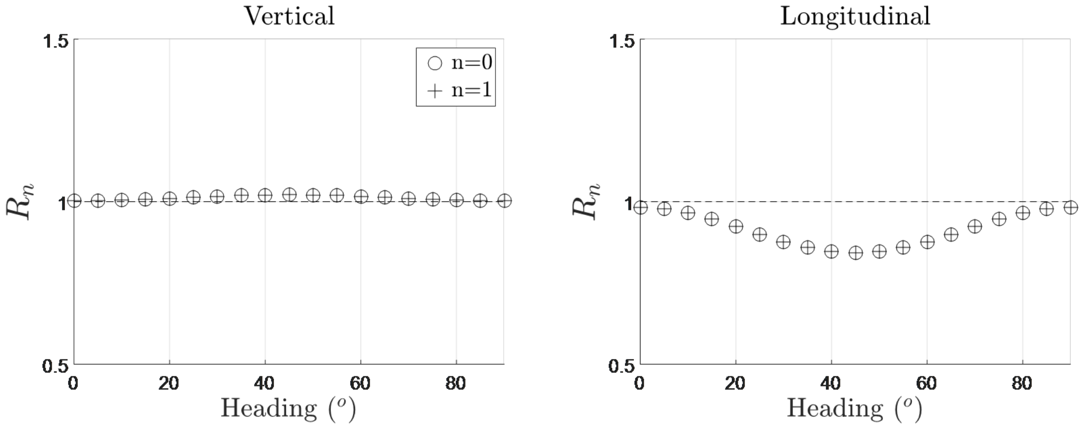

Figure 6.7: VDCP sampling accuracy with heading variation; for a regular wave of 2m height and 5s period, sampled at -21m depth.

Tidal currents are included according to a sheared 1/7th power law where the velocity is calculated for the specified depth from the mean current velocity ($\overline{u}$) at a reference depth (z_ref) using equation 5.13. The relative wave number and angular frequency are calculated using the mean current velocity in the wave direction, as described in section 5.1, and are used to modify the wave spectrum as well as in the equations for linear wave kinematics. In Figure 6.8 a mean current velocity ($z_{ref} = -15m$) increasing from 0 to $4ms^{-1}$ in $0.2ms^{-1}$ increments is applied in the following and opposing wave direction. In the following case (blue) VDCP vertical velocity is overpredicted whilst longitudinal velocity sampling accuracy is underpredicted, fluctuating as a function of wavelength (modified by current). In the opposing cases DCP sampling of vertical and longitudinal velocity is increasingly poor as current speed increases. For strong currents opposing these relatively short period (high frequency) waves, wave blocking occurs, as wavenumber extends to infinity.

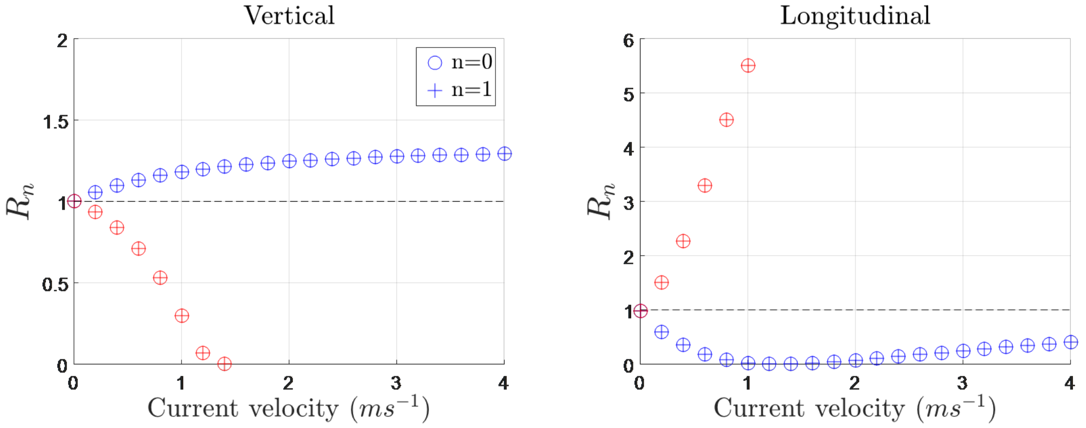

Figure 6.8: VDCP sampling accuracy with current speed variation; for a regular wave of 2m height and 5s period following (blue) and opposing (red) current direction, sampled at -21m depth.

VDCP sampling accuracy of regular wave orbital velocities has been shown to be dependent on wave phase difference across the instrument. Phase difference is dependent on VDCP sampling depth and orientation, wave period and current speed. Vertical velocities are typically better represented than longitudinal velocities.

Irregular waves

Irregular waves of 2m significant height and 5s mean period are simulated using JONSWAP spectra. Figure 6.9 shows the ratio of the two longitudinal velocity spectra, (the spectra of the VDCP sampled sub-surface velocities due to wave action and the spectra of the point sampled sub-surface velocities due to wave action) plotted against the phase difference ($d\phi$) resulting from each frequency component (f), at four depths.

$$d\phi(f) = k(f)dx \tag{6.12}$$

A fluctuation in accuracy analogous to that shown in the regular wave case (Figure 6.5) is observed, with the result identical at any chosen depth. For in phase frequency components VDCP accuracy is good, whilst those out of phase poorly represent the true wave velocities. There is some noise at the low phase end of the spectrum. This is linked to the low frequency components of the sampled spectra which relate to long period waves. Due to the relatively short timescale (10mins) of the simulation neither the point or VDCP measurement can accurately capture these long periods wave components.

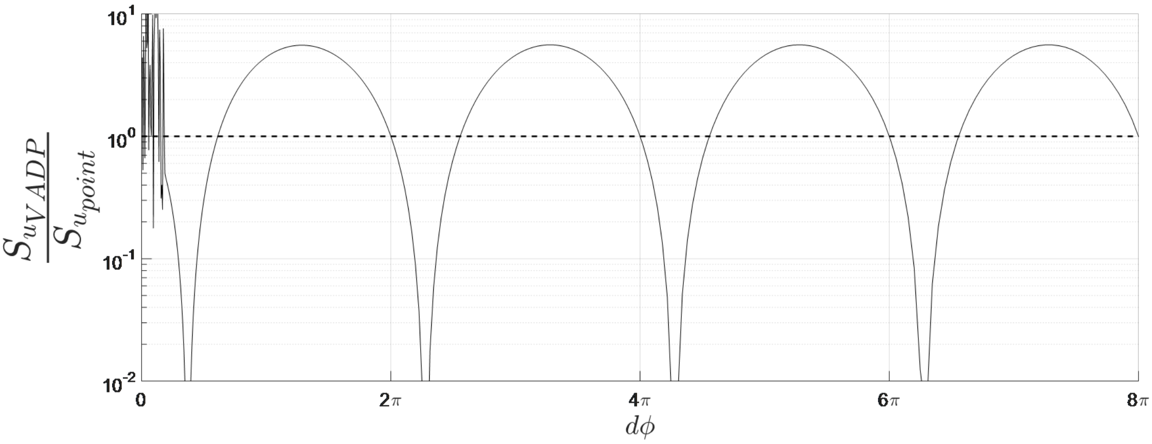

Figure 6.9: Longitudinal velocity sampling accuracy of VDCP for irregular waves: $H_s = 2m$, $T_m = 5s$, sampled at -15m depth.

Vertical and longitudinal velocity VDCP sampling accuracy fluctuate as a function of beam separation and wavelength; this is shown for the longitudinal case in Figure 6.10. For irregular waves a phase relationship occurs for each frequency component in the spectrum. Therefore, unlike in the regular wave cases, the accuracy of VDCP sampling does not improve as mean phase approaches 2π, since many frequency components of the spectrum remain out of phase. Instead the VDCP continues to over predict the energy in the longitudinal velocity spectrum.

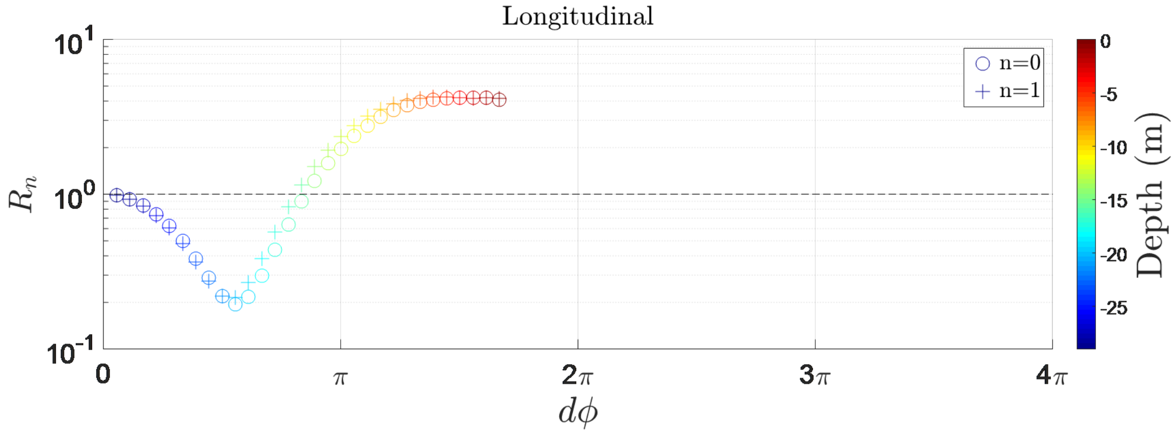

Figure 6.10: Longitudinal velocity sampling accuracy of VDCP with phase difference due to depth variation across upstream and downstream beams, for an irregular wave of 2m height and 5s period.

Figure 6.11 illustrates the effect of currents of varying strength on following and opposing irregular wave surface elevation spectra.

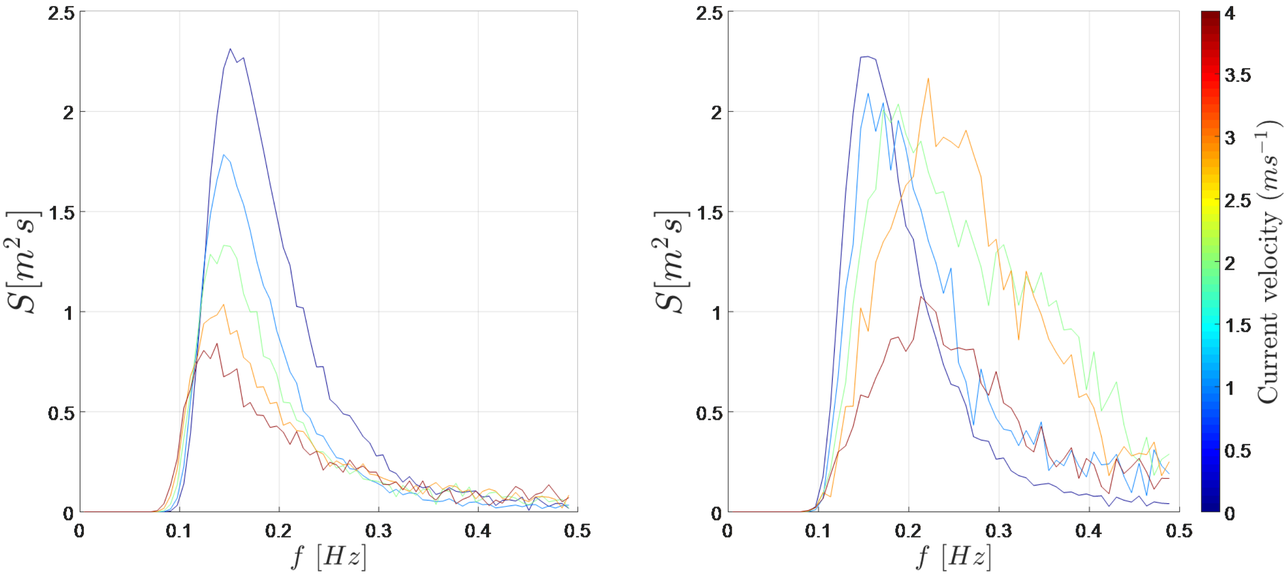

Figure 6.11: Following (left) and opposing (right) current velocity effect on surface elevation spectra for irregular waves ($H_s = 2m$ and $Tm = 5s$).

The effect of a 1/7th power law $2ms^{-1}$ mean current speed on both the point measured and VDCP measured longitudinal velocities during following and opposing waves is shown in Figure 6.12 at depth -15m. Energy in the velocity spectra is significantly reduced during opposing waves, and in both cases the VDCP is ineffective at capturing the energy across the entire spectra.

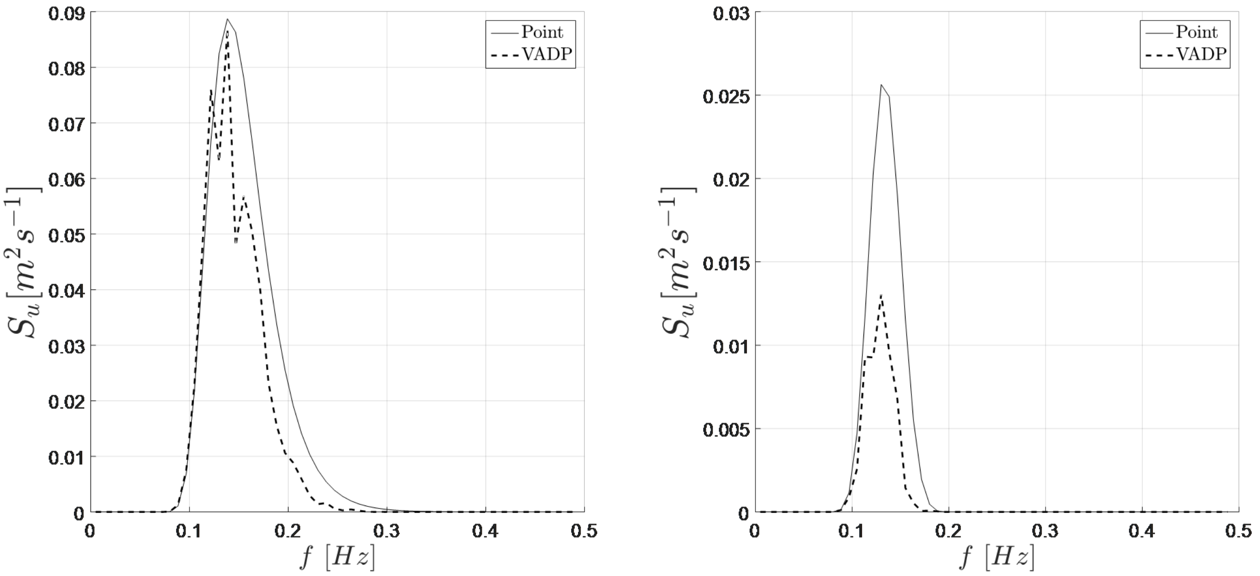

Figure 6.12: Comparison of VDCP and point sampled longitudinal velocity spectra for following (left) and opposing (right) irregular waves ($H_s = 2m$ and $Tm = 5s$) on $2ms^{-1}$ mean current at -15m depth.

Figure 6.13 demonstrates, using spectral moments, the effects of VDCP sampling methods on the velocity spectra (illustrated in Figure 6.11) for current velocity increasing from 0 to 4 ms^{-1} for following and opposing waves at -15m depth. VDCP vertical velocity decreases in accuracy with increasing current velocity, and VDCP longitudinal velocity sampling accuracy decreases asymptotically for the following case, and for the opposing case fluctuates significantly with increasing current velocity.

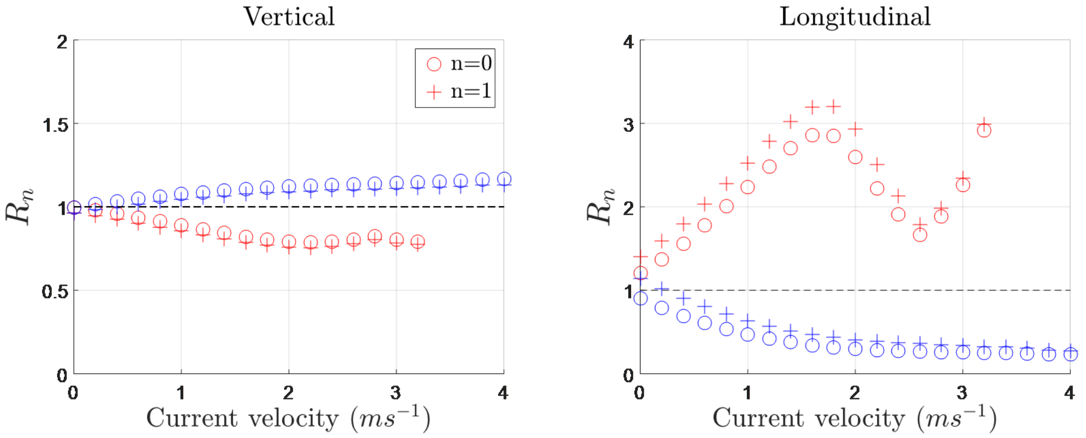

Figure 6.13: Velocity sampling accuracy of VDCP with current speed variation; for an irregular wave of 2m significant wave height and 5s mean period following (blue) and opposing (red) current direction, sampled at -15m.

The results of the VDCP irregular wave model analysis demonstrate phase dependency when sampling horizontal wave orbital velocities by averaging over multiple sample points. Where spatial separation and wave length result in individual samples being in phase, good accuracy is achieved. However very large overestimation and underestimation of velocities can be seen for out-of-phase samples.

6.3.2 Turbulence

Turbulence is simulated at $1ms^{-1}$ mean current velocity with a uniform profile and longitudinal, component length scales of 34m, 4m, and 1m. The length-scales chosen are specific to the current velocity, according to studies conducted in the ReDAPT project (Parkinson & Collier 2016), for a flood tide at the Falls of Warness in Orkney, UK. Longitudinal, lateral and vertical turbulence intensities are set at 8%, 7.5% and 6%, based upon the same study. The accuracy of turbulence sampling by the VDCP is initially studied in terms of velocity spectra compared to point samples, and as with the wave case the phase relationship is observed. Associated with the Von Karman turbulence model is an analytical expression for the cross-correlation of points separated in space which is a function of turbulent 'wave-number' as presented in equation 5.25. Therefore, VDCP sampling of the turbulent flow field is affected by beam separation and turbulent wave-number. Plotting the ratio of the two longitudinal velocity spectra (the spectra of the VDCP sampled sub-surface velocities and the spectra of the point sampled sub-surface velocities) against the phase difference, as was done for irregular waves, the result is identical for any chosen depth. In Figure 6.14 mid-depth (-15m) is plotted, demonstrating that best sampling accuracy is achieved when frequency components sampled at each beam are in phase ($d\phi = kdx$) or 180 degrees out of phase, i.e. the length of the turbulent structure is a multiple of half the beam separation distance.

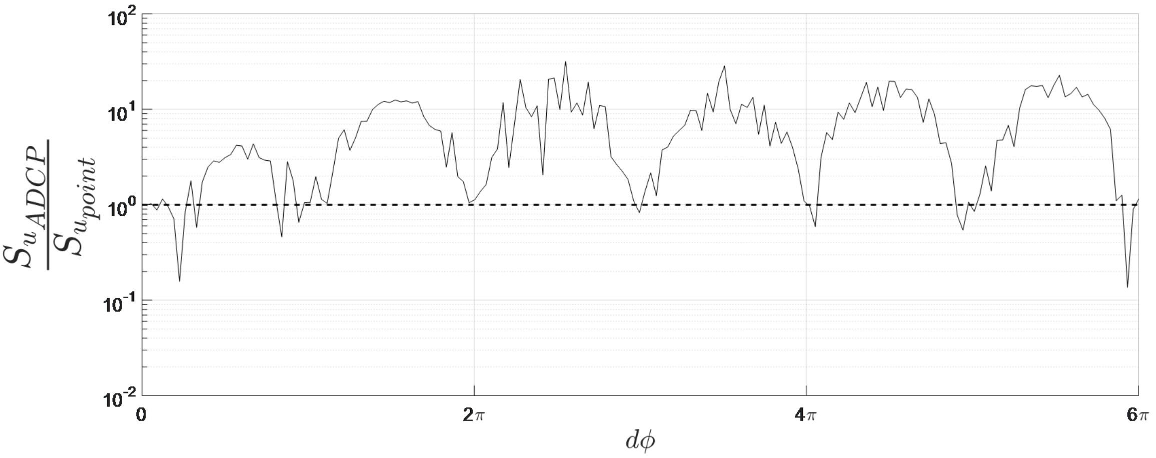

Figure 6.14: Longitudinal velocity VDCP sampling accuracy with measurement depth for Von Karman turbulence at $1ms^{-1}$, sampled at -15m depth.

The random nature of turbulence is such that the regular fluctuation in space seen in the model is unlikely to be seen in site data, however it highlights the deficiency of the DCP averaging method for measurement of a turbulence spectrum. Turbulence is highly complex and can be described by numerous parameters. Given that the focus of this work is to accurately replicate tidal flows, the parameters of interest are those which are to be applied to the model. The Von Karman model requires inputs of turbulence intensity in three dimensions, and three components of length scale. Turbulence intensities can be determined from mean longitudinal flow speed, $\overline{u}$ and velocity component standard deviation, $\sigma_i (i = x, y, z)$, taken from DCP averaged velocities. However due to averaging (section 6.2) the typical three or four beam method is likely to give inaccurate estimates of standard deviation.

$$TI_i = \frac{\sigma_i}{\overline{u}} \tag{6.13}$$

By determining the autocorrelation of the estimated ENU velocities, estimates of longitudinal length scale can be calculated from the field data using the methodology defined in section 3.3.2. The auto-covariance function ($C_u u$) can be calculated according to the velocity spectra ($S_u u$) such that:

$$C_{uu}(\tau) = \int_0^\infty S_{uu}(f) \cos \pi f \tau df \tag{6.14}$$

The auto-correlation function (ρ_{uu}) is written:

$$\rho_{uu}(r, r', \tau) = \frac{C_{uu}(r, r', \tau)}{\sigma_u \sigma_u} \tag{6.15}$$

Time-scales are calculated by integrating the cross correlation function up to the shortest time lag for which it falls to zero:

$$T_u = \int_0^{\rho_{uu}=0} \rho_{uu} \tau d\tau \tag{6.16}$$

And according to Taylors hypothesis (Taylor 1937) length-scales are estimated according to mean current velocity $\overline{u}$. For example, for the longitudinal component (subscript u) in the longitudinal direction (subscript x):

$$^xL_u = T_u \overline{u} \tag{6.17}$$

Figure 6.15 compares longitudinal length scale and turbulence intensity in three dimensions. For each parameter (n), VDCP samples are compared to point samples using the ratio Q_n. For $n =^x L_u$, TI_x, TI_y, or TI_z.

$$Q_n = \frac{n_V DCP}{n_p oint} \tag{6.18}$$

VDCP sampled estimates of longitudinal length-scale, using the equations described above, consistently underestimate the simulated length-scale. Turbulence intensities are again poorly estimated by the VDCP at most depths.

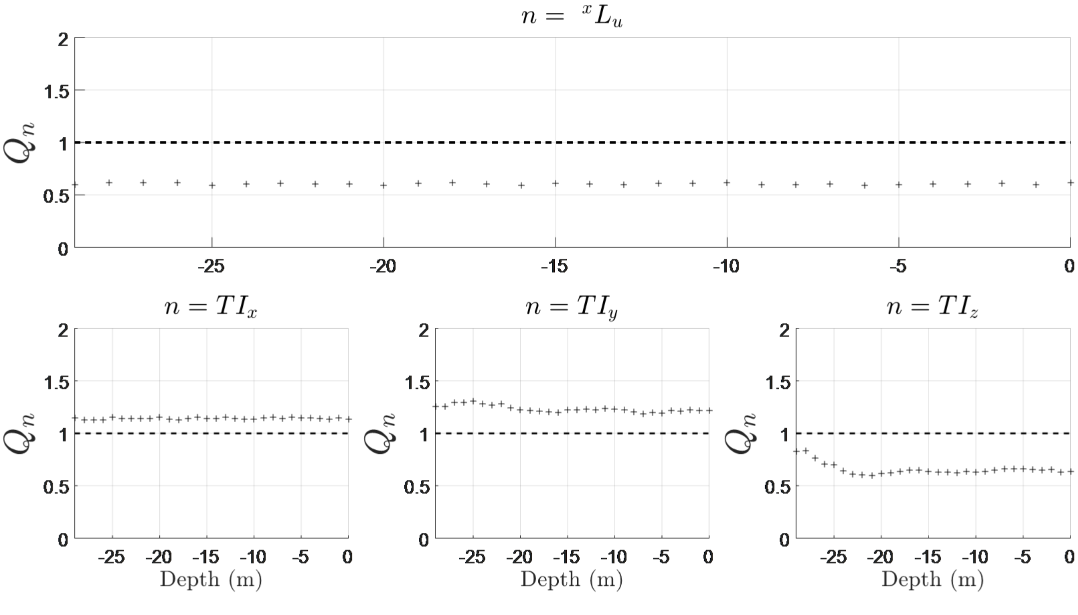

Figure 6.15: Turbulence parameter accuracy with VDCP measurement depth for $1ms^{-1}$ mean current velocity Von Karman turbulence of longitudinal component length scales 30, 4 and 1m.

The method helps in understanding the uncertainty in turbulence parameters measured at site, and the theoretical error can be estimated for any DCP configuration and environmental condition.

6.3.3 Waves and turbulence

At some sites, there is very low wave activity, and at others wave conditions can be significant. At sites with waves, turbulence parameters are best taken from periods of low wave activity, however surveys often aim to cover the more extreme annual weather conditions, and thus, few low wave periods would be present in the record. It is therefore useful to understand the impact of waves on measurement of turbulence conditions such that inputs to model parameters can be modified with an appropriate level of uncertainty attached. Since turbulence will always be present it is useful to understand the impact of turbulence on measurement of wave characteristics across a broader range of conditions.

Using the same turbulence simulation used in the previous example and measuring at -15m water depth, irregular waves of 5s period and increasing significant wave height (up to 1m) are applied. Figure 6.16 demonstrates the effect of this variation in wave height on the sampling of turbulence characteristics. Unlike in previous examples VDCP and point sampled estimates are compared to simulation inputs, since point sampled estimates of turbulence characteristics are also affected by changes in the wave conditions. For each parameter (n), point samples and VDCP samples are compared to the simulation input using the ratio Q_{n_s}.

For $n =^x L_u$, TI_x, TI_y, or TI_z. And $s = point$, or $VDCP$.

$$Q_{n_s} = \frac{n_s}{n_i nput} \tag{6.19}$$

As expected, increasing wave height results in considerable increases in the inaccuracy of turbulence intensity measurement, though not on length scale. Wave period variations have similar impact.

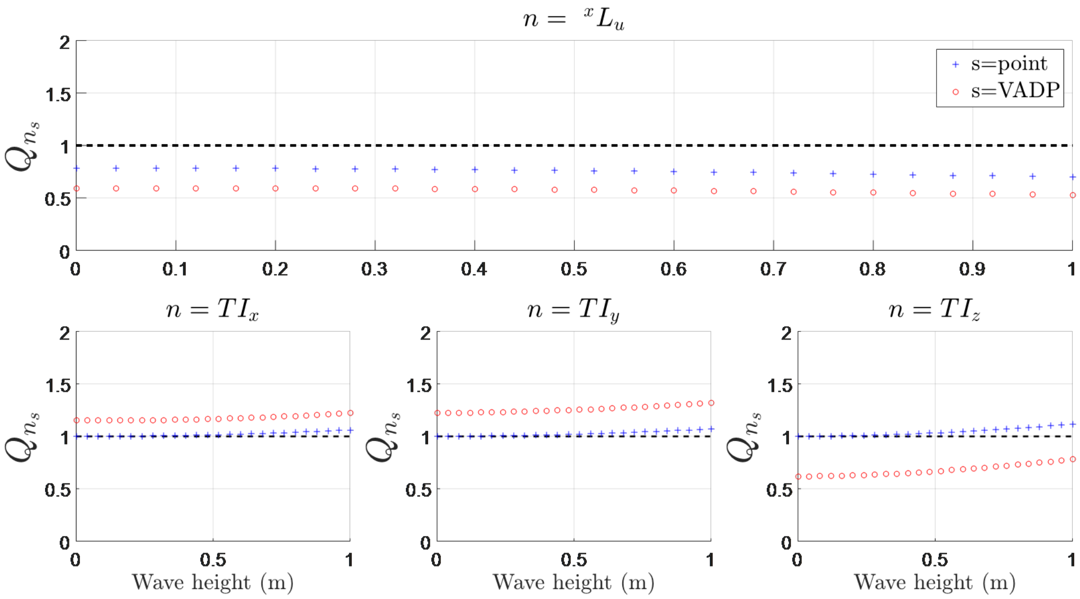

Figure 6.16: VDCP Turbulence parameter accuracy with significant wave height for irregular waves of period 5s, on $1ms^{-1}$ mean current velocity, with Von Karman turbulence.

Similarly, turbulence influences the measurement of waves. For example, in Figure 6.17 the effect of increasing longitudinal turbulence intensity (TI_x) is observed for a Hs=2m Tm=5s irregular wave spectrum on a $1ms^{-1}$ following current at -15m depth. The zeroth and first spectral moments are estimated between 0.1 and 0.3 Hz, between which frequencies wave kinematics dominate. Increase in longitudinal turbulence intensity is shown to decrease VDCP estimates of the zeroth and first spectral moments of longitudinal velocity.

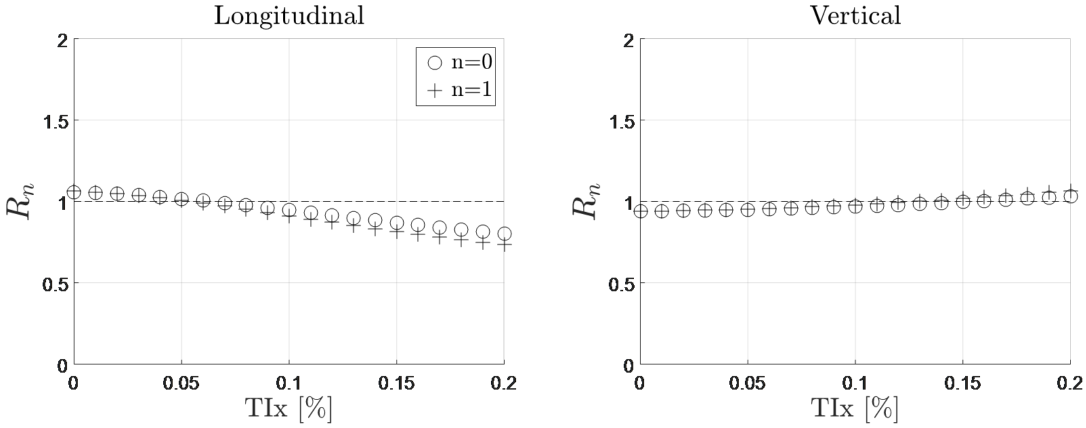

Figure 6.17: Turbulence intensity effect on VDCP wave measurement, for irregular waves ($H_s = 2m, T_m = 5s$) following a $1ms^{-1}$ turbulent current, sampled at -15m.

6.4 VDCP Error overview

The results have shown several examples that demonstrate the effect of variations in idealised environmental conditions and DCP configuration on sampling accuracy, and clearly demonstrate the difficulty in separating wave and turbulent components from flow measurements for characterisation. Wave sampling accuracy has been shown to be particularly susceptible to sampling depth, wave period and current velocity. Characterisation of turbulence using the VDCP was shown to be poor in many cases, and heavily impacted by the presence of waves.

In this section, significant results are summarized; demonstrating the error (E) between VDCP sampled characteristics and simulated characteristics. The results are presented for a depth of -10m below the sea surface, where the seabed is at approximately -50m. This is representative of a likely turbine hub height for a floating device, positioned for maximum current flow, avoiding the worst impact from waves.

The vertical velocity profile is characterised with a 1/7th power law and turbulence of longitudinal component length scales of 34m, 4m, and 1m and longitudinal, lateral and vertical turbulence intensities of 8%, 7.5% and 6% are applied, as in section 6.3.2. The influence of wave height and period, current speed and turbulence intensity are displayed as errors in the appropriate characteristics of each desired parameter. For waves, error is quantified according to differences in first spectral moment, within a range of wave specific frequencies (Δf):

$$\Delta f = 0.1 - 0.3 \; E_{m_1}(\Delta f) = \frac{m_{1_{VDCP}}(\Delta f)}{m_{1_{point}}(\Delta f)} \tag{6.20}$$

Figure 6.18 and Figure 6.19 show the error in the first spectral moments for an irregular JONSWAP spectrum of 3m significant wave height and 8s period (on following and opposing turbulent currents respectively) with variations in mean velocity and turbulence intensity. Whilst measures of the spectral moments of vertical velocity display relatively small deviations in accuracy, the spectral moments of longitudinal velocities sampled by the VDCP can be up to 9 times greater than measurements from a central point.

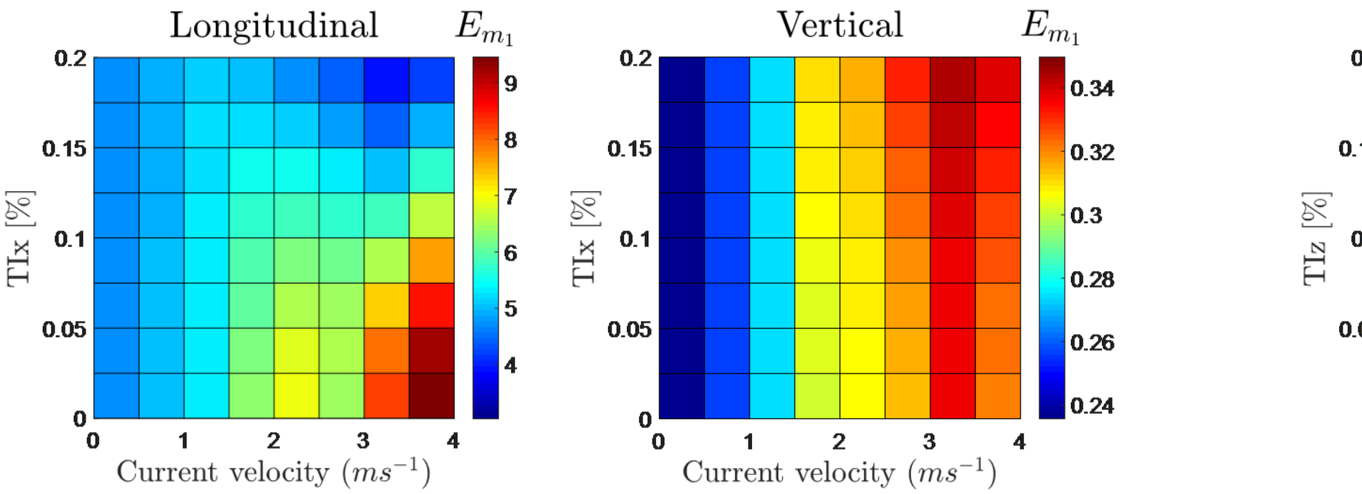

Figure 6.18: Error in VDCP sampling of wave velocity spectra, at -10m sampling depth, for irregular waves of Hs=3m and Tm=8 on *following* current with Von Karman turbulence (xLu=30m, yLu=4m, zlu=1m).

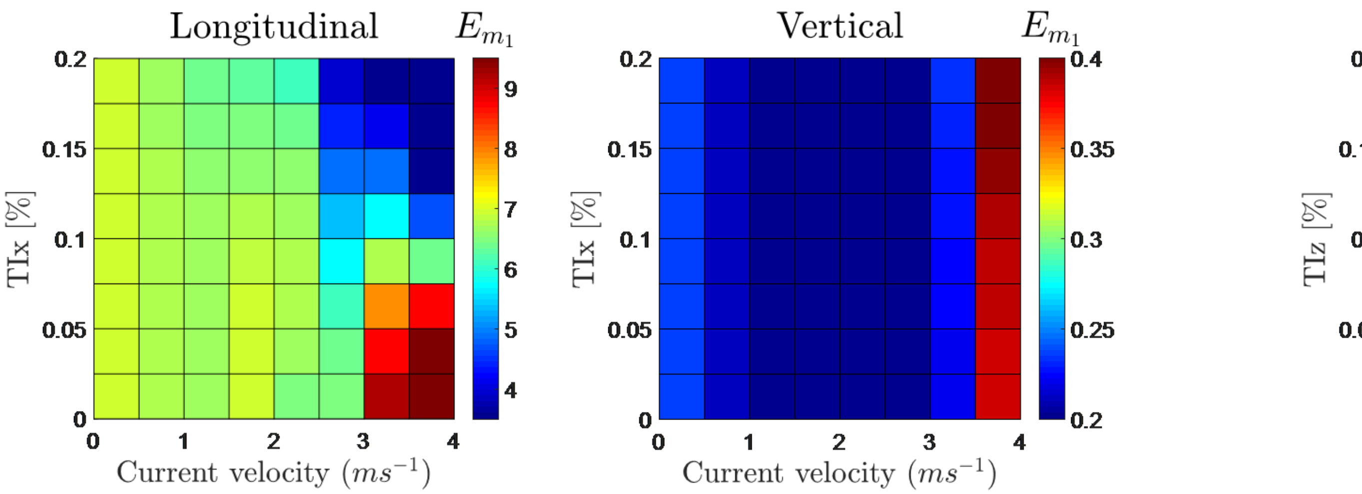

Figure 6.19: Error in VDCP sampling of wave velocity spectra, at -10m sampling depth, for irregular waves of Hs=3m and Tm=8 on *opposing* current with Von Karman turbulence (xLu=30m, yLu=4m, zlu=1m).

Turbulence intensity measurements are limited by averaging effects of the VDCP velocity resolving method, and are also affected in particular by the presence of waves. For turbulence: $(n = x, z)$

$$E_{TI_n} = \frac{TI_{n_VDCP}}{TI_{n_input}} \tag{6.21}$$

Figure 6.20 and Figure 6.21 demonstrate the error resulting from variation in significant wave height and mean period on turbulence intensity measurements by the VDCP for an irregular JONSWAP spectrum on turbulent currents described by intensities and length scales described above. Figure 6.20 is for waves following current direction and Figure 6.21 for waves opposing current direction. Standard deviation (σ_u) in longitudinal velocities used in turbulence intensity calculations (6.13) is increased significantly by the presence of waves, whilst in the vertical is actually diminished by VDCP averaging methods. Note should be made of these results when attempting to calculate turbulence intensity during periods of wave activity, even if wave activity is low.

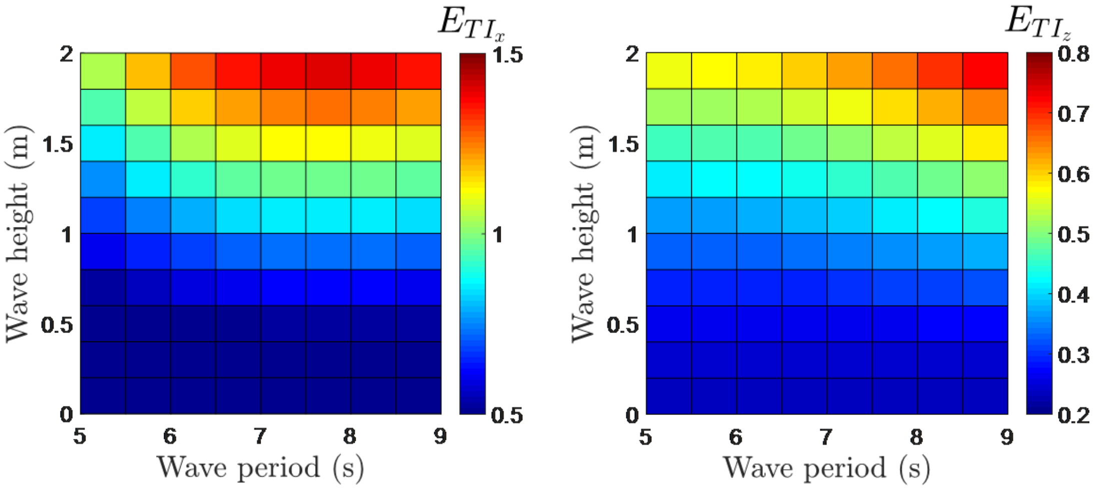

Figure 6.20: Error in VDCP sampling of turbulence intensity, at -10m sampling depth, for irregular waves on *following* $1ms^{-1}$ currents with Von Karman turbulence (xLu=30m, yLu=4m, zlu=1m).

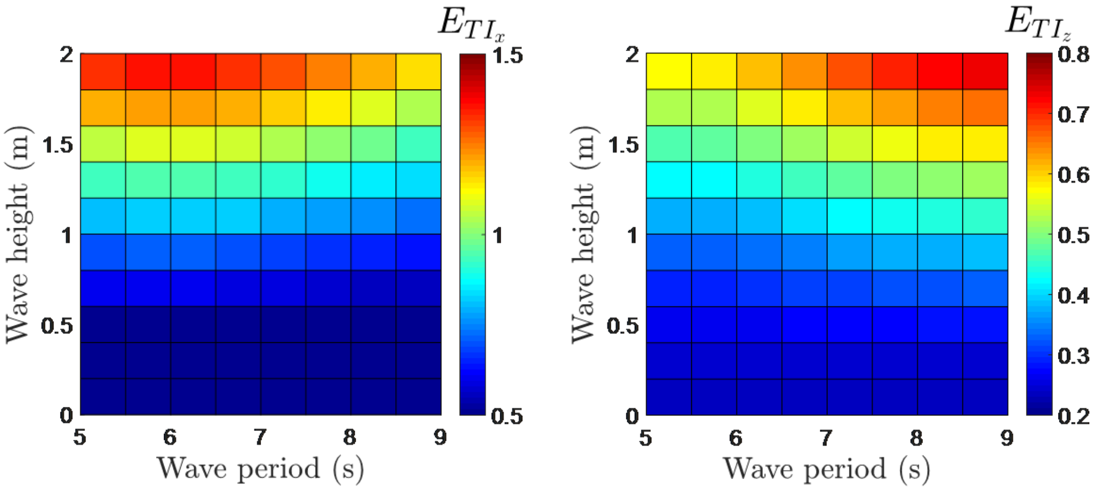

Figure 6.21: Error in VDCP sampling of turbulence intensity, at -10m sampling depth, for irregular waves on *opposing* $1ms^{-1}$ currents with Von Karman turbulence (xLu=30m, yLu=4m, zlu=1m).

Length-scales can be calculated from VDCP measurements as described in section 6.3.2. There is typically some error due to VDCP averaging so it is useful to understand the characteristics that influence these errors. Length scale estimation is influenced by a broad range of conditions but most significantly mean current velocity and significant wave height as illustrated in Figure 6.22 and Figure 6.23 which demonstrate these effects for following and opposing currents respectively.

$$(n = x, z)\ E^{n}L_{u} = \frac{{}^{n}L_{u_{V}DCP}}{{}^{n}L_{u_{i}nput}} \tag{6.22}$$

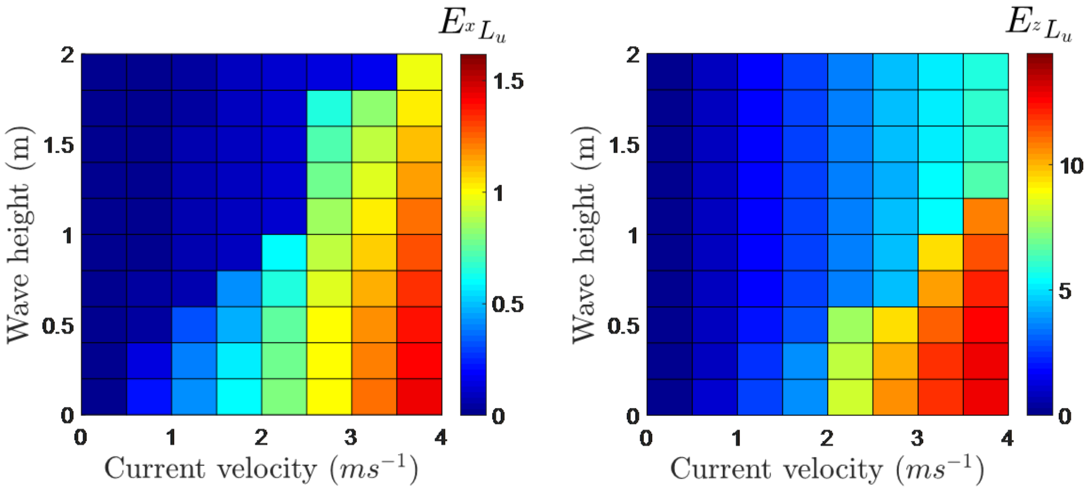

Figure 6.22: Error in VDCP sampling of turbulence length scale, at -10m sampling depth, for irregular waves of Hs=3m and Tm=8 on *following* current with Von Karman turbulence (xLu=30m, yLu=4m, zLu=1m).

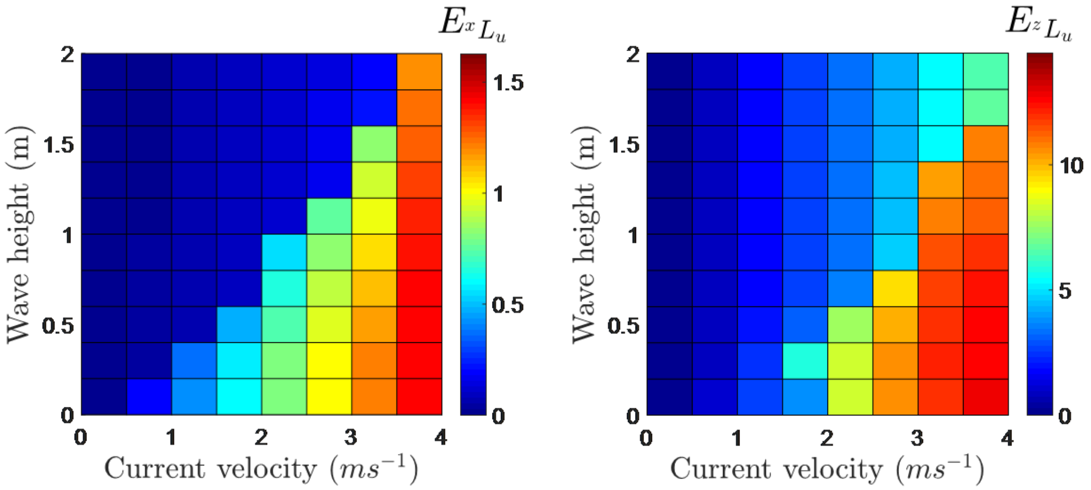

Figure 6.23: Error in VDCP sampling of turbulence length scale, at -10m sampling depth, for irregular waves of Hs=3m and Tm=8 on *opposing* current with Von Karman turbulence (xLu=30m, yLu=4m, zLu=1m).

Waves and turbulence particularly influence the fatigue loading of tidal turbine blades (Barltrop, Varyani, a.D. Grant, Clelland & Pham 2007)(Barltrop & Varyani 2006)(Milne et al. 2010), therefore whilst mean current velocity is well predicted and validated for loads modelling purposes, the results presented will enable more accurate representation of wave and turbulence effects, enabling improvements in design to reduce the impacts of fatigue.

Chapter 7

Model validation and sensitivity studies

Numerical simulation of tidal flows allows loads on, and performance of, tidal turbine designs to be analysed before committing to the considerable expense of installing devices at sea. Of course, for this analysis to be effective the simulated flow must be representative of the conditions at the site of intended installation. With limited information about any particular site, typically in the form of several short (2/3 week) DCP surveys, it is impossible to exactly replicate these flows. Hence numerical models will attempt to replicate the flow based on a range of time-averaged statistics aimed at covering a broad range of potential conditions. Using data that is available from a specific site it is possible to make comparisons between field and model data during certain conditions and to make conclusions on the validity of the model for representing such a site. In this study field measured water particle velocities are used to validate modelled water particle velocities simulated by a linear model for tidal flows. Field data is measured using a Doppler Current profiler (DCP) according to the techniques and methods described in chapter 3, with the results presented in chapter 4. The model includes waves, currents and turbulence, as described in chapter 5, and incorporates numerous options for simulating wave-current interactions which are the focus of this study. Using a 'Virtual' Doppler Current Profiler (VDCP), to measure the simulated flow, direct comparisons are made between model and site kinematics recorded using acoustic Doppler technology. The VDCP is designed to be a numerical tool that mimics the measurement technique of a real DCP, instead sampling a simulated flow field to compare directly to DCP measured field data. The model is validated, against data from the available data set, whilst sensitivity studies are conducted to assess the suitability of different wave-current interaction options for replicating the combined wave and current conditions experienced during the measurement survey.

Simulations are run for all the conditions seen during the December 2014 survey (4) that meet the quality criteria outline in section 3.5.2. Currents range between 0 and $3.7ms^{-1}$, with wave heights between 0.7 and 5 meters. Flood and ebb currents for the full range of magnitudes are considered for following and opposing waves of varying height. Following cases include all ten-minute instances where wave directions are +/-30 degrees either side of the current direction and opposing cases include all instances where wave directions are +/-30 degrees either side of the direction opposite to the current direction. For this data set, due to the location, the majority of wave instances travel in the same direction as the flood tide, therefore all instances of waves 'following' current direction used in this study are during the flood tide and all instances of waves opposing current direction are during the ebb tide. This is convenient for this particular analysis, however is also a limitation to the study, due to the differences in variability between two flow directions. The field data are processed and analysed as in chapter 4. To recap, for every ten-minute data sample, the following information is recorded:

- DCP setup: sampling frequency, mean depth, depth bin size and locations.
- DCP orientation: mean heading, pitch, and roll
- Current: mean current velocity (at specified depth), mean current direction, mean velocity depth profile
- Turbulence: Turbulence intensities, Turbulence length-scales
- Waves: Omni-directional and multi-directional surface elevation spectra, mean wave spectral parameters, mean wave directional statistics.

The model uses this information to simulate velocities at VDCP beam locations, whereupon the VDCP resolves these velocities into along beam velocities which can be compared to field records of along beam velocity. As defined in section 3.1, DCP setup, orientation, and noise are input to the model. DCP set-up and orientation are read directly from the instrument and averaged over the sample. DCP noise is calculated from the measured spectra as in section 3.4. Current, turbulence, and wave conditions for each ten-minute sample are also input to the model. This ten-minute averaged information is corrected for theoretical DCP error where appropriate (as discussed in chapter 6). Mean current at the specified depth is applied using the method defined in section 5.2, and turbulence parameters are estimated and corrected for error as discussed in section 4.3. Waves are input to the model according to three overarching modes, defined in section 5.1; the measured multi-directional or omni-sea surface elevation spectrum can be used as input, or alternatively a Bretschneider model spectrum can be input using measured parameters of wave height, and period.

From the field data ten-minute instances are first categorized into flood and ebb. Instances are binned according to mean current speed and significant wave height normalised by peak current speed ($\overline{u_p}$) and peak significant wave height (H_{s_p}) respectively, as shown in Figure 4.7 (chapter 4). For each instance a model case is simulated. The spectral density of the model along beam velocity (as determined by the VDCP im chapter 6) for each instance at the specified depth is calculated. The spectra are then compared to field along beam velocity spectra. ENU velocity spectra are also compared. Velocities are compared at approximate turbine hub height, which in this case is taken to be 10m below the surface, as if for a floating tidal turbine. Field and model velocities are also compared for the range of depths covered by the field DCPs 'waves' mode operation (as discussed in chapter 4), using spectra and metrics including standard deviation, maximum and damage equivalent velocity. Observations of following and opposing cases highlight the interaction between waves and currents and the adequacy of the chosen model, before a study of the sensitivity of the model to differing wave-current interaction options is conducted. The field velocity spectra for an example ten-minute instance are plotted against the three principle components (waves, turbulence, and noise) of the model in Figure 7.1 for along beam and ENU velocities.

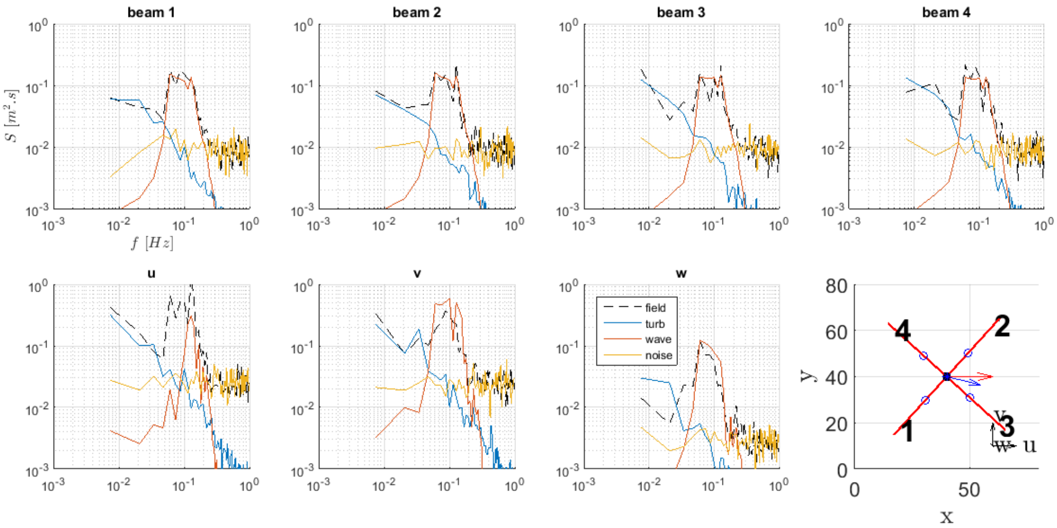

Figure 7.1: Example model velocity spectra broken down into wave turbulence and noise and compared to field velocity spectra for all along beam velocities and ENU velocities at one ten-minute instance of $2 < H_s < 2.5m$ and $2 < \overline{u} < 2.5ms^{-1}$, where waves are *following* the current direction. DCP position,and wave direction (blue) relative to zeroed current direction (red) are also plotted. Axis labels and units for each subplot are identical to the top left subplot.

Figure 7.1 illustrates just one ten minute instance of $2 < H_s < 2.5m$ and $2 < \overline{u}2.5ms^{-1}$ where waves are *following* the current direction. Multiple instances of spectra within each wave-current velocity bin are averaged in order to enable effective comparison of a large number of instances within each bin across a range of current and wave conditions. Figure 7.2 shows averaged instances of each component of the model for all four along beam velocities. Figure 7.3 shows averaged instances of each component of the model for East, North and Up (ENU) velocities.

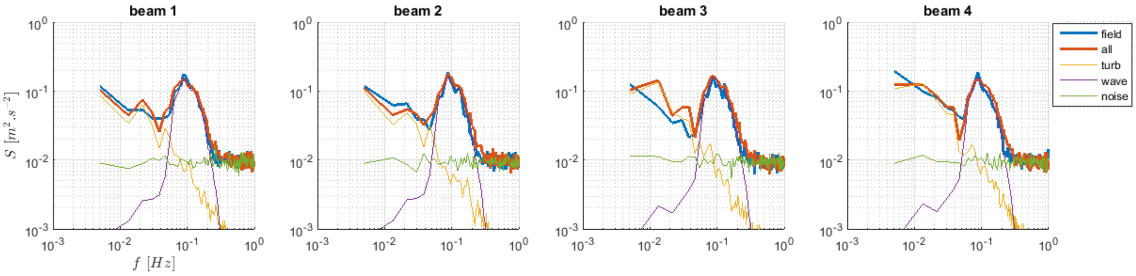

Figure 7.2: Example model velocity spectra, during $2 < H_s < 2.5m$ and $2 < \overline{u} < 2.5ms^{-1}$, where waves are *following* the current direction, broken down into wave, turbulence and noise and compared to field velocity spectra for all along beam velocities averaged over 10 similar wave-current instances.

The two figures, particularly figure 7.3, help to demonstrate the advantage of comparing 'beam-to-beam' velocities, in particular for the wave component, where substantial discrepancies are seen between field and model spectra when comparing for ENU velocities. This comes as a result of the assumption used in the DCP processing methodology that the flow is homogeneous, when over short time-scales and for certain frequencies it is not. This is particularly notable across the frequency range occupied by waves, as seen in the in the left-hand plot of figure 7.3 where the discrepancy in the field and model wave spectra is clear for longitudinal velocities. This is further discussed in chapter 6. As intended, the development of the 'Virtual' DCP negates the necessity to compare two sets of measurements that are not, in fact, directly comparable.

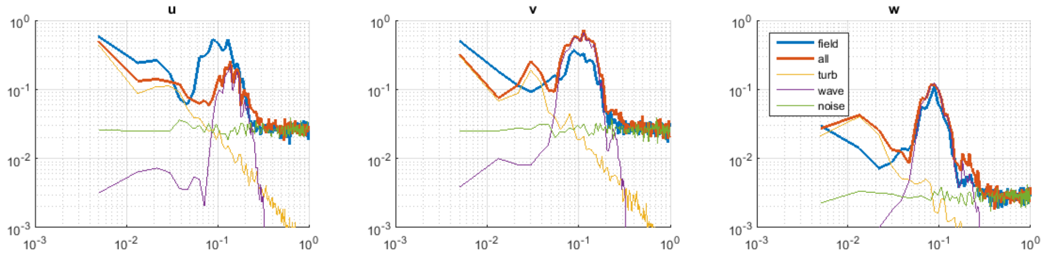

Figure 7.3: Example model velocity spectra, during $2 < H_s < 2.5m$ and $2 < \overline{u} < 2.5ms^{-1}$, where waves are *following* the current direction, broken down into wave, turbulence and noise and compared to field velocity spectra for all ENU velocities averaged over 10 similar wave-current instances.

In the remainder of this study, only beam 1 velocities are compared. This allows for direct comparison of velocities measured in that particular beam direction in the field and by the VDCP in the model. Equally, any other beam could be used. Data is normalised around the peak field spectral density and plotted as in Figure 7.4, where the 3 methods for wave input to the model are compared. To recap: the 'multi' wave input mode takes a multi-directional spectrum measured using all 5 beams of the DCP. The 'omni' wave input mode takes an omni-directional (i.e. 1D) spectrum measured by the vertical beam of the DCP and the wave direction determined from the multi-directional spectrum. The 'model' wave input mode calculates a Bretschneider spectrum based on measures of H_s and T_p calculated from the omni-directional spectrum, and modifies it according to one of the methods outlined in section 5.1 according to current speed and relative wave-current direction.

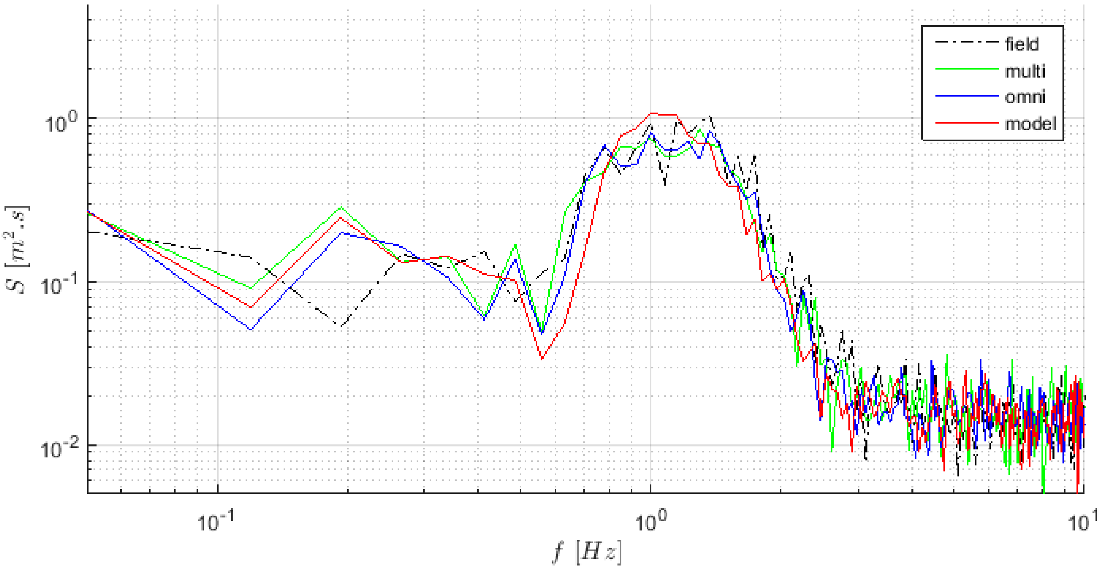

Figure 7.4: Field and model, normalised, averaged, along beam (1) velocity spectra for $2 < H_s < 2.5m$ and $2 < \overline{u}2.5ms^{-1}$ instances, where waves are *following* the current direction, using three different wave model inputs

7.1 Calibration of wave-current module

As seen in figure 7.4 good agreement is seen between field and model spectra across the whole frequency range, for all wave input modes, at the chosen, example wave-current bin. The three overarching wave input modes are now studied in greater detail across a broader range of conditions. Velocity spectra are compared across a range of wave heights and current speeds at approximate tidal turbine hub height. Figure **??** shows tide in flood (i.e. following waves) and Figure **??** in ebb (i.e. opposing waves).

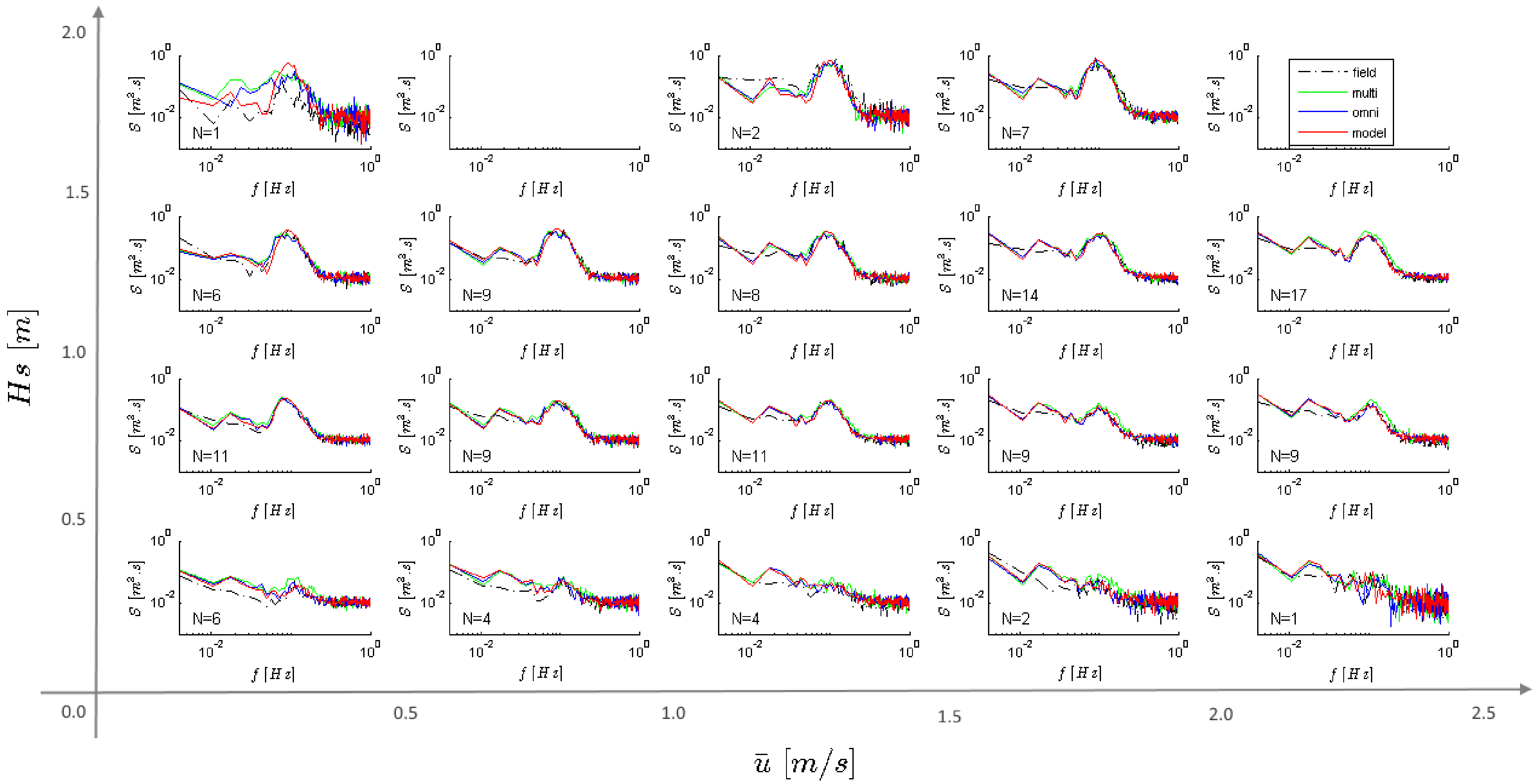

Figure 7.5: Field and model, averaged, along beam (1) velocity spectra for full range of wave-current instances, where waves are *following* the current direction. N indicates number of ten-minute instances of wave-current bin.

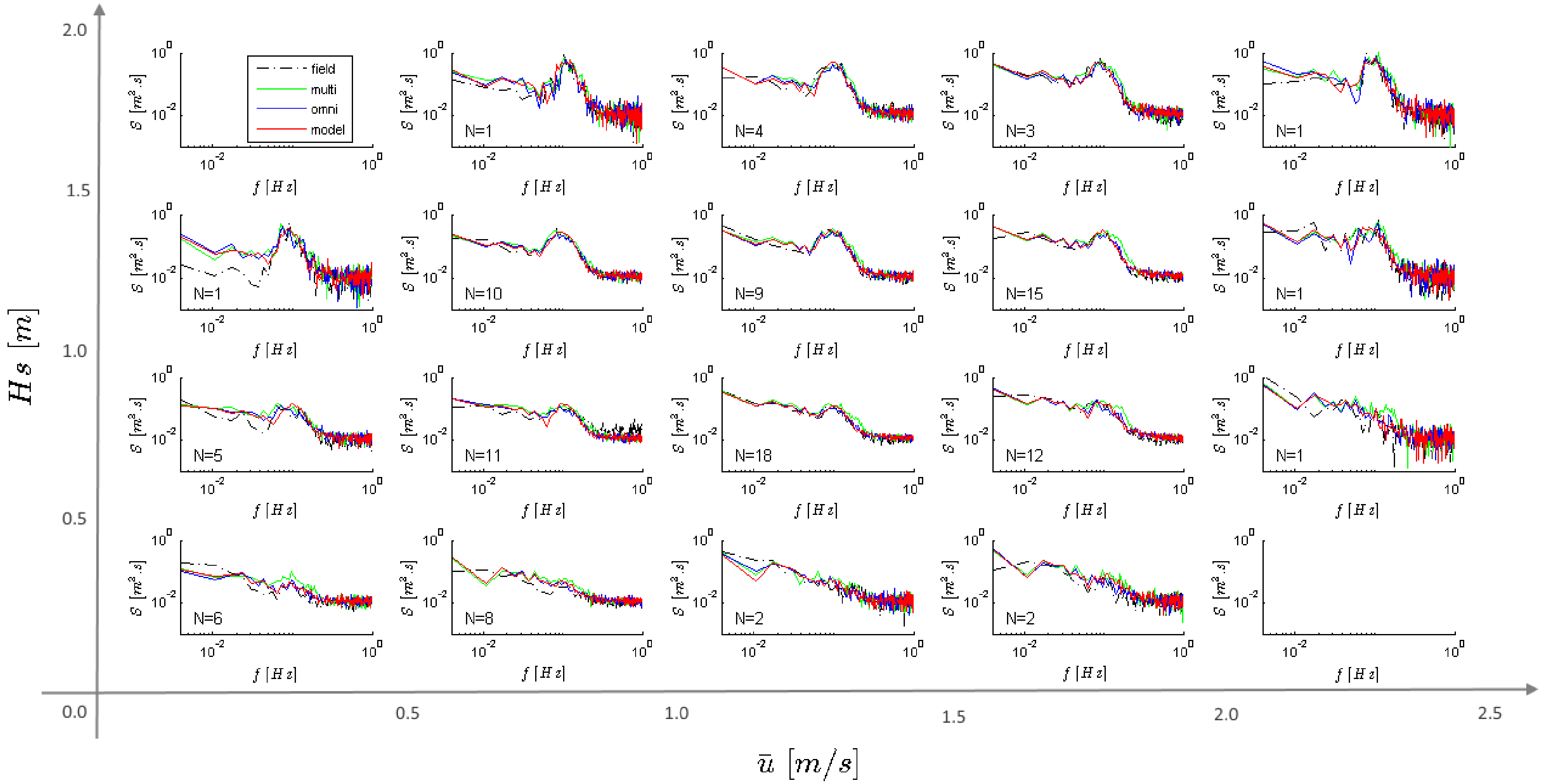

Figure 7.6: Field and model, averaged, along beam (1) velocity spectra for full range of wave-current instances, where waves are *opposing* the current direction. N indicates number of ten-minute instances of wave-current bin.

The following subsections closer identify the attributes, advantages and disadvantages of the three model wave input modes.

7.1.1 Multi-directional wave input mode

The multi-directional wave input mode uses field data from all 5 of the DCP beams to estimate a spectrum for each ten-minute instance of surface elevation, which is then input as the wave component of the model. Particularly in the ebb case (7.6, the energy in the low frequency end of the spectra, where turbulent effects dominate, is subject to some discrepancy, thought to be largely caused by the variability in turbulence measurement for a relatively small sample size, as discussed in section 4.3. In both flood and ebb the multi-directional wave input mode, as discussed in section 4.2 (Figure 4.9), tends to over predict energy in the spectrum above 0.2Hz. Due to the over prediction in the higher frequencies of the wave spectrum seen in figures 7.5 and 7.6 analysis is continued using the omni-directional wave input mode.

7.1.2 Omni-directional wave input mode

The omni-directional wave input mode uses field data from the single vertical beam of the DCP to estimate a spectrum for every ten-minute instance of field data which can be input as the wave component of the model. All input modes require a wave number calculation in determining wave subsurface velocities from sea surface elevation. For this, two choices are available from the model: a relative wave number, i.e. that which is seen by an observer moving with the current (thus not subject to current), or an absolute wave number, i.e. that seen by a stationary observer (hence modification for current as described in chapter 5). The effect on the velocity spectra of the incorporation of current into the dispersion relation calculation is seen in figure 7.7 using an 'omni' input for one specific wave-current bin. There is only a very slight modification to spectra through the change in methods. Tested over a full range of instances little difference is found in the model when applying a dispersion relation affected by current, however towards the higher end of the wave frequency range, the absolute wave number method performs slightly better (as seen in figure 7.7)and as such further modelling is conducted using this wave number calculation, taking currents into account.

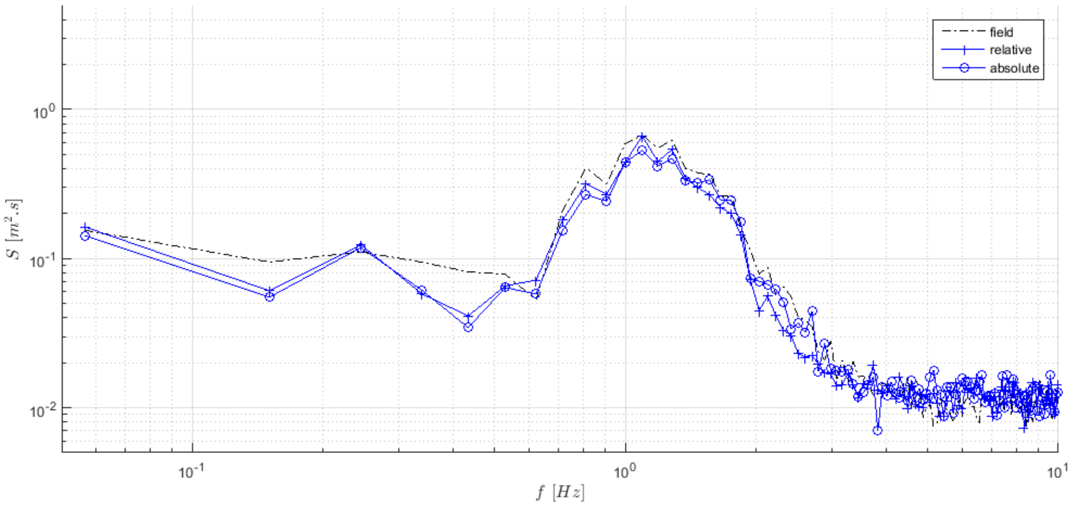

Figure 7.7: Field and model, normalised, averaged, along beam velocity spectra for $2 < H_s < 2.5m$ and $2 < \overline{u} < 2.5ms^{-1}$ instances, where waves are *following* the current direction, using two different methods for calculating the wave number, with a measured, omni-directional wave model input

Using the omni-directional wave input to the model, velocity spectra are again compared at approximate tidal turbine hub height of 10m below the water surface over a range of wave-current conditions. Figure **??** shows tide in flood (i.e. following waves) and Figure 7.6 in ebb (i.e. opposing waves). Over the frequencies through which waves dominate the spectral agreement is very good across all wave heights and current speeds in both following and opposing cases.

7.1.3 Model wave input mode

Often surface elevation records will not be available and wave spectral parameters will be estimated using pressure and velocity records as described in section 3.2.1. These parameters can be corrected if necessary according to the errors determined in chapter 6. Alternatively wave statistics from wave buoys could be used. These parameters are used to simulate a model wave spectra using spectral shapes defined in section 2.1. The one dimensional model spectra can be modified for current according to one of two methods; Huang or Hedges, as discussed in section 5.1. The effect of these modification methods can be seen in figure 7.8. Tested over a full range of instances no modification to the shape of the wave spectrum (i.e. 'none') is found to produce the best agreement with field data, and as such further modelling is conducted with no modification. To further exemplify, the same wave-current bin, but for waves opposing currents, is given in figure 7.9

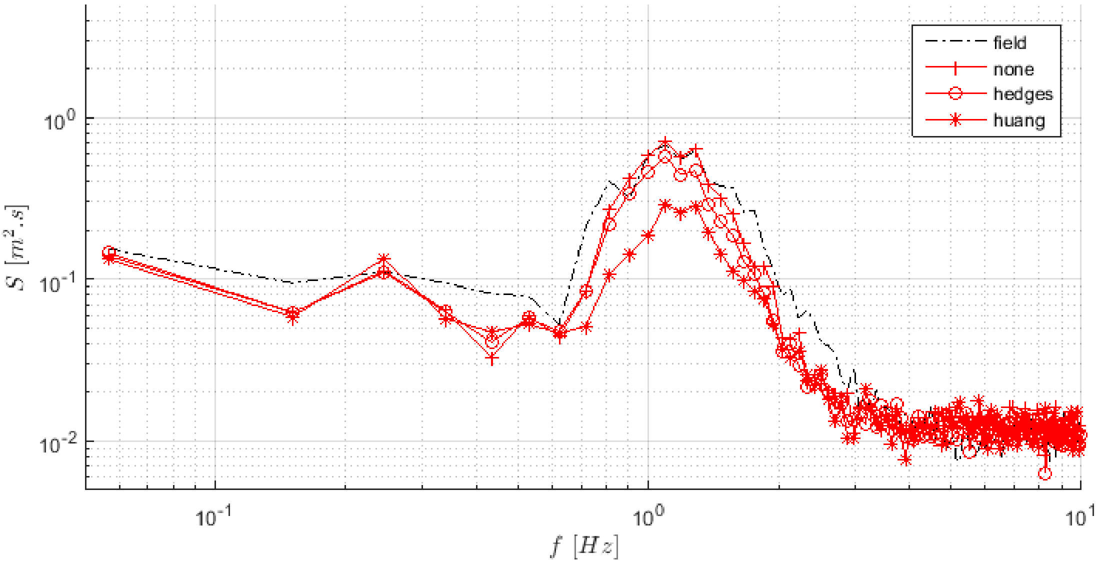

Figure 7.8: Field and model, normalised, averaged, along beam (1) velocity spectra for $2 < H_s < 2.5m$ and $2 < \overline{u} < 2.5ms^{-1}$ instances, where waves are *following* the current direction, using two different methods for modifying the wave spectrum for currents

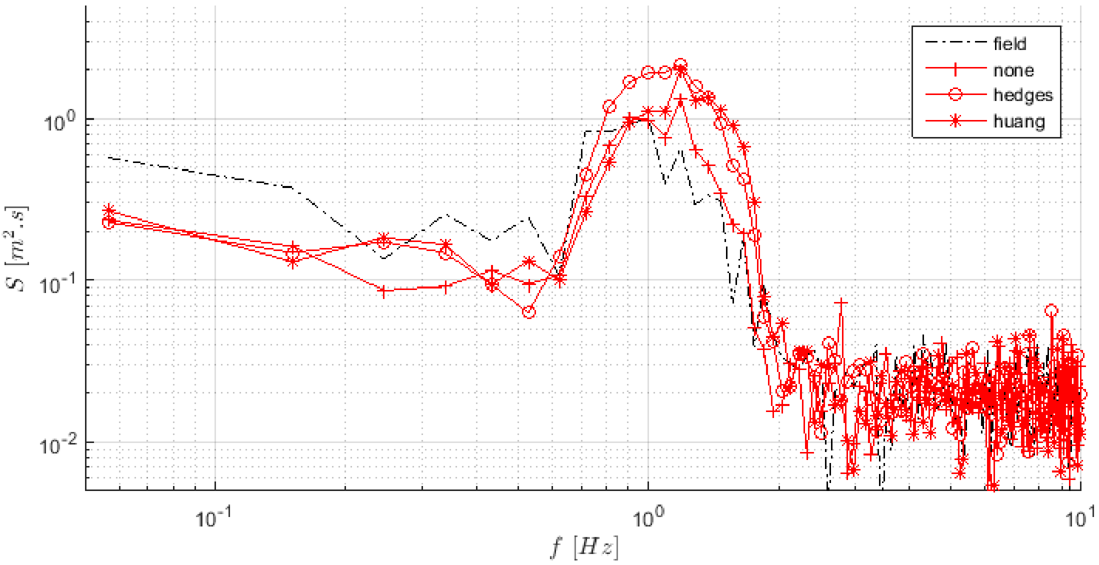

Figure 7.9: Field and model, normalised, averaged, along beam (1) velocity spectra for $2 < H_s < 2.5m$ and $2 < \overline{u} < 2.5ms^{-1}$ instances, where waves are *opposing* the current direction, using two different methods for modifying the wave spectrum for currents

Using the model wave input to the model, velocity spectra are compared at approximate tidal turbine hub height. Figure 7.5 shows tide in flood (i.e. following waves) and Figure 7.6 in ebb (i.e. opposing waves). Over the frequencies through which waves dominate the spectral agreement is very good across all wave heights and current speeds in both following and opposing cases.

7.2 Validation of model over a range of depths

Thus far only one depth has been investigated. The depth used was ten meters below the sea surface, a location likely to be occupied by a tidal turbine on a floating structure aiming to maximise the potential of a profiled tidal current. However it is useful to understand the effectiveness of the model at predicting velocities over a larger range of depths. High resolution, simultaneous surface elevation and subsurface velocity records are available for the top twenty meters of the water column. Taking one wave-current bin as an example, the effect of depth on the accuracy of model velocity outputs is investigated. Agreement is comparative across a range of depths, as shown in Figure 7.10, though the model spectra tend to be narrower than the field spectra.

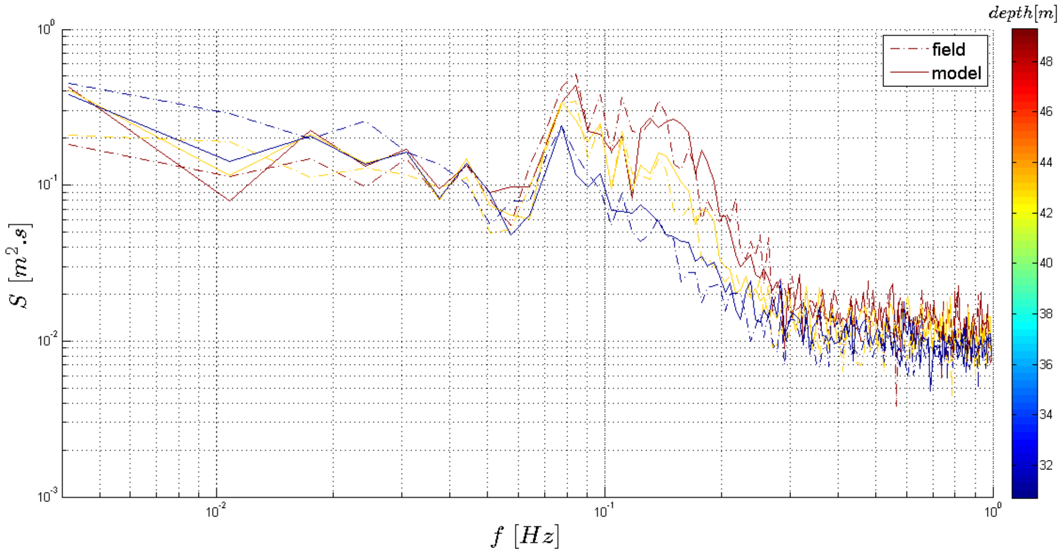

Figure 7.10: Field vs model along beam (1) velocity spectra across a range of depths, for $1 < H_s < 1.5m$ and $1 < \overline{u} < 1.5ms^{-1}$ instances, where waves are following the current direction, using omni wave input.

To explore the effectiveness of the models representation of field velocities, at a range of depths, for varying wave and current conditions, a number of parameters are used as metrics to compare field with model velocities. Firstly standard deviations (normalised) are compared, in Figure 7.11, for following and opposing wave-current cases, for a full range of depths and wave-current instances. Reasonable agreement in standard deviation is seen for all instances, though towards the seabed the model tends to under-predict fluctuations in subsurface velocity and towards the sea surface the model marginally over-predicts fluctuations in subsurface velocity. The regression fit for all wave current cases slopes at just under one, (between 0.84 and 0.99) for all wave-current cases. In both following and opposing cases the model agrees similarly with field velocities. The regression suggests that the model replicates field velocities over a range of conditions, however where standard deviations in field velocity are particularly high, the model underestimates this.

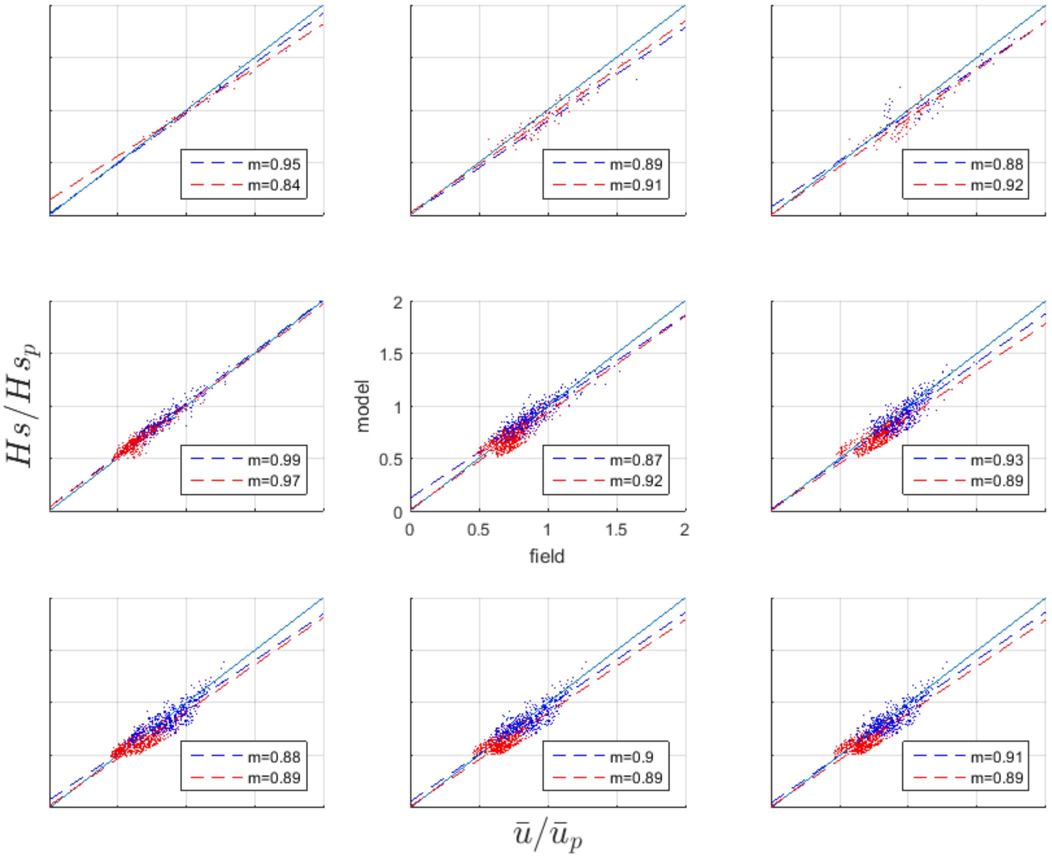

Figure 7.11: Field (x-axis) vs model (y-axis), **standard deviations** of along beam (1) velocity spectra for full range of wave-current instances, over a range of depths, where waves are following (blue) and opposing (red)the current direction, using omni wave spectra input. All sub-plot axes are identical to the central subplot, significant wave height ranges from 0 to 1 times the peak significant wave height and mean current speed ranges from 0 to 1 of the peak mean current speed. m indicates the slope of the regression line.

Velocity maxima are useful in understanding the ultimate loads on a tidal turbine. A similar trend is seen in comparisons of model and field absolute maxima as seen in figure 7.12, however there is larger variability and scatter in these results

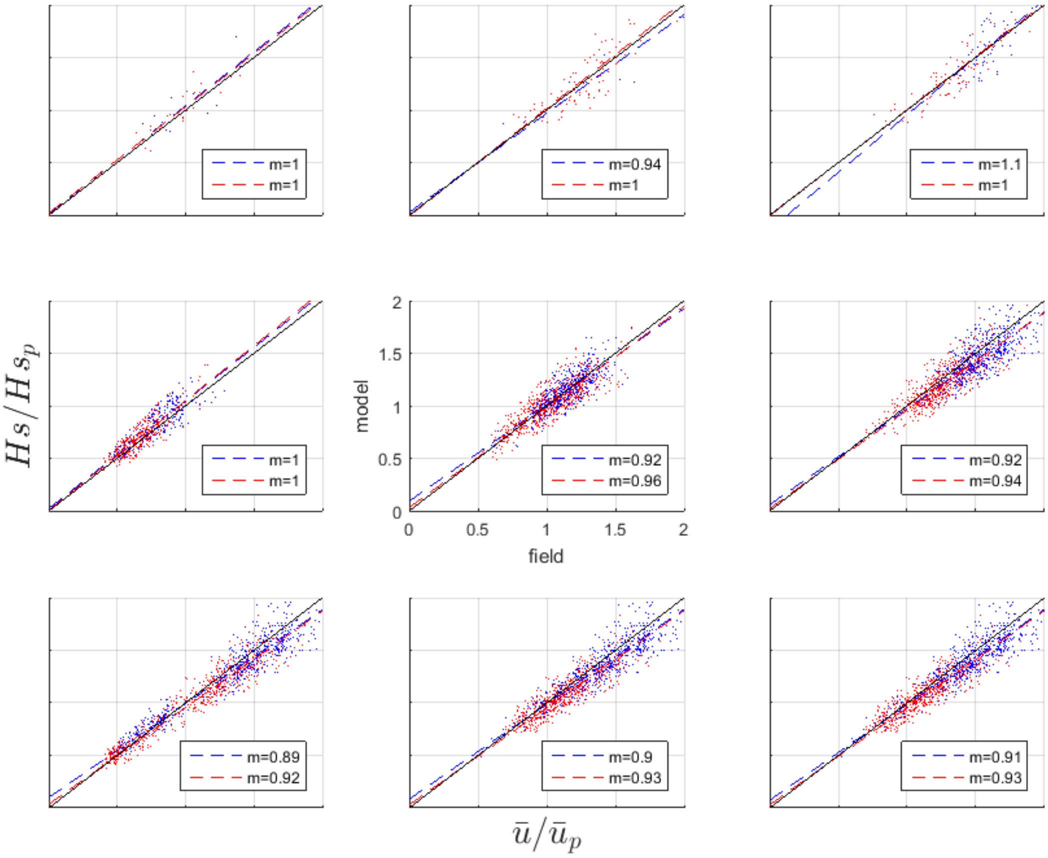

Figure 7.12: Field (x-axis) vs model (y-axis), **maxima** of along beam (1) velocity spectra for full range of wave-current instances, over a range of depths, where waves are following (blue) and opposing (red)the current direction, using omni wave spectra input. All subplot axes are identical to the central subplot, significant wave height ranges from 0 to 1 times the peak significant wave height and mean current speed ranges from 0 to 1 of the peak mean current speed. m indicates the slope of the regression line.

Plots of the zeroth spectral moment (i.e the area under the velocity spectrum) are shown in figure 7.13. Spectral moments are taken over the wave frequency range only, indicating that the models underestimation of standard deviations and maxima is a result of under prediction of the wave spectra by the model.

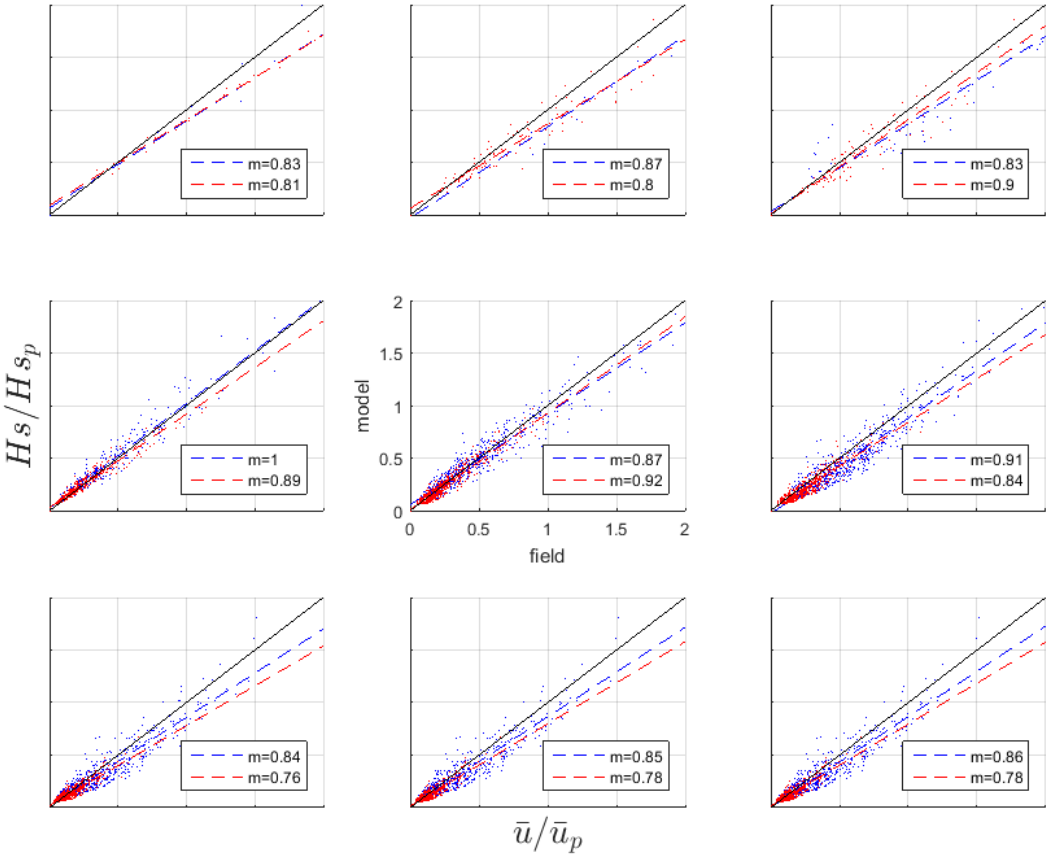

Figure 7.13: Field (x-axis) vs model (y-axis), **zeroth spectral moment** of along beam (1) velocity spectra for full range of wave-current instances, over a range of depths, where waves are following (blue) and opposing (red)the current direction, using omni wave spectra input. All subplot axes are identical to the central subplot, significant wave height ranges from 0 to 1 times the peak significant wave height and mean current speed ranges from 0 to 1 of the peak mean current speed. m indicates the slope of the regression line.

It is seen that much of the discrepancy between model and field velocity standard deviations is in the top ten meters of the water column. It is in this region that larger errors caused by acoustic interference are often found in the field data due to the large distance from the instrument transducer/receiver. This interference is, however, not modelled by the VDCP and this may be one cause for the small mismatch between field and model velocities, demonstrated by standard deviation, maximum and moment metrics.

7.2.1 Damage equivalent velocity

To demonstrate the usefulness of the model for estimation of fatigue on tidal turbines damage equivalent velocity (DEV) is used. DEV is a metric calculated using the rainflow method. The rainflow method is normally applied in the analysis of fatigue loads, reducing a spectrum of varying stress to a set of simple stress reversals. Typically a stress time history is generated from a load time history and fatigue analysis is based upon cycle count data. The cycle counting procedure is presented in Downing & Socie (1982). This calculation can also be extended to generate damage equivalent loads. One or more inverse S-N slopes m are specified and a frequency f, such that an equivalent load can be calculated. The equivalent load is the peak-to-peak amplitude (i.e. the range) of a sinusoidal load of constant frequency f which would produce the same fatigue damage as the original signal.

The equivalent load is therefore given by:

$$DEL = \left(\frac{\sum_i n_i S_i^m}{Tf} \right)^{\frac{1}{m}} \tag{7.1}$$

where n_i is the number of cycles in load range S_i, and T is the duration of the original time history. In this case an S-N slope of 1 is assumed in order to calculate the damage equivalent velocity from rainflow cycle counting of each along beam velocity time history. The DEV during waves following and opposing currents is plotted to compare field and model data in figure 7.14, using the omni wave input. Model DEV compares well with field DEV over a range of depths, current speeds and wave heights in both flood and ebb, implying that the velocities simulated by the model would suitably represent the velocities measured at the site for the purpose of understanding the fatigue loads on a tidal turbine.

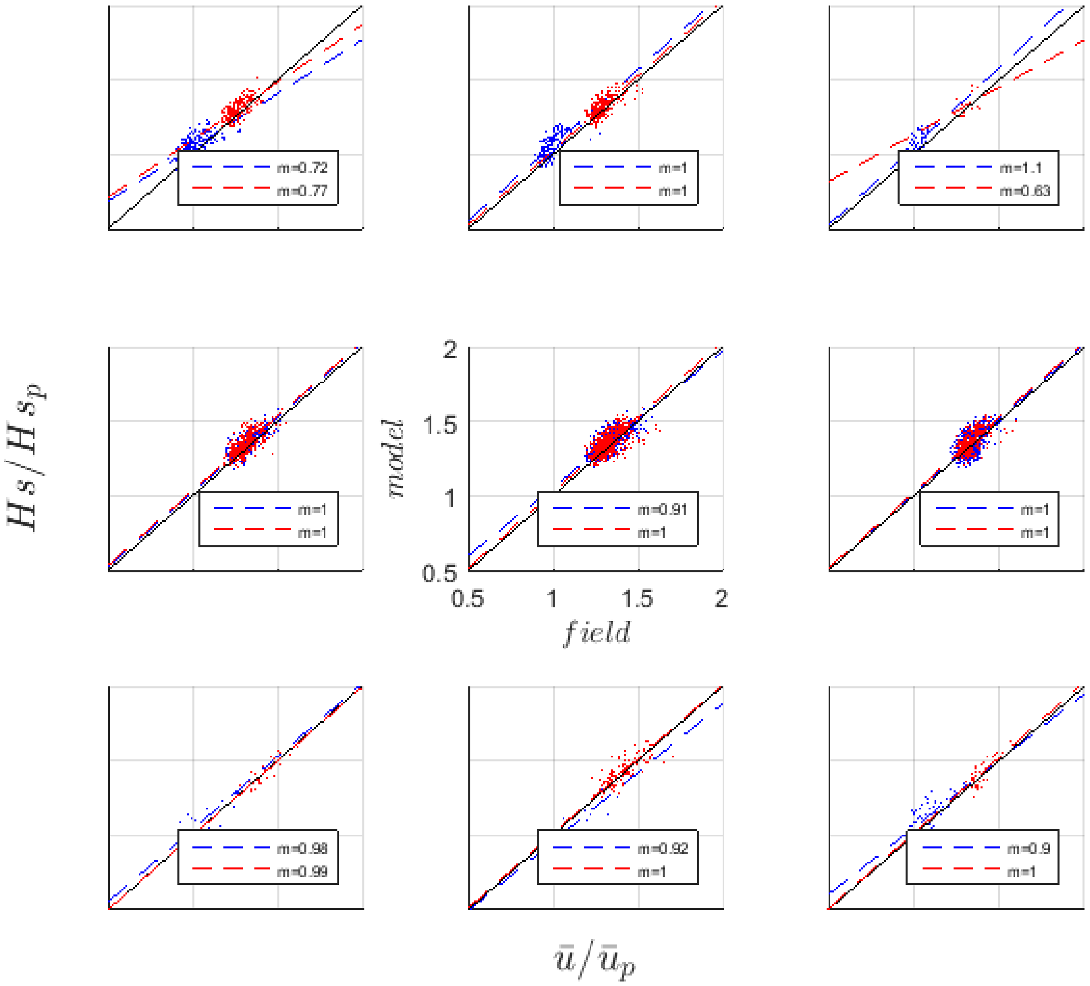

Figure 7.14: Field (x-axis) vs model (y-axis), **damage equivalent velocities** of along beam (1) velocity spectra for full range of wave-current instances, over a range of depths, where waves are following (blue) and opposing (red) the current direction, using omni wave input.

7.3 Discussion

Use of the Virtual Doppler current Profiler method has enabled 'like for like' comparisons of along beam field and model velocities. Comparisons of along beam field and model velocity spectra, as well as standard deviations, maxima, spectral moments and damage equivalent velocity, demonstrate that the model can closely simulate field velocities over a range of depths, for a broad range of wave and current conditions.

The VDCP also allowed, as discussed in chapter 6, correction to model inputs for DCP error in turbulence intensities. Turbulence model input parameters (intensity and length scale) are calculated from ENU velocities resolved by the field DCP and then corrected for DCP error, according to the methods discussed in chapter 6, before being fed to the tidal flow model. As seen at the lower frequency end of velocity spectra there is often some discrepancy between field and modelled data. This is largely a result of uncertainty in the field measurements of turbulence, and the variability of conditions effecting turbulence parameters, for a relatively small sample size, that cannot be fully accounted for by the VDCP error correction method. This is particularly noted during ebb tide. During the ebb tide, whilst turbulence length scales are similar to those measured during the flood tide, turbulence intensities deviate significantly more from the mean. This may be a result of bathymetric differences and the passage of flow leading up to the measurement area, or alternatively it may be as a result of waves, not only interfering with measurements but interacting with the turbulence itself. This is a subject which could be researched in much greater detail (see Clark et al. (2015)) however has not been the focus of this study.

The wave-current aspect of the model was calibrated against field data. Firstly three overarching methods for the input of waves to the model were applied: the first using the measured, ten-minute, multi-directional surface elevation spectrum, the second using the measured, ten-minute, omni directional surface elevation spectrum, and the third using a model Bretschneider surface elevation spectrum with measured inputs of significant wave height, mean period and mean directions. All three methods can reasonably replicate field subsurface velocities at a range of depths. The first method tends to over-predict the wave induced spectrum of velocity, whilst the second two methods perform better, only slightly under-predicting wave spectra close to the surface. This has been determined through visual inspection of velocity spectra and quantified with the use of time-series and spectral metrics. The discrepancy close to the surface is not affected by current speed, and is thought to be a result of measurement error in the three-dimensional surface elevation estimation. This is likely to be caused by increased distance from transducer/receivers, angle of beams to the surface and subsequent interference, when using divergent beam records. Scatter in velocity maxima will require further investigation. Comparisons of damage equivalent velocity, agree well, indicating that the model is suitable for representing field velocities when modelling the fatigue loads that could effect a tidal turbine. All methods are subject to two options in the calculation of the dispersion equation; one taking currents into account and the other in the absence of currents. It is expected that the former would reproduce the most accurate representation when applying linear theory to infer subsurface velocities from the surface elevation spectrum, however whilst this is true, it has been shown that the difference is negligible, across the range of wave-current instances compared, and accurate results can be attained whilst using the simpler version of the dispersion equation where currents are not accounted for. The third wave input method, where a Bretschneider model spectrum is applied, has two options for modifying the shape of the surface elevation spectrum to account for current magnitude and direction: a method developed by Hedges, and a method by Huang. Alternatively the spectrum is not modified.

It is the third option that consistently produces the best representation of subsurface velocities when comparing to field data taken at this site. Modifications are made to the surface Bretschneider model spectrum generated using wave statistics H_s and T_m taken from the field data. It is worth considering that these measured waves have already been affected by currents and as such modification of the spectrum generated according to these previously may not be appropriate unless it is applied to a wave data set previously unaffected by currents. It was however considered that whilst the measured surface elevation may indeed have been modified by current, the subsurface velocities might continue to act as if unaffected by current. As such the reverse of the Hedges and Huang methods was tested, whereby the measured spectrum was converted to its 'original' form and subsurface velocities subsequently derived. The result was that this hypothesis was not true and that those velocities derived from the measured surface elevation spectrum (unmodified for currents) again provided the best agreement with field data.

Chapter 8

Conclusions

For the first time a novel 'Virtual' Doppler Current Profiler has been developed and successfully implemented to quantify errors in field measurements, and to validate a numerical model aiming to replicate tidal flow kinematics, incorporating wave-current interactions. This new software tool, presented in Ocean Engineering (Crossley et al. 2017), samples from a simulated flow field as if it were a physical instrument mounted on the sea bed, and has proved itself extremely versatile in both quantifying measurement uncertainty and in the validation of a numerical model incorporating waves, currents, and turbulence. Respectively there are two major conclusions to this work; the first, that linear wave-current interaction provides a good representation of the kinematics at the tidal site in question, from zero to twenty meters below the sea surface, and the second, that large errors in wave orbital velocities, turbulence intensities and turbulence length scales are recorded by DCPs in normal operation dependent on set-up and environmental conditions.

8.1 Quantifying measurement uncertainty

Chapter 6 explains the methodology behind the VDCP and, by sampling idealised model flow conditions, demonstrates the limitations of Acoustic Doppler technology in accurately recording the subsurface velocity characteristics of waves and turbulence. These characteristics are typically frequency dependent statistics such as significant wave height and mean period, as well as turbulence intensity and length-scale. Instruments are designed to measure mean current velocities, assuming homogeneity across the volume separating acoustic beams, and therefore whilst mean current velocities are consistently well estimated, some of the details of wave and turbulence kinematics are obscured. Results show that longitudinal and vertical velocity characteristics of waves and turbulence, resolved from the along beam measurements of DCPs, are typically inaccurate representations of these components of the flow. Longitudinal measurements are typically worse as a result of having fewer beams to average over during estimation and due to the beams' relatively large angle to the horizontal. When a wave, or wave component of a specific frequency, is out of phase at the two sampling depths on an upstream and downstream beam, longitudinal velocity measurement error regularly exceeds 100%. Accuracy of wave orbital velocity records are therefore dependent on DCP sampling depth and orientation, as well as wave, current and turbulence variables. Turbulence measurements by the VDCP are also phase dependent, and accurate recording of turbulence is heavily influenced by the presence of waves.

The VDCP is used to establish theoretical accuracy of wave and turbulence measures, so that for a specific set of field conditions, the uncertainty in measured parameters can be quantified and subsequently modified for site characterisation purposes and to improve inputs to tidal flow models. Spectral moments taken over a range of wave specific frequencies give VDCP sampled longitudinal wave orbital velocities up to 9 times greater than those sampled at a point and vertical wave orbital velocities of as low as 0.1 times, for a range of turbulence intensities and current speeds. VDCP sampled longitudinal turbulence intensity estimates vary between 0.5 and 1.5 times the input turbulence intensity dependent on wave height and period conditions whilst vertical turbulence intensity varies between 0.2 and 0.8. Length scales calculated using the autocorrelation function of frequency spectra taken from VDCP measurements vary, in the longitudinal component, between 0.1 and 1.5 times the inputted value, and for the vertical component up to 10 times. These results are idealised and can vary significantly for the vast range of environmental and configuration conditions that may occur, and hence use of other measurement techniques, including convergent acoustic beams, could significantly enhance characterisation, and also the method developed here. However, where some of these conditions are known substantial improvements can be made when attempting to estimate input characteristics to flow models combining waves and turbulent currents. The method therefore enables fair comparison when validating a wave-current model against field measurements, in order that the loads on, and the performance of, tidal turbines can be determined with improved confidence.

8.2 Calibrating and validating the tidal flow model

The model developed for this study aims to replicate tidal flow kinematics, focusing on the development of the interaction between waves and currents. The model aims to replicate, in particular, the velocities at a typical tidal turbine hub height, when waves and tidal currents of varying respective shape and speed, are present. The numerical model was built based on previously developed theory and newly incorporates numerous options for simulating wave-current interactions. This model required validating, and, as concluded in chapter 6, ENU velocities resolved from the divergent beams of a DCP are subject to error, particularly during conditions where waves are present at the site. To avoid this, direct measurements from the field were used. These measurements were of velocities in the direction of the divergent DCP 'beams' and therefore not in a typical coordinate system. This is where the VDCP again proves its usefulness, sampling the model flow field as if it were the DCP at the site. Taking into account its orientation and set-up parameters, along beam velocities measured by a DCP in the field could be compared with modelled along beam velocities measured by a VDCP. The method enables circumvention of the assumptions used when calculating three dimensional (ENU) velocities from divergent beam Doppler instruments, and as such, allows direct comparison of field and modelled data.

As discussed, the tidal flow model contains a number of options for simulating wave-current interaction, since theory developed for this behaviour is unsubstantiated for cases of high speed currents in real sea environments. These options were calibrated against the field data to determine the best model options for this site. Wave number, and hence wave angular frequency can be calculated from the dispersion equation according to two methods; one accounting for the presence of currents, as if from the perspective of an stationary observer (absolute), and one without, as if from the perspective of an observer moving at the speed of the current (relative). Whilst small improvements were noted in the shape of the wave spectra for certain wave-current instances when using an absolute method, the difference between using this method versus using the relative method is considered to be negligible across the whole range of wave-current conditions present in the data. Hedges and Huang methods for modifying spectral shape for the presence of currents were ineffectual in improving agreement with field data. This is largely due to the consideration that measurements used to inform the generation of a model wave spectra have already been affected by current in the field, and therefore modifications to the spectra would only be appropriate should a wave set have been measured on quiescent water before adding a current.

Similar comparisons will need to be conducted on other sites before true conclusions can be drawn on the validity of this calibration, as these may be the result of site specific behaviours that may not be common to all tidal sites affected by waves. Non-linear effects were excluded from this work and this assumption has been proved suitable, however for conditions such as increased wave heights or oblique wave-current incidence angles, this assumption may become less valid. Furthermore this study has only been conducted over a range of depths in the uppermost 20m of the water column, since this data was available with simultaneous high frequency vertical beam surface tracking ('waves' mode).

Results of the model validation using the VDCP show that the model is effective in simulating field subsurface velocities over a range of depths, for waves of up to $3m$ significant wave height and following and opposing currents of up to $3.5ms^{-1}$. Field and model velocity spectra compare very well over the frequency range dominated by waves. At the low frequency end of the spectra, where large turbulent eddies dominate there is some deviation in model accuracy, particularly during the ebb tide where recorded turbulence parameters are extremely variable. In comparing model and field velocity time-series over a greater range of depths, surrounding typical hub height, a number of parameters are used. Maxima, standard deviations and spectral moments are often under predicted close to the sea surface, largely over the wave dominated frequencies. This may be a result of increased interference and DCP error in field records close to the sea surface, due to increased distance from the transducer-receivers. Though noise is simulated by the VDCP model other interference phenomena are not currently incorporated. Model-field comparisons of maxima, which are a useful representative for ultimate loads on a tidal turbine, are quite scattered indicating some uncertainty when undertaking this type of loads analysis, with the potential for over, and under-estimation of modelled ultimate loads. Damage equivalent velocities, however, all agree well, demonstrating the validity of a linear wave current model for prediction of fatigue loads at tidal sites impacted by waves.

Wave directions within 30 degrees of following and opposing current directions are used in the analysis and the effect of any difference in incidence angle is accounted for in the dispersion equation as described in chapter5. Investigating a selection of instances of varying wave-current incidence angle demonstrates that the method functions well, however further study of oblique wave-current incidence angles would be useful.

8.3 Contribution to industry

The tools developed during this study, in particular the VDCP, can be reconstructed based on this thesis, and will also be available to DNV GL as a part of the companies suite of tools. The VDCP will be used in further validation studies much like that conducted in this work and also in further site characterisation studies. The tool is also useful in estimating DCP velocity and surface elevation measurement errors during site characterisation, and also in determining directional surface elevation spectra. The wave-current module of the tidal flow model will also be available for the development of company software. A number of other software tools have also been developed for use in the processing of field data. These include the extraction of binary data from DCP storage, the processing of this data into useful velocity and surface elevation data, as well as quality checking and analysis algorithms.

Using the VDCP method will enable prospectors, developers, designers, oceanographers and the marine sector as a whole to better understand the environment which a DCP measures. Improved accuracy of these measurements will enable better knowledge of subsurface kinematics and processes, and hence more informed design and location of tidal turbines. The module of the model that has been calibrated and validated, and the theory upon which it was based, can be used to confidently simulate tidal flows at sea aiding in the design of turbines and other devices for a broad range of conditions.

8.4 Further work & recommendations to the industry

This body of work leaves scope for a number of future studies, that, using the methodology developed here, could helpfully inform the tidal energy industry as well as the broader maritime sector. Based on the comparisons between field and model subsurface velocities presented in this work the interaction between waves and currents is deemed insignificant with linear superposition of wave and turbulent current velocities proving to be a suitable representation of those velocities occurring at the particular site investigated. Calculation of an absolute wavenumber (i.e. wave frequency seen by a stationary observer) does however make marginal improvements to model agreement with field velocities. Care should be taken in interpreting this result, given that it is based on just a small volume of data from a specific site, and comparison of the model with other tidal sites affected by waves will need to be undertaken.

More data of good quality needs to be measured at tidal sites. In comparison with, for example, the wind energy industry, a tiny amount of data is available for tidal site conditions. Wind measurements are ubiquitous, not only for wind energy, but for meteorology, aviation and many other applications, and as such a huge amount of information is available with which to validate simulations of wind. Tidal flow measurements are limited to very few, short data sets, using instruments that, whilst effective in measuring certain aspects of the flow, are deficient in other areas. Big efforts have been made in the UK and globally to increase the volume of good quality data available for analysis and it is important that this work continues. Data sets can be analysed using the techniques developed in this thesis for further validation and calibration of tidal flow models. A greater volume of data will be beneficial to site characterisation of all flow components, not least turbulence, which despite the improvements to the measurement process aided by the VDCP, was still subject to considerable scatter in measures of turbulence intensity and length scale, which are still subject to some uncertainty, making comparison between field and model data difficult. This is a problem directly related to the randomness of turbulence, however steps could be made to reduce these limitations simply by increasing the quantity of data recorded, both by increasing recording frequency and lengthening survey time. It would be possible to conduct further analysis at greater depth and over a greater number of instances, with the other part of this same data set ('currents' mode), subject to limitations of low frequency surface tracking as well as larger depth bin sizes and subsequently lower resolution. Whilst these limitations are present, this study would provide useful insight into the attenuation of waves at greater depths for a range of current speeds.

Several other studies could further this work. One is the study of the interaction between waves and turbulence. The methodology used in this work leaves scope for undertaking this kind of study with the potential to separate and characterise components of the flow. As discussed previously this may require larger samples of data. Another useful study would look at the change of spectral shape as waves move from still water onto a current. Several theories have been developed however have not been validated for fast moving currents at tidal sites. Additionally, whilst the VDCP was foremost intended for the sampling of simulated subsurface velocities, it also incorporates surface tracking, such that a better understanding of DCP capabilities in measurement of the sea surface can be understood. This functionality is still undergoing testing and improvements.

Appendix A

Appendix 1

A review of literature shows the convergence of a large amount of work in tank testing, with relatively minor discrepancies. Part of this study analyses reasons for this disparity and areas for further work. Computational Fluid Dynamic (CFD) methods are briefly discussed, but whilst these methods are useful for comparison, they can be computationally prohibitive for the timescales and detail required for commercial projects. Designers of turbines require low computational approaches for assessing dynamic blade loads in a range of environmental conditions.

Wave theory is well defined in a number of well-established texts (Tucker & Pitt 2001, Boccotti 2015, Holthuijsen 2007) and a good understanding of the relevant theories for regular, and irregular wind generated waves is fundamental to the basis of this research. Linear (Airy) theory is covered in detail, with some discussion of further order (Stokes) theories for more realistic wind generated waves, and the Stream function theory as developed by Dean (1965) and furthered by Dalrymple (1974). Wave particle kinematics are typically predicted by linear theory in the form:

A.1 Fourier transform method

It is often helpful to look at the measured record in the frequency domain by calculating a function of spectral density. Spectral density is usually calculated by use of a Fourier Transform. The Fourier theorem states that a continuous variable such as surface elevation η can be represented as the sum of a number of sinusoidal components with an integral number of waves over a finite time duration D.

$$\eta(t) = \frac{1}{2}a_0 + \sum_{n=1}^{\infty} a_n \cos(2\pi nt/D) + b_n sin(2\pi nt/D) \tag{A.1}$$

The Fourier transforms of η are a_n and b_n.

$$a_n = 2/D \int_{-D/2}^{+D/2} \eta(t)\cos(2\pi nt/D)dt \tag{A.2}$$

$$b_n = 2/D \int_{-D/2}^{+D/2} \eta(t)\sin(2\pi nt/D)dt \tag{A.3}$$

When the sea surface is sampled at regular intervals the sum in equation A.1 is taken to $n = D/2\Delta t$ and equations 2 and 3 are converted to sums. There is a small difference between values of a_n and b_n from those obtained from transformations of a continues variable however this difference is negligible as long as the set up procedure is such that any frequencies above $1/2\Delta t$ have negligible amplitude. The estimate of spectral density within the chosen resolution Δf is hence:

$$S(f)\Delta f = 1/2 \sum_{\Delta} f(a_n^2 + b_n^2) \tag{A.4}$$

The relationship of spectral density estimates and true spectral density is a complex subject and is discussed in a number of texts including Tucker & Pitt (2001).

Appendix B

Papers

Ocean Engineering 137 (2017) 404–416

Contents lists available at ScienceDirect

Ocean Engineering

journal homepage: www.elsevier.com/locate/oceaneng

Quantifying uncertainty in acoustic measurements of tidal flows using a 'Virtual' Doppler Current Profiler

George Crossley[a,*], Armando Alexandre[a], Steven Parkinson[a], Alexander H. Day[b], Helen C.M. Smith[c], David M. Ingram[d]

[a] DNV GL, Bristol, UK, BS2 0PS
[b] University of Strathclyde, Henry Dyer Building, 100 Montrose St, Glasgow G4 0LZ, UK
[c] University of Exeter, Penryn Campus, Treliever Road, Penryn, Cornwall TR10 9FE, UK
[d] School of Engineering, University of Edinburgh, Colin MacLaurin Road, Edinburgh EH9 3DW, UK

ARTICLE INFO

Keywords:
Wave
Current
Turbulence
Interaction
Validation
Loads

ABSTRACT

Accurate characterisation of flows at tidal sites can enable the developers of tidal stream energy projects to design and model the loads on, and the performance of, tidal energy converters. Acoustic Doppler technology is versatile in the measurement of sea conditions; however, this technology can be limited in its effectiveness at measuring the small-scale kinematic fluctuations caused by waves and turbulence. A Virtual Doppler Current Profiler (VDCP) is used to sample a simulated tidal flow to understand the limitations of this type of measurement instrument whilst recording the small timescale kinematics of waves and turbulence in tidal currents. Results demonstrate the phase dependency of velocity measurements averaged between two acoustic beams and provide a theoretical error for wave and turbulence characteristics sampled under a range of conditions. Spectral moments of the subsurface longitudinal wave orbital velocities recorded by the VDCP can be between 0.1 and 9 times those measured at a point for certain turbulent current conditions, turbulence intensity measurements may vary between 0.2 and 1.5 times the inputted value in low wave conditions and turbulence length scale calculation can also vary hugely dependent on both current and wave conditions. The continuation of this work will enable effective comparison of a linear model for tidal flow kinematics against field measurements from UK tidal site data, and subsequently validate numerical models for the testing of tidal turbines.

1. Introduction

To optimise the design of tidal stream turbines, many of which will be exposed to sea conditions, robust design procedures are required. This includes the use of validated models to represent current kinematics in the presence of waves and turbulence for pre-construction site specific load calculations. Many early prospected UK sites such as the sound of Islay, Kyle Rhea (Neill et al., 2016a), and Strangford Lough (Neill et al., 2016b) were sheltered from ocean waves however tidal sites such as the Pentland Firth, Fairhead, and St David's suffer from wave heights which may reach extremes of up to 10 m. Impacts on the velocity profile by waves could reduce the theoretical tidal resource by 10% (Lewis et al., 2014), and have a significant effect on blade loads (Barltrop and Varyani, 2006), however this theory must be validated with field measurements of subsurface velocities.

This paper will focus on the characterisation of combined wave and turbulent current conditions at tidal races using Acoustic Doppler (AD) technology. AD technology is commonly used in measurement of subsurface velocities and sea surface elevation. Upward looking devices emit sound pulses from transducers which are reflected by particles suspended in the water column returning a signal to the instrument. The signal is frequency shifted (Doppler shift) according to the velocity in the pulse direction at which the particle was travelling. By emitting pulses at high frequency and trigonometrically transforming the resultant velocities in combination with two or three other transducer records, a three-dimensional velocity time-series can be calculated. The typical assumption is that the flow is homogeneous over the volume between the instrument's transducer beams (Lu and Lueck, 1999). This is effective for measuring a range of current conditions; however, the smaller fluctuations resulting from waves and turbulence can be obscured by this method (Nystrom and Rehmann, 2007). Improved methods have been published for resolving mean current (Gilcoto et al.,

---

* Corresponding author.
E-mail addresses: george.crossley@dnvgl.com (G. Crossley), armando.alexandre@dnvgl.com (A. Alexandre), steven.parkinson@dnvgl.com (S. Parkinson), sandy.day@strath.ac.uk (A.H. Day), h.c.m.smith@exeter.ac.uk (H.C.M. Smith), david.ingram@ed.ac.uk (D.M. Ingram).

http://dx.doi.org/10.1016/j.oceaneng.2017.04.015
Received 11 January 2017; Received in revised form 31 March 2017; Accepted 14 April 2017
Available online 19 April 2017
0029-8018/ © 2017 The Authors. Published by Elsevier Ltd. This is an open access article under the CC BY-NC-ND license (http://creativecommons.org/licenses/BY-NC-ND/4.0/).

2009; Ott, 2002), turbulence (Gargett, 1994; Vermeulen et al., 2011; Wiles, Nov et al., 2006; Stacey et al., 1999; Stacey, 2003; Souza, 2010; Lohrmann, 1990; Guerra Paris and Thomson, 2017), and wave velocities (Filipot et al., 2013), however this paper focuses on using a conventional Doppler Current Profiler (DCP) configuration with the aim of improving site characterisation of wave and turbulence sub-surface velocities by understanding its limitations.

In this study a 'Virtual' DCP (VDCP) is used to mimic field measurements taken by a generic DCP. Specifically, the study aims to quantify theoretical errors in measurements affecting the design of tidal turbines. Therefore, whilst a range of depths are considered in initial studies, under focus are those wave and turbulence induced velocities at turbine hub height. Velocity time series combining the effect of currents, turbulence and waves are simulated as described in Section 2.1. The VDCP samples ten-minute velocity time series using the commonly used Janus configuration; four transducers separated by 90 degrees in the horizontal plane, each at 25 degrees from the vertical, using the method covered in more detail in Section 2.2. Sampling of combined wave, current and turbulence simulations are presented in the results in Section 3 highlighting the difficulty in separating and characterising the different components within a flow. Section 4 summarizes some of the more critical effects at turbine hub height on measures of wave and turbulence characteristics in realistic combined wave-current flows.

2. Methodology

The methodology proposed here, incorporates a Virtual Doppler Current Profiler (VDCP) which is designed to be a numerical tool that mimics the measurement technique of a real DCP, instead sampling a simulated flow field, and quantifying the theoretical limitations of DCP subsurface velocity measurements.

2.1. *Simulation of tidal flows*

For this study velocity time series are generated at 1 Hz for ten minutes. The simulated tidal flow defines a velocity time series of specified length at any desired point within a grid of specified size, considering the velocities resulting from waves (U_{wave}), currents ($U_{mean\ flow\ shear}$), and turbulence ($U_{turbulence}$):

$$U_{total} = U_{meanflowshear} + U_{wave} + U_{turbulence} \tag{2.1}$$

The wave conditions, turbulence conditions and flow shear are simulated separately and combined linearly to form a time series of velocities generated at specified frequency. The turbulence field is generated prior to running the combined model on a grid of specified width, height and cell size. Turbulence is then applied to the model by taking the velocity time series from the nearest point. Decreasing cell size increases turbulence resolution, however increases computational time. Interpolation methods to estimate turbulence velocities at the designated point were found to be largely ineffectual, improving accuracy little due to the spatial coherence of the turbulence simulated. Subsequently the optimum cell size compromising between accuracy and computer time was found to be 1 m^2.

2.1.1. *Flow shear*

A mean flow shear profile, u, at chosen depth, z, is added; calculated using the mean velocity $\bar{u}$, at reference depth, z_{ref}, according to the specified power law profile:

$$u(z) = \bar{u}(z_{ref})\left(\frac{z}{z_{ref}}\right)^{\alpha} \tag{2.2}$$

The exponent α is typically chosen to be 1/7, however a value of 0 can also be used to define a uniform current for some of the investigations described in this paper.

2.1.2. *Waves*

The irregular wave velocity field is defined using linear wave theory from a simulated omnidirectional JONSWAP (Hasselmann et al., 1973) sea surface elevation spectrum defined using significant wave height (H_s), mean period (T_m) and a peak enhancement factor of 1. The spectrum is given directionality using a cosine^{2s} directional distribution (Krogstad and Barstow, 1999) defined with power, s, equal to 1. The simulated spectrum is modified according to the strength and direction of the mean current ($\bar{u}$) with respect to the wave direction. The method takes into account current effects on the relative angular frequency and wavenumber, according to Hedges (Hedges, 1987). Therefore, if currents are included, the spectral density of the surface elevation, S_{η_M}, is modified to give the resultant spectrum, S_η, where g is acceleration due to gravity.

$$S_\eta = S_{\eta_M}\frac{\omega_a^2}{\omega_r^2}\left(\frac{1}{1 + 2\bar{u}\frac{\omega_a}{g}}\right) \tag{2.3}$$

Relative wave number, k_r and angular frequency, ω_r are calculated iteratively using the dispersion relationship according to Guo (2002), where ω_a is the absolute angular frequency, and $\bar{u}$ is the mean current velocity in the wave direction.

$$\omega_r = \omega_a - k_r\bar{u} \tag{2.4}$$

The spectrum of the stream-wise velocity and the vertical velocity are derived from the surface elevation spectrum using linear wave theory (Mackay, 2012), depending on the height of the water column, the required depth, and the wave direction relative to the current. A velocity time series is calculated using an inverse Fourier transform of the velocity amplitudes derived from the velocity spectrum with phase calculated according to wavenumber, and location.

No stretching (i.e. Wheeler (1969)) has been included to take account for changes in water particle velocities due to deformation of the sea surface. Tidal turbines will tend to avoid at least the top 5 m of the water column due to severe impact from waves. Furthermore, side-lobe interference in 'real' DCPs will render much of the data in this part of the water column unusable. It is therefore not deemed necessary within the scope of this work to account for changes due to proximity to the sea surface.

2.1.3. *Flow turbulence*

Turbulence can be included in the current field model and is synthesised, prior to running the combined flow model, numerically using the "Sandia method" for simulating 3 dimensional flows, described in Veers (1988). A turbulent time history is generated for the current field on a grid of equally spaced points in a 2D plane which spans the y and z-axes. The time history of velocities in three dimensions is generated for each of these points such that each point has correct spectral characteristics and each pair of points has the correct coherence and cross-spectral characteristics. For example, for the stream-wise component of velocity (u), the coherence (C_u) of points separated by distance (Δr) is a function of η_u which is defined using the local length-scale (L_u) and the wave number (k) calculated for a range of frequencies (f) at mean current speed ($\bar{u}$). Further detail can be found in appropriate turbulence texts (Tennekes and Lumley, 1972).

$$\eta_u = \sqrt{\left(\frac{0.747\Delta r}{2L_u}\right)^2 + (70.8\ \Delta r\ k)^2} \tag{2.5}$$

The longitudinal local length scale (L_u) is calculated using lateral and vertical components of longitudinal length scale (${}^{y}L_u$ and ${}^{z}L_u$) , as well as the lateral and vertical separation of the points (dy and dz).

$$L_u = \sqrt{\frac{({}^{y}L_u dy)^2 + ({}^{z}L_u dz)^2}{dy^2 + dz^2}} \tag{2.6}$$

$$k = \frac{2\pi f}{\bar{u}} \tag{2.7}$$

For this model the auto-spectral density is taken from a Von Karman turbulence model with inputs of mean velocity, and nine length-scale parameters. Supposing the velocity components $(p, q = u, v, w)$ of a three-dimensional turbulent current are measured at two separate points r and r' at positions (x, y, z) and (x', y', z') respectively then the Euclidean distance between the two points is defined by $d\tau$.

$$d\tau = \sqrt{(x - x')^2 + (y - y')^2 + (z - z')^2} \tag{2.8}$$

The standard deviations of the velocity signal p and q are denoted by σ_p and σ_q respectively. A generalised cross-correlation function, between the velocity component p and q at two points separated in space can be written:

$$\rho_{pq}(d\tau) = \frac{C_{pq}(d\tau)}{\sigma_p \sigma_q} \tag{2.9}$$

Where:

$$C_{pq}(\tau) = \lim_{\tau \to \infty} \frac{1}{\tau} \int_0^{\tau} p(x, y, z).\ q(x', y', z') \tag{2.10}$$

The nine turbulent length scales are then defined as follows:

$$^{x}L_p = \int_0^{\infty} \rho_{pp}(x' - x) d(x - x') \tag{2.11}$$

$$^{y}L_p = \int_0^{\infty} \rho_{pp}(y' - y) d(y - y') \tag{2.12}$$

$$^{z}L_p = \int_0^{\infty} \rho_{pp}(z' - z) d(z - z') \tag{2.13}$$

The method assumes Taylor's frozen turbulence hypothesis such that a velocity spectra can be used to describe the auto-spectral density of the current, and flow coherence is defined empirically.

The Sandia method has been used extensively to describe turbulent boundary layer flow at land sites in order to compute unsteady loads of wind turbines (von Karman, 1948). Given that tidal races are primarily boundary layer flows the same method has been applied in the characterisation of turbulence flow and prediction of unsteady loading for tidal stream turbines. The method has been applied and validated in a number of studies such as in the ReDAPT project (Parkinson and Collier, 2016) and by Milne et al. (2013) who suggest that Von Karman velocity spectra can provide an accurate representation of tidal site turbulence.

2.2. Virtual DCP

The VDCP is set up in a typical 'Janus' configuration typically used to collect current data from tidal races. The system comprises 4 beams slanted at 25 degrees to the vertical. The tidal flow model simulates velocities at the beam locations for the specified depth in the 'Earth' coordinate system which describes the easting, northing and up-down (ENU) velocities in the standard Eulerian frame of reference. The VDCP first converts the simulated velocities at the beam sampling location (u_{bi}, v_{bi}, w_{bi}) into an along beam velocity (b_i), and then (like a 'real' DCP) resolves all four along beam velocities into ENU velocities (U, V, W). Ten-minute samples of velocity time series, resolved by the VDCP, are then analysed in the frequency domain to determine wave and turbulence characteristics.

A 'real' instrument would typically emit bursts at several hundred Hertz, averaging the returned signal to several Hertz, and averaging to the specified bin depth. This reduces the intrinsic errors in along beam velocity measurements to an acceptable level, accounting for variations in acoustic return of the water. Velocities are typically then averaged over 10–15 min samples. Further processing algorithms are often used to account for error due to side-lobe interference as well as transducer ringing. These processes are not discussed further here, since the VDCP itself does not use acoustic technology, however they are discussed as the subject of, and alongside a number of other studies (Nystrom and Rehmann, 2007; Nystrom et al., 2002; Muste et al., 2004).

To cope with changes in heading, pitch and roll of the instrument the rotation matrix (RM) is applied to the three components of velocity (u, v, w) defined in the simulated flow field. The rotation matrix considers heading (H), pitch (P) and roll (R); where heading is the rotation about the z axis, pitch is the rotation about the y axis and roll is the rotation around the x axis.

$$[u \quad v \quad w] = RM^{-1}[u_0 \quad v_0 \quad w_0] \tag{2.14}$$

where:

$$RM = \begin{bmatrix} cos\,(H) & sin\,(H) & 0 \\ -\,sin\,(H) & cos\,(H) & 0 \\ 0 & 0 & 1 \end{bmatrix} \begin{bmatrix} 1 & 0 & 0 \\ 0 & cos\,(P) & -\,sin\,(P) \\ 0 & sin\,(P) & cos\,(P) \end{bmatrix} \begin{bmatrix} cos\,(R) & 0 & sin\,(R) \\ 0 & 1 & 0 \\ -\,sin\,(R) & 0 & cos\,(R) \end{bmatrix} \tag{2.15}$$

Along beam velocities, b_1, b_2, b_3 and b_4 at each specified depth are calculated, from the three components of velocity (u, v, w) at their respective grid points, according to the equations below (Teledyne, 2010); where θ_b refers to the angle of the transducer beams from the vertical. The error velocity (er) is assumed to be zero.

$$\begin{bmatrix} b_1 \\ b_2 \\ b_3 \\ b_4 \end{bmatrix} = M^{-1} \begin{bmatrix} u \\ v \\ w \\ er \end{bmatrix} \tag{2.16}$$

where:

$$M = \begin{bmatrix} a & -a & 0 & 0 \\ 0 & 0 & a & -a \\ b & b & b & b \\ c & c & -c & -c \end{bmatrix} \tag{2.17}$$

And:

$$a = \frac{1}{2sin\,(\theta_b)} \tag{2.18}$$

$$b = \frac{1}{4cos\,(\theta_b)} \tag{2.19}$$

$$c = \frac{a}{\sqrt{2}} \tag{2.20}$$

To resolve these along beam velocities back into three components of velocity (U, V, W), as if by a DCP, the reverse method is used.

$$\begin{bmatrix} U_0 \\ V_0 \\ W_0 \\ er \end{bmatrix} = M \begin{bmatrix} b_1 \\ b_2 \\ b_3 \\ b_4 \end{bmatrix} \tag{2.21}$$

$$[U \quad V \quad W] = RM\,[U_0 \quad V_0 \quad W_0] \tag{2.22}$$

The difference now is that there is only one set of U, V and W velocities averaged between the four beams, where before u, v and w were known at a point on each beam. Furthermore, included in this calculation is a record of error, which gives an indication of the level of homogeneity between the beam records.

3. Results

Investigations were undertaken using numerically simulated current fields accounting for combinations of waves and currents in 30 m of water. By sampling a simulated flow with the VDCP analysis is

Table 1
Sea conditions and investigation variables.

Sea condition	Variables
Regular waves	*Measurement depth* *Wave period* *VDCP Heading* *Current velocity*
Irregular waves	*Measurement depth* *Current velocity*
Turbulence	*Measurement depth*
Irregular Waves & Turbulence	*Wave height* *Turbulence intensity*

conducted on the effect of certain variables on recording accuracy of sub-surface velocities. Results are analysed in the frequency domain taking Fourier transforms of ten-minute velocity samples. Any set of environmental conditions and setup configurations can be simulated to determine the theoretical accuracy of a DCP. In this paper, a few relevant examples are given, as in Table 1, where a type of sea condition is simulated, and the effect on sampling accuracy is observed when modifying certain environmental or DCP variables.

The sub-surface velocity components of the simulated current field are sampled by depth bin in several ways:

- **Point** sampling of the velocities (u, v, w) in Earth coordinates from a point centred directly above the VDCP, cf. dashed line numbered '5' in Fig. 1.
- **VDCP** averaging of the along beam velocities resolved into (U, V, W) Earth coordinates.

The sampled velocity time-series are parametrised appropriately:

- When investigating waves, spectral moments are used. Spectral moments define the energy in, and the shape of a spectrum (within a specified frequency range), and can be used to determine parameters such as significant wave height (H_s), mean period (T_m), peak period (T_p), etc.
- When investigating turbulence, intensity and length-scale are used.

3.1. Waves

Waves of 2 m height and 5 s period are used for regular and irregular wave cases. Short period waves are chosen since one wavelength or more fits between the separation of the beams, making it easier to demonstrate the relationship between beam separation and wavelength, for a DCP of the chosen configuration. Velocities are recorded and the spectral density of each record calculated. The ratio (R_n) of the spectral moments (m_n, where n is the n^{th}order) of point sampled and VDCP averaged velocity spectra (S) are calculated to quantify the accuracy of VDCP sampling.

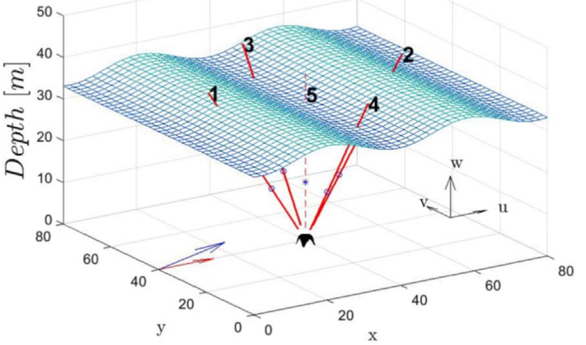

Fig. 1. Illustration of 'Virtual' DCP. Arrows indicate current (red) and wave (blue) directions. (For interpretation of the references to color in this figure legend, the reader is referred to the web version of this article.)

$$R_n = \frac{m_{nVADP}}{m_{n\,point}} \tag{3.1}$$

$$m_n = \int_0^\infty f^n S(f)df \tag{3.2}$$

In the following analysis zeroth and first order spectral moments are presented. The zeroth moment is useful to characterise the energy in the spectrum whilst the first moment better indicates the frequencies over which this energy is distributed.

3.1.1. Regular waves

Sampling of simulated regular waves presents simple test cases that allow for a better understanding of the more realistic irregular wave cases to follow. In Fig. 2 the effect of varying measurement depth is investigated. Longitudinal and vertical velocity measurement accuracy fluctuates as a function of measurement depth. The model is idealised, not considering the effect of surface deformation on velocities near the surface, as discussed in Section 2.1.2. Lack of a 'stretching' method (Wheeler, 1969) subsequently decreases the validity of those velocities taken at depths indicated by the shaded box in Fig. 2.

As a result of averaging across the distance between transducer beams a change in energy levels at particular frequencies is often noted. Fig. 3 shows that at a specified depth (−20 m), and thus beam separation, along beam velocity measurements at locations on two opposing beams are out of phase, and subsequently result in a VDCP measurement that is significantly magnified in amplitude. See Eq. (2.21).

The phase difference, $d\phi$, defines the relationship between wavelength and the longitudinal beam separation, dx, between the upstream and downstream beam (1 and 2). It is calculated using the wavenumber, k, such that $d\phi = kdx$. Beam separation is a function of height, such that $dx = 2h\tan\theta_b$, where h is the vertical distance above the DCP and θ_b is the beam angle from the vertical. Fig. 4 demonstrates the effect of phase difference on longitudinal velocity measurement accuracy, for the regular wave. VDCP measurement accuracy is good at each full phase cycle (0, 2π, etc).

The effect of varying wave period has a very similar phase relationship to that of changing the sampling depth. Fig. 5 demonstrates the effectiveness of VDCP vertical and longitudinal velocity sampling with period varying from 5 to 10 s, a likely range of periods for waves of 2 m significant wave height, given standard steepness limitations (Veritas, 2007). An optimum depth of −21 m (below the sea surface) is chosen from the 5 s period regular wave used in the previous example.

The VDCP is rotated through 90 degrees around its z axis (heading). With this change in heading comes a variance in the accuracy of VDCP sampling, as seen in Fig. 6. Vertical and longitudinal velocity sampling accuracy fluctuates as a function of longitudinal beam separation, returning to unity with each full phase cycle (2π), at 0 and 90 degrees.

Tidal currents are included according to a sheared 1/7th power law where the velocity is calculated for the specified depth from the mean current velocity ($\overline{u}$) at a reference depth (z_{ref}) using Eq. (2.2). The relative wave number and angular frequency are calculated using the mean current velocity in the wave direction, as described in Section 2.1, and are used to modify the wave spectrum as well as in the equations for linear wave kinematics. In Fig. 7a mean current velocity (z_{ref}=−15 m) increasing from 0 to 4 ms^{-1} in 0.2 ms^{-1} increments is applied in the following and opposing wave direction. In the following case (blue) VDCP vertical velocity is overpredicted whilst longitudinal velocity sampling accuracy is underpredicted, fluctuating as a function of wavelength (modified by current). In the opposing cases DCP

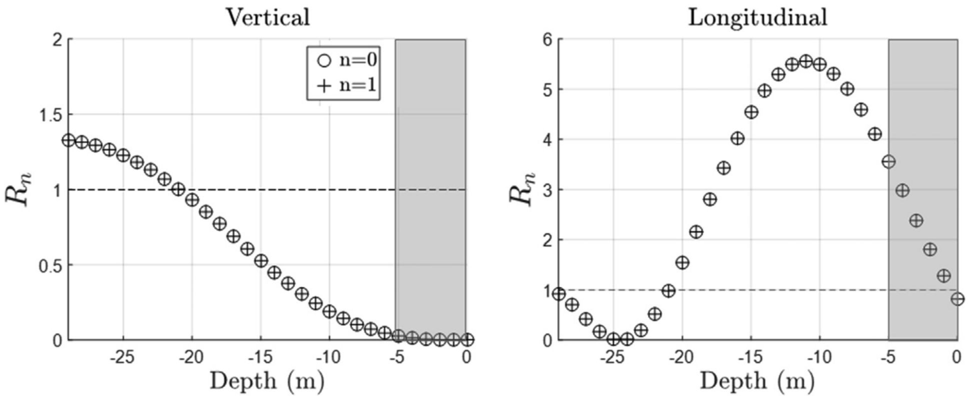

Fig. 2. Sampling accuracy with VDCP sampling depth variation, for a regular wave of 2 m height and 5 s period. Shaded area indicates inaccuracy due to idealisation of surface deformation.

sampling of vertical and longitudinal velocity is increasingly poor as current speed increases. For strong currents opposing these relatively short period (high frequency) waves, wave blocking occurs, as wavenumber extends to infinity.

VDCP sampling accuracy of regular wave orbital velocities has been shown to be dependent on wave phase difference across the instrument. Phase difference is dependent on VDCP sampling depth and orientation, wave period and current speed. Vertical velocities are typically better represented than longitudinal velocities.

3.1.2. Irregular waves

Irregular waves of 2 m significant height and 5 s mean period are simulated using JONSWAP spectra. Fig. 8 shows the ratio of the two longitudinal velocity spectra, (the spectra of the VDCP sampled sub-surface velocities due to wave action and the spectra of the point sampled sub-surface velocities due to wave action) plotted against the phase difference ($d\phi$) resulting from each frequency component (f), at four depths.

$$d\phi(f) = k(f)dx \tag{3.3}$$

A fluctuation in accuracy analogous to that shown in the regular wave case (Fig. 4) is observed, with the result identical at any chosen depth. For in phase frequency components VDCP accuracy is good, whilst those out of phase poorly represent the true wave velocities. There is some noise at the low phase end of the spectrum. This is linked to the low frequency components of the sampled spectra which relate to long period waves. Due to the relatively short timescale (10 mins) of the simulation neither the point or VDCP measurement can accurately capture these long periods wave components.

Vertical and longitudinal velocity VDCP sampling accuracy fluctuate as a function of beam separation and wavelength; this is shown for the longitudinal case in Fig. 9. For irregular waves a phase relationship occurs for each frequency component in the spectrum. Therefore, unlike in the regular wave cases, the accuracy of VDCP sampling does not improve as *mean* phase approaches 2π, since many frequency components of the spectrum remain out of phase. Instead the VDCP continues to over predict the energy in the longitudinal velocity spectrum.

Fig. 10 illustrates the effect of currents of varying strength on following and opposing irregular wave surface elevation spectra.

The effect of a 1/7th power law 2 ms^{-1} mean current speed on both the point measured and VDCP measured longitudinal velocities during following and opposing waves is shown in Fig. 11 at depth −15 m. Energy in the velocity spectra is significantly reduced during opposing waves, and in both cases the VDCP is ineffective at capturing the energy across the entire spectra.

Fig. 12 demonstrates, using spectral moments, the effects of VDCP sampling methods on the velocity spectra (illustrated in Fig. 11) for current velocity increasing from 0 to 4 ms^{-1} for following and opposing waves at −15 m depth. VDCP vertical velocity decreases in accuracy with increasing current velocity, and VDCP longitudinal velocity sampling accuracy decreases asymptotically for the following case, and for the opposing case fluctuates significantly with increasing current velocity.

The results of the VDCP irregular wave model analysis demonstrate phase dependency when sampling horizontal wave orbital velocities by averaging over multiple sample points. Where spatial separation and wave length result in individual samples being in phase, good accuracy is achieved. However very large overestimation and underestimation of velocities can be seen for out-of-phase samples.

3.2. Turbulence

Turbulence is simulated at 1 ms^{-1} mean current velocity with a uniform profile and longitudinal, component length scales of 34 m, 4 m, and 1 m. The length-scales chosen are specific to the current velocity, according to studies conducted in the ReDAPT project (Parkinson and Collier, 2016), for a flood tide at the Falls of Warness in Orkney, UK. Longitudinal, lateral and vertical turbulence intensities are set at 8%, 7.5% and 6%, based upon the same study. The accuracy

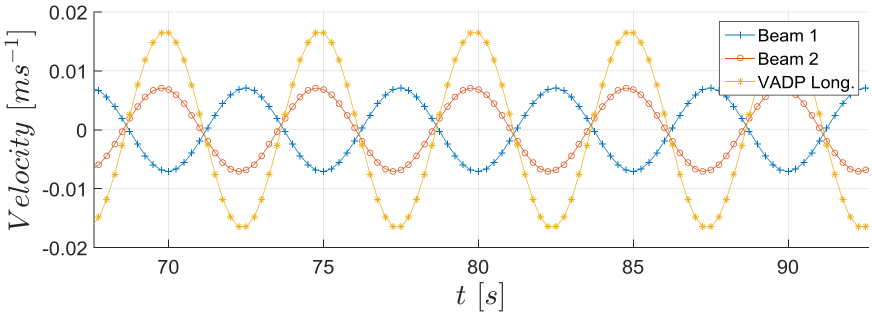

Fig. 3. Along beam velocity sampled at two points on opposing beams and longitudinal velocity measured by VDCP at −20 m depth. Regular wave of height 2 m, and period 5 s.

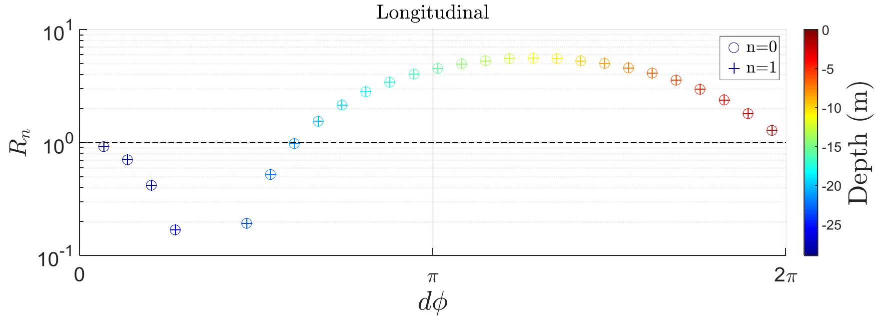

Fig. 4. Longitudinal velocity sampling accuracy with phase difference due to depth variation across upstream and downstream beams, for a regular wave of 2 m height and 5 s period.

of turbulence sampling by the VDCP is initially studied in terms of velocity spectra compared to point samples, and as with the wave case the phase relationship is observed. Associated with the Von Karman turbulence model is an analytical expression for the cross-correlation of points separated in space which is a function of wave-number as presented in equation 2.72.72.7. Therefore, VDCP sampling of the turbulent flow field is affected by beam separation and wave-number. Plotting the ratio of the two longitudinal velocity spectra (the spectra of the VDCP sampled sub-surface velocities and the spectra of the point sampled sub-surface velocities) against the phase difference, as was done for irregular waves, the result is identical for any chosen depth. In Fig. 13 mid-depth (−15 m) is plotted, demonstrating that best sampling accuracy is achieved when frequency components sampled at each beam are in phase ($d\phi = kdx$).

The random nature of turbulence is such that the regular fluctuation in space seen in the model is unlikely to be seen in site data, however it highlights the deficiency of the DCP averaging method for measurement of a turbulence spectrum. Turbulence is highly complex and can be described by numerous parameters. Given that the focus of this work is to accurately replicate tidal flows, the parameters of interest are those which are to be applied to the model. The Von Karman model requires inputs of turbulence intensity in three dimensions, and three components of length scale. Turbulence intensities can be determined from mean longitudinal flow speed, $\bar{u}$, and velocity component standard deviation, σ_i ($i = x, y, z$), taken from DCP averaged velocities. However due to averaging (Section 2.2) the typical three or four beam method is likely to give inaccurate estimates of standard deviation.

$$TI_i = \frac{\sigma_i}{\bar{u}} \tag{3.4}$$

By determining the autocorrelation of the estimated ENU velocities, estimates of longitudinal length scale can be calculated from the field data using the methodology defined in Section 2.1.3. The cross-covariance function (C_{uu}) can be calculated according to the velocity spectra (S_{uu}) such that:

$$C_{uu}(\tau) = \int_0^\infty S_{uu}(f)\cos\,(2\pi f\tau)df \tag{3.5}$$

Eq. (2.9) for the cross-correlation function (ρ_{uu}) can subsequently be re-written:

$$\rho_{uu}(r, r', \tau) = \frac{C_{uu}(r, r', \tau)}{\sigma_u \sigma_u} \tag{3.6}$$

Time-scales are calculated by integrating the cross correlation function up to the shortest time lag for which it falls to zero:

$$T_u = \int_0^{\rho_{uu}=0} \rho_{uu}(\tau)d\tau \tag{3.7}$$

And according to Taylors hypothesis (Taylor, 1937) length-scales are estimated according to mean current velocity ($\bar{u}$). For example, for the longitudinal component (subscript u) in the longitudinal direction (subscript x):

$${}^xL_u = T_u\bar{u} \tag{3.8}$$

Fig. 14 compares longitudinal length scale and turbulence intensity in three dimensions. For each parameter (n), VDCP samples are compared to point samples using the ratio Q_n.

$$\text{For } n = {}^xL_u,\ TI_x,\ TI_y,\ \text{or } TI_z.\ \ Q_n = \frac{n_{VADP}}{n_{point}} \tag{3.9}$$

VDCP sampled estimates of longitudinal length-scale, using the equations described above, consistently underestimate the simulated length-scale. Turbulence intensities are again poorly estimated by the VDCP at most depths.

The method helps in understanding the uncertainty in turbulence parameters measured at site, and the theoretical error can be estimated for any DCP configuration and environmental condition.

3.3. Waves and turbulence

At some sites, there is very low wave activity, and at others wave conditions can be significant. At sites with waves, turbulence para-

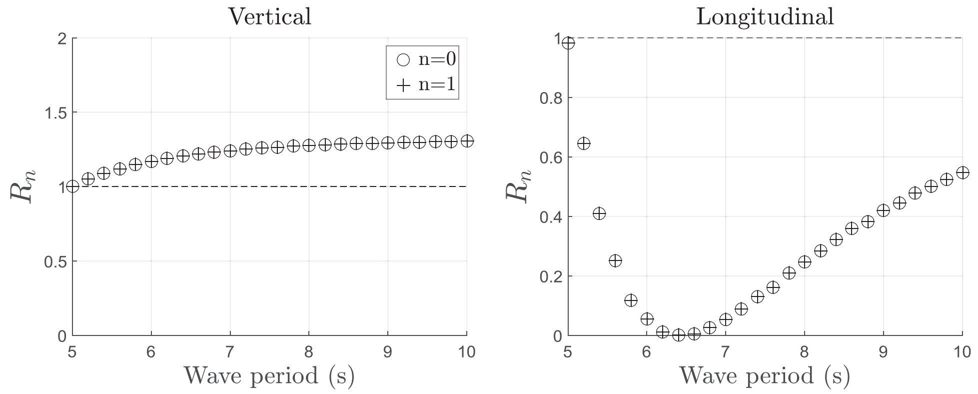

Fig. 5. Sampling accuracy with wave period variation, for a regular wave of 2 m height, sampled at −21 m depth.

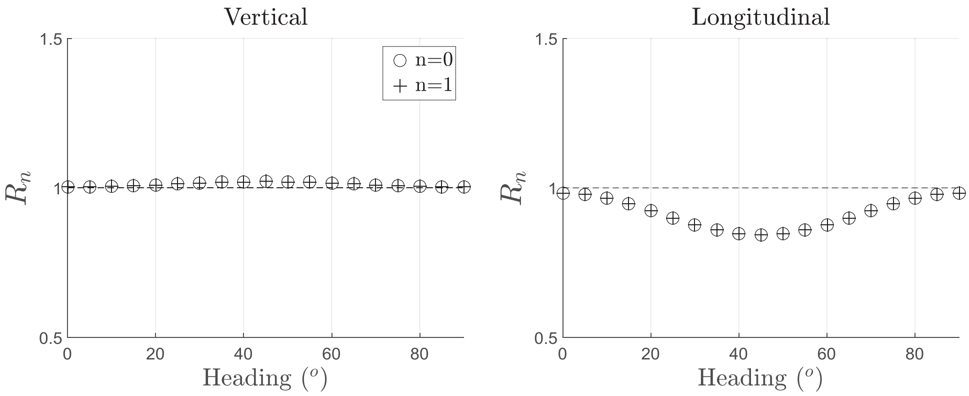

Fig. 6. Sampling accuracy with VDCP heading variation; for a regular wave of 2 m height and 5 s period, sampled at −21 m depth.

meters are best taken from periods of low wave activity, however surveys often aim to cover the more extreme annual weather conditions, and thus, few low wave periods would be present in the record. It is therefore useful to understand the impact of waves on measurement of turbulence conditions such that inputs to model parameters can be modified with an appropriate level of uncertainty attached. Since turbulence will always be present it is useful to understand the impact of turbulence on measurement of wave characteristics across a broader range of conditions.

Using the same turbulence simulation used in the previous example and measuring at −15 m water depth, irregular waves of 5 s period and increasing significant wave height (up to 1 m) are applied. Fig. 15 demonstrates the effect of this variation in wave height on the sampling of turbulence characteristics. Unlike in previous examples VDCP and point sampled estimates are compared to simulation inputs, since point sampled estimates of turbulence characteristics are also affected by changes in the wave conditions. For each parameter (n), point samples and VDCP samples are compared to the simulation input using the ratio Q_{n_s}.

$$\text{For } n = {}^{x}L_u,\ TI_x,\ TI_y, \text{ or } TI_z. \text{ And } s = point, \text{ or } VADP.\quad Q_{(n_s)} = \frac{n_s}{n_{input}} \tag{3.10}$$

As expected, increasing wave height results in considerable increases in the inaccuracy of turbulence intensity measurement, though not on length scale. Wave period variations have similar impact.

Similarly, turbulence influences the measurement of waves. For example, in Fig. 16 the effect of increasing longitudinal turbulence intensity (TI_x) is observed for a 2 m 5 s irregular wave spectrum on a 1 ms^{-1} following current at −15 m depth. The zeroth and first spectral moments are estimated between 0.1 and 0.3 Hz, between which frequencies wave kinematics dominate. Increase in longitudinal turbulence intensity is shown to decrease VDCP estimates of the zeroth and first spectral moments of longitudinal velocity.

4. Discussion

The results have shown several examples that demonstrate the effect of variations in idealised environmental conditions and DCP configuration on sampling accuracy, and clearly demonstrate the difficulty in separating wave and turbulent components from flow measurements for characterisation. Wave sampling accuracy has been shown to be particularly susceptible to sampling depth, wave period and current velocity. Characterisation of turbulence using the VDCP was shown to be poor in many cases, and heavily impacted by the presence of waves.

In this section, significant results are summarized; demonstrating the error (E) between VDCP sampled characteristics and simulated characteristics. The results are presented for a depth of −10 m below the sea surface, where the seabed is at approximately −50 m. This is representative of a likely turbine hub height positioning. The vertical velocity profile of tidal currents is characterised with a 1/7th power law, and turbulence of longitudinal component length scales of 34 m, 4 m, and 1 m and longitudinal, lateral and vertical turbulence intensities of 8%, 7.5% and 6% are applied, as in Section 3.2. The influence of wave height and period, current speed and turbulence intensity are displayed as errors in the appropriate characteristics of each desired parameter. For waves, error is quantified according to differences in first spectral moment, within a range of wave specific frequencies (Δf):

$$\Delta f = 0.1 - 0.3 E_{m1}(\Delta f) = \frac{m_{1VADP}(\Delta f)}{m_{1point}(\Delta f)} \tag{4.1}$$

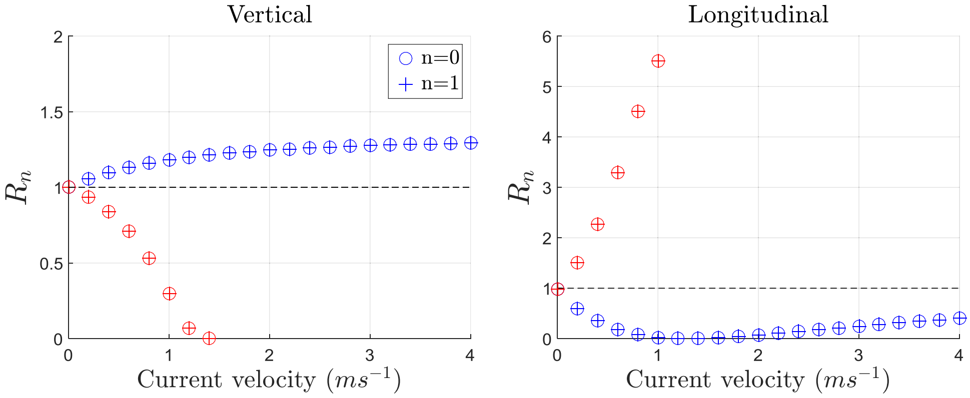

Fig. 7. Sampling accuracy with current speed variation; for a regular wave of 2 m height and 5 s period following (blue) and opposing (red) current direction, sampled at −21 m depth. (For interpretation of the references to color in this figure legend, the reader is referred to the web version of this article.)

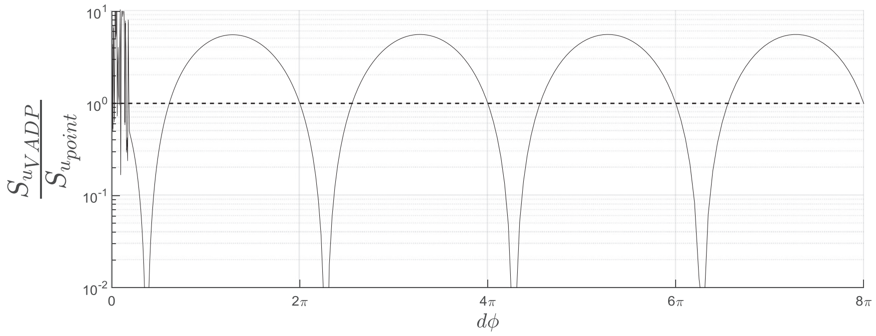

Fig. 8. Longitudinal velocity sampling accuracy for irregular waves: Hs=2 m, Tm=5 s, sampled at −15 m depth.

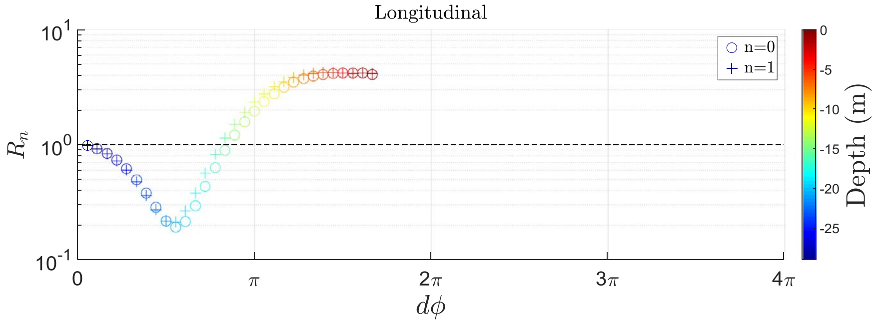

Fig. 9. Longitudinal velocity sampling accuracy with phase difference due to depth variation across upstream and downstream beams, for an irregular wave of 2 m height and 5 s period.

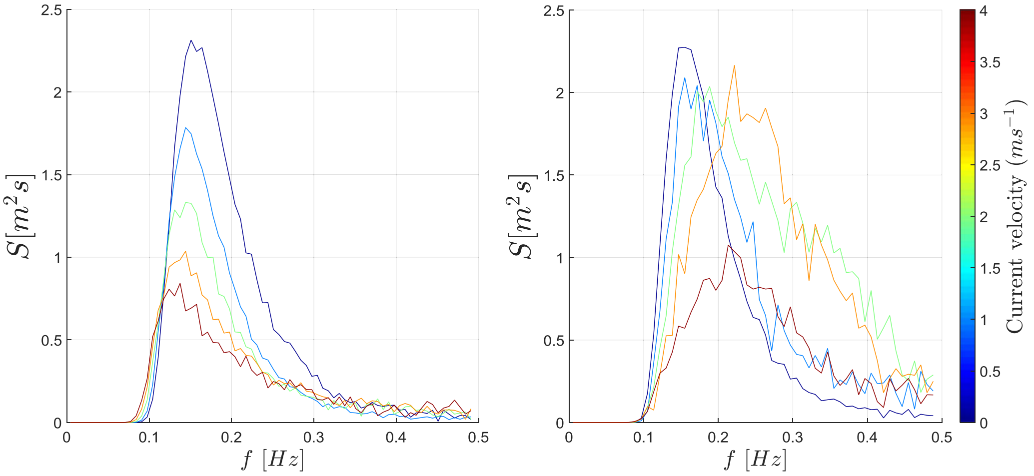

Fig. 10. Following (left) and opposing (right) current velocity effect on surface elevation spectra for irregular 2 m 5 s waves.

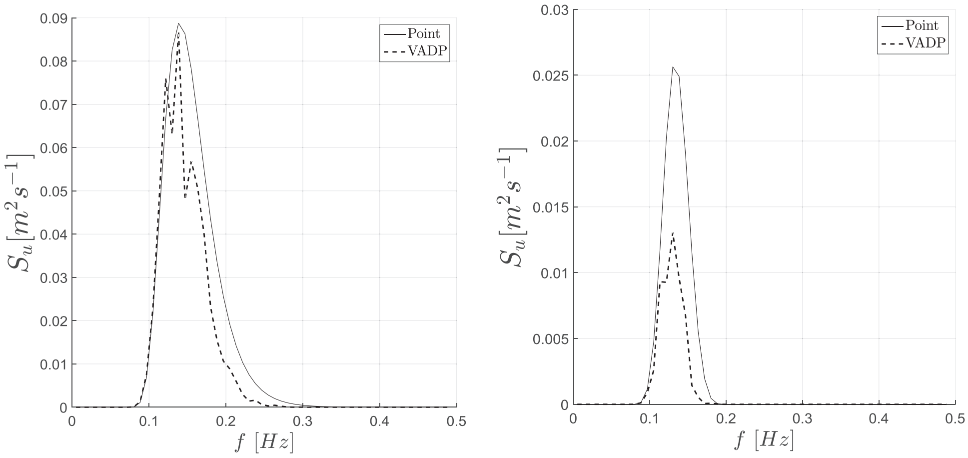

Fig. 11. Comparison of VDCP and point sampled longitudinal velocity spectra for following (left) and opposing (right) 2 m 5 s irregular waves on 2 ms^{-1} mean current at −15 m depth.

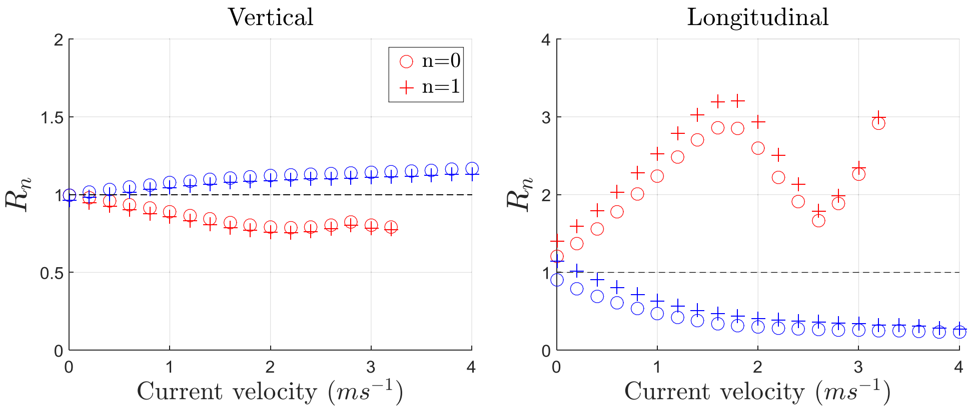

Fig. 12. Velocity sampling accuracy with current speed variation; for an irregular wave of 2 m height and 5 s period following (blue) and opposing (red) current direction, sampled at −15 m. (For interpretation of the references to color in this figure legend, the reader is referred to the web version of this article.)

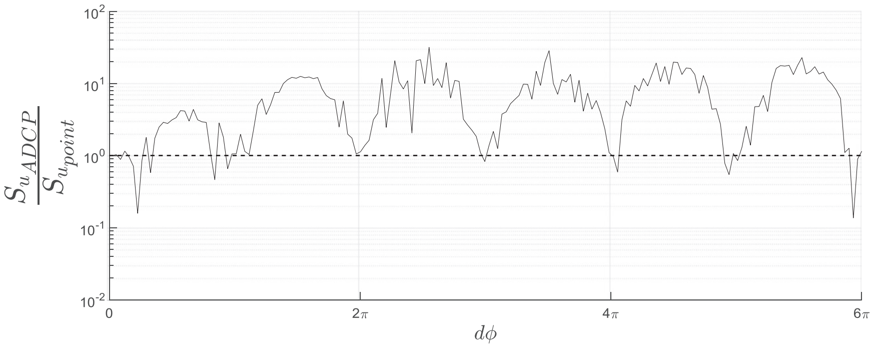

Fig. 13. Longitudinal velocity sampling accuracy with measurement depth for Von Karman turbulence at 1 ms^{-1}, sampled at −15 m depth.

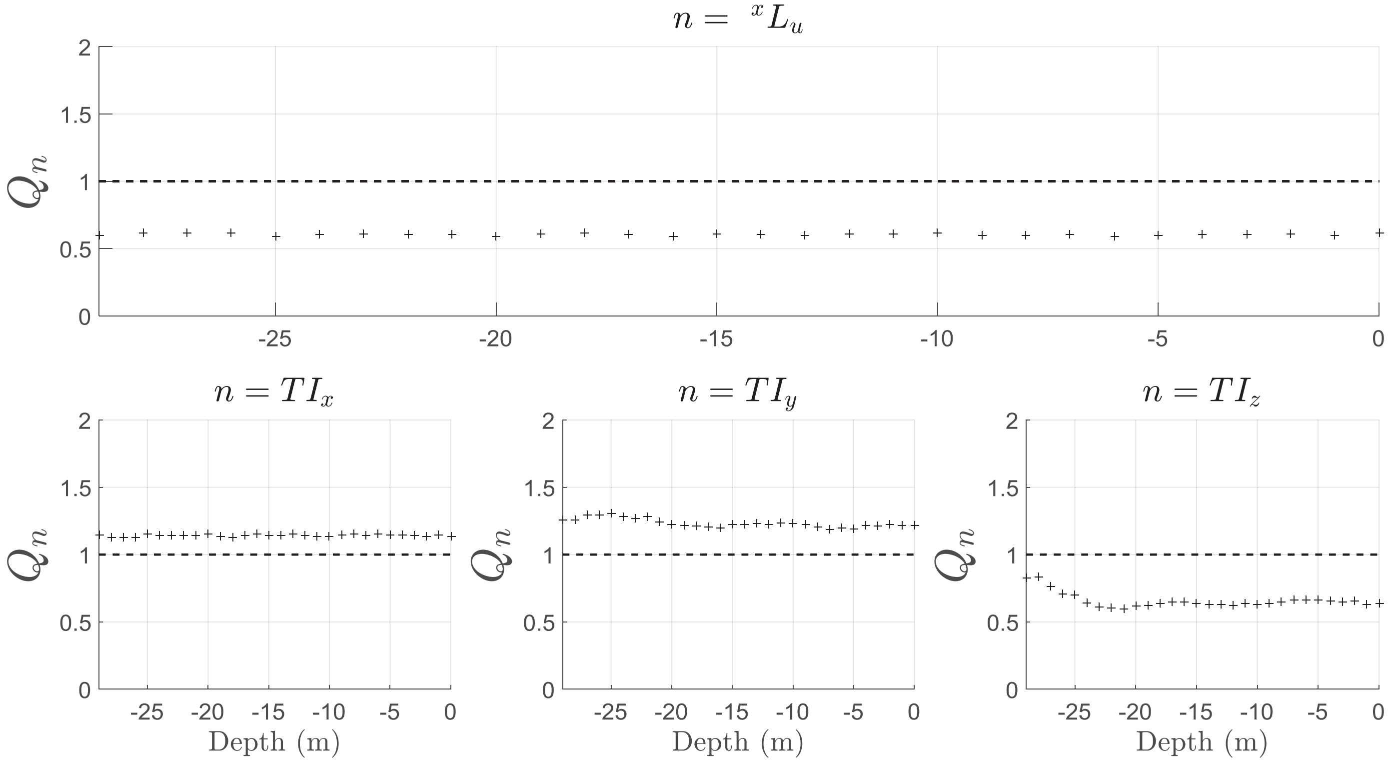

Fig. 14. Turbulence parameter accuracy with measurement depth for 1 ms^{-1} mean current velocity Von Karman turbulence of longitudinal component length scales 30, 4 and 1 m.

Figs. 17 and 18 show the error in the first spectral moments for an irregular JONSWAP spectrum of 3 m significant wave height and 8 s period (on following and opposing turbulent currents respectively) with variations in mean velocity and turbulence intensity. Whilst measures of the spectral moments of vertical velocity display relatively small deviations in accuracy, the spectral moments of longitudinal velocities sampled by the VDCP can be up to 9 times greater than point measurements.

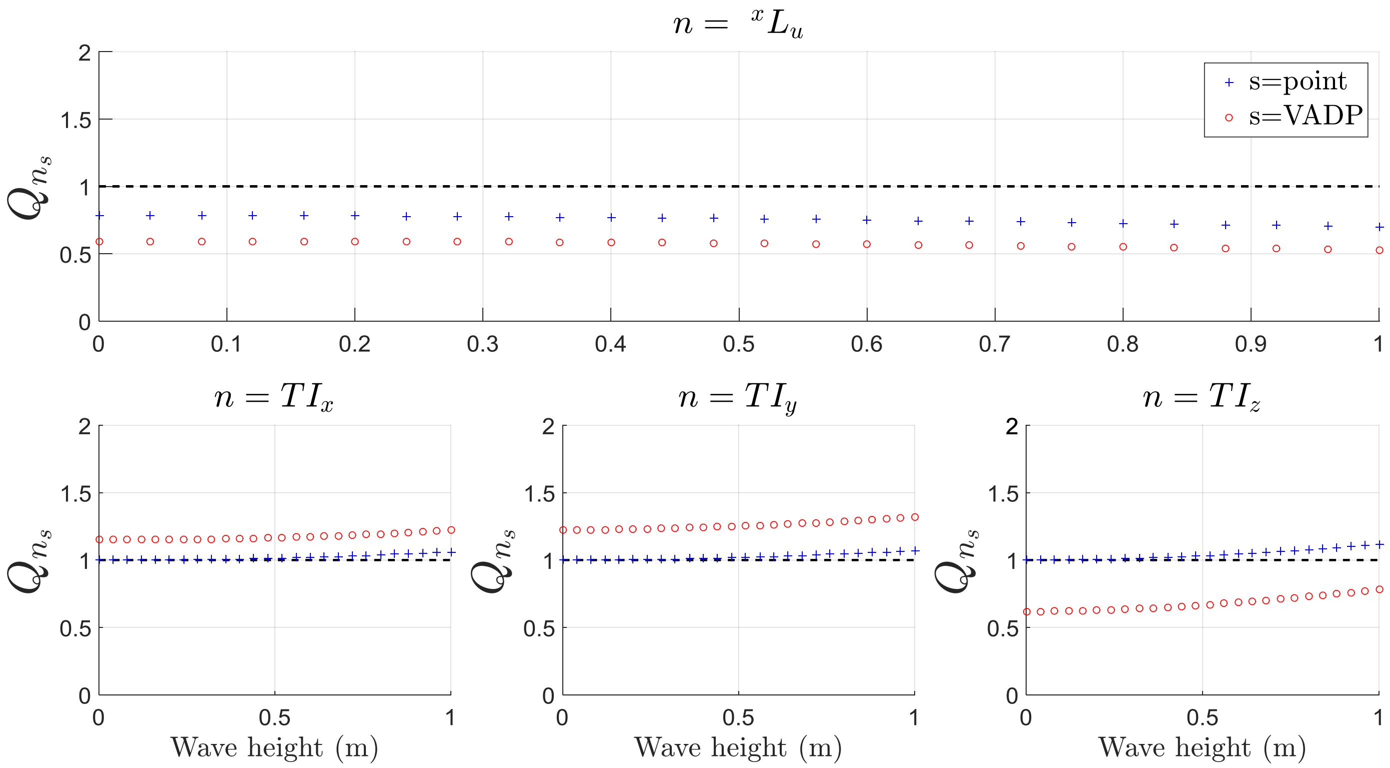

Fig. 15. Turbulence parameter accuracy with wave height for irregular waves of period 5 s, on 1 ms^{-1} mean current velocity, with Von Karman turbulence.

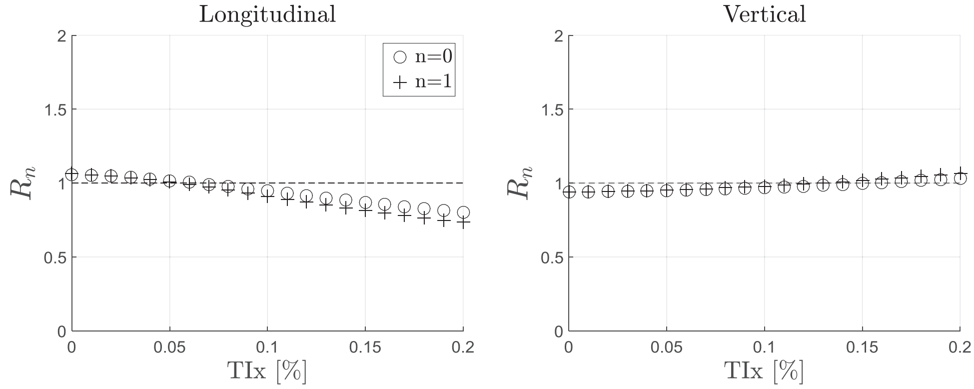

Fig. 16. Turbulence intensity effect on wave measurement, for 2 m 5 s irregular waves following a 1 ms^{-1} turbulent current, sampled at −15 m.

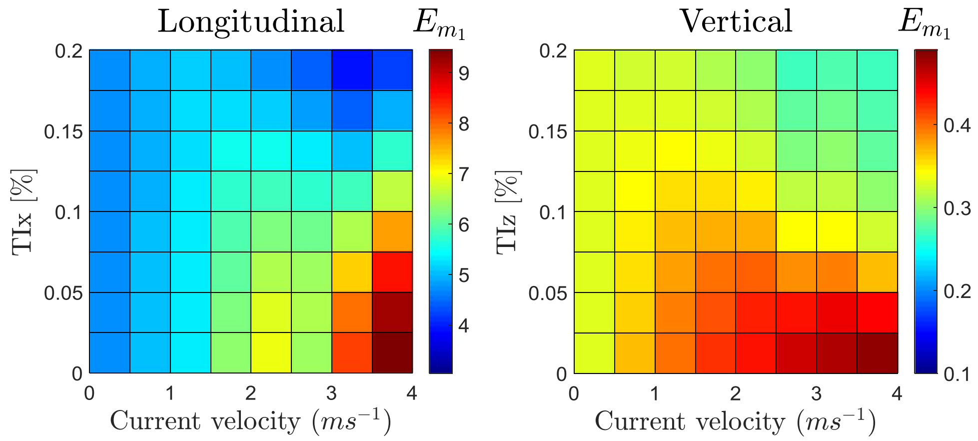

Fig. 17. Error in VDCP sampling of wave velocity spectra, at −10 m sampling depth, for irregular waves of Hs=3 m and Tm=8 on following current with Von Karman turbulence (xLu=30 m, yLu=4 m, zlu=1 m).

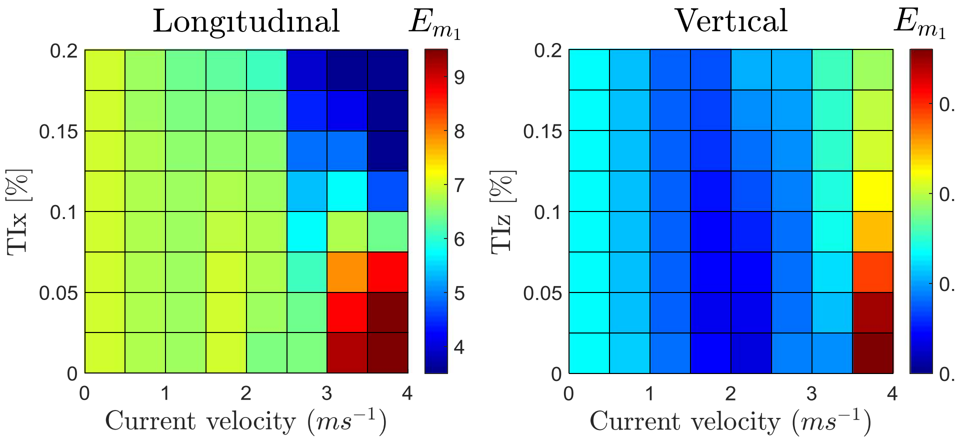

Fig. 18. Error in VDCP sampling of wave velocity spectra, at −10 m sampling depth, for irregular waves of Hs=3 m and Tm=8 on opposing current with Von Karman turbulence (xLu=30 m, yLu=4 m, zlu=1 m).

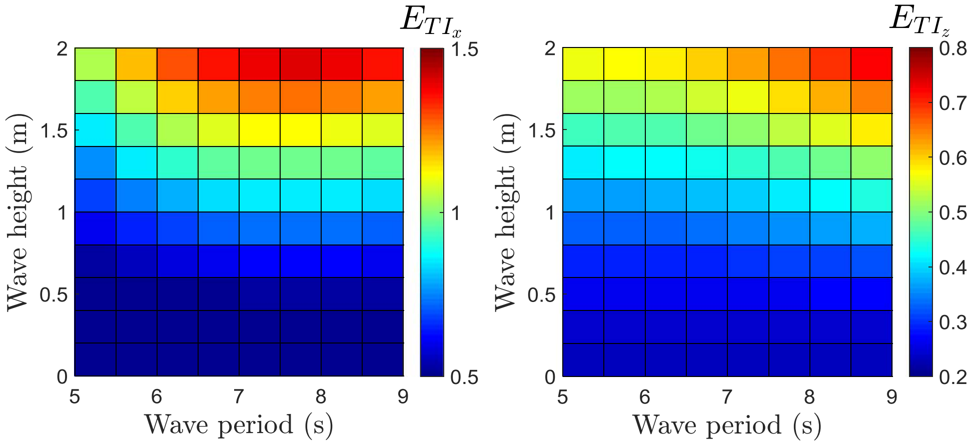

Fig. 19. Error in VDCP sampling of turbulence intensity, at −10 m sampling depth, for irregular waves on following 1 ms^{-1} currents with Von Karman turbulence (xLu=30 m, yLu=4 m, zlu=1 m).

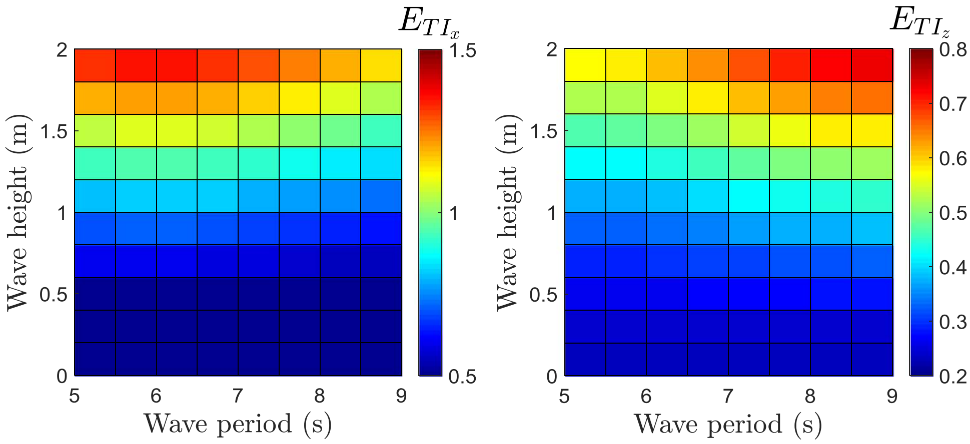

Fig. 20. Error in VDCP sampling of turbulence intensity, at −10 m sampling depth, for irregular waves on opposing 1 ms^{-1} currents with Von Karman turbulence (xLu=30 m, yLu=4 m, zlu=1 m).

Turbulence intensity measurements are limited by averaging effects of the VDCP velocity resolving method, and are also affected in particular by the presence of waves.

$$\text{For turbulence:}(n = x,\ z)E_{TI_n} = \frac{TI_{nVADP}}{TI_{ninput}} \tag{4.2}$$

Figs. 19 and 20 demonstrate the error resulting from variation in significant wave height and mean period on turbulence intensity measurements by the VDCP for an irregular JONSWAP spectrum on turbulent currents described by intensities and length scales described above. Fig. 19 is for waves following current direction and Fig. 20 for waves opposing current direction. Standard deviation (σ_u) in longitudinal velocities used in turbulence intensity calculations (Eq. (3.4)) is increased significantly by the presence of waves, whilst in the vertical is actually diminished by VDCP averaging methods. Note should be made of these results when attempting to calculate turbulence intensity during periods of wave activity, even if wave activity is low.

Length-scales can be calculated from VDCP measurements as

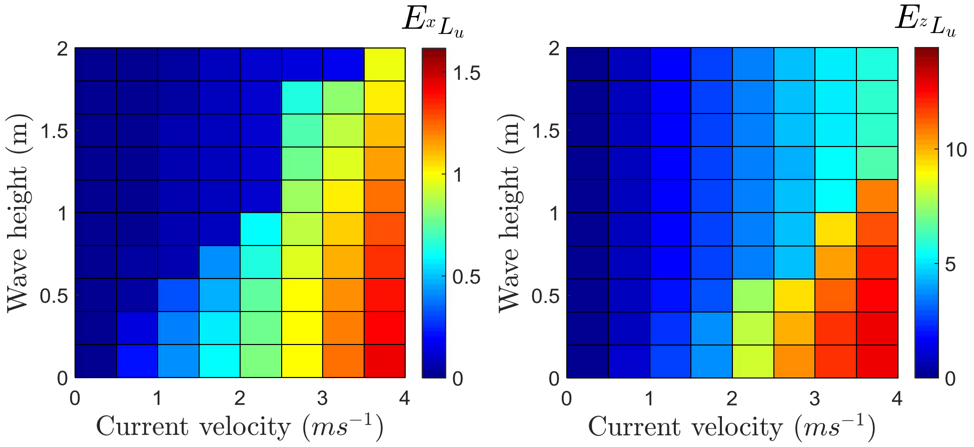

Fig. 21. Error in VDCP sampling of turbulence length scale, at −10 m sampling depth, for irregular waves of Hs=3 m and Tm=8 on following current with Von Karman turbulence (xLu=30 m, yLu=4 m, zLu=1 m).

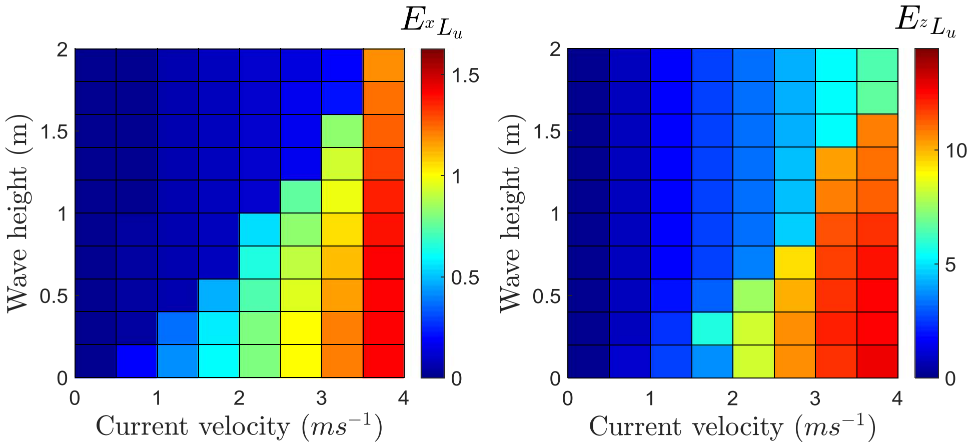

Fig. 22. Error in VDCP sampling of turbulence length scale, at −10 m sampling depth, for irregular waves of Hs=3 m and Tm=8 on opposing current with Von Karman turbulence (xLu=30 m, yLu=4 m, zLu=1 m).

described in Section 3.2. There is typically some error due to VDCP averaging so it is useful to understand the characteristics that influence these errors. Length scale estimation is influenced by a broad range of conditions but most significantly mean current velocity and significant wave height as illustrated in Figs. 21 and 22 which demonstrate these effects for following and opposing currents respectively.

Waves and turbulence particularly influence the fatigue loading of tidal turbine blades (Barltrop et al., 2007; Barltrop and Varyani, 2006; Milne et al., 2010), therefore whilst mean current velocity is well predicted and validated for loads modelling purposes, the results presented will enable more accurate representation of wave and turbulence effects, enabling improvements in design to reduce the impacts of fatigue.

5. Conclusions

Virtual Acoustic Doppler Profiler sampling of idealised model flow conditions has demonstrated limitations of Acoustic Doppler technology in accurately recording the subsurface velocity characteristics of waves and turbulence. Instruments are designed to measure mean current velocities, assuming homogeneity across the volume separating acoustic beams, and therefore whilst mean current velocities are consistently well estimated, some of the details of wave and turbulence kinematics are obscured. Results show that VDCP resolved longitudinal and vertical velocity characteristics of waves and turbulence are typically poorly represented. Longitudinal measurements are typically worse as a result of having fewer beams to average over during estimation and due to the beams' relatively small angle to the vertical. When a wave, or wave component of a specific frequency, is out of phase at the two sampling depths on an upstream and downstream beam, longitudinal velocity measurement error regularly exceeds 100%. Accuracy of wave orbital velocity records are therefore dependent on DCP sampling depth and orientation, as well as wave, current and turbulence variables. Turbulence measurements by the VDCP are also phase dependent, according to turbulence calculated using the "Sandia method", and furthermore accurate recording of turbulence is heavily influenced by the presence of waves.

The VDCP is used to establish theoretical accuracy of wave and turbulence measures, so that for a specific set of field conditions, the uncertainty in measured parameters can be quantified and subsequently modified for inputs to tidal flow models. Spectral moments taken over a range of wave specific frequencies give VDCP sampled longitudinal wave orbital velocities up to 9 times greater than those sampled at a point and vertical wave orbital velocities of as low as 0.1 times, for a range of turbulence intensities and current speeds. VDCP sampled longitudinal turbulence intensity estimates vary between 0.5 and 1.5 times the inputted turbulence intensity dependent on wave height and period conditions whilst vertical turbulence intensity varies between 0.2 and 0.8. Length scales calculated using the autocorrelation function of frequency spectra taken from VDCP measurements vary, in the longitudinal component, between 0.1 and 1.5 times the inputted value, and for the vertical component up to 10 times.

These results are idealised and can vary significantly for the vast range of environmental and configuration conditions that may occur. However, where some of these conditions are known substantial improvements can be made when attempting to estimate input characteristics to flow models combining waves and turbulent currents. The method therefore, enables fair comparison when validating a wave-current model against field measurements, in order that the loads on, and the performance of, tidal turbines can be determined with improved confidence.

Acknowledgements

This work was supported by the Industrial Centre for Offshore Renewable Energy (IDCORE) with funding from the Energy Technologies Institute and the Research Councils Energy Programme [grant number EP/J500847/1] and DNV GL.

References

Neill, S.P., Vögler, A., Baston, A., Goward-Brown, J., Lewis, M.J., Gillibrand, P., Waldman, S., Woolf, D., 2016. The wave and tidal resource of Scotland.

Barltrop, N., Varyani, K.S., Grant, a.D., Clelland, D., Pham, X.P., 2007. Investigation into wave-current interactions in marine current turbines 221, 233–242.

Filipot, J.-F., Prevosto, M., Maisondieu, C., Le Boulluec, M., Thompson, J., 2013. Wave and turbulence measurements at a tidal energy site. Tidal Energy Site.

Gargett, A.E., 1994. Observing turbulence with a modified acoustic doppler current profiler. Atmos. Ocean. Technol. 2, 1592–1610.

Gilcoto, M., Jones, E., Farina-Busto, L., 2009. Robust estimations of current velocities with four-beam broadband ADCPs. Atmos. Ocean. Technol. 26, 2642–2654.

Guerra Paris, M., Thomson, J., 2017. Turbulence measurements from 5-beam acoustic Doppler current profilers. J. Atmos. Ocean. Technol.

Guo, J., 2002. Simple and explicit solution of wave dispersion equation. Coast. Eng. 45 (2), 71–74.

Hasselmann, K., Barnett, T.P., Bouws, E., Carlson, H., Cartwright, D.E., Enke, K., Ewing, J.A., Gienapp, H., Hasselmann, D.E., Kruseman, P., Meerburg, A., Muller, P., Olbers, D.J., Richter, K., Sell, W., Walden, H., 1973. Measurements of wind-wave growth and swell decay during the joint North Sea wave project (JONSWAP). Erganz. Zur. Dtsch. Hydrogr. Z.

Hedges, T.S., 1987. Combinations of waves and currents: an introduction, introduction. pp. 567–585.

Krogstad, H.E., Barstow, S.F., 1999. Directional distributions in ocean wave spectra. Ninth Int. Offshore Polar Eng. Conf.Vol. LID., 79–86.

Lewis, M.J., Neill, S.P., Hashemi, M.R., Reza, M., 2014. Realistic wave conditions and their influence on quantifying the tidal stream energy resource. Appl. Energy 136, 495–508.

Lohrmann, R., Hackett, B., 1990. High resolution measurements of turbulence, velocity and stress using a pulse to pulse coherent sonar. AMS J., 19.

Lu, Y., Lueck, R., 1999. Using a broadband ADCP in a tidal channel. Part I: mean flow and shear. J. Atmos. Ocean. Technol. 16, 1556–1567.

Mackay, E., 2012. Resource assessment for wave energy. Compr. Renew. Energy, 11–77.

Milne, I.A., Sharma, R.N., Flay, R.G.J., Bickerton, S., 2010. The role of waves on tidal turbine unsteady blade loading. 1, 1–6.

Milne, I.A., Sharma, R.N., Flay, R.G.J., Bickerton, S., 2013. Characteristics of the turbulence in the flow at a tidal stream power site.

Muste, M., Yu, K., Spasojevic, M., 2004. Practical aspects of ADCP data use for quantification of mean river flow characteristics; Part I: moving-vessel measurements. Flow. Meas. Instrum. 15 (1), 1–16.

Neill, S.P., Vögler, A., Baston, S., Goward-Brown, A.J., Lewis, M.J., Gillibrand, P., Waldman, S., Woolf, D., 2016a. Wave Tidal Resour. Scotl.

Neill, S.P., Hashemi, M.R., Lewis, M.J., 2016b. Tidal energy leasing and tidal phasing. Renew. Energy 85, 580–587.

Nystrom, E. a., Oberg, K. a., Rehmann, C.R., 2002. Measurement of turbulence with acoustic doppler current profilers - sources of error and laboratory results. Hydraul. Meas. Exp. Methods 2002, 1–10.

Nystrom, E.A., Rehmann, C.R., Oberg, K.A., 2007. Evaluation of mean velocity and turbulence measurements with ADCPs. J. Hydraul. Eng. 133 (12), 1310–1318.

Ott, M., 2002. An improvement in the calculation of ADCP velocities. J. Atmos. Ocean. Technol., 1738–1741.

Parkinson, S., Collier, W., 2016. Model validation of hydrodynamic loads and performance of a full-scale tidal turbine using Tidal Bladed. Int. J. Mar. Energy 16, 279–297.

Souza, A.J., 2010. The use of ADCPs to measure turbulence and SPM in shelf seas. In: Proceedings of the 2nd International Conference Exhib. Underw. Acoust. Meas. Technol. Results.

Stacey, M., 2003. Estimation of Diffusive Transport of Turbulent Kinetic Energy from Acoustic Doppler Current Profiler Data, 927–935.

Stacey, M.T., Monismith, S.G., Burau, J.R., 1999. Measurements of Reynolds stress profiles in unstratified tidal flow. (pp. 933–10)J. Geophys. Res. 104949 (15), (pp. 933–10).

Taylor, G.I., 1937. The spectrum of turbulence. Proc. R. Soc. Soc. 164 (919), 476–489.

Teledyne, R.D.I., 2010. ADCP Coord. Transform.: Formulas Calc.

Tennekes, H., Lumley, J., 1972. A first course in turbulence.

Veers, P., 1988. Three-Dimensional Wind Simulation, Sandia Natl. Lab.

Veritas, Det Norske, 2007. Environ. Conditions Environ. Loads.

Vermeulen, B., Hoitink, a.J.F., Sassi, M.G., 2011. Coupled ADCPs can yield complete Reynolds stress tensor profiles in geophysical surface flows. Geophys. Res. Lett. 38 (6), 2–7.

von Karman, T., 1948. Progress in the statistical theory of turbulence. Proc. Natl. Acad. Sci., 530–539.

Wheeler, J.D., 1969. Method for Calculating Forces Produced by Irregular Waves,.

Wiles, P.J., Rippeth, T.P., Simpson, J.H., Hendricks, P.J., 2006. A novel technique for measuring the rate of turbulent dissipation in the marine environment. Geophys. Res. Lett. 33 (21), L21608.

COMPARISON OF COMBINED WAVE AND TURBULENCE MODEL WITH FIELD MEASUREMENTS.

G. Crossley#1, S. Parkinson*2, A. Alexandre*3, H.C.M. Smith#, A. H. Day#, D. Ingram#

#IDCORE, University of Edinburgh, University of Exeter & University of Strathclyde, UK

1george.crossley@dnvgl.com

**DNV GL Wave & Tidal, Bristol, UK*

Abstract— **Field measured water particle kinematics are used to validate wave-current interactions within a linear model for tidal flows. Using a 'Virtual' Doppler Current Profiler (VDCP), to measure the simulated flow, direct comparisons are made between model and site kinematics recorded using acoustic Doppler technology.**

Flood and ebb currents of a range of magnitudes are considered for following and opposing waves of varying height, measured at approximate turbine hub height. Field and model spectra are compared. Observations of following and opposing cases highlight the interaction between waves and currents and the adequacy of the chosen model. The model achieves good correlation with field records, and the source of discrepancies are highlighted.

Keywords— **Wave, current, interaction, validation, loads.**

I. INTRODUCTION

To optimise the design of tidal stream turbines, many of which will be exposed to sea conditions, robust design procedures are required. This includes the use of validated models to represent current kinematics in the presence of waves and turbulence for pre-construction site specific load calculations. Many early prospected UK sites such as the Sound of Islay, Kyle Rhea [1], and Strangford Lough [2] were sheltered from ocean waves however tidal sites such as the Pentland Firth, Fairhead, and St David's suffer from wave heights which may reach extremes of up to 10m. Impacts on the velocity profile by waves could reduce the theoretical tidal resource by 10% [3], and have a significant effect on blade loads [4].

In order to validate the theory behind the models used to estimate the loads and performance of tidal turbines it is necessary to have field data that is directly comparable to the outputs of a model. Doppler Current Profiler (DCP) technology is commonly used in measurement of subsurface velocities and sea surface elevation. Upward looking devices emit sound pulses from transducers which are reflected by particles suspended in the water column returning a signal to the instrument. The signal is frequency shifted according to the velocity in the pulse direction at which the particle was travelling. By emitting pulses at high frequency and trigonometrically transforming the resultant velocities in combination with two or three other transducer records, a three-dimensional velocity time-series can be calculated. The assumption being that the flow is homogeneous over the volume between the instrument's transducer beams [5]. This is effective for measuring a range of current conditions; however, the smaller fluctuations resulting from waves and turbulence can be obscured by this method [6].

A previous part of this study [7], investigated the limitations and error arising from estimates of wave and turbulence sub-surface velocity characteristics using a 'Virtual' Doppler Current Profiler (VDCP) under a range of environmental and set up conditions. This next part of the study takes flow data from a UK tidal site for development and uses it to validate a tidal flow model. The configuration of the TRDI DCP setup and its positioning at the site are input into the VDCP. Specific sea conditions are selected from the data and fed to the flow model which simulates subsurface velocities based on averaged current, wave and turbulent conditions. The VDCP is used to sample a simulated tidal flow enabling 'beam-to-beam' comparison of model and field kinematics, subsequently eliminating the assumptions made about the flow when resolving to three dimensional velocities.

The paper briefly describes the tidal flow model which combines waves and currents according to Hedges and Phillips, using Von Karman turbulence, combining the theory of Veers and Taylor to formulate a grid of coherent velocities [8]–[12]. Further detail can be found in the preceding study [7]. The VDCP system and the methods used for determining wave and turbulence parameters using an DCP are also explained. This includes a method for correcting measured turbulence characteristics for DCP error. The study then investigates the field-model subsurface velocity comparisons and suggests future work.

II. METHODS

The methodology proposed here incorporates a Virtual Doppler Current Profiler (VDCP), which is designed to be a numerical tool that mimics the measurement technique of a real DCP, instead sampling a simulated flow field to compare directly to DCP measured field data. The field data are first processed and analysed. For every ten-minute data sample the following information is recorded:

- DCP setup: sampling frequency, mean depth, depth bin size and locations.
- DCP orientation: mean heading, pitch, and roll
- Current: mean current velocity (at specified depth), mean current direction, mean velocity depth profile
- Turbulence: Turbulence intensities, Turbulence length-scales
- Waves: Omni-directional and multi-directional surface elevation spectra, mean wave spectral parameters, mean wave directional statistics.

This ten-minute averaged information is corrected for theoretical DCP error where appropriate and fed to the tidal flow model. For the instrument used to collect field data for this study, turbulence intensities and turbulence length scales are corrected. Expansion of this methodology is found in the preceding work [7].

A. Field data

Flow data containing simultaneous measures of subsurface velocity and surface elevation from a UK tidal site for development were measured with a 5 beam TRDI Sentinel V deployed in the winter of 2014/2015. The device records in two modes: ‘waves’ mode and ‘currents’ mode. Each operate at different bin depths: the former concentrating on the top 20m of the water column, with 0.6m bin heights, and the latter over the entire water depth, with 1m bin depths. In this study, which is primarily interested in the interaction between wave and current velocities, ‘waves’ mode is used.

For the duration of the survey, which contains two weeks of good quality data, water depth averages 52m with peak flow at 3.7 ms^{-1} and significant wave height ranging between 0.7 and 5.0 m. Fig. 1 shows mean DCP heading, current magnitude and direction, and wave height and direction. The flood tide heads eastward and ebbs westward. The majority of the waves arrive from the North West approximately following the direction of the flood tide current and opposing it during the ebb tide.

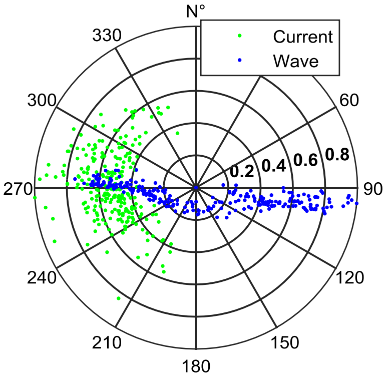

Fig. 1: Current direction with normalised current magnitude, wave direction with normalised significant wave height.

Every ten-minutes of data is processed and quality checked providing the averaged characteristics fed to the model outlined above (II). Frequency spectra for each 2Hz subsurface along beam velocity time-series are calculated and binned according to wave-current relative direction, significant wave height and current speed, as shown in Fig. 2. Significant wave height (Hs) and mean current speed ($\bar{u}$) bins are normalised by peak significant wave height (Hs_p) and peak current speed ($\bar{u}_p$) respectively, and spectra are normalised around the peak field spectral density. These will be directly compared with the simulated beam velocities ‘sampled’ from the tidal flow model by the VDCP.

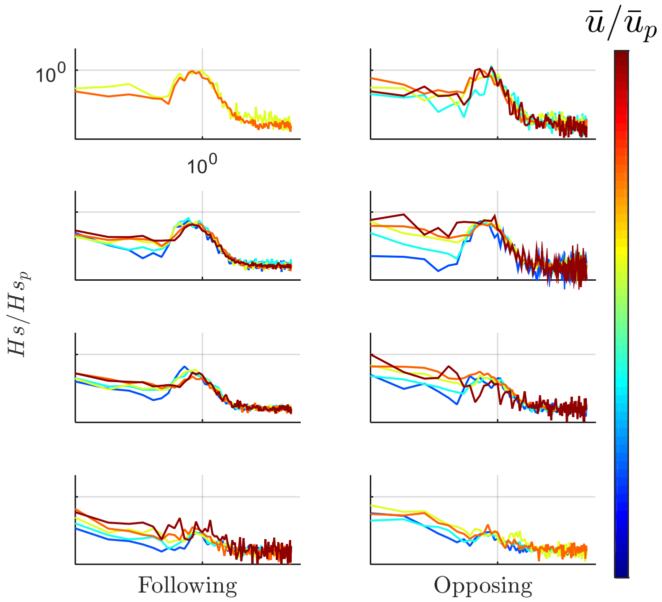

Fig. 2: Normalised along beam (1) field velocity spectra for waves following and opposing current direction for a range of current speeds and significant wave heights. All axes are identical to that labelled in the top right subplot, wave heights (rows) range from 0 to 1 times the peak recorded significant wave height, and mean current speeds (colours) range from 0 to 1 times the peak recorded mean current speed.

Wave and Turbulence characteristics are calculated as follows.

1) *Wave:*

Multi-directional surface elevation spectra are calculated, from which mean wave spectral parameters and mean wave directional statistics can be determined. The spectra are determined using surface elevations recorded by all five beams. Data from the four slanted beams require some smoothing, and then using the VDCP to determine the exact (x,y) locations where beams pierce the surface, the cross spectral matrices are used to estimate the three-dimensional spectra. An Iterative Maximum Likelihood Method is used to determine mean wave direction[13]–[15].

2) *Turbulence:*

Turbulence parameters are taken at specified depths from instances of low wave conditions (i.e. $H_s < 1$ m) using the spectrum of surface elevation and linear turbulence. Turbulence intensity can subsequently be determined from mean current speed ($\bar{u}$), and the velocity component standard deviation (σ_i), calculated from the spectrum (S_i) at frequencies (f), where i represents u, v, or w.

$$TI_i = \frac{\sigma_i}{\bar{u}} \qquad [1.]$$

$$\sigma_i = \sqrt{\int_0^\infty S_i(f)df} \qquad [2.]$$

Turbulence length scale can be calculated from the field data using the auto-covariance (C_{uu}) of the longitudinal component (subscript u) of the velocity spectra (S_{uu}) such that [16]:

$$C_{uu}(\tau) = \int_0^\infty S_{uu}(f)\cos(2\pi f\tau)df \qquad [3.]$$

The auto-correlation function (ρ_{uu}) can subsequently be written:

$$\rho_{uu}(r, r', \tau) = \frac{C_{uu}(r, r', \tau)}{\sigma_u \sigma_u} \qquad [4.]$$

Time-scales are calculated by integrating the auto-correlation function up to the shortest time lag for which it falls to zero:

$$T_u = \int_0^{\rho_{uu}=0} \rho_{uu}(\tau)d\tau \qquad [5.]$$

According to Taylors hypothesis [12] length-scales are estimated according to mean current velocity. For example, for the longitudinal component in the longitudinal direction (superscript x):

$$^{x}L_u = T_u \bar{u} \qquad [6.]$$

Length scales are calculated during low wave conditions for flood and ebb tides, in order that waves do not influence turbulence calculations and can be treated separately.

B. *Simulation of tidal flows*

For this study velocity time series are generated at 2Hz for ten minutes to match the field data. The simulated tidal flow defines a velocity time series of specified length at any desired point within a grid of 0.5m width and height, considering the velocities resulting from waves (U_{wave}), currents ($U_{mean\,flow\,shear}$), and turbulence ($\mathrm{U}_{turbulence}$):

$$U_{total} = U_{mean\,flow\,shear} + U_{wave} + U_{turbulence} \qquad [7.]$$

The wave conditions, turbulence conditions and flow shear are simulated separately and combined linearly to form a time series of velocities generated at a specified frequency. Detail on simulation methodology can be found in preceding work[7] and is summarized below.

1) *Flow shear*

A mean flow shear profile is defined, calculated using the mean velocity at a reference depth according to the power law profile attained from the data survey. The power law exponent is typically chosen to be 1/7, however a value of 0 can also be used to define a uniform current for some of the investigations described in this paper.

2) *Waves*

Three methods can be used to simulate the wave-induced velocities in the flow. The preferred method uses measured multi-directional sea surface elevation data. The second method uses measured omni-directional sea surface elevation data, and the third uses a model spectrum based on estimated sea surface elevation spectral parameters. The RDI Sentinel V used to gather data for this study provides enough information to estimate, every ten-minutes, a multi-directional wave spectrum, hence this, the preferred method, is used to inform the model in this analysis. The spectrum of the stream-wise velocity and the vertical velocity are subsequently derived from the surface elevation spectrum using linear wave theory [17]. Absolute wave number and angular frequency are calculated iteratively using the dispersion relationship according to Guo [18].

3) *Flow turbulence*

Turbulence can be included in the current field model and is synthesised numerically, prior to running the combined flow model, using the "Sandia method" for simulating 3 dimensional flows, described in Veers [11]. A turbulent time history is generated for the current field on a grid of equally spaced points in a 2D plane which spans the y and z-axes. The time history of velocities in three dimensions is generated for each of these points such that each point has correct spectral characteristics and each pair of points has the correct coherence and cross-spectral characteristics. For this model the auto-spectral density is taken from a Von Karman turbulence model with inputs of mean velocity, and nine length-scale parameters. More detail on this method is found in the preceding work[7]. The method assumes Taylor's frozen turbulence hypothesis such that a velocity spectrum can be used to describe the auto-spectral density of the current, and flow coherence is defined empirically.

The Sandia method has been used extensively to describe turbulent boundary layer flow at land sites in order to compute unsteady loads of wind turbines [10]. Given that tidal races are primarily boundary layer flows the same method has been applied in the characterisation of turbulence flow and prediction of unsteady loading for tidal stream turbines. The method has been applied and validated in a number of studies such as in the ReDAPT project [19] and by Milne et al. [20] who suggest that Von Karman velocity spectra can provide an accurate representation of tidal site turbulence.

Turbulence intensities and length scales are calculated from low wave instances in the field data and fitted with trends dependent on mean current velocity. Each trend is then corrected for DCP error dependent on wave height and mean current velocity. Length scale components of the lateral and vertical velocities are estimated based on studies conducted during the ReDAPT project [19].

C. Virtual Doppler Current Profiler

The VDCP is set up in the 'Janus' configuration typically used to collect current data from tidal races, as shown in Fig. 3. The system comprises 4 beams slanted at 25 degrees to the vertical. The tidal flow model simulates velocities at the beam locations for the specified depth in the 'Earth' coordinate system which describes the easting, northing and up-down (ENU) velocities in the standard Eulerian frame of reference. The VDCP converts the simulated velocities at the beam sampling location (u, v, w) into an along beam velocity (b_i). Ten-minute samples of along beam velocity time series, resolved by the VDCP, are then analysed in the frequency domain.

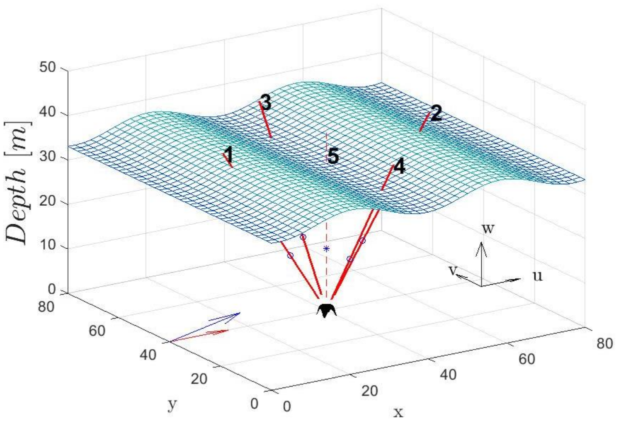

Fig. 3: Illustration of 'Virtual' DCP. Arrows indicate current (red) and wave (blue) directions.

To replicate changes in heading, pitch and roll that may occur in the field DCP a rotation matrix (RM) is applied to the three components of velocity (u, v, w) defined in the simulated flow field. The rotation matrix considers heading (), pitch and roll of the instrument.

$$[u \quad v \quad w] = RM^{-1}[u_0 \quad v_0 \quad w_0] \qquad [8.]$$

Along beam velocities, b_1, b_2, b_3 and b_4 at each specified depth are calculated from the three components of velocity (u, v, w) at their respective grid points, according to the equations below[23], where θ_b refers to the angle of the transducer beams from the vertical. The error velocity (er) is assumed to be zero.

$$\begin{bmatrix} b_1 \\ b_2 \\ b_3 \\ b_4 \end{bmatrix} = M^{-1} \begin{bmatrix} u \\ v \\ w \\ er \end{bmatrix} \qquad [9.]$$

$$M = \begin{bmatrix} a & -a & 0 & 0 \\ 0 & 0 & a & -a \\ b & b & b & b \\ c & c & -c & -c \end{bmatrix} \qquad [10.]$$

$$a = \frac{1}{2sin(\theta_b)} \qquad [11.]$$

$$b = \frac{1}{4cos(\theta_b)} \qquad [12.]$$

$$c = \frac{a}{\sqrt{2}} \qquad [13.]$$

III. RESULTS

As defined in the method (II), DCP setup, orientation, and noise are input to the model. Current, turbulence, and wave conditions for each ten-minute sample are also input to the model. DCP setup and orientation are read directly from the instrument and averaged over the sample. DCP noise is calculated from the measured spectra [24]. Mean current at the specified depth is found using the method defined in section IIA, and turbulence parameters are estimated as in section IIA and corrected for DCP error. In this study the measured multi-directional sea surface elevation spectrum is used as the wave input.

From the field data ten-minute instances are first categorized into flood and ebb. Since in almost all instances waves come from the northeast all following cases used in this study are during the flood tide and all opposing cases are during the ebb tide. Subsequently instances are binned according to mean current speed and significant wave height normalised by peak significant wave height (Hs_p) and peak current speed ($\bar{u}_p$) respectively. For each instance a model case is simulated. The spectral density of each instance at the specified depth is calculated for both field and model velocity data. The data are normalised around the peak field spectral density. This is plotted, as an example, for one particular case in Fig. 4. Multiple instances of along beam spectra within each bin are averaged. In this paper, beam 1 velocities results are presented. Equally, any other beam could be used, with similar parity, due to the VDCP's ability to match the orientation of the field DCP.

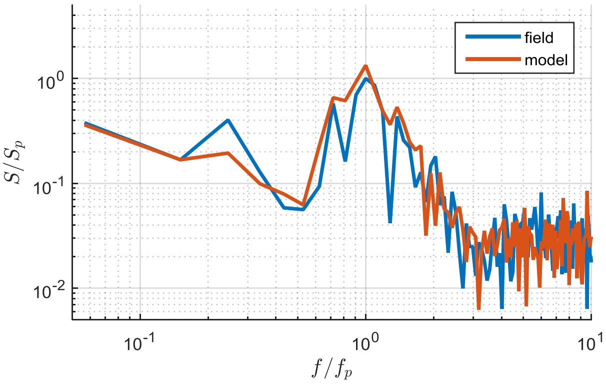

Fig. 4: Example of single instance of normalised field and model along beam(1) velocity spectra at -10m depth for waves of 2m significant height following currents of 2ms^{-1}.

The model described in the methodology (IIB) above compares well with field data for a range of significant wave heights and currents speeds during flood tide as shown in Fig. **5** for a tidal turbine hub height equivalent depth of approximately 10m below the sea surface. With increasing current speed the wave part of the spectrum slightly shifts to higher frequencies in both the field and model data as expected due to the modification of wave number and angular frequency due to currents. The lower frequency, turbulence dominated end of the spectrum is less well predicted due to the limitations in measuring and quantifying turbulence with a DCP and the intrinsic variability in turbulence itself over a range of binned instances.

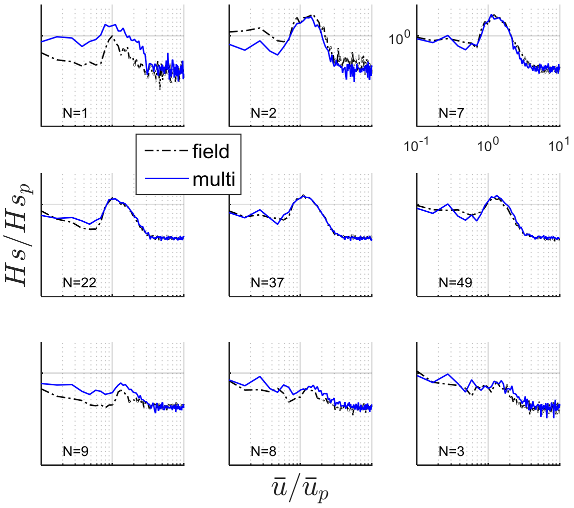

Fig. 5: Field (blue) to model (red) comparison of normalised along beam(1) velocity spectra with normalised significant wave height and normalised current velocity for waves **following** current direction at approx. -10m water depth. *All axes are identical to that labelled in the top right subplot, wave heights (rows) range from 0 to 1 times the peak recorded significant wave height, and mean current speeds (columns) range from 0 to 1 times the peak recorded mean current speed.*

For the wave opposing ebb tide case shown in Fig. 6 the agreement at the low frequency end of the spectrum is less accurate than for the following cases. This discrepancy can be largely attributed to uncertainty in the inputs to the turbulence model which comes as a result of the large variation in turbulence characteristics during the ebb tide (as seen in Fig. 2). Concentrating on the wave part of the spectra, again good agreement is seen between the field and model velocities. At higher current speeds a slight shift to lower frequency is noted in the field and model spectra as expected.

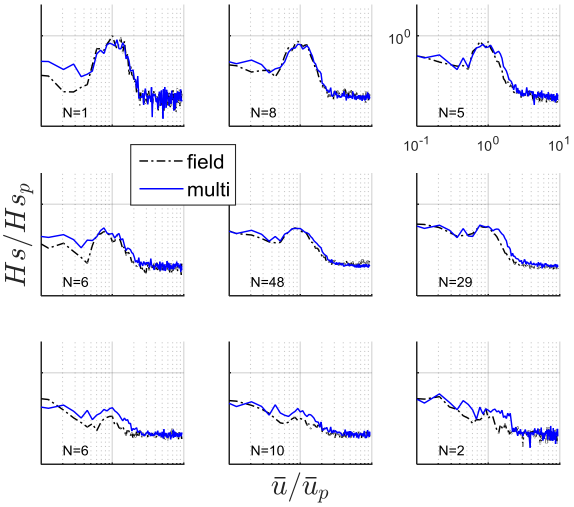

Fig. 6: Field (blue) to model (red) comparison of normalised along beam(1) velocity spectra with normalised significant wave height and normalised

current velocity for waves **opposing** current direction at approx. -10m water depth**.** *All axes are identical to that labelled in the top right subplot, wave heights (rows) range from 0 to 1 times the peak recorded significant wave height, and mean current speeds (columns) range from 0 to 1 times the peak recorded mean current speed.*

Thus far only one depth has been investigated. The depth used was ten meters below the sea surface, a location likely to be occupied by a tidal turbine on a floating structure aiming to maximise the potential of a profiled tidal current. However it is useful to understand the effectiveness of the model at predicting velocities over a larger range of depths. High resolution, simultaneous surface elevation and subsurface velocity records are available for the top twenty meters of the water column. Taking one wave-current bin as an example, the effect of depth on the accuracy of model velocity outputs is investigated. Agreement is comparative across a range of depths, as shown in Fig. 7.

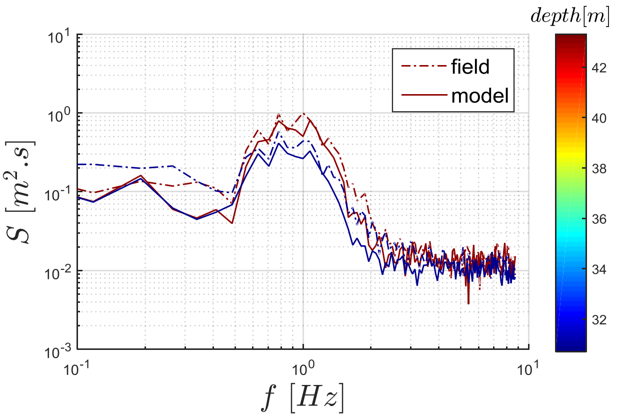

Fig. 7: Field to model comparison of along beam (1) velocity spectra across a range of depths, for medium current, medium wave instances, where waves are **following** the current direction.

To explore the effectiveness of the models representation of field velocities, at a range of depths, for varying wave and current conditions, maximum along beam velocity, and standard deviation of along beam velocity are used as metrics. The two metrics in the time domain are compared in **Fig. 8** and **Fig. 9**. Maxima and standard deviations are largely consistent for a range of depths over a range of wave heights and current speeds, however the slope of the regression is slightly less than one for the majority of cases and decreases with wave height.

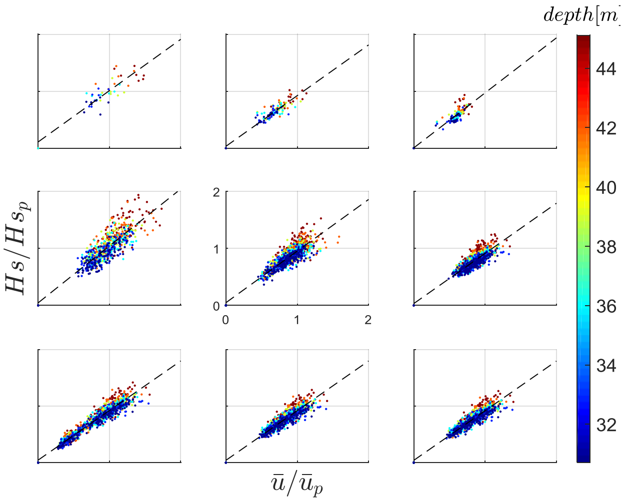

Fig. 8: Field (x-axis) vs model (y-axis), **maxima** of along beam (1) velocity spectra for full range of wave-current instances, over the depths illustrated by the colour bar.

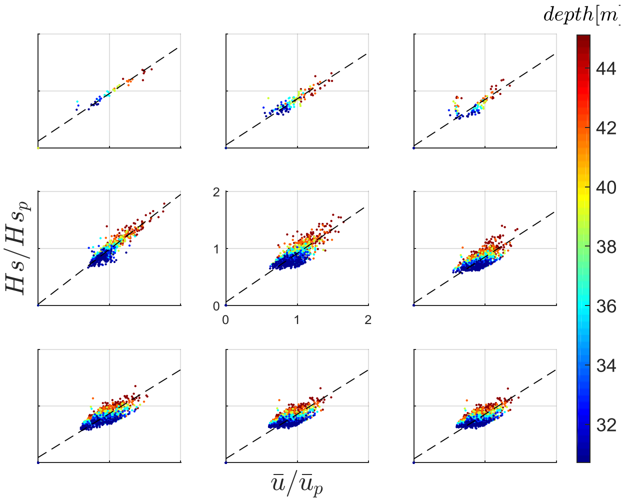

Fig. 9: Field (x-axis) vs model (y-axis), **standard deviations** of along beam (1) velocity spectra for full range of wave-current instances, over the depths illustrated by the colour bar.

IV. Discussion

The results show though visual inspection of spectra that the model can accurately predict subsurface velocities for a range of sea states at the specified depth. Using maxima and standard deviations as metrics to compare between model and field along beam velocities, results indicate that the model again shows agreement with field data over a range of depths, however the trend indicates that at greater depths the model overpredicts velocities, and at shallower depths it under predicts velocities, particularly for smaller wave heights. This is likely to be an effect of the uncertainty in turbulence inputs; however, this study is ongoing and will further explore the effects and interactions of waves and turbulent currents in order to further develop this model.

V. CONCLUSIONS

Hub height velocity spectra measured by a Doppler Current Profiler (DCP) in the field are compared with modelled velocity spectra measured by a 'Virtual' DCP. The method enables circumvention of the assumptions used when calculating three dimensional velocities from divergent beam Doppler instruments, and as such, direct comparison of field and modelled data. Use of the Virtual Doppler current Profiler method has enabled 'like for like' comparisons of along beam field and model velocities. The modelled wave spectra show good agreement with field spectra for a range of wave heights on a range of following and opposing currents. Turbulence parameters input to the model are still subject to some uncertainty (particularly noted during the ebb tide) and are the subject of continuing study.

ACKNOWLEDGMENT

The authors would like to thank DP Energy for supplying the field data and Applied Renewables Research Ltd for their assistance with DCP data analysis. This work was supported by the Industrial Centre for Offshore Renewable Energy (IDCORE) with funding from the Energy Technologies Institute and the Research Councils Energy Programme [grant number EP/J500847/1] and DNV GL.

REFERENCES

[1] S. P. Neill, A. Vogler, A. J. Goward-Brown, S. Baston, M. J. Lewis, P. A. Gillibrand, S. Waldman, and D. K. Woolf, "The wave and tidal resource of Scotland," *Renew. Energy*, 2016.

[2] S. P. Neill, M. R. Hashemi, and M. J. Lewis, "Tidal energy leasing and tidal phasing," *Renew. Energy*, vol. 85, pp. 580–587, 2016.

[3] M. J. Lewis, S. P. Neill, M. R. Hashemi, and M. Reza, "Realistic wave conditions and their influence on quantifying the tidal stream energy resource," *Appl. Energy*, vol. 136, pp. 495–508, 2014.

[4] N. Barltrop, K. S. Varyani, a Grant, D. Clelland, and X. Pham, "Wave-current interactions in marine current turbines," *Proc. Inst. Mech. Eng. Part M J. Eng. Marit. Environ.*, vol. 220, no. 4, pp. 195–203, Jan. 2006.

[5] Y. Lu and R. Lueck, "Using a Broadband ADCP in a Tidal Channel. Part I: Mean Flow and Shear," *J. Atmos. Ocean. Technol.*, vol. 16, pp. 1556–1567, 1999.

[6] E. A. Nystrom, C. R. Rehmann, and K. a. Oberg, "Evaluation of Mean Velocity and Turbulence Measurements with ADCPs," *J. Hydraul. Eng.*, vol. 133, no. 12, pp. 1310–1318, 2007.

[7] G. Crossley, A. Alexandre, S. Parkinson, A. H. Day, H. C. M. Smith, and D. M. Ingram, "Quantifying uncertainty in acoustic measurements of tidal flows using a 'Virtual' Doppler Current Profiler," *Ocean Eng.*, no. January, pp. 1–13, 2017.

[8] T. S. Hedges, "Combinations of waves and currents : an introduction," no. June, pp. 567–585, 1987.

[9] O. M. Phillips, "The equilibrium range in the spectrum of wind-generated waves," *J. Fluid Mech.*, vol. 4, no. 4, p. 426, 1958.

[10] T. von Karman, "Progress in the statistical theory of turbulence," in *Proceedings of the National Academy of Sciences*, 1948, pp. 530–539.

[11] P. Veers, "Three-Dimensional Wind Simulation," *Sandia Natl. Lab.*, 1988.

[12] G. I. Taylor, "The Spectrum of Turbulence," *Proc. R. Soc. Soc.*, vol. 164, no. 919, pp. 476–489, 1937.

[13] M. Benoit, P. Frigaard, and H. A. Schaffer, "Analysing multidirectional wave spectra- a tentative classification of available methods," 1997.

[14] Y. Goda, *Random seas and design of maritime structures*. 2010.

[15] J. Cruz, *Ocean Wave Energy*. Springer, 2008.

[16] K. Eaton, R. Harris, J. Jones, T. Lawson, and J. Woods, "Characteristics of atmospheric turbulence near the ground. Part I: Definition and General information.," *Eng. Sci. Data Unit 74030*, 1974.

[17] E. Mackay, "Resource Assessment for Wave Energy.," in *Comprehensive Renewable Energy*, 2012, pp. 11–77.

[18] J. Guo, "Simple and explicit solution of wave dispersion equation," *Coast. Eng.*, vol. 45, no. 2, pp. 71–74, 2002.

[19] S. Parkinson and W. Collier, "Model validation of hydrodynamic loads and performance of a full-scale tidal turbine using Tidal Bladed," *Int. J. Mar. Energy*, vol. 16, pp. 279–297, 2016.

[20] I. A. Milne, R. N. Sharma, R. G. J. Flay, and S. Bickerton, "Characteristics of the turbulence in the flow at a tidal stream power site," no. January, 2013.

[21] E. a. Nystrom, K. a. Oberg, and C. R. Rehmann, "Measurement of Turbulence with Acoustic Doppler Current Profilers - Sources of Error and Laboratory Results," *Hydraul. Meas. Exp. Methods 2002*, pp. 1–10, 2002.

[22] M. Muste, K. Yu, and M. Spasojevic, "Practical aspects of ADCP data use for quantification of mean river flow characteristics; Part I: Moving-vessel measurements," *Flow Meas. Instrum.*, vol. 15, no. 1, pp. 1–16, 2004.

[23] Teledyne RDI, "ADCP Coordinate Transformation: formulas and calculations," 2010.

[24] J. Richard, J. Thomson, B. Polagye, and J. Bard, "Method for Identification of Doppler Noise Levels in Turbulent Flow Measurements Dedicated to Tidal Energy."

References

Anderson, J. (1998), *A History of Aerodynamics*, Cambridge University Press.

Andritz Hydro Hammerfest (2017), 'Andritz Hydro Hammerfest'.
URL: *http://www.andritzhydrohammerfest.co.uk/*

Atlantis Resources Limited (2017), 'Atlantis Resources'.
URL: *https://www.atlantisresourcesltd.com/*

Barber, N. F. (1948), 'The behaviour of waves on tidal streams', *Proc. R. Soc.* **198**, 82–93.

Barltrop, N. & Varyani, K. (2006), 'Wave-current interactions in marine current turbines', **220**, 195–203.
URL: *http://eprints.gla.ac.uk/15258/*

Barltrop, N., Varyani, K., a.D. Grant, Clelland, D. & Pham, X. (2007), 'Investigation into wave-current interactions in marine current turbines', **221**, 233–242.
URL: *http://dx.doi.org/10.1243/09576509JPE315*

Barltrop, N., Varyani, K. S., Grant, a., Clelland, D. & Pham, X. (2006), 'Wave-current interactions in marine current turbines', *Proc. Inst. Mech. Eng. Part M J. Eng. Marit. Environ.* **220**(4), 195–203.
URL: *http://pim.sagepub.com/lookup/doi/10.1243/14750902JEME45*

Barltrop, N., Varyani, K. S., Grant, A. D., Clelland, D. & Pham, X. P. (2007), 'Investigation into wave-current interactions in marine current turbines', *Proc. Inst. Mech. Eng. Part A J. Power Energy* **221**(2), 233–242.
URL: *http://dx.doi.org/10.1243/09576509JPE315*

Benoit, M., Frigaard, P. & Schaffer, H. A. (1997), Analysing multidirectional wave spectra- a tentative classification of available methods, Proc. seminar on multidirectional waves and their interaction with structures.

Bijker, E. W. (1967), 'Some considerations about scales for coastal models with movable bed', *Delft Hydraul. Lab.* **50**, 142.

Boccotti, P. (2015), *Wave Mechanics and Wave Loads on Marine Structures.*

Bretherton, F. P. & Garrett, C. J. R. (1969), 'Wavetrains in inhomogeneous moving media', *Proc. R. Soc.* **302**, 529–554.

Burton, T., Sharpe, D., Jenkins, N. & Bossanyi, E. (2001), *Wind Energy Handbook.*

Clark, T., Roc, T., Fisher, S. & Minns, N. (2015), Turbulence : Best Practices for the Tidal Power Industry in turbine and array engineering, Technical report, Partrac, Ocean Array Systems, ABP Mer, ITP, The Scottish Government, Carbon Trust.

Crossley, G., Alexandre, A., Parkinson, S., Day, A. H., Smith, H. C. & Ingram, D. M. (2017), 'Quantifying uncertainty in acoustic measurements of tidal flows using a 'Virtual' Doppler Current Profiler', *Ocean Eng.* (January), 1–13.
URL: *http://linkinghub.elsevier.com/retrieve/pii/S0029801817302007*

Cruz, J. (2008), *Ocean Wave Energy*, Springer.

Dalrymple, R. (1977), 'A Numerical Model for Periodic Finite Amplitude Waves on a Rotational Fluid', **24**, 29–42.

Dalrymple, R. a. (1974), 'A finite amplitude wave on a linear shear current', *J. Geophys. Res.* **79**(30), 4498–4504.
URL: *http://doi.wiley.com/10.1029/JC079i030p04498*

Dean, R. G. (1965), 'Stream Function Representation', **70**(18).

Det Norske Veritas (2007), 'ENVIRONMENTAL CONDITIONS AND ENVIRONMENTAL LOADS', (APRIL).

DNV GL (2015), Tidal Turbines Standard DNVGL-ST-0164, Technical Report October.

Downing, S. D. & Socie, D. F. (1982), 'Simple rainflow counting algorithms', *Int. J. Fatigue* **4**(1), 31–40.

Eastwood, J. & Watson, C. (1989), 'Implications of wave current interactions for offshore design'.

Edmunds, M., Malki, R., Williams, A. J., Masters, I. & Croft, T. N. (2014), 'Aspects of tidal stream turbine modelling in the natural environment using a coupled BEM – CFD model', *Int. J. Mar. ENERGY* pp. 1–23.
URL: *http://dx.doi.org/10.1016/j.ijome.2014.07.001*

Ewans, K. C. (1998), 'Observations of the Directional Spectrum of Fetch-Limited Waves', **28**, 495–512.

Ewans, K. C. (2001), Directional Spreading in Ocean Swell, *in* 'Proc. Ocean Wave Meas. Anal.', pp. 517–529.

Faudot, C. & Dahlhaug, O. G. (2012), 'Prediction of Wave Loads on Tidal Turbine Blades', *Energy Procedia* **20**, 116–133.
URL: *http://linkinghub.elsevier.com/retrieve/pii/S1876610212007448*

Fenton, J. D. (1990), 'Nonlinear Wave Theories', **9**.

Filipot, J.-F., Prevosto, M., Maisondieu, C., Boulluec, M. L. & Thompson, J. (2013), 'Wave and turbulence measurements at a tidal energy site'.

Fleming, C. & Willden, R. (2013), 'Influence of free surface waves on the performance and wake structure of a horizontal axis tidal turbine', *Energy Technol. Inst. PerAWaT* pp. 1–62.

Fredsoe, J. (1984), 'Turbulent boundary layer in wave-current motion', *Hydr. Eng.* **110**, 1103–1120.

Galloway, P. W. (2013), Performance Quantification of Tidal Turbines Subjected to Dynamic Loading, PhD thesis.

Gargett, A. E. (1994), 'Observing Turbulence with a Modified Acoustic Doppler Current Profiler', *Atmos. Ocean. Technol.* **2**, 1592–1610.

Garrad Hassan (2012), 'Tidal Bladed'.

Gaurier, B., Davies, P., Deuff, A. & Germain, G. (2013), 'Flume tank characterization of marine current turbine blade behaviour under current and wave loading', *Renew. Energy* **59**, 1–12.
URL: *http://dx.doi.org/10.1016/j.renene.2013.02.026*

Gilcoto, M., Jones, E. & Farina-Busto, L. (2009), 'Robust Estimations of Current Velocities with Four-Beam Broadband ADCPs', *Atmos. Ocean. Technol.* **26**, 2642–2654.

Goda, Y. (2010), *Random seas and design of maritime structures.*

Guerra Paris, M. & Thomson, J. (2017), 'Turbulence measurements from 5-beam acoustic Doppler current profilers', *J. Atmos. Ocean. Technol.* **In Review**.

Guo, J. (2002), 'Simple and explicit solution of wave dispersion equation', *Coast. Eng.* **45**(2), 71–74.

Hashemi, M. R., Neill, S. P., Robins, P. E., Davies, A. G. & Lewis, M. J. (2015), 'Effect of waves on the tidal energy resource at a planned tidal stream array', *Renew. Energy* **75**, 626–639.
URL: *http://www.sciencedirect.com/science/article/pii/S0960148114006569*

Hasselmann, K., Barnett, T. P., Bouws, E., Carlson, H., Cartwright, D. E., Enke, K., Ewing, J. A., Gienapp, H., Hasselmann, D. E., Kruseman, P., Meerburg, A., Muller, P., Olbers, D. J., Richter, K., Sell, W. & Walden, H. (1973), 'Measurements of Wind-Wave Growth and Swell Decay during the Joint North Sea Wave Project (JONSWAP)', *Erganzungsh. zur Dtsch. Hydrogr. Zeitschrift* .

Hedges, T. S. (1987), 'Combinations of waves and currents : an introduction', (June), 567–585.

Hedges, T. S. & Lee, B. W. (1992), 'The equivalent uniform current in wave-current computations', **16**, 301–311.

Herbers, T. H. C. & Lentz, S. J. (2010), 'Observing directional properties of ocean swell with an acoustic doppler current profiler (ADCP)', *J. Atmos. Ocean. Technol.* **27**(1), 210–225.

Hoitink, A. J. F. & Schroevers, M. (2004), 'Validation of ADCP surface wave measurements in a shelf sea', *Ocean. '04 MTS/IEEE Techno-Ocean '04 (IEEE Cat. No.04CH37600)* **3**, 1444–1451.

Holthuijsen, L. H. (2007), 'Waves in Oceanic and Coastal Waters'.

Isobe, M. & Kondo, K. (1984), Method for estimating directional wave spectrum in incident and reflected wave field, *in* 'Proc. 19th Conf. Coast. Eng.', chapter 32, pp. 467–483.
URL: *http://journals.tdl.org/icce/index.php/icce/article/viewArticle/3813*

Jesus Henriques, T. a. D., Tedds, S. C., Botsari, a., Najafian, G., Hedges, T. S., Sutcliffea, C. J., Owen, I. & Poole, R. J. (2014), 'The Effects of Wave-Current Interactions on the Performance of a Model Horizontal Axis Tidal- Stream Turbine', *Int. J. Mar. Energy* **8**, 17–35.
URL: *http://dx.doi.org/10.1016/j.ijome.2014.10.002*

Jonsson, I., Skougaard, C. & Wang, J. (1970), 'Interaction between waves and currents', *Coast. Eng. ...* .
URL: *http://journals.tdl.org/icce/index.php/icce/article/viewArticle/2634*

Kaimal, J. C., Wyngaard, J. C., Izumi, Y. & Cote, O. R. (1972), 'Spectral characteristics of surface-layer turbulence', (98), 563–589.

Kemp, P. H. & Simons, R. R. (1983), 'The interaction of waves and a turbulent current: waves propagating against the current', *J. Fluid Mech.* **130**(1), 73.
URL: *http://www.journals.cambridge.org/abstract_S0022112083000981*

Klopman, G. (1994), Vertical Structure of the Flow due to Waves and Currents, Technical report.

Kobune, K. & Hashimoto, N. (1986), 'Estimation of directional spectra from the maximum entropy principle'.

Kokkinowrachos, K. (1980), Offshore-Bauwerke, *in* 'Handb. der Werften XV. Band'.

Krogstad, H. E. & Barstow, S. F. (1999), 'Directional Distributions In Ocean Wave Spectra', *Ninth Int. Offshore Polar Eng. Conf.* **lID**, 79–86.
URL: *https://www.onepetro.org/conference-paper/ISOPE-I-99-237*

Lewis, M., Neill, S., Hashemi, M. & Reza, M. (2014), 'Realistic wave conditions and their influence on quantifying the tidal stream energy resource', *Appl. Energy* **136**, 495–508.
URL: *http://linkinghub.elsevier.com/retrieve/pii/S0306261914010095*

Lewis, M., Neill, S. P., Robins, P., Hashemi, M. R. & Ward, S. (2016), 'Characteristics of the velocity profile at tidal-stream energy sites', *Renew. Energy* pp. 1–15.
URL: *http://dx.doi.org/10.1016/j.renene.2017.03.096*

Lohrmann, Hackett, R. (1990), 'High resolution measurements of turbulence, velocity and stress usinga pulse to pulse coherent sonar'.

Lu, Y. & Lueck, R. (1999*a*), 'Using a Broadband ADCP in a Tidal Channel. Part I: Mean Flow and Shear', *J. Atmos. Ocean. Technol.* **16**, 1556–1567.

Lu, Y. & Lueck, R. (1999*b*), 'Using a Broadband ADCP in a Tidal Channel. Part II: Turbulence', *Atmos. Ocean. Technol.* **16**, 1568–1579.

Lucas, C. & Soares, C. G. (2015), 'Bivariate distributions of significant wave height and mean wave period of combined sea states', *Ocean Eng.* **106**, 341–353.
URL: *http://dx.doi.org/10.1016/j.oceaneng.2015.07.010*

Luznik, L., Flack, K. a., Lust, E. E. & Taylor, K. (2013), 'The effect of surface waves on the performance characteristics of a model tidal turbine', *Renew. Energy* **58**, 108–114.
URL: *http://linkinghub.elsevier.com/retrieve/pii/S0960148113001316*

Lygre, a. & Krogstad, H. E. (1986), 'Maximum entropy estimation of the directional distribution in ocean wave spectra'.

Mackay, E. (2012), Resource Assessment for Wave Energy., *in* 'Compr. Renew. Energy', pp. 11–77.

Mann, J. (2006), 'The spatial structure of neutral atmospheric surface-layer turbulence', *J. Fluid Mech.* **273**(-1), 141.
URL: *http://www.journals.cambridge.org/abstract_S0022112094001886*

Markus, D., Wüchner, R. & Bletzinger, K.-U. (2013), 'A numerical investigation of combined wave current loads on tidal stream generators', *Ocean Eng.* **72**, 416–428.
URL: *http://linkinghub.elsevier.com/retrieve/pii/S0029801813003223*

Mathisen, J. A. N. (1990), 'Joint distributions for significant wave height and wave zero-up-crossing period', **12**(2), 93–103.

Mccann, G. N. (2007), 'Tidal current turbine fatigue loading sensitivity to waves and turbulence: a parametric study .'.

McNaughton, J., Rolfo, S., Apsley, D., Afgan, I., Stansby, P. & Stallard, T. (2012), CFD prediction of turbulent flow on an experimental tidal stream turbine using RANS modeling., *in* '1st Asian Wave Tidal Energy Conf. Jeju Island, Korea'.

Méhauté, B. L. (n.d.), *An introduction to hydrodynamics and water waves*, Springer.

MeyGen (2013), 'The Project'.
URL: *http://www.meygen.com/the-project/*

Milne, I. A., Day, A. H., Sharma, R. N. & Flay, R. G. J. (2012), Horizontal-axis tidal turbine blade loading for multi-frequency oscillatory motion, *in* '18th Australas. Fluid Mech. Conf.'.

Milne, I. A., Day, A. H., Sharma, R. N. & Flay, R. G. J. (2013), 'Blade loads on tidal turbines in planar oscillatory flow', *Ocean Eng.* **60**, 163–174.
URL: *http://linkinghub.elsevier.com/retrieve/pii/S0029801812004465*

Milne, I. A., Day, A. H., Sharma, R. N., Flay, R. G. J. & Bickerton, S. (2011), Tidal Turbine Blade Load Experiments for Oscillatory Motion, *in* '9th Eur. Wave Tidal Energy Conf.'.

Milne, I. A., Sharma, R. N., Flay, R. G. J. & Bickerton, S. (2010), 'A Preliminary Analysis of the Effect of the Onset Flow Structure on Tidal Turbine Blade Loads', pp. 1–8.

Milne, I. A., Sharma, R. N., Flay, R. G. J. & Bickerton, S. (2013), 'Characteristics of the turbulence in the flow at a tidal stream power site', (January).

Muste, M., Yu, K. & Spasojevic, M. (2004), 'Practical aspects of ADCP data use for quantification of mean river flow characteristics; Part I: Moving-vessel measurements', *Flow Meas. Instrum.* **15**(1), 1–16.

Musumeci, R. E., Cavallaro, L., Foti, E., Scandura, P. & Blondeaux, P. (2006), 'Waves plus currents crossing at a right angle: Experimental investigation', *J. Geophys. Res.* **111**(C7), C07019.
URL: *http://doi.wiley.com/10.1029/2005JC002933*

Neill, S. P., Hashemi, M. R. & Lewis, M. J. (2016), 'Tidal energy leasing and tidal phasing', *Renew. Energy* **85**, 580–587.
URL: *http://dx.doi.org/10.1016/j.renene.2015.07.016*

Neill, S. P., Vogler, A., Goward-Brown, A. J., Baston, S., Lewis, M. J., Gillibrand, P. A., Waldman, S. & Woolf, D. K. (2016), 'The wave and tidal resource of Scotland', *Renew. Energy* .

Nerzic, R., Frelin, C. & Prevosto, M. (2007), 'Joint distributions of Wind / Waves / Current in West Africa and derivation of multivariate extreme I-FORM contours', pp. 36–42.

Nichols, B. D. & Hirt, C. W. (1973), 'Calculating three-dimensional free surface flows in the vicinity of submerged and exposed structures', *Comput. Phys.* **12**(2), 234–246.

Nortek (2008), System Integrator Guide, Technical Report June.

Nortek (2016), 'Nortek'.
URL: *http://www.nortek-as.com/*

Nystrom, E. a., Oberg, K. a. & Rehmann, C. R. (2002), 'Measurement of Turbulence with Acoustic Doppler Current Profilers - Sources of Error and Laboratory Results', *Hydraul. Meas. Exp. Methods 2002* pp. 1–10.
URL: *http://ascelibrary.org/doi/abs/10.1061/40655(2002)55*

Nystrom, E. A., Rehmann, C. R. & Oberg, K. a. (2007), 'Evaluation of Mean Velocity and Turbulence Measurements with ADCPs', *J. Hydraul. Eng.* **133**(12), 1310–1318.

Olabarrieta, M., Medina, R. & Castanedo, S. (2010), 'Effects of wave-current interaction on the current profile', *Coast. Eng.* **57**, 643–655.

Ott, M. (2002), 'An Improvement in the Calculation of ADCP Velocities', *J. Atmos. Ocean. Technol.* pp. 1738–1741.

Parkinson, S. & Collier, W. (2016), 'Model validation of hydrodynamic loads and performance of a full-scale tidal turbine using Tidal Bladed', *Int. J. Mar. Energy* **16**, 279–297.
URL: *http://linkinghub.elsevier.com/retrieve/pii/S2214166916300534*

Pawka, S. S. (1982), Wave directional characteristics on a partially sheltered coast, PhD thesis.

Pedersen, T., Lohrmann, A. & Krogstad, H. E. (2005), 'WAVE MEASUREMENT FROM A SUBSURFACE PLATFORM', (2), 1–10.

Pedersen, T., Malzone, C. & Siegel, E. (2005), 'Analysis of band-passed directional wave data', *Proc. MTS/IEEE Ocean. 2005* **2005**, 1–8.

Pedersen, T. & Nylund, S. (2004), 'Wave height measurements using acoustic surface tracking', *USA-Baltic Int. Symp.* pp. 1234–1241.

Pedersen, T. & Siegel, E. (2006), 'Directional Wave Measurements from a Subsurface Buoy with an Acoustic Wave and Current Profiler (AWAC)'.

Peregrine, D. H. & Thomas, G. P. (1978), 'Finite-amplitude deep-water waves on currents', *Proc. R. Soc.* .

Phillips, O. M. (1958), 'The equilibrium range in the spectrum of wind-generated waves', *J. Fluid Mech.* **4**(04), 426.

Phillips, O. M., George, W. K. & Mied, R. P. (1968), 'On the interaction between internal gravity waves and a shear flow', *Deep Sea Res.* **15**, 267–273.

RDI (2001), 'Waves User's Guide'.

Richard, J.-b., Thomson, J., Polagye, B. & Bard, J. (n.d.), 'Method for Identification of Doppler Noise Levels in Turbulent Flow Measurements Dedicated to Tidal Energy'.

Rippeth, T. P., Simpson, J. H., Williams, E. & Inall, M. E. (2003), 'Measurement of the Rates of Production and Dissipation of Turbulent Kinetic Energy in an Energetic Tidal Flow: Red Wharf Bay Revisited', *J. Phys. Oceanogr.* **33**(9), 1889–1901.
URL: *http://dx.doi.org/10.1175/1520-0485(2003)033%3C1889:MOTROP%3E2.0.CO%5Cn2*

Robinson, B. M. E. & Tawn, J. A. (1997), 'Statistics for Extreme Sea Currents', (2).

Sabella (2017), 'Sabella'.
URL: *http://www.sabella.fr*

Souza, A. J. (2010), 'The use of ADCPs to measure turbulence and SPM in shelf seas', *2nd Int. Conf. Exhib. Underw. Acoust. Meas. Technol. Results* .

Srisuwan, C. & Work, P. a. (2013), 'Directional surface wave spectra from acoustic Doppler current profiler data in sheared and stratified flows', *Ocean Eng.* **72**, 149–159.
URL: *http://linkinghub.elsevier.com/retrieve/pii/S0029801813002424*

Srokosz, M. (1985), 'Wave-Current Interaction - A review of some problems'.
URL: *http://adsabs.harvard.edu/abs/1985STIN...8622910S*

Stacey, M. (2003), 'Estimation of Diffusive Transport of Turbulent Kinetic Energy from Acoustic Doppler Current Profiler Data', pp. 927–935.

Stacey, M. T., Monismith, S. G. & Burau, J. R. (1999), 'Measurements of Reynolds stress profiles in unstratified tidal flow', *J. Geophys. Res.* **104949**(15), 933–10.

Stewart, R. W. & Longuet-Higgins, M. S. (1960), 'The changes in amplitude of short gravity waves on steady non-uniform currents'.

Strong, B., Brumley, B., Stone, G. W. & Introduction, I. (2000), 'The Performance of ADCP-Derived Directional Wave Spectra and Comparison with Other Independent Measurements III . Performance Considerations', pp. 1195–1203.

Swan, C. (1972), A stream function solution for waves on a strongly sheared current, chapter 51, pp. 684–697.

Taylor, G. I. (1937), 'The Spectrum of Turbulence', *Proc. R. Soc. Soc.* **164**(919), 476–489.

Teledyne RDI (2010), ADCP Coordinate Transformation: formulas and calculations, Technical report.

Tennekes, H. & Lumley, J. (1972), *A first course in turbulence.*
URL: *http://books.google.com/books?hl=en&lr=&id=h4coCj-lN0cC&oi=fnd&pg=PR11&dq=A+FIRST+COURSE+IN+*

Thomson, J., D'Asaro, E. a., Cronin, M. F., Rogers, W. E., Harcourt, R. R. & Shcherbina, a. (2013), 'Waves and the equilibrium range at Ocean Weather Station P', *J. Geophys. Res. Ocean.* **118**(11), 5951–5962.
URL: *http://doi.wiley.com/10.1002/2013JC008837*

Tocardo (2017), 'Tocardo Tidal Power'.
URL: *http://www.tocardo.com/*

Togneri, M., Masters, I. & Orme, J. (2011), 'Incorporating Turbulent Inflow Conditions in a Blade Element Momentum Model of Tidal Stream Turbines', **8**, 757–762.

Tucker, M. J. & Pitt, E. G. (2001), *Waves in Ocean Engineering.*

Umeyama, M. (2005), 'Reynolds Stresses and Velocity Distributions in a Wave-Current Coexisting Environment', (October), 203–213.

Unna, P. J. H. (1942), 'Waves and Tidal Streams', *Nature* **149**(3773), 219–220.

Van der Kaaij, T. & Nieuwjaar, M. W. C. (1987), 'Sediment concentrations and sediment transport in case of irregular non-breaking waves with a current'.

Veers, P. (1988), 'Three-Dimensional Wind Simulation', *Sandia Natl. Lab.* .

Vermeulen, B., Hoitink, a. J. F. & Sassi, M. G. (2011), 'Coupled ADCPs can yield complete Reynolds stress tensor profiles in geophysical surface flows', *Geophys. Res. Lett.* **38**(6), 2–7.

Visser, P. J. (1986), 'Wave basin experiments on bottom friction due to current and waves', pp. 807–821.

von Karman, T. (1948), Progress in the statistical theory of turbulence, *in* 'Proc. Natl. Acad. Sci.', pp. 530–539.

Waais, O., Aalbers, A. B. & Pinkster, J. A. (2002), 'Maximum Likelihood Method As a Means To Estimate the Directional Wave Spectrum and the Mean Wave Drift Force on a Dynamically Positioned Vessel', *Offshore (Conroe, TX)* pp. 1–9.

Way, S. & Collier, W. (2012), 'INITIAL VALIDATION OF TIDAL BLADED MODELLING OF THE TGL 500KW TIDAL TURBINE'.

Wheeler, J. D. (1969), 'Method for Calculating Forces Produced by Irregular Waves'.

Whitham, G. (1974), *Linear and Nonlinear Waves.*

Wiles, P. J., Rippeth, T. P., Simpson, J. H. & Hendricks, P. J. (2006), 'A novel technique for measuring the rate of turbulent dissipation in the marine environment', *Geophys. Res. Lett.* **33**(21), L21608.
URL: *http://doi.wiley.com/10.1029/2006GL027050*

Glossary

ADV Acoustic Doppler Velocimeter. 50

AST Acoustic Surface Tracking. 35, 38, 49

auto -spectra Spectrum of the correlation of a time-series with itself. 37

beam the sound emitted from an acoustic transducer. 31

cross -spectra Spectrum of the correlation of two time-series. 37

DCP Doppler Current Profiler. 36, 49

dispersion (frequency dispersion) waves of different wavelengths travelling at differing phase speeds. 9

EI Echo Intensity. 39, 40

ENU East, North, Up (velocities). 32, 33, 51, 53

FFT Fast Fourier Transform. 37

HRCP High Resolution Current Profiler. 50

incompressible Incompressible flow (isochoric flow) refers to a flow in which the material density is constant within a fluid parcel—an infinitesimal volume that moves with the flow velocity.. 7

inviscid Not viscous; having no viscosity. An inviscid flow is the flow of an ideal fluid that is assumed to have no viscosity. In fluid dynamics there are problems that are easily solved by using the simplifying assumption of an inviscid flow.. 7

irrotational Irrotational flow has no rotation, or vorticity. The velocity field is therefore a conservative one where the curl of velocity is zero. Vorticity acts as a measure of local rotation. This does not imply anything about the global behaviour of the fluid.. 7

Janus Refers to the 4 beam configuration of a DCP. 33, 36, 51

MLM Maximum Likelihood Method. 36

Nyquist The Nyquist frequency, named after electronic engineer Harry Nyquist, is half of the sampling rate of a discrete signal processing system.. 38

PUV Pressure, U (i.e. longitudinal velocity), V (i.e. lateral velocity). 38

SBD Single Beam Doppler. 51

SNR Signal to Noise Ratio. 36, 37

SUV Surface, U (i.e. longitudinal velocity), V (i.e. lateral velocity). 36, 38

Swell (Swell waves are surface gravity waves not generated by the immediate local wind, instead by distant weather systems, where wind blows for a duration of time over a fetch of water. Therefore a swell consists of wind-generated waves that are not—or are hardly—affected by the local wind at that time. Swell waves often have a long wavelength dependant on the size, strength and duration of the weather system and the size of the water body responsible for the swell. Swells have a narrower range of frequencies and directions than locally generated wind waves, because swell waves have dispersed from their generation area, have dissipated and therefore lost an amount of randomness, taking on a more defined shape and direction in the conservation of energy.. 13